This is to certify that the
dissertation entitled

EXPLORATORY SYNTHESIS OF COMPLEX INTERMETALLIC GERMANIDES AND INDIDES USING MOLTEN INDIUM AS A FLUX

presented by

MARIA CHONDROUDI

has been accepted towards fulfillment
of the requirements for the

Ph.D degree in Chemistry

Major Professor's Signature

3/23/09

Date

EXPLORATORY SYNTHESIS OF COMPLEX INTERMETALLIC GERMANIDES AND INDIDES USING MOLTEN INDIUM AS A FLUX

VOLUME I

By

Maria Chondroudi

A DISSERTATION

Submitted to
Michigan State University
in partial fulfillment of the requirements
for the degree of

DOCTOR OF PHILOSOPHY

Chemistry

2009

ABSTRACT

EXPLORATORY SYNTHESIS OF COMPLEX INTERMETALLIC GERMANIDES AND INDIDES USING MOLTEN INDIUM AS A FLUX

By

Maria Chondroudi

Molten metal fluxes can be excellent alternative to the conventional synthetic methods for the exploratory synthesis of new intermetallic compounds. Our group has initiated a project where molten Al and Ga are used to investigate the reactivity of the quaternary systems RE/TM/Al/Si or Ge and RE/TM/Ga/Si or Ge which has resulted in a numerous new ternary and quaternary phases. We have recently expanded this work to also include molten In as a synthetic medium in parallel to Al and Ga systems. The main goal of this dissertation was to exploit the ability of liquid In as a reactive flux in the system RE/TM/Ge/In and discover new complex multinary compounds that could exhibit interesting structural features as well as chemical and physical properties.

Particularly we have performed explorations in the system RE/Co(Ni)/Ge/In and we have succeeded in isolating two new quaternary compounds: the $RE_7Co_4InGe_{12}$ and $Yb_7Ni_4InGe_{12}$. Their 3D-network features three different types of channels, propagating along the *c*-axis, in which the Yb atoms are situated. The Yb analogs exhibit mixed-valence behavior and the Yb^{3+}/Yb^{2+} ratio is slightly temperature dependent. Interestingly, the reaction targeting the $Dy_7Co_4InGe_{12}$ member also produced the $Dy_4CoInGe_4$ phase which crystallizes as a new structure-type. The $Dy_4CoInGe_4$ structure is related to the $RE_7TM_4InGe_{12}$ structure and possesses 12-membered and 5-membered channels propagating along the *b*-axis in which the Dy atoms are found and $Co_2Ge(1)_2$ ribbons.

$Dy_4CoInGe_4$ exhibits ferromagnetic ordering at ~ 40 K and a complex magnetic behavior below this temperature.

By studying the system RE/Au/Ge/In we obtained three new quaternary compounds $Yb_3AuGe_2In_3$, CeAuGeIn and $EuAuGeIn_2$. $Yb_3AuGe_2In_3$ crystallizes as an ordered variant of the YbAuIn structure. Both Yb compounds, which were studied in parallel, are intermediate- or mixed-valence compounds and display intriguing magnetic properties which are strongly dependent on the form of the measured sample and other experimental conditions and vary from being paramagnetic to exhibit ferromagnetic ordering. The ordered orthorhombic CeAuGeIn and the disordered tetragonal $EuAuGeIn_2$ compounds have closely related layered structures. Both compounds seem to undergo antiferromagnetic and ferromagnetic transitions below 12 K whereas $EuAuGeIn_2$ shows possible additional magnetic structures as seen in the low field magnetic measurements.

Synthetic investigations of the systems Yb/TM/Ge in liquid In resulted in the particularly interesting Yb_4TMGe_8 (TM = Fe, Cr, Co) compounds for which (3+1)D crystallography revealed the existence of superstructures due to modulated Ge nets and partial TM occupancies. All three compounds exhibit Yb mixed-valence behavior with the valence constantly changing with the temperature and anomalous thermal expansion behavior below ~ 100 K. Additionally, heat capacity measurements for the Cr analog suggest possible heavy-fermion behavior whereas resistivity measurements for the Fe analog show unusual temperature dependence.

Finally, explorations in the ternary systems RE/Cu(Ag)/In led to the formation of the $RECu_{6+x}In_6$ and $YbAg_{5.18}In_{6.83}$ compounds which the crystallize as an orthorhombic variant of the $ThMn_{12}$ structure-type. The Yb analogs exhibit mixed-valence behavior.

ACKNOWLEDGMENTS

First and foremost I would like to express my deep and sincere gratitude to my advisor, Professor Mercouri G. Kanatzidis, for giving me guidance and encouragement both as mentor and a friend during my PhD years. I am grateful to him for the opportunity to work at Argonne National Laboratory (ANL) for the last two years where I had the opportunity to grow and mature as a scientist and to access facilities not otherwise available at Michigan State University.

I would also like to thank my committee members, Professors Smith, Weliky, Mahanti and Duxbury for their valuable suggestions and discussions. My collaborators and mentors both at MSU and at the Materials Science Division at ANL Dr Lolee, Dr Mitchell, Dr Gray, Dr Clauss, Dr Q'Li, Dr Welp, Dr Schlueter, Dr Kwok, Dr Osborne and many others. I owe special thanks to Dr Balasubramanian at the Advanced Photon Source at ANL for being an exceptional collaborator, mentor and friend and for being willing to work endless hours day and night with me at the beamline.

It would have not been possible for me to succeed without the unconditional love and support of my parents who have dedicated their lives into giving the highest education and opportunities to their kids. The love, faith and advice from my brothers Stelios and Kostas and my dearest friend D. Rivera helped me through the tough and demanding years of my Ph.D study.

Finally, I would like to thank all the Kanatzidis group members for their help and friendship particularly, Dr Malliakas for breaking down all the crystallographic mysteries, Dr Salvador and Dr Todorov.

TABLE OF CONTENTS

LIST OF TABLES

LIST OF FIGURES

CHAPTER 1

Introduction

1-1. Introduction to Intermetallics, Selected Properties and Applications

Solid state chemistry is a multidisciplinary field that deals with the synthesis, structural determination and physical properties characterization of various solids, and it has been playing an increasingly significant role in the design and preparation of new advanced materials. Solid state compounds have been the foundation of the electronics industry for many years and contribute extensively in many other emerging technologies, such as microelectronics, nonlinear optics, superconductivity, thermoelectric and photovoltaic energy conversion and storage, nanotechnology, advanced ceramics, information packaging and aerospace applications.[1-10]

Intermetallic compounds consist one of the oldest and largest class of solid state materials. The evolution of intermetallic compounds can be traced back to ancient times (e.g. amagalm use, Cu_4Hg, Ag_2Hg_3, for dental applications)[11] but the recognition of their existence and some basic study of their physical properties started only in 1839,[12] and it took more than a century for the first systematic investigation results to be reported.[13,14] During that time an increasing number of binary and ternary compounds were found and considerable efforts were made in an attempt to establish the rules relating to the stability of different phases. Thus intermetallics had come into focus as high-performance materials.[13] Ever since a growing attention to these metallic compounds has been given by both pure and applied materials scientists and has resulted in the discovery of a vast

variety of intermetallic compounds that exhibit numerous structures[15] and a wealth of interesting physico-chemical and mechanical properties.[11,16,17]

A class of such materials the intermetallic tetrelides (Si, Ge, Sn) are both scientifically and technologically important. They are the subject of continuous interest because of their intrinsic properties such as hardness, chemical stability, high melting points[18] and superconductivity[4] and they found intriguing applications including high-temperature structural materials,[19] high-*T* furnaces,[18] high-*T* coatings[20] and thermoelectric energy conversion.[3] A notable compound is the $MoSi_2$ and its alloys, which combines very high melting point, low density and outstanding oxidation resistance and finds applications such as electronic devices, heating elements, energy conversion devices, glass melting and other.[17]

Intermetallic compounds are like any other compound that is they have precise proportions of two or more metallic elements (or metalloids) that form periodic crystalline solids with different structures from those of the component elements. They should not be confused with the conventional metal alloys, as they differ greatly. An intermetallic compound is a chemical compound that has a definite atomic formula, with a fixed or narrow range of chemical composition. An example is the binary Ni_3Al_2. Conventional alloys, on the other hand, comprise a homogeneous solid solution or a multiphase mixture of one or more metals, with randomly distributed atoms (disordered) and without having any particular chemical formula. Essentially, they consist of a base material to which certain percentages of other elements have been added as in the case of the very well-known stainless steel, an alloy with a composition of Fe-18%Cr-8%Ni.

Another significant difference between the two types of materials is also the way the atoms are connected. In the conventional alloys, the atoms are connected with weak metallic bonds and the electrons freely move amongst the atoms (good conductors). On the contrary, in intermetallics the bonds can be metallic but they can also be partly ionic or covalent, and therefore stronger. The stronger bonding and the high degree of ordering as the individual atoms occupy preferred positions within the crystal lattice, leads to the characteristic mechanical properties of intermetallics.

Crystal structures of intermetallic compounds vary significantly with the particular combination of constituent elements in them and in turn, the physical and chemical properties of intermetallic compounds depend strongly on the adopted structures. The formation of a particular structure is largely because the bonding between unlike atoms is often stronger than between like atoms. The result is an ordered atom distribution where atoms are preferentially surrounded by unlike atoms. In the past, various criteria, models, rules, and theories based on atomic size effects, electronic effects and electronegativity had been developed in order to explain the nature of the complex relationship between structure types and the kinds of the combining metal atoms.[13] However, despite the great effort to rationalize the rules governing the existence of the huge number of intermetallic phases there is still a great difficulty in fully understanding the compositions, bonding and assignment of oxidation states for individual atoms.

Due to the vast diversity of the intermetallic phases and their behaviour, it is a very difficult task to classify them into groups and it is even harder to try and generalize their properties. Nonetheless, there are some fundamental properties that can be roughly

observed in every group: high melting point, high hardness, high wear resistance, low ductility and good oxidation or corrosion resistance in many cases. These properties make the intermetallics exceptional materials for structural, heat resistant and corrosion resistant applications.[17] However, some intermetallics, mainly polycrystalline ones, are brittle at room temperature and this is the main obstacle to structural applications. For that reason many attempts have been made to improve their properties through structural modification, for example, by adding ternary elements into mother compounds. This is why the prediction of crystal structures is indeed a first step to the successful design of intermetallic compounds.

Furthermore, many intermetallic materials are widely used in many other technological applications such as electronic, magnetic and battery applications[17] due to their important physical properties such as superconductivity and permanent magnetism,[21,22] shape memory effects (mainly NiTi, NiAl, CuZn),[23,24] catalytic activity[25] as well as lithium and hydrogen storage capacity.[26-28] It can thus logically concluded that intermetallic compounds are useful materials and marks the importance of developing and utilizing low temperature and practical methods for their synthesis.

1-2. Motivation for the Use of Molten Metal Fluxes as Synthetic Media

The majority of the melting points of the starting materials employed in the synthesis of intermetallics such as the rare earth metals, the transition metals and some main group elements are generally over 1000 °C. The melting points of some examples are 1407 °C for Dy, 1072 °C for Sm, 1875 °C for Cr, 1495 °C for Co, 2500 °C for Ru, 1410 °C for Si. For this reason, intermetallic compounds have been traditionally prepared

through high temperature methods (often > 1500 °C) usually by means of techniques such as arc-melting, induction heating or powder metallurgy. This is required to facilitate the solid-state diffusion of the high melting solids involved.[29] Such reaction conditions, combined with long annealing times and frequent regrinding steps for powder preparations, are often necessary to overcome the limitations of solid-solid diffusion.

The synthetic conditions, presented above, lead to two important limitations. Such high temperature reactions generally afford the most thermodynamically stable phases (usually simple binary or ternary compounds) which frequently prevent the exploration of possible complex phases that could be more kinetically stable. At the same time, the fast overall reaction times involved in these reactions and the frequent regrinding steps in some cases, normally result in microcrystalline products which limit their accurate structural and physical characterization, especially if they are anisotropic in nature.

A variety of techniques have been developed to overcome the limitations inherent in this traditional approach and yield intermetallics at lower temperatures. Examples of low temperature approaches include solvothermal techniques,[30] high-energy ball milling,[31] electrodeposition,[32] chemical vapor deposition (CVD), gas-phase condensation and solution-mediated routes,[33-35] and molten flux synthesis.[36,37] Particularly, crystal growth employing metals[38-42] or salts[41,43,44] as fluxes has been known for a long time, while in recent years, the use of molten metals as solvents for the synthesis of new materials has attracted increasing attention.[36,45-54] The advantages of this method which uses an excess of a molten metal as a flux in which the reactant elements dissolve include enhanced diffusion of the reactants facilitated by the solvent and usually large, high-

quality crystal growth directly from the solution. Additionally, the lower reaction temperatures allow better kinetic control and the trapping of kinetically stable phases, giving more flexibility to yield novel multinary compounds that are unattainable through traditional high temperature synthetic techniques.

In the cases where the employed molten metal flux acts only as a solvent and is not included in the final product it is called a "non-reactive flux," whereas when the flux element gets incorporated into the product compound it is characterized as a "reactive flux." Nevertheless, in order for a metal to be a suitable flux for synthetic reactions several key conditions must be met. Firstly, the metal should melt at relatively low temperatures so it does not require the use of special containers or heating equipment while at the same time there should be a big difference between its melting and boiling point. Additionally, the solvent should dissolve sufficient amounts of the solutes and it should not react with them to form stable binary phases that could prevent the formation of the desired product. Finally, the excess metal should be easily removed by means of chemical or mechanical methods from the final products.

1-3. Use of Molten Al, Ga and In for the Exploratory Synthesis of Rare Earth Transition Metal and Tetrel Containing Intermetallic Compounds

Under the above mentioned criteria the group III elements (mainly Al, Ga, and In) constitute excellent candidates for use as liquid synthetic media. In the past few decades, our group, as well as others, has investigated the use of molten Al and Ga which has proven invaluable for exploring new intermetallic systems. Particularly, Al melts at 660 ^{o}C while it has a boiling point of 2792 ^{o}C. Additionally, inspection of the Al-containing

alloy phase diagram directly reveals the large number of compounds that are soluble in molten Al,[55,56] whereas the excess of aluminum can be easily removed from the products by submersion in a base solution of NaOH. Investigations of molten Al in the system RE/TM/Al (where RE = rare earth metal and TM = transition metal) by Jeitschko and his coworkers resulted in numerous ternary compounds, where Al principally acts as reactive flux and produces often Al-rich products.[57-62]

Our group has recently initiated a project where molten Al is used to investigate the reactivity of the quaternary systems RE/TM/Al/Si or Ge (RE = rare earth metal, TM = transition metal) which readily gave rise to new complex quaternary phases with some adopting new structure types or exhibiting interesting magnetic properties.[63-66] Some examples include the $Sm_2Ni(Si_{1-x}Ni_x)Al_4Si_6$,[67] $RE_8Ru_{12}Al_{49}Si_9$[68] and $RE_2NiAl_4Ge_2$[69] compounds. In these cases, notable features revealed from this chemistry is the inclusion of Al into the crystal structure as well as the reducing ability of Al which allows it to reduce stable oxides such as perovskites $MTiO_3$ (M = Ca, Sr, Ba) to intermetallic compounds, as it has be shown in the case of $M_3Au_{6+x}Al_{26}Ti$.[70] Furthermore, we observed that even though the Si and Ge in these systems exhibit parallel chemistry, however they do not always produce isostructural analogs. Similar explorations of the reactivity of Si and Ge in the system RE/Au/Al resulted in the homologous series of tetragonal compounds $RE(AuAl_2)_nAl_2(Au_xSi_{1-x})$[65] for Si while for Ge gave the rhombohedral $REAuAl_4Ge_2$ and the tetragonal $REAuAl_4(Au_xGe_{1-x})_2$ families of compounds.[71]

The remarkable success observed in the systematic investigations of molten Al as a preparative tool for the synthesis of ternary and quaternary intermetallic phases led us to extend this research to Ga. Ga holds similar properties that make Al such a viable

synthetic flux. In particular, Ga has a quite low melting point of 29 °C and a high enough boiling point of 2200 °C. Furthermore, it readily dissolves Si and Ge without forming binary phases while it dissolves a number of rare earth and transition metals.[56] Finally, it can be easily removed from the products by chemical or mechanical means. Interestingly, when Ga was employed in analogous reactions within the RE/TM/Si system as Al, generally yielded Ga-free products (e.g. $SmNiSi_3$)[72] or Si-free products (e.g. $Sm_2Ni_3Si_5$ and Sm_2NiGa_{12}).[73,74] This is in contrast with the corresponding Al work where it was found that it is impossible to synthesize Al-free silicides. When Si is replaced by Ge in the Ga flux reactions however, quaternary compounds such as $RE_3Ni_3Ga_8Ge_3$[75] and $GdCo_{1-x}Ga_3Ge_8$[76] are readily observed. These are surprising differences in reactivity given the close relationship of Al to Ga and Si to Ge respectively. These results imply that there is much new chemistry and reactivity to be learned by studying fluxes of related elements.

Upon this concept, we have recently expanded this work to also include molten In as a synthetic medium in parallel to Al and Ga systems. Indium possesses similar characteristics that make Al and Ga ideal metals for the flux technique, which are its low melting point at 156 °C and high boiling point at 2080 °C, it does not form binary phases with Ge or Si,[77] and it's easy to remove through mechanical or chemical means. Furthermore, In has the ability to dissolve Si, Ge and a host of lanthanide and transition metals, resulting in highly reactive forms of the elements. Indium flux, although it has been commonly used in the past for the crystal growth of primarily known binary and ternary phases[78-83] it has been less exploited as a synthetic tool for the discovery of new compounds compared to Al and Ga, particularly for quaternary phases, despite the most

recent efforts,[84-89] so this area is relatively unexplored. Some of the intermetallic systems that have been prepared with liquid In by other groups are $CeTIn_5$ and Ce_2TIn_8,[82,90,91] $YbTIn_5$,[92,93] RE_2Cu_2In[80] and $EuCu_2Si_2$.[94]

Preliminary results from the synthetic investigations of molten In as a solvent in the system RE/TM/Ge conducted by previous member of our group, Dr. J. R. Salvador, suggested that indium acts mainly as a non reactive flux with germanides in the same way that gallium acts as a non reactive flux with silicides. That work resulted in the new ternary germanides $RE_2Zn_3Ge_6$ (RE = La, Ce, Pr, Nd) which exhibit near Zintl phase behavior[95] and in the stabilization of a new β-form of the $RENiGe_2$ (RE = Dy, Er, Tm, Yb, Lu) compounds that could only be synthesized exclusively from In flux.[96] Additionally, the new ternary orthorhombic indides $REAu_2In_4$[97] were formed with the rare earth metals of La, Ce, Pr and Nd while Yb metal gave a different compound that has the same composition of $YbAu_2In_4$ but crystallizes in a monoclinic space group.[98] Finally, after careful experimental condition control the first quaternary compound in the system RE/TM/Ge/In, $RE_4Ni_2InGe_4$ (RE = Dy, Ho, Er, Tm) was formed.[99]

The tremendous success of our systematic investigations of Al and Ga fluxes as well as the preliminary results of In, justifies the present work which constitutes an expansion of that research to include molten In as preparative tool for the discovery of new intermetallic compounds. The biggest part of this project represents the exploratory synthesis of novel quaternary compounds in the system containing a rare earth, a transition metal, germanium metal and indium metal. Intermetallic compounds of the ternary systems RE/TM/In and RE/TM/Ge include numerous new intermetallic phases that exhibit rich structural variety and interesting physical properties and have been

extensively investigated in the last few decades.[15,100-104] Thus, our goal is to exploit the ability of liquid In as a reactive flux in the system RE/TM/Ge/In and discover new complex multinary compounds that could exhibit interesting structural features as well as chemical and physical properties. Additionally, by studying In/Ge systems analogous to Al/Ge and Ga/Ge ones could help us draw parallel and trends in this chemistry, which could further shed light in understanding the chemical reactivity of the systems as well as the composition, structure and properties of the resulting products. Under this scope, we have performed studies of the systems RE/Co/Ge/In, RE/Ni/Ge/In and RE/Au/Ge/In and we have succeeded in isolating a number of novel quaternary compounds. Results of the study of their structural features and physical behavior are discussed in chapters 2-5 of this work.

Among intermetallics that are likely to be stabilized in metallic fluxes, we are particularly interested in the Ce and Yb-containing ones because they can display a wealth of intriguing properties which are associated with their valence instability.[105,106] Both RE ions can exhibit two electronic configurations that are closely spaced in energy: the magnetic Ce^{3+} ($4f^1$) and the nonmagnetic Ce^{4+} ($4f^0$) for Ce and the magnetic Yb^{3+} ($4f^{13}$) and the nonmagnetic Yb^{2+} ($4f^{14}$) one for Yb. Due to this feature Yb is usually considered as the "*f*-hole" analogue of Ce. The intriguing physical phenomena that these compounds often exhibit include intermediate valence (*IV*) or valence fluctuating behavior, unusual magnetism, Kondo and heavy-fermion (*HF*) behavior and superconductivity.[102-104,107-111] These properties are generally believed to arise from the strong hybridization (interaction) between the localized 4f electrons and the delocalized s,p,d conduction electrons.[105,112] Due to these phenomena that these materials may

display focus of the physical characterization of the compounds discovered in this project is placed in the magnetic properties and the Yb-, Ce-valency of the corresponding compounds which is studied with X-ray Absorption Near Edge Spectroscopy measurements (XANES).

In our explorations of the systems Yb/TM/Ge/In we have also found the new ternary Yb_4TMGe_8 (TM = Cr, Fe, Co) compounds where In acted only as a solvent without being incorporated into the final product and are presented in Chapter 6. Finally, in Chapter 7 we present results of our studies of the ternary systems RE/Cu/In and RE/Ag/In.

References:

(1) Chen, G.; Dresselhaus, M. S.; Dresselhaus, G.; Fleurial, J. P.; Caillat, T. *International Materials Reviews* **2003**, *48*, 45-66.

(2) Datta, S. K.; Tewari, S. N.; Gatica, J. E.; Shih, W.; Bentsen, L. *Metallurgical and Materials Transactions a-Physical Metallurgy and Materials Science* **1999**, *30*, 175-181.

(3) Rowe, D. M. *CRC Thermoelectric Handbook* CRC Press: Boca Raton, FL, 1995.

(4) King, R. B. *Inorg Chem.* **1990**, *29*, 2164.

(5) McCarthy, B. P.; Pederson, L. R.; Chou, Y.; Zhou, X. D.; Surdoval, W. A.; Wilson, L. C. *Journal of Power Sources* **2008**, *180*, 294-300.

(6) Williams, M. C.; Strakey, J. P.; Surdoval, W. A.; Wilson, L. C. 2006, p 2039-2044.

(7) Gadow, R.; Kern, F.; Killinger, A. 2008, p 58-64.

(8) Ivanov, E. Y.; Shapiro, A. E.; Horne, M. G. *Welding Journal* **2006**, *85*, 196S-199S.

(9) Liu, H. K.; Wang, G. X.; Guo, Z. P.; Wang, J. Z.; Konstantinov, K. *Journal of Nanoscience and Nanotechnology* **2006**, *6*, 1-15.

(10) Kanatzidis, M. G.; Poeppelmeier, K. R. *Prog. Solid State Chem.* **2008**, *36*, 1.

(11) Sauthoff, G. *Intermetallics*; VCH: Verlagsgesellschaft, Weinheim, 1995.

(12) Karsten, K. *Annln. Phys.* **1839**, *46*, 1960.

(13) Westbrook, J. H. *Intermetallic compounds*; Wiley and Sons: New York, 1967.

(14) Gschneidner, K.A. *Rare earth alloys*; Van Nostrand, 1961.

(15) Villars, P.; Calvert, L. D. *"Pearson's Handbook of Crystallographic Data for Intermetallic Phases", 2nd ed.; American Society for Metals* OH 44073, 1991.

(16) Fähnle, M.; Welsch, F. *Physica B* **2002**, *321*, 198.

(17) Slotoff, N. S.; Liu, C. T.; Deevi, S. C. *Intermetallics* **2000**, *8*, 1313.

(18) Fitzer, E. *Plansee Proceedings 1955*; Benesovsky, F. ed. London, 1956; Vol. Chapter 7.

(19) Shah, D. M.; Berczik, D.; Anton, D. L.; Hecht, R. *Mater. Sci. Eng. A.* **1992**, *155*, 45.

(20) Meier, G. H. ; Stoloff, N.S.; Koch, C.; Liu, C. T.; Izumi, O. In *Materials Research Society Symposium Proceedings 81*; Materials Research Society: 1987; Vol. 443.

(21) Nagamatsu, J.; Nakagawa, N.; Muranaka, T.; Zenitani, Y.; Akimitsu, J. *Nature* **2001**, *410*, 63.

(22) Sun, S.; Murray, C. B.; Weller, D.; Folks, L.; Moser, A. *Science* **2000**, *287*, 1989.

(23) Cui, J.; Shield, T. W.; James, R. D. *Acta Mater.* **2004**, *52*, 35.

(24) Stern, R. A.; Willoughby, S. D.; MacLaren, J. M.; Cui, J.; Pan, Q.; James, R. D. *J. Appl. Phys.* **2003**, *93*, 8644.

(25) Casado-Rivera, E.; Volpe, D. J.; Alden, L.; Lind, C.; Downie, C.; Vazquez-Alvarez, T.; Angelo, A. C. D.; DiSalvo, F. J.; Abruna, H. D. *J. Am. Chem. Soc.* **2004**, *126*, 4043.

(26) Shi, L.; Li, H.; Wang, Z.; Huang, X.; Chen, L. *J. Mater. Chem.* **2001**, *11*, 1502.

(27) Rönnebro, E.; Yin, J.; Kitano, A.; Wada, M.; Sakai, T. *Solid State Ionics* **2005**, *176*, 2749.

(28) Mukaibo, H.; Osaka, T.; Reale, P.; Panero, S.; Scrosati, B.; Wachtler, M. *J. Power Sources* **2003**, *132*, 225.

(29) West, A.R. *Solid State Chemistry and its Applications*; Wiley: New York, N.Y., 1984.

(30) Heibel, M.; Kumar, G.; Wyse, C.; Bukovec, P.; Bocarsly, A. B. *Chem. Mater.* **1996**, *8*, 1504.

(31) Meitl, M. A.; Dellinger, T. M. ; Braun, P. V. *AdV. Funct. Mater.* **2003**, *13*, 795.

(32) Martin-Gonzalez, M.; Prieto, A. L.; Knox, M. S.; Gronsky, R.; Sands, T.; Stacy, A. M. *Chem. Mater.* **2003**, *15*, 1676.

(33) Sanchez-Lopez, J. C.; Gonzalez-Elipe, A. R.; Fernandez, A. *J. Mater. Res.* **1998**, *13*, 703.

(34) Leonard, B. M.; Bhuvanesh, N. S. P.; Schaak, R. E. *J. Am. Chem. Soc.* **2005**, *127*, 7326.

(35) Ung, D.; Soumare, Y.; Chakroune, N.; Viau, G.; Vaulay, M.-J.; Richard, V.; Rievet, F. *Chem. Mater.* **2007**, *19*, 2084.

(36) Kanatzidis, M. G.; Pottgen, R.; Jeitschko, W. *Angewandte Chemie-International Edition* **2005**, *44*, 6996.

(37) Fisk, Z.; Remeika, J. P. *Handbook on the Physics and Chemistry of Rare Earths*, 1989; Vol. 12.

(38) Deitch, R. H. *Crystal Growth*; Pamplin, B. R. ed.; Pergamon Press: Oxford, New York, 1975; Vol. 100.

(39) Lundstrom, T. *J. Less-Common Met.* **1984**, *100*, 215.

(40) Canfield, P.C.; Fisk, Z. *Philos. Mag. B* **1992**, *65*, 1117.

(41) Elwell, D.; Scheel, H. J. *Crystal growth from high-temperature solution*; Academic Press: London, New York, 1975.

(42) Morelli, D.T.; Canfield, P.C.; Drymiotis, P. *Phys. Rev. B* **1996**, *53*, 12896.

(43) Kanatzidis, M. G.; Sutorik, A. *Prog. Inorg. Chem.* **1995**, *43*, 151.

(44) Kanatzidis, M. G. *Curr. Opin. Solid State Mater. Sci.* **1997**, *2*, 139.

(45) Schaefer, J.; Bluhm, K. Z. *Anorg. Allg. Chem.* **1994**, *620*, 1578.

(46) Utzolino, A.; Bluhm, K. Z. *Naturforsch., B: Chem. Sci.* **1996**, *51*, 305.

(47) DiSalvo, F. J. *Solid State Commun.* **1997**, *102*, 79.

(48) Schluter, M.; Jeitschko, W. *Inorg Chem.* **2001**, *40*, 6362.

(49) Williams, W.M.; Moldovan, M.; Young, D.P.; Chan, J.Y. *J. Solid State Chem.* **2005**, *178*, 52.

(50) Williams, W.M.; Macaluso, R.T.; Moldovan, M.; Chan, J.Y. *Inorg Chem.* **2003**, *42*, 7315.

(51) Bauer, E.D.; Bobev, S.; Thompson, J.D.; Hundley, M.F.; Sarrao, J.L.; Lobos, A.; Aligia, A.A. *J. Phys. Cond. Matter* **2004**, *16*, 4025.

(52) Bobev, S.; To, P.H.; Thompson, J.D.; Hundley, M.F.; Sarrao, J.L.; Lobos, A.; Aligia, A.A. *J. Solid State Chem.* **2005**, *178*, 2091.

(53) Bie, H. Y.; Zelinska, O. Y.; Tkachuk, A. V.; Mar, A. *Chemistry of Materials* **2007**, *19*, 4613.

(54) Tobash, P. H.; Meyers, J. J.; DiFilippo, G.; Bobev, S.; Ronning, F.; Thompson, J. D.; Sarrao, J. L. *Chemistry of Materials* **2008**, *20*, 2151.

(55) Hansen, M.; Anderko, K. *Constitution of Binary Alloys*; 2nd ed. McGraw-Hill, New York, 1958.

(56) Massalski, T.B. *Binary Alloy Phase Diagrams* ASM, Metals Park, 1986.

(57) Nierman, J.; Jeischko, W. *Z. Anorg. Allg. Chem.* **2002**, *628*, 2549.

(58) Fehrmann, B.; Jeitschko, W. *J. Alloys Compd.* **2000**, *298*, 153.

(59) Thiede, V. M. T.; Fehrmann, B.; Jeischko, W. *Z. Anorg. Allg. Chem.* **1999**, *625*, 1417.

(60) Fehrmann, B.; Jeitschko, W. *Inorg Chem.* **1999**, *38*, 3344.

(61) Reehuis, M.; Wolff, M.W.; Krimmel, A.; Scheidt, E.W.; Stusser, N.; Loidl, A.; Jeitschko, W. *J. Phys. Cond. Matter* **2003**, *15*, 1773.

(62) Thiede, V.M.T.; Ebel, T.; Jeitschko, W. *J. Mater. Chem.* **1998**, *8*, 125.

(63) Latturner, S. E.; Bilc, D.; Mahanti, S. D.; Kanatzidis, M. G. *Chem. Mater.* **2002**, *14*, 1695-1705.

(64) Latturner, S. E.; Bilc, D.; Mahanti, S. D.; Kanatzidis, M. G. *Inorg. Chem.* **2003**, *42*, 7959-7966.

(65) Latturner, S. E.; Kanatzidis, M. G. *Inorg. Chem.* **2008**, *47*, 2089-2097.

(66) Sieve, B.; Sportouch, S.; Chen, X. Z.; Cowen, J. A.; Brazis, P.; Kannewurf, C. R.; Papaefthymiou, V.; Kanatzidis, M. G. *Chem. Mater.* **2001**, *13*, 273.

(67) Chen, X. Z.; Sportouch, S.; Sieve, B.; Brazis, P.; Kannewurf, C. R.; Cowen, J. A.; Patschke, R.; Kanatzidis, M. G. *Chem. Mater.* **1998**, *10*, 3202.

(68) Sieve, B.; Chen, X. Z.; Henning, R.; Brazis, P.; Kannewurf, C. R.; Cowen, J. A.; Schultz, A. J.; Kanatzidis, M. G. *J. Am. Chem. Soc.* **2001**, *123*, 7040.

(69) Sieve, B.; Trikalitis, P. N.; Kanatzidis, M. G. *Z. Anorg. Allg. Chem.* **2002**, *628*, 1568.

(70) Latturner, S. E.; Kanatzidis, M. G. *Inorg Chem.* **2004**, *43*, 2.

(71) Wu, X. N.; Kanatzidis, M. G. *J. Solid State Chem.* **2005**, *178*, 3233.

(72) Chen, X. Z.; Larson, P.; Sportouch, S.; Brazis, P.; Mahanti, S. D.; Kannewurf, C. R.; Kanatzidis, M. G. *Chem. Mater.* **1999**, *11*, 75.

(73) Zhuravleva, M. A.; Kanatzidis, M. G. *Z. Naturforch B : Sec. B* **2003**, *58*, 649-657.

(74) Chen, X. Z.; Small, P.; Sportouch, S.; Zhuravleva, M. ; Brazis, P.; Kannewurf, C. R.; Kanatzidis, M. G. *Chem. Mater.* **2000**, *12*, 2520.

(75) Zhuravleva, M. A.; Pcionek, R. J.; Wang, X. P.; Schultz, A. J.; Kanatzidis, M. G. *Inorg. Chem.* **2003**, *42*, 6412.

(76) Zhuravleva, M. A.; Evain, M.; Petricek, V.; Kanatzidis, M. G. *J. Am. Chem. Soc* **2007**, *129*, 3082.

(77) Massalski, T, B. *Binary Allory Phase Diagrams*; 2nd ed.; ASM International: New York, 1990.

(78) Canfield, P. C.; Fisk, Z. *Z. Philos. Mag. B* **1992**, *65*, 1117.

(79) Bud'ko, S. l.; Islam, Z.; Wiener, T. A.; Fisher, I. R.; Lacerda, A. H.; Canfield, P. C. *J. Magn. Magn. Mater.* **1999**, *205*, 53.

(80) Fisher, I. R.; Islam, Z.; Canfield, P. C. *J. Magn. Magn. Mater.* **1999**, *202*, 1.

(81) Hundley, M. F.; Sarrao, J. L.; Thompson, J. D.; Movshovich, R.; Jaime, M.; Petrovic, C.; Fisk, and Z. *Phys. Rev. B* **2001**, *65*, 024401.

(82) Macaluso, R. T.; Sarrao, J. L.; Moreno, N. O.; Pagliuso, P.G.; Thompson, J. D.; Fronczek, F. R.; Hundley, M. F.; Malinowski, A.; Chan, J. Y. *Chem. Mater.* **2003**, *15*, 1394.

(83) Sakamoto, I.; Shomi, Y.; Ohara, S. *Physica B* **2003**, *329-333*, 607.

(84) Bailey, M. S.; McCuire, M. A.; DiSalvo, and F. J. *J. Solid State Chem.* **2005**, *178*, 3494.

(85) Benbow, E. M.; Latturner, S. E. *Inorg. Chem.* **2006**, *179*, 3989.

(86) Klunter, W.; Jung, W. *J. Solid State Chem.* **2006**, *179*, 2880.

(87) Zaremba, V. I.; Dubenskiy, V. P.; Rodewald, U. C.; Heying, B.; Pottgen, R. *J. Solid State Chem.* **2006**, *179*, 891.

(88) Lukachuk, M.; Galadzhun, Y. V.; Zaremba, R. I.; Dzevenko, M. V.; Kalychak, Y. M.; Zaremba, V. I.; Rodewald, U. C.; Pottgen, R. *J. Solid State Chem.* **2005**, *178*, 2724.

(89) Macaluso, R. T.; Sarrao, J. L.; Pagliuso, P.G.; Moreno, N. O.; Goodrich, R. G.; Browne, D. A.; Fronczek, F. R.; Chan, J. Y. *J. Solid Sate Chem.* **2002**, *166*, 245.

(90) Hegger, H.; Petrovic, C.; Moshopoulou, E. G.; Hundley, M. F.; Sarrao, J. L.; Fisk, Z.; Thompson, J. D. *Phys. Rev. Lett.* **2000**, *84*, 4986.

(91) Moshopoulou, E. G.; Fisk, Z.; Sarrao, J. L.; Thompson, J. D. *J. Solid State Chem.* **2001**, *158*, 25.

(92) Zaremba, V. I.; Rodewald, U. Ch.; Hoffmann, R. –D.; Kalychak, Ya. M.; Pottgen, R. *Z. Anorg. Allg. Chem.* **2003**, *629*, 1157.

(93) Zaremba, V. I.; Rodewald, U. Ch.; Pottgen, R. *Z. Naturforsch.* **2003**, *58b*, 805.

(94) Pagliuso, P, G.; Sarrao, J. L.; Thompson, J. D.; Hundley, M. F.; Sercheli, M. S.; Urbano, R. R.; Rettori, C.; Fisk, Z.; Oseroff, S. B. *Phys. Rev. B* **2001**, *63*, 092406-1.

(95) Salvador, J. R.; Bilc, D.; Gour, J. R.; Mahanti, S. D.; Kanatzidis, M. G. *Inorg. Chem.* **2005**, *44*, 8670

(96) Salvador, J. R.; Gour, J. R.; Bilc, D.; Mahanti, S. D.; Kanatzidis, M. G. *Inorg. Chem.* **2004**, *43*, 1403.

(97) Salvador, J. R.; Hoang, K.; Mahanti, S. D.; Kanatzidis, M. G. *Inorg. Chem.* **2007**, *46*, 6933

(98) Salvador, J. R. *Molten metal flux synthesis and crystal growth of intermetallic silicides, germanides and indides.*; Michigan State University: Dissertation, East Lansing, MI, 2004

(99) Salvador, J. R.; Kanatzidis, M. G. *Inorg. Chem.* **2006**, *45*, 7091.

(100) Kalychak, Ya. M. *J. Alloys Compd.* **1997**, *341*, 262.

(101) Szytula, A.; Leciejewicz, J. *"Handbook of Crystal Structures and Magnetic Properties of Rare Earth Intermetallics"*; CRC Press: Boca Raton, Fl, 1994.

(102) Maple, M. B. *J. Phys. Soc. Jpn* **2005**, *74*, 222.

(103) Hossain, Z.; Gupta, L. C.; Geibel, C. *J. Phys.: Condens. Matter* **2002**, *14*, 9687.

(104) Gamza, M.; Slebarski, A; Rosner, H. *J. Phys.: Condens. Matter* **2008**, *20*, 025201.

(105) Lawrence, J. M.; Riseborough, P. S.; Park, R. D. *Rep. Progr. Phys.* **1981**, *44*, 1.

(106) Lawrence, J.; Chen, Y.-Y.; Thompson, J. *Theoretical and Experimental Aspects of Valence Fluctuations and Heavy Fermions*; Plenum: New York and London, 1987.

(107) Kindler, B.; Finsterbusch, D.; Graf, R.; Ritter, F.; Assmus, W.; Luthi, B. *Phys. Rev. B* **1994**, *50*, 704.

(108) Stewart, G. R. *Rev. Mod. Phys.* **2006**, *78*, 743.

(109) Wachter, P. *Handbook on the Physics and Chemistry of Rare Earths* **1994**, *(Elsevier Science, Amsterdam)*, 177.

(110) Paglione, J.; Tanatar, M. A.; Hawthorn, D. G.; Boaknin, E.; Hill, R. W.; Ronning, F.; Sutherland, M.; Taillefer, L.; Petrovic, C.; Canfield, P. C. *Phys. Rev. Lett.* **2003**, *91*, 4.

(111) Izawa, K.; Yamaguchi, H.; Matsuda, Y.; Shishido, H.; Settai, R.; Onuki, Y. *Phys. Rev. Lett.* **2001**, *8705*, 4.

(112) Fisk, Z.; Hess, D. W.; Pethick, C. J.; Pines, D.; Smith, J. L.; Thomson, J. D.; Willis, J. O. *Science* **1988**, *239*, 33.

CHAPTER 2

Mixed Valency in $Yb_7TM_4InGe_{12}$ (TM = Co, Ni): a Novel Intermetallic Compound Stabilized in Liquid Indium

2-1. Introduction

Molten metals can be excellent solvents for the synthesis of new intermetallic compounds.[1] For example, molten Al when used to investigate the reactivity of the quaternary systems RE/TM/Si(Ge) (RE = rare earth metal, TM = transition metal) readily gave rise to new complex quaternary phases such as $Sm_2Ni(Si_{1-x}Ni_x)Al_4Si_6$[2] $RE_8Ru_{12}Al_{49}Si_9$[3] and $RE_2NiAl_4Ge_2$.[4] In these cases a notable feature of this chemistry is the inclusion of Al into the crystal structure. Interestingly, when Ga was employed in analogous reactions within the RE/TM/Si system, generally yielded Ga-free products (e.g. $SmNiSi_3$[5]) or Si-free products (e.g. $Sm_2Ni_3Si_5$[6] and Sm_2NiGa_{12}).[7] When Si is replaced by Ge in the Ga flux reactions however, quaternary compounds such as $RE_3Ni_3Ga_8Ge_3$[8] and $GdCo_{1-x}Ga_3Ge$[9] are readily observed. These are surprising differences in reactivity given the close relationship of Al to Ga and Si to Ge respectively. These results imply that there is much new chemistry and reactivity to be learned by studying fluxes of related elements.

Recently, we extended this work to include molten In as a solvent in the system RE/TM/Ge.[10, 11] Indium has been extensively used for the crystal growth of primarily known binary and ternary phases;[1] however, it has been less exploited as a synthetic flux medium compared to Al and Ga, especially for quaternary compounds.[12-16] Our work in In flux has led to very few quaternary phases such as the $RE_4Ni_2InGe_4$.[17]

Among intermetallics that are likely to be stabilized in metallic fluxes, the Yb-containing ones are particularly attractive because they can display intriguing properties caused by the diverse character of their f electrons.[18] These electrons can play a dynamic role in bonding leading to intermediate valence, unusual magnetism, Kondo and heavy-fermion behavior, to name just a few.[19] Yb can exhibit two valence states concerning the non-magnetic $4f^{14}$ (Yb^{2+}) and magnetic $4f^{13}$ (Yb^{3+}) electronic configurations. For this reason we investigated the reactivity of the Yb/Co/Ge system in liquid indium. Here, we present the ordered quaternary intermetallic compounds $RE_7Co_4InGe_{12}$ (RE = Dy, Ho and Yb) as well as the Ni analog $Yb_7Ni_4InGe_{12}$. This is another example besides $RE_4Ni_2InGe_4$ where In is acting as a reactive flux in the RE/TM/Ge system. The Yb analogs are mixed valence compounds with predominant Yb^{3+} ions with $Yb_7Co_4InGe_{12}$ exhibiting negative magnetoresistance.

2-2. Experimental Section

Reagents:

The following reagents were used as purchased without further purification: Yb, Dy, Ho (in the form of powder ground from metal chunk, 99.9%, Chinese Rare Earth Information center, Inner Mongolia, China), Co (-325 mesh 99.9% Cerac Milwaukee WI), Ni (-325 mesh 99.9% Cerac Milwaukee WI), Ge (ground from 2-5 mm pieces 99.999% Plasmaterials Livermore, CA) and In (tear drops 99.99% Cerac Milwaukee, WI).

Synthesis:

Method A: The $RE_7Co_4InGe_{12}$ (RE = Dy, Ho, Yb,) and $Yb_7Ni_4InGe_{12}$ compounds were obtained by combining 3 mmol of the corresponding rare earth metal, 2 mmol cobalt or nickel, 3 mmol germanium and 15 mmol In in an Al_2O_3 (alumina) crucible under an inert nitrogen atmosphere inside a glove-box. The crucible was placed in a 13 mm fused silica tube, which was flame sealed under vacuum of 10^{-4} Torr, to prevent oxidation during heating. The reactants were then heated to 1000 ^{0}C over 10 h, maintained at that temperature for 4 h to allow proper homogenization, followed by cooling to 850 ^{0}C in 2 h and held there for 48 h. Finally, the system was allowed to slowly cool to 50 ^{0}C in 48 h. The reaction product was isolated from the unreacted In by heating at 350 ^{0}C and subsequent centrifugation through a coarse frit. The remaining flux was removed by immersion and soniqation in glacial acetic acid for 48 h. The final crystalline product was rinsed with water and dried with acetone. The yields of the reactions were 20-70% with purity ranging from 30% to 80% depending on the RE metal. Several crystals, which grow as metallic silver needles and tend to aggregate, were carefully selected for elemental analysis, structure characterization, differential thermal analysis, magnetic susceptibility, XPS, XANES and resistivity measurements.

Method B: $Yb_7Co_4InGe_{12}$ was also prepared by combining 6 mmol ytterbium metal, 2 mmol cobalt, 5 mmol germanium and 15 mmol In in an Al_2O_3 (alumina) crucible under an inert nitrogen atmosphere inside a glove-box. The reactants were then heated under the same heating profile as in method A. This method increased the purity (90 %) and the yield (80 %) of the target phase. Attempts to generate the $Yb_7Co_4InGe_{12}$ phase by

direct combination of the elements in their stoichiometric ratios and heating in a RF induction heating furnace were not successful.

$Yb_7Ni_4InGe_{12}$ was initially prepared by combining 6 mmol ytterbium metal, 2 mmol cobalt, 5 mmol germanium and 15 mmol In in an Al_2O_3 (alumina) crucible under an inert nitrogen atmosphere inside a glove-box. The reactants were then heated under the same heating profile as in method A. It was later found that by mixing the reactants in the alternative ratio of 4:1:4:15 for Yb/Ni/Ge/In improved the yield in $Yb_7Ni_4InGe_{12}$.

Elemental Analysis:

Semi-quantitative microprobe elemental analysis was performed on several crystals of the compound using a JEOL JSM-35C scanning electron microscope (SEM) equipped with a Noran Vantage Energy Dispersive Spectroscopy (EDS) detector. Data were acquired by applying a 25 kV accelerating voltage and an acquisition time of 40 s. A typical needle-like crystal of $Yb_7Co_4InGe_{12}$ is shown in Figure 1. The EDS analysis taken on visibly clean surfaces of the $Yb_7Co_4InGe_{12}$ crystals gave the atomic composition of 31.5% Yb, 17.3% Co, 3.9% In and 48.4% Ge ($Yb_8Co_{4.4}InGe_{12.5}$), which is in good agreement with the results derived from the single crystal X-ray diffraction refinement. Similar stoichiometric ratios were determined for the other RE analogs as well as the Ni one.

X-ray Crystallography:

$RE_7Co_4InGe_{12}$. The X-ray intensity data were collected at room temperature using a Bruker SMART Platform CCD diffractometer with graphite monochromatized Mo Ka (λ = 0.71073 Å) radiation. The SMART software was used for data acquisition and SAINT for data extraction and reduction.[20] An empirical absorption correction was applied using the program SADABS[20] and the structure of $Yb_7Co_4InGe_{12}$ was solved by direct methods and refined with the SHELXTL package programs.[21] A stable refinement was accomplished only in the tetragonal space group *P4/m*. Standardization of the atomic positions of $Yb_7Co_4InGe_{12}$ was performed with Platon-Structure Tidy application of the WinGX package software.[22] Solutions of the Dy and Ho analogs were obtained by using the solution of $Yb_7Co_4InGe_{12}$ as a starting point, with the final refinement done using SHELXTL. Interestingly, the Co and Ge(2) positions in the Dy and Ho analogs are switched compared to the Yb analog, and the Ge(3) atom is repositioned. This model gave a far better R values. For example, for the Dy and Ho analogs we obtain R1=0.0258 and 0.0464 respectively. This compares to R_1 = 0.0500 and wR_2 = 0.0515 for the wrong model i.e. the one with the positions left unswitched (Yb-analog model). In addition, when these two sites are positioned as in the Yb analog the thermal displacement parameters become unreasonable. Data collection and structure refinement details are given in Table 2-1. The final atomic positions, equivalent isotropic displacement parameters and anisotropic displacement parameters are listed in Table 2-2 and 2-3.

$Yb_7Ni_4InGe_{12}$. The X-ray intensity data were collected at room temperature using a STOE IPDS 2T (with additional capability of 2θ swing of the detector) diffractometer with graphite-monochromatized Mo Kα (λ = 0.71073 Å) radiation. The X-AREA (and X-

RED and X-SHAPE within) package suite[23] was used for data extraction and integration and to apply empirical and analytical absorption corrections. The structure of $Yb_7Ni_4InGe_{12}$ single crystals were solved by direct methods and refined with the SHELXTL package programs.[23, 24] A stable refinement was accomplished only in the tetragonal space group *P4/m*. Data collection and structure refinement details are given in Table 2-4. The final atomic positions, equivalent isotropic displacement parameters and anisotropic displacement parameters are listed in Table 2-5 and 2-6.

To determine phase identity and purity, powder X-ray diffractions patterns of the $RE_7TM_4InGe_{12}$ were collected at room temperature on a CPS 120 INEL diffractometer with Cu Ka radiation and equipped with a position-sensitive detector.

Table 2-1. Crystal data and structure refinement data for $RE_7Co_4InGe_{12}$ (RE = Dy, Ho, Yb).

Emprirical formula	$Dy_7Co_4InGe_{12}$	$Ho_7Co_4InGe_{12}$	$Yb_7Co_4InGe_{12}$
Formula weight	2359.12	2376.13	2432.90
Temperature (K)	293(2)	293(2)	293(2)
Wavelength (Å)	0.71073	0.71073	0.71073
Crystal system	Tetragonal	Tetragonal	Tetragonal
Space group	*P4/m*	*P4/m*	*P4/m*
a, *b* (Å)	10.3522(5)	10.357(3)	10.2937(7)
c (Å)	4.1784(5)	4.1538(15)	4.1518(5)
Volume ($Å^3$)	447.79(6)	445.6(2)	439.93(7)
Z / $Density_{calc}$ (Mg/m^3)	1 / 8.748	8.855	9.183
Absorption coefficient (mm^{-1}) / F(000)	53.380 / 1003	55.370 / 1010	61.813 / 1031
θ range for data collection (^{o})	1.97 to 28.12	1.97 to 28.18	1.98 to 28.39
Index ranges	$-13 \le h \le 13$ $-13 \le k \le 13$ $-5 \le l \le 5$	$-13 \le h \le 13$ $-13 \le k \le 13$ $-5 \le l \le 5$	$-12 \le h \le 13$ $-13 \le k \le 12$ $-5 \le l \le 5$
Reflections collected / unique	4986 / 607	4844 / 606	4942 / 612
R(int)	0.0498	0.0364	0.0461
Completeness to θ (%)	96.2	96.0	96.8
Refinement method		Full-matrix least-squares on F^2	
Data / restraints / parameters	607 / 0 / 40	606 / 0 / 40	612 / 0 / 40
Goodness-of-fit on F^2	1.138	1.299	1.126
Final R indices [$I>2\sigma(I)$] (R_1 / wR_2)[a]	0.0258 / 0.0552	0.0464 / 0.1141	0.0304 / 0.0710
R indices (all data) (R_1 / wR_2)[a]	0.0336 / 0.0580	0.0496 / 0.1152	0.0332 / 0.0723
Extinction coefficient	0.0069(4)	0.0042(5)	0.0090(5)
Largest diff. peak and hole (e. $Å^{-3}$)	1.444 and -2.178	6.830 and -3.493	3.620 and -1.670

[a] $R_1 = \Sigma \| F_o | - | F_c \| / \Sigma | F_o |; wR_2 = \left[\Sigma w \{ | F_o | - | F_c | \}^2 / \Sigma w | F_o |^2 \right]^{1/2}; w = 1/\sigma^2 \{ | F_o | \}$.

Table 2-2. Atomic coordinates (x 10^4) and equivalent isotropic displacement parameters ($Å^2$ x 10^3) for $RE_7Co_4InGe_{12}$ (RE = Dy, Ho, Yb).

Atom	Wyckoff	x	y	z	U(eq)[a]
Dy(1)	4*k*	3232(1)	3259(1)	5000	7(1)
Dy(2)	1*a*	0	0	0	8(1)
Dy(3)	2*f*	0	5000	5000	8(1)
Ge(1)	4*j*	2139(1)	5124(1)	0	7(1)
Ge(2)	4*j*	1131(1)	2860(1)	0	10(1)
Ge(3)	4*k*	1950(1)	655(1)	5000	11(1)
Co	4*j*	2797(1)	1181(1)	0	7(1)
In	1*c*	5000	5000	0	8(1)
Ho(1)	4*k*	3245(1)	3260(1)	5000	8(1)
Ho(2)	1*a*	0	0	0	8(1)
Ho(3)	2*f*	0	5000	5000	10(1)
Ge(1)	4*j*	2139(2)	5102(2)	0	10(1)
Ge(2)	4*k*	1133(3)	2853(3)	0	18(1)
Ge(3)	4*j*	-664(3)	1957(3)	5000	17(1)
Co	4*j*	2811(3)	1182(3)	0	9(1)
In	1*c*	5000	5000	0	9(1)
Yb(1)	4*k*	3262(1)	3243(1)	5000	5(1)
Yb(2)	1*a*	0	0	0	5(1)
Yb(3)	2*f*	0	5000	5000	7(1)
Ge(1)	4*j*	2164(1)	4886(1)	0	5(1)
Ge(2)	4*j*	2865(2)	1130(1)	0	12(1)
Ge(3)	4*k*	679(2)	1931(1)	5000	9(1)
Co	4*j*	1191(2)	2800(2)	0	5(1)
In	1*c*	5000	5000	0	7(1)

[a]U(eq) is defined as one third of the trace of the orthogonalized U^{ij} tensor.

Table 2-3. Anisotropic displacement parameters ($Å^2$ x 10^3) for $RE_7Co_4InGe_{12}$ (RE = Dy, Ho, Yb). The anisotropic displacement factor exponent takes the form: $-2\pi^2[h^2a^{*2}U^{11} + ... +2hka^*b^*U^{12}]$

Atom	U^{11}	U^{22}	U^{33}	U^{23}	U^{13}	U^{12}
Dy(1)	7(1)	7(1)	8(1)	0	0	1(1)
Dy(2)	7(1)	7(1)	8(1)	0	0	0
Dy(3)	7(1)	9(1)	8(1)	0	0	0(1)
Ge(1)	8(1)	5(1)	9(1)	0	0	-1(1)
Ge(2)	5(1)	6(1)	19(1)	0	0	0(1)
Ge(3)	11(1)	15(1)	7(1)	0	0	-6(1)
Co	6(1)	8(1)	7(1)	0	0	-2(1)
In	6(1)	6(1)	11(1)	0	0	0
Ho(1)	8(1)	8(1)	7(1)	0	0	2(1)
Ho(2)	8(1)	8(1)	9(1)	0	0	0
Ho(3)	9(1)	11(1)	9(1)	0	0	-1(1)
Ge(1)	10(1)	9(1)	10(1)	0	0	-1(1)
Ge(2)	14(1)	14(1)	27(2)	0	0	3(1)
Ge(3)	25(2)	17(1)	9(1)	0	0	11(1)
Co	8(2)	9(2)	8(2)	0	0	-3(1)
In	8(1)	8(1)	12(2)	0	0	0
Yb(1)	3(1)	3(1)	10(1)	0	0	1(1)
Yb(2)	3(1)	3(1)	10(1)	0	0	0
Yb(3)	4(1)	6(1)	11(1)	0	0	0(1)
Ge(1)	4(1)	1(1)	11(1)	0	0	1(1)
Ge(2)	5(1)	3(1)	26(1)	0	0	0(1)
Ge(3)	12(1)	6(1)	10(1)	0	0	-6(1)
Co	2(1)	3(1)	10(1)	0	0	-1(1)
In	4(1)	4(1)	14(1)	0	0	0

Table 2-4. Crystal data and structure refinement data for $Yb_7Ni_4InGe_{12}$.

Emprirical formula	$Yb_7Ni_4InGe_{12}$
Formula weight	2432.02
Temperature (K)	293(2)
Wavelength (Å)	0.71073
Crystal system	Tetragonal
Space group	*P4/m*
a, *b* (Å)	10.3091(15)
c (Å)	4.1691(8)
Volume ($Å^3$)	443.08(12)
Z / Density(calculated) (Mg/m^3)	1 / 9.114
Absorption coefficient (mm^{-1}) / F(000)	61.878 / 1035
θ range for data collection (°)	3.95 to 31.60
Index ranges	$-15 \le h \le 15$ $-15 \le k \le 15$ $-5 \le l \le 6$
Reflections collected / unique	5126 / 834
R(int)	0.0503
Completeness to θ (%)	99.3
Refinement method	Full-matrix least-squares on F^2
Data / restraints / parameters	834 / 0 / 40
Goodness-of-fit on F^2	1.394
Final R indices [$I>2\sigma(I)$] (R_1 / wR_2)[a]	0.0276 / 0.0538
R indices (all data) (R_1 / wR_2)[a]	0.0294 / 0.0544
Largest diff. peak and hole (e. $Å^{-3}$)	1.996 and -1.725

[a] $R_1 = \Sigma\|\|F_o\| - \|F_c\|\| / \Sigma|F_o|$; $wR_2 = \left[\Sigma w\{|F_o| - |F_c|\}^2 / \Sigma w|F_o|^2\right]^{1/2}$; $w = 1/\sigma^2\{|F_o|\}$.

Table 2-5. Atomic coordinates ($\times 10^4$) and equivalent isotropic displacement parameters ($Å^2 \times 10^3$) for $Yb_7Ni_4InGe_{12}$.

Atom	Wyckoff position	x	y	z	U(eq)[a]
Yb(1)	4*k*	6751(1)	3275(1)	5000	6(1)
Yb(2)	1*a*	10000	0	0	6(1)
Yb(3)	2*f*	5000	0	5000	7(1)
Ge(1)	4*j*	7812(1)	5111(1)	0	6(1)
Ge(2)	4*j*	8863(1)	2879(1)	0	10(1)
Ge(3)	4*k*	10674(1)	1915(1)	-5000	12(1)
Ni	4*j*	8810(2)	2794(2)	0	6(1)
In	1*c*	5000	5000	0	7(1)

[a] U(eq) is defined as one third of the trace of the orthogonalized U^{ij} tensor.

Table 2-6. Anisotropic displacement parameters ($Å^2 \times 10^3$) for $Yb_7Ni_4InGe_{12}$ (RE = Dy, Ho, Yb). The anisotropic displacement factor exponent takes the form: $-2\pi^2[h^2a^{*2}U^{11} + ... +2hka^*b^*U^{12}]$

Atom	U^{11}	U^{22}	U^{33}	U^{23}	U^{13}	U^{12}
Yb(1)	6(1)	6(1)	6(1)	0	0	-1(1)
Yb(2)	5(1)	5(1)	7(1)	0	0	0
Yb(3)	9(1)	6(1)	7(1)	0	0	0(1)
Ge(1)	6(1)	4(1)	7(1)	0	0	0(1)
Ge(2)	4(1)	6(1)	19(1)	0	0	0(1)
Ge(3)	21(1)	11(1)	5(1)	0	0	-10(1)
Ni	6(1)	7(1)	6(1)	0	0	2(1)
In	7(1)	7(1)	9(1)	0	0	0

Differential Thermal Analysis:

Differential Thermal Analysis (DGA) was conducted with a Shimadzu TDA-50 analyzer. The sample was flame sealed under a reduced atmosphere in fused silica ampoules that were carbon coated to prevent glass attack upon melting of the products. α-Al_2O_3 standard was used as a reference. The analysis was performed by heating the sample up to 1000 ^{0}C at a rate of 10 ^{0}C per min, held at 1000 ^{0}C for 1 min then cooling to 100 ^{0}C at the same rate, and then repeating the cycle.

Magnetic Measurements:

Magnetic susceptibility measurements for $RE_7Co_4InGe_{12}$ (RE = Yb and Dy) were carried out with a Quantum Design MPMS SQUID magnetometer. EDS-analyzed crystals were soaked in ~ 6M of HCl acid for 15-30 min, washed out with water, and dried out in a dry oven. The crystals were then randomly placed and sealed in Kapton tape which was inserted into the SQUID magnetometer. Temperature dependent data were collected between 3 and 400 K, with an applied field of 500 G. Field dependent magnetic measurements were acquired at 3 K with field sweeping from - 50000 to 50000 G.

X-Ray Photoemission Spectroscopy:

X-ray Photoemission Spectroscopy was performed on a Perkin Elmer Phi 5400 ESCA system equipped with a Magnesium Kα X-ray source. Samples were analyzed at pressures between 10^{-9} and 10^{-8} torr with a pass energy of 29.35 eV and a take-off angle

of 45°. The spot size was roughly 250 μm^2. All peaks were referenced to the signature C1s peak for adventitious carbon at 284.6 eV.

X-ray Absorption Near Edge Spectroscopy (XANES):

X-ray absorption fine Structure (XAFS) experiments were performed in Sector 20, bending magnet beamline (PNC/XOR, 20-BM) of the Advanced Photon Source at the Argonne National Laboratory, IL, USA. Measurements at the Yb L_{III}-edge for $Yb_7TM_4InGe_{12}$ (TM = Co, Ni) were performed in the transmission mode using gas ionization chambers to monitor the incident and transmitted X-ray intensities. A third ionization chamber was used in conjunction with a copper foil to provide internal calibration for the alignment of the edge positions. Monochromatic X-rays was obtained using a Si (111) double crystal monochromator. The monochromator was calibrated by defining the inflection point (first derivative maxima) of Cu foil as 8980.5 eV. A Rh-coated x-ray mirror was utilized to suppress higher order harmonics. The Yb sample was prepared as a pellet from fine grounded amounts of around 1.8 mg and 180 mg of hexagonal BN. Measurements were performed at a range of temperatures from 15 K to 300 K using a closed cycle refrigerator. XAFS samples were prepared by mixing an appropriate amount of the finely ground Yb compound with BN. The mixture was pressed to form a self-supporting pellet, which was mounted on the cold finger of a closed-cycle refrigerator. Care was taken to suppress distortion in the data from thickness effects.

Magneto-Transport Measurements:

Magneto-transport measurements were performed on a needle-shaped crystal of $Yb_7Co_4InGe_{12}$ with approximate dimensions of 648 x 56 x 75 μm and the long direction oriented parallel to the crystallographic c-axis. Four gold wires were attached with silver paint, and the resistance of the sample was obtained in a standard four-probe measurement with a current of 100 μA. By averaging the sample voltage corresponding to positive and negative currents we eliminated artifacts due to the thermal voltages. The sample was inserted into a superconducting magnet equipped with a variable temperature insert that allows controlling of the sample's temperature between 1.2 K and 320 K. The magnetic field was oriented perpendicular to the needle.

2-3. Results and Discussion

Reaction Chemistry:

$Yb_7Co_4InGe_{12}$ was first observed from indium flux as silvery thin needles frequently aggregated in bundles. Figure 2-1(A) and (B) shows scanning electron micrographs of typical $Yb_7Co_4InGe_{12}$ and $Dy_7Co_4InGe_{12}$ crystals, respectively. Other reaction products for the Yb analog included Yb_2InGe_2,[25, 26] $Yb_5Co_4Ge_{10}$,[27] the cubic phase $YbIn_3$ and recrystallized germanium. Subsequent tuning of the reaction conditions increased the yield and eliminated all byproducts except Yb_2InGe_2 which, due to its very different crystal morphology, was easily distinguishable. When other RE metals such as La, Ce, Sm, Eu, Dy, Ho and Er were employed under the same reaction conditions only Dy and Ho were able to form the same phase but in much smaller yield. This suggests that the size of the rare-earth cations likely plays a decisive role for the formation of

$RE_7Co_4InGe_{12}$. The reaction targeting the $Dy_7Co_4InGe_{12}$ member of the present compounds also produced the quaternary phase $Dy_4CoInGe_4$, which will be discussed in the following chapter. The $Yb_7Co_4InGe_{12}$ compound does not melt up to 1000 °C, as confirmed by differential thermal analysis.

$Yb_7Ni_4InGe_{12}$ grows similarly as silvery thin needles often aggregated in bundles. From the reactions designed to produce the Ni quaternary compound a ternary compound was also observed, in which In was excluded from the product, as resulted from EDS analysis on many crystals. Subsequent single crystal X-ray diffraction analysis on those crystals gave the new ternary $Yb_2Ni_{1.5}Ge_{2.5}$ (or $Yb_4Ni_3Ge_5$) phase which will be described in a future work. It should be noted at this point, that when Yb was employed as the RE in the reactions targeted to form the Yb analog of the $RE_4Ni_2InGe_4$ family[17] $Yb_7Ni_4InGe_{12}$ was produced instead. This reinforces the suggestion stated above, that the size of the rare-earth cations probably plays a crucial role for the formation of these compounds.

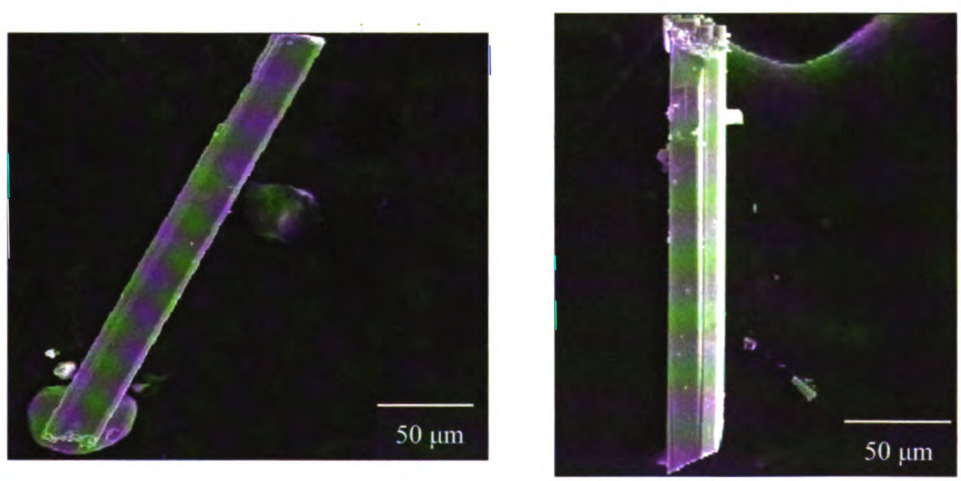

Figure 2-1. Scanning Electron micrograph (SEM) images of flux-grown crystals of (A) $Yb_7Co_4InGe_{12}$ and (B) $Dy_7Co_4InGe_{12}$.

Structure:

The $RE_7Co_4InGe_{12}$ (RE = Dy, Ho, Yb) compounds and $Yb_7Ni_4InGe_{12}$ crystallize in the tetragonal *P4/m* space group with the $Ca_7Ni_4Sn_{13}$ structure type.[28] $RE_7TM_4InGe_{12}$ is an ordered quaternary variant of this ternary phase, with the RE atoms occupying the Ca positions, the Co/Ni atoms the Ni sites and the Ge atoms adopting the Sn positions. The fact that the quaternary compound orders in this way is consistent with the more electropositive nature of the RE (compared to Co/Ni, In and Ge) and that they are more likely to adopt the electropositive Ca site within the compound. Additionally, it is expected for the transition metals of Co/Ni to adopt the Ni position, and as Ge is in the same group as Sn, it is not surprising that Ge atoms order on the Sn sites. Because of their isostructural nature we will describe the structure in terms of the $Yb_7Co_4InGe_{12}$ analog.

The overall structure of $Yb_7Co_4InGe_{12}$ as viewed down the *c*-axis is depicted in Figure 2-2. The bonds to the Yb atoms were omitted to emphasize the three-dimensional (3D) $[Co_4InGe_{12}]$ framework and its channels. This network is characterized by three different types of channels, propagating along the *c*-axis, in which the Yb atoms are situated. Another way to look at the $[Co_4InGe_{12}]$ sub-structure is in terms of columns of octagonal and hexagonal rings that run along the *a* and *b*-axes, while the void space between them is filled up by four pentagons related by the 4-fold axis of the tetragonal symmetry. The polygonal rings are connected down the *c*-axis via Co-Ge(3)-Co zigzag chains.

The biggest channels in the structure are built up from stacked alternating planar layers of distorted octagons and square planes, Figure 2-3. The octagons are comprised

from alternating Co(1) and Ge(2) atoms while the Yb(2) atoms are sitting in their center. The two Co(1)-Ge(2) interatomic distances at 2.390(2) and 2.434(2) Å, fall in the Co-Ge bond range found in other binary or ternary intermetallics.[29, 30] Similar octagonal channels can be found in $Yb_5T_4Ge_{10}$[27] and in general in the $RE_5TM_4X_{10}$ series[31, 32] (RE = rare earth, Sc or Y, TM = Co, Rh, Ir or Os and X = Si, Ge or Sn) which they all adopt the tetragonal $Sc_5Co_4Si_{10}$ (*P4/mbm*) structure[33].

Another structural feature is the hexagonal tunnels, Figure 2-3. In these, two Ge(1)-Ge(2) dimers are interconnected with two Co atoms to form distorted hexagonal rings which are stacked parallel to the *c*-axis and are connected via Ge(3) atoms. In contrast to the octagonal tunnels, here, the Yb(3) atoms are sandwiched between the hexagons. The Ge(1)-Ge(2) interatomic distances at 2.548(2) Å, are comparable with Ge-Ge contacts observed in many RE germanides with 2D and 3D networks including the $Ho_5Rh_4Ge_{10}$[29] at 2.539 Å.

The final noteworthy structural moiety is the pentagonal channels which are fused in groups of four that share a central column of square planar In atoms, see Figure 2-2. A Ge(1)-Ge(2) dimer is linked to a Co and an In atom from the Ge(2) and Ge(1) site, correspondingly; both of them connect to another Ge(1) atom, thus forming pentagonal rings that extend along the *c*-axis through one Co-Ge(3)-Co zigzag chain (Figure 2-3). The Co-Ge(2) and Co-Ge(1) distances at 2.434(2) Å and 2.369(2) Å, respectively, are also found in the two other types of rings. The four-coordinated In atoms are bonded to four Ge(1) atoms (with In-Ge(1) bond at 2.9214(14) Å) in a square-planar environment. This is a rare coordination environment for a group 13 element. A similar In coordination environment was also found in RE_2InGe_2.[25, 26] In the pentagonal channels, as in the case

of the hexagonal ones, the Yb(1) atoms are located between the pentagonal layers. There are no direct Co-Co bonds in the structure.

An alternative way to view the $Yb_7Co_4InGe_{12}$ structure is in polyhedral representation. Figure 2-4(A) depicts the connectivity of the Co-centered Ge tetragonal pyramids as viewed down the *c*-axis. Four such polyhedra share their Ge(2) corners in the *a*,*b*-plane, forming square rings, see Figure 2-4(B). These squares stack along the *c*-axis by connecting trough the Ge(3) corners of the pyramids to form square tubes that extend down the *c*-axis, Figure 2-4(C). These tubes are aligned parallel to each other, and every such tube is connected directly to four other neighboring tubes through Ge(1)-Ge(2) bonds at 2.548(2) Å to build the 3D $[Co_4InGe_{12}]$ framework. The Yb(2) atoms reside within the tubes, whereas Yb(1) and Yb(3) atoms are located between adjacent square tunnels.

The local coordination environments (within 3.5 Å) of the RE atoms are illustrated in Figure 2-5. RE(1) atoms are 11-coordinate and are sitting in the center of a pentagonal prism, made up of six Ge(1), two Co and two In atoms, and are capped with one Ge(3) atom. The RE(2) atoms have 16 neighbors in their immediate coordination sphere. These include four Ge(2) and four Co atoms in a form of a flat octagonal ring (where the RE(2) is the center) and eight additional Ge(3) atoms with four located above and four below the octagon in a square prismatic geometry. Finally, RE(3) exhibit a coordination number of fourteen, in an arrangement that is best described as a hexagonal prism comprising four Ge(1), four Ge(2) and four Co atoms, capped by two Ge(3) atoms. Tables 2-7 and 2-8 give a complete list of the bond distances for $RE_7Co_4InGe_{12}$ and $Yb_7Ni_4InGe_{12}$, correspondingly.

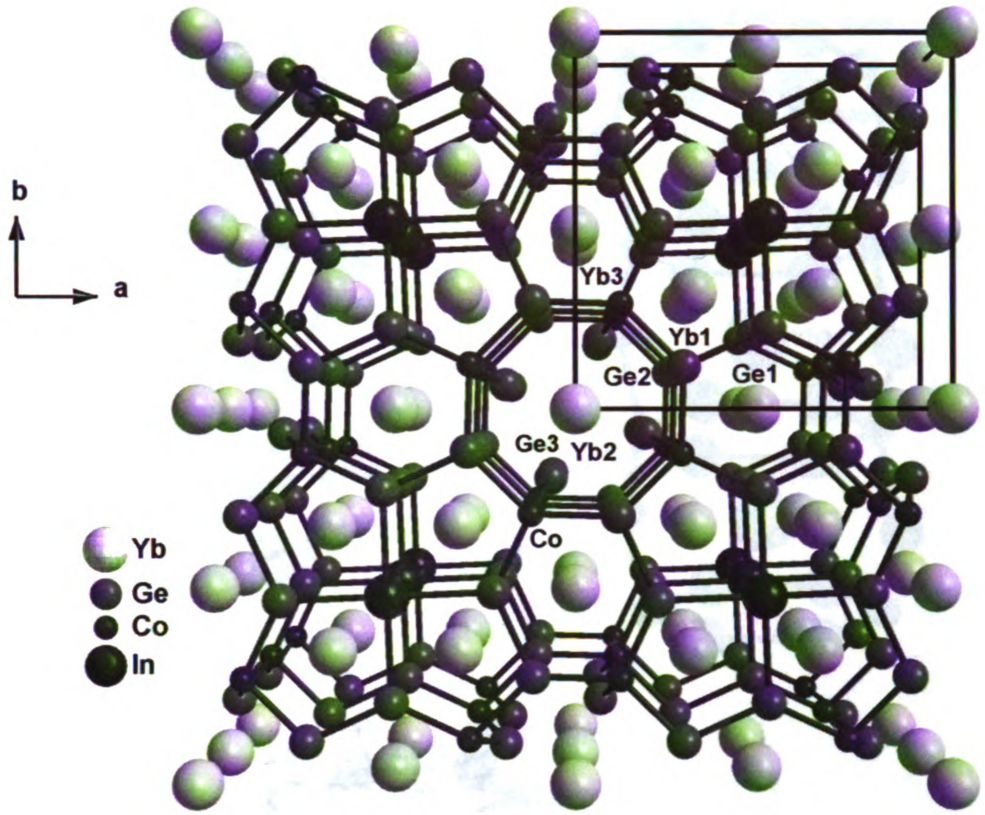

Figure 2-2. The overall structure of $Yb_7Co_4InGe_{12}$ as viewed onto the *a,b*-plane. For clarity the bonds to the Yb atoms are not drawn.

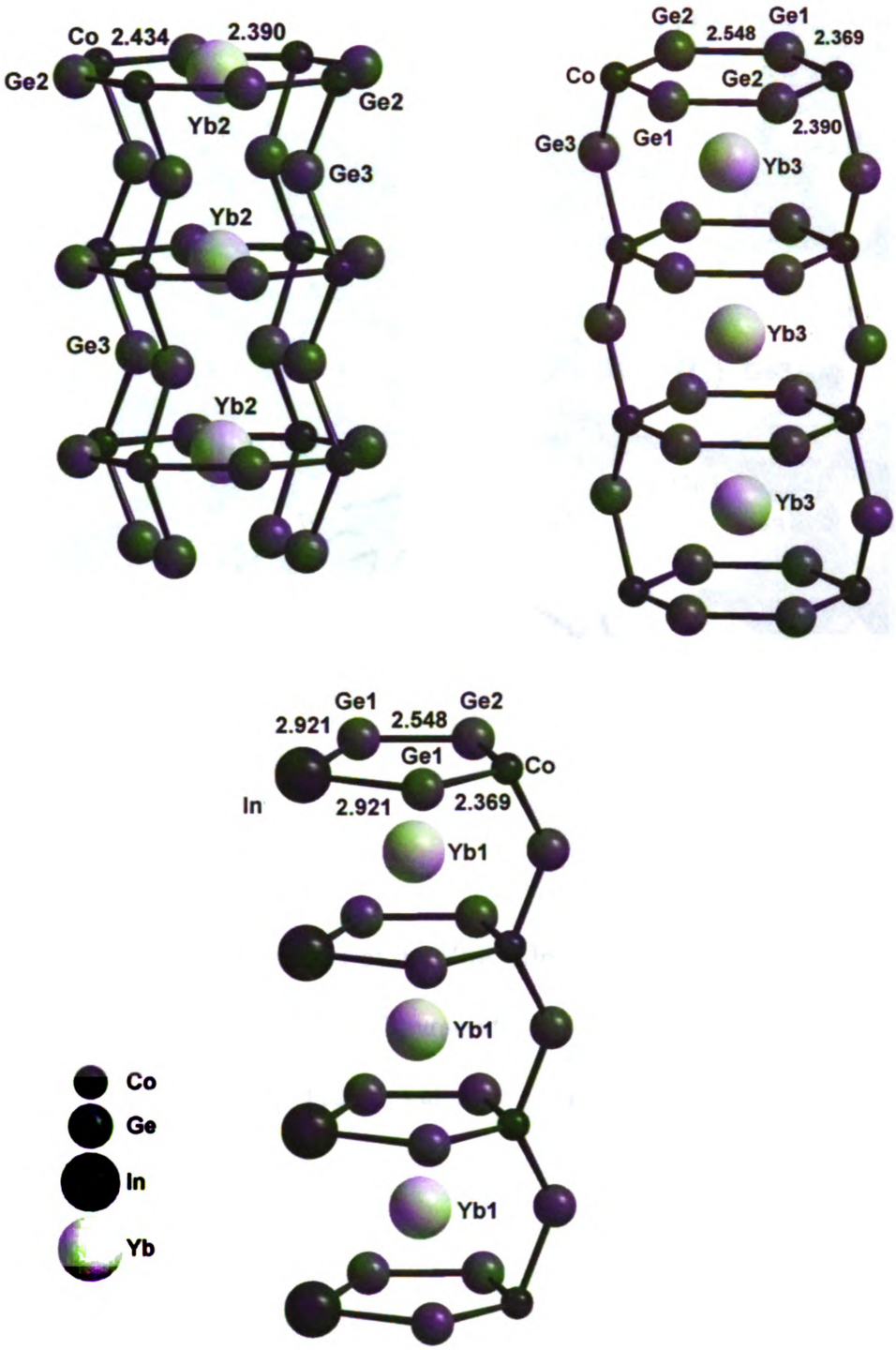

Figure 2-3. The octagonal, hexagonal and pentagonal rings and their interconnection to form the corresponding tunnels running down the *c*-axis.

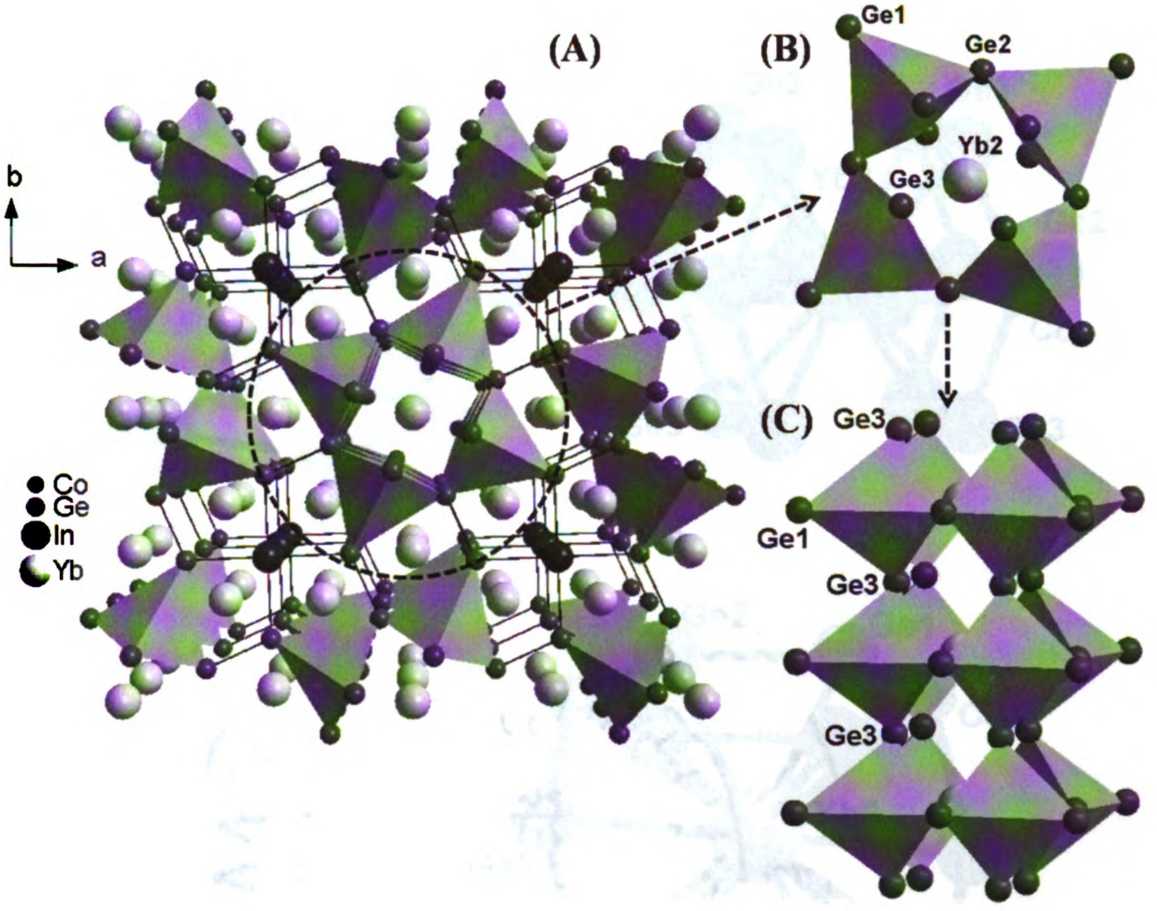

Figure 2-4. (A) Polyhedral view of the $Yb_7Co_4InGe_{12}$ structure featuring the connectivity between Co-centered Ge tetragonal pyramids. (B) The polyhedra share Ge(2) corners to form squares. (C) Stacking of squares along the *c*-axis forming square tubes.

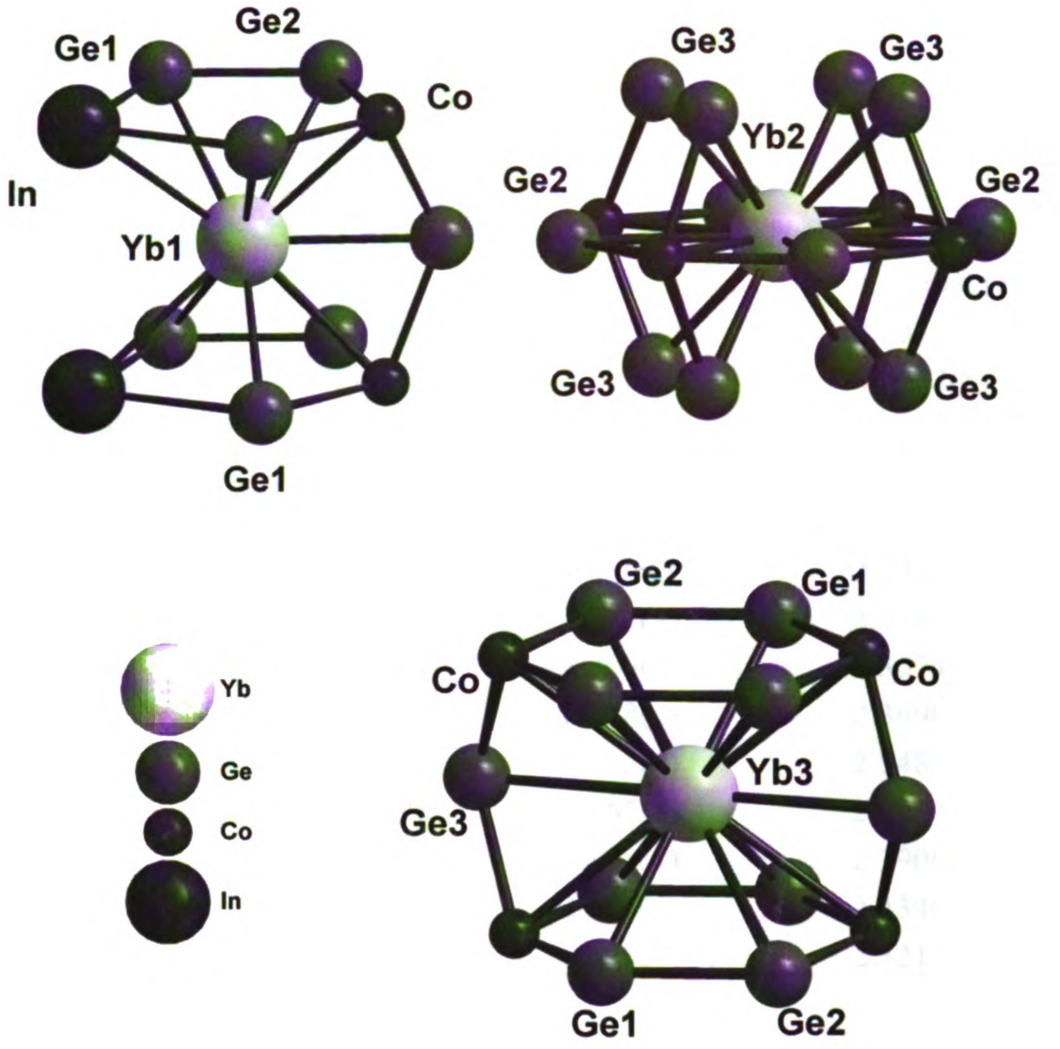

Figure 2-5. The coordination environment of the RE atoms. The coordination sphere cutoff is 3.4 Å.

Table 2-7. Bond lengths [Å] for $RE_7Co_4InGe_{12}$ (RE = Dy, Ho, Yb).

Bond	RE = Dy	RE = Ho	RE = Yb
RE(1)-Ge(1)	2.9336(9)	2.932(1)	2.9060(10)
RE(1)-Ge(3)	3.0048(13)	3.001(3)	2.9820(16)
RE(1)-Co	3.0329(11)	3.025(2)	3.0102(13)
RE(1)-Ge(1)	3.0610(9)	3.043(2)	3.0298(10)
RE(1)-Ge(2)	3.0441(9)	3.045(2)	3.0340(11)
RE(1)-In	3.3109(4)	3.2965(11)	3.2838(5)
RE(1)-RE(1)	3.6324(8)	3.6204(18)	3.5983(8)
RE(2)-Ge(3)	2.9829(9)	2.983(2)	2.9575(10)
RE(2)-Co	3.1428(14)	3.158(3)	3.1323(17)
RE(3)-Ge(1)	3.0473(9)	3.039(2)	3.0473(10)
RE(3)-Ge(3)	3. 2300(12)	3. 226(3)	3.2360(15)
RE(3)-Ge(2)	3.2620(9)	3.262(2)	3.2392(12)
RE(3)-Co	3.3257(11)	3.309(3)	3.3074(14)
Ge(1)-Co	2.3702(18)	2.378(4)	2.369(2)
Ge(1)-Ge(2)	2.5652(17)	2.552(4)	2.548(2)
Ge(1)-In	2.9643(12)	2.965(3)	2.9214(14)
Ge(2)-Co	2.3937(19)	2.398(4)	2.390(2)
Ge(2)-Co	2.4493(19)	2.453(4)	2.434(2)
Ge(3)-Co	2.3302(9)	2.3203(19)	2.3213(10)

Table 2-8. Selected Bond lengths [Å] for $Yb_7Ni_4InGe_{12}$.

Bond	Length
Yb(1)-Ge(1)	2.9086(7)
Yb(1)-Ge(1)	3.0208(7)
Yb(1)-Ge(3)	3.0139(11)
Yb(1)-Ge(2)	3.0419(8)
Yb(1)-Ni	3.0316(9)
Yb(1)-In	3.2809(5)
Yb(1)-Yb(1)	3.5831(7)
Yb(2)-Ge(3)	2.9539(8)
Yb(2)-Ni	3.1290(11)
Yb(3)-Ge(1)	3.0732(7)
Yb(3)-Ge(2)	3.2405(8)
Yb(3)-Ge(3)	3.2553(11)
Yb(3)-Ni	3.3209(9)
Ge(1)-Ni	2.3938(14)
Ge(2)-Ni	2.4383(15)
Ge(2)-Ni	2.4002(15)
Ge(3)-Ni	2.3336(7)
Ge(1)-Ge(2)	2.5430(13)
Ge(1)-In	2.9016(10)

Magnetic Measurements:

Magnetic susceptibility data for $Yb_7Co_4InGe_{12}$ are presented in Figure 2-6(A). The temperature dependence of the molar susceptibility (χ_m) displays paramagnetic behavior suggesting the existence of Yb^{3+} moments in the material. No magnetic ordering was observed down to 3.5 K. The inverse susceptibility does not follow the Curie-Weiss law especially at the temperature region below 100 K, which can be attributed to crystal-field contributions and / or to a possible onset of a valence fluctuation. The weak linearity of the data precluded the unequivocal determination of the μ_{eff}. However, analyzing the susceptibility data in a proper temperature range (T > 100 K) with the modified Curie-Weiss law $\chi(T) = \chi_0 + C / (T - \theta_p)$ yields information concerning the sum of the temperature-independent conributions χ_o, e.g. van Vleck paramagnetism, paramagnetism due to conduction electrons, and core-electron diamagnetism, the effective magnetic moment μ_{eff} (deduced from the Curie constant C), and the Weiss constant θ_p. A nonlinear least-squares fit to this equation resulted in $\chi_0 = 1.9 \times 10^{-3}$ emu/mol Yb, $\theta_p = -38$ K indicating antiferromagnetic interactions among the Yb atoms, and an effective moment of 3.1 μ_B / Yb, which is ~68% of the value expected for the free-ion Yb^{3+}, 4.54 μ_B. This means that more than half of the Yb atoms are in the Yb^{3+} state. This is supported by the XANES studies presented below.

The field dependence of magnetization for $Yb_7Co_4InGe_{12}$ at 3 K can be found in Figure 2-6(B). The magnetization increases linearly up to a field of 20 kG, at which point the slope continuously changes until approximately 33 kG where it becomes linear again, but with a much shallower slope. The response remains linear up to the highest attainable field with no signs of saturation up to 50 kG. The moment reaches a value of only 2.7 μ_B

per formula which is about 30 % of the value anticipated for the fully saturated moment of seven Yb^{3+} ions..

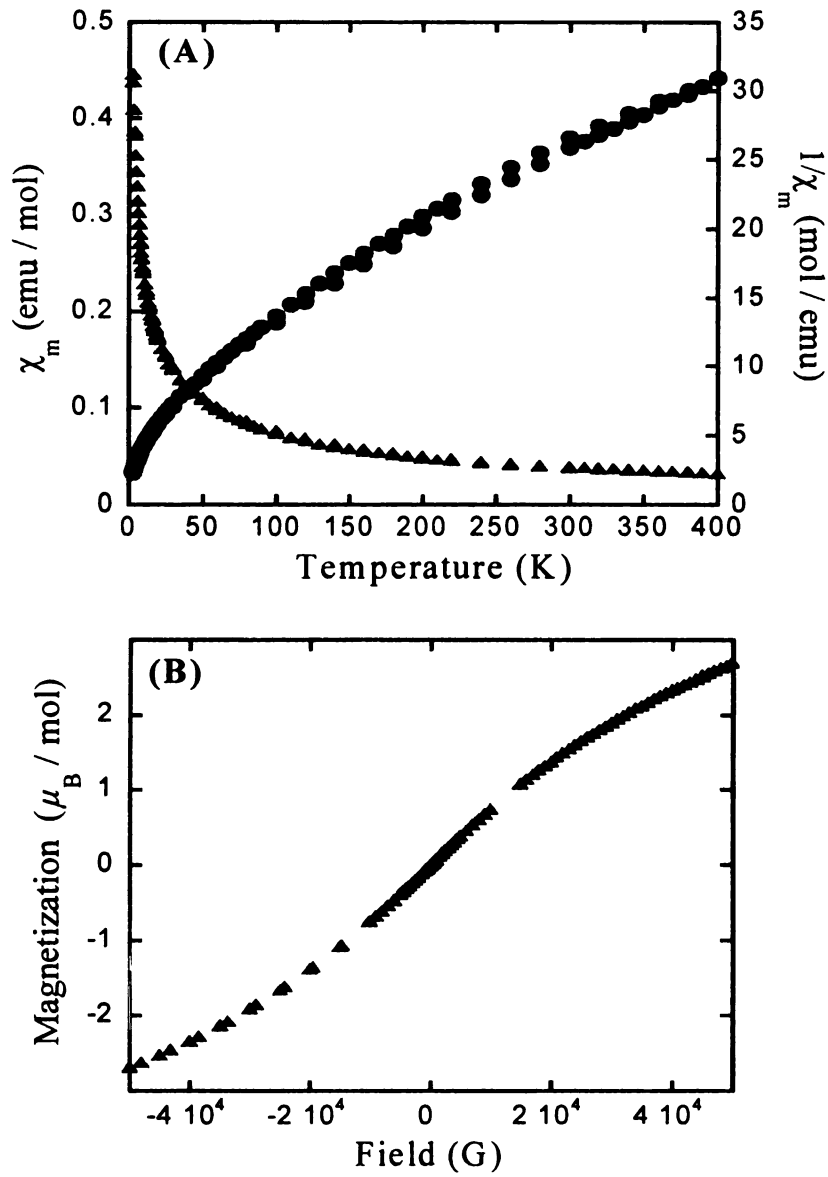

Figure 2-6. (A) Temperature dependence of the molar susceptibility χ_m (triangles) and inverse 1 / χ_m (circles) for $Yb_7Co_4InGe_{12}$ with an applied field of 500 G. (B) Magnetization data for $Yb_7Co_4InGe_{12}$ collected at 3 K.

Temperature dependent magnetic susceptibility χ(M/H) data performed on randomly oriented single crystals of $Dy_7Co_4InGe_{12}$ are plotted in Figure 2-7(A). Due to the very small size of the sample we were not able to determine the weight and as result we could not calculate the molar susceptibility. Nevertheless, the compound seems to undergo a ferromagnetic transition that onsets at a *T*c of ~ 21 K as indicated by a change in the slope of χ. As it can be clearly seen from the inset in Figure 2-7(A), the ZFC (zero field cooled) and FC (field cooled) data reveal considerable different behavior at the low temperature range starting at ~ 8 K. The ferromagnetic order of the spins is also confirmed from the field dependent magnetic moment data measured at 3 K, given in Figure 2-7(B). Apparent hysteresis loops appear up to at least 20 kG and – 20 kG, while the moment does not seem to saturate up to the highest attainable field of 50 kG.

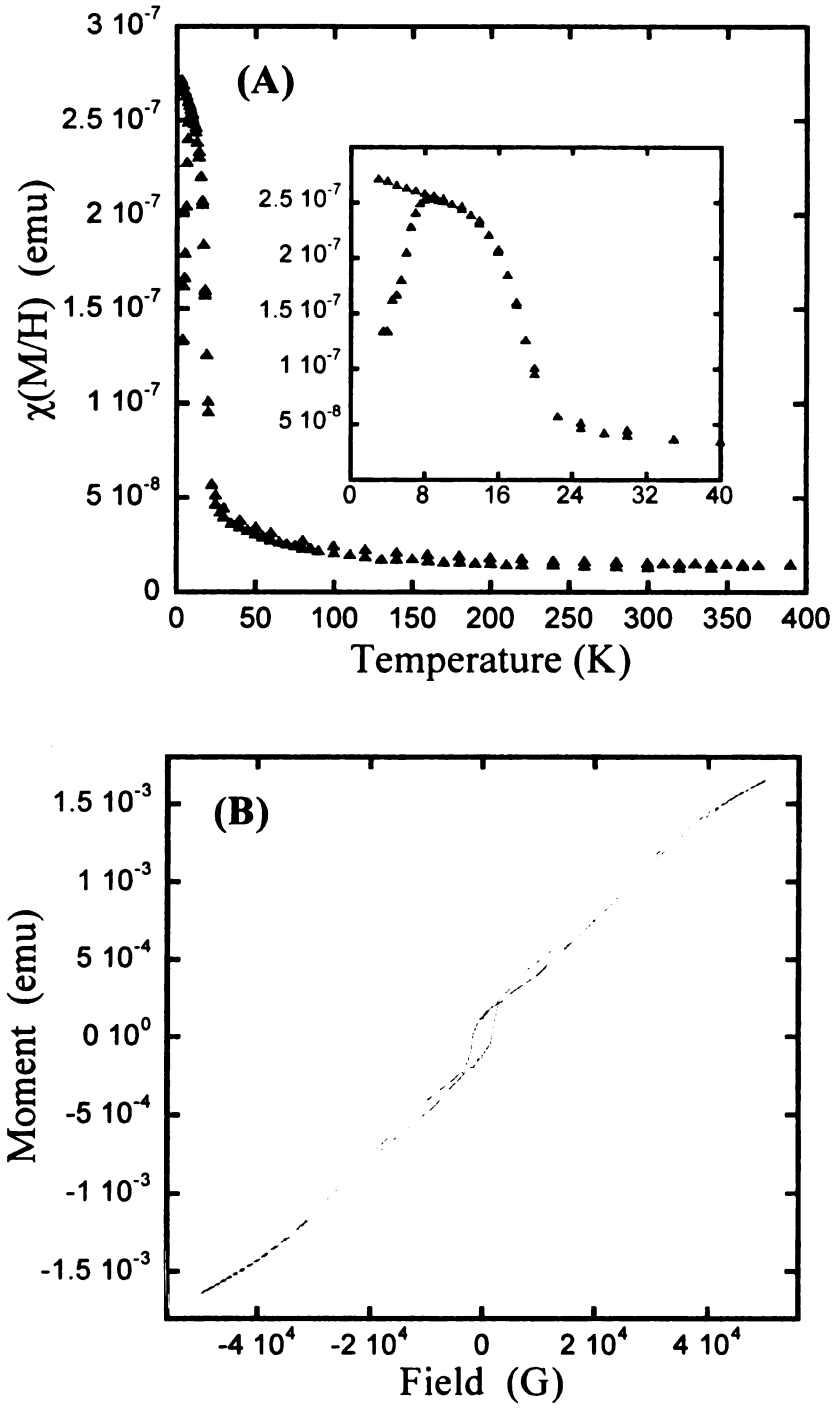

Figure 2-7. (A) Temperature variation of the susceptibility χ(M/H) for $Dy_7Co_4InGe_{12}$ with an applied field of 500 G. Inset shows the low temperature (0-40 K) data. (B) Magnetic moment data for $Dy_7Co_4InGe_{12}$ collected at 3 K.

XPS Measurements:

To further probe the Yb oxidation state in $Yb_7Co_4InGe_{12}$ we performed X-ray photoelectron spectroscopy (XPS) measurements. The XPS spectrum revealed a strong peak at ~ 185 eV and a multiplet structure at higher energies (Figure 2-8). This type of spectrum is consistent with the presence of Yb^{3+} ions.[34, 35] With careful inspection of the spectra, we see two very weak peaks at ~181 and 191 eV. This double peak is known from the literature that is attributed to Yb^{2+} ions.[34]

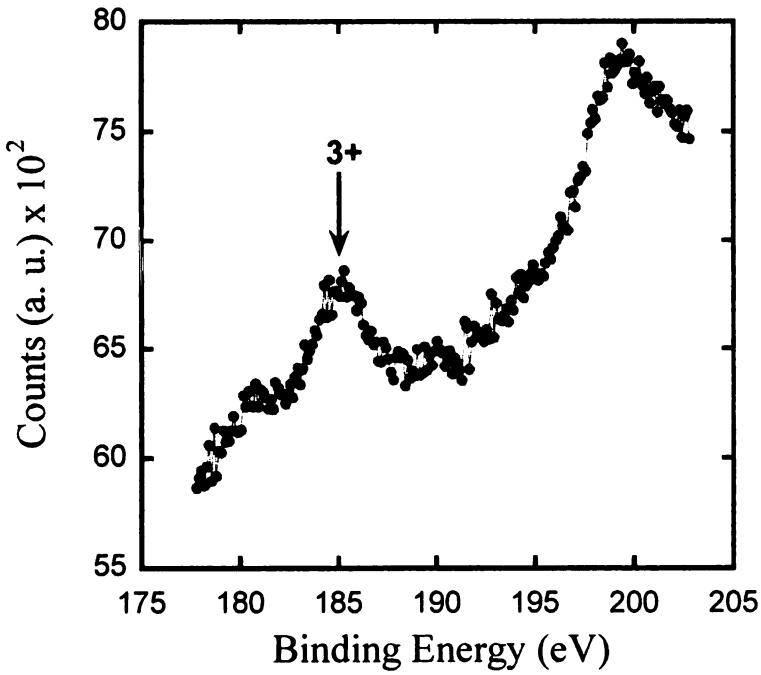

Figure 2-8. XPS spectra of Yb 4d core level for $Yb_7Co_4InGe_{12}$ at 300 K.

XANES Measurements:

Because XPS is a surface analytical technique it was crucial to carry out X-ray absorption near-edge spectroscopy (XANES) measurements at the Yb L_{III}-edge, which is an established method for studying the valence of the absorbing element. XANES fundamentally probes the bulk of the sample. The near-edge spectra of an $Yb_4Co_7InGe_{12}$ sample obtained at 15 K and 300 K are given in Figure 2-9. The main absorption peak (white line) for both spectra is centered at ~ 8948 eV, which is typical of trivalent Yb, both in oxide form as well as in Yb intermetallics.[36-38] Relative to Yb^{3+}, divalent Yb exhibits a white line which is ~ 8 eV lower in energy.[36-38] The spectra also reveal the presence of a weaker feature (shoulder) at ~ 8940 eV, indicating that some divalent Yb is also present.

Another interesting observation in the XANES spectra is that the relative ratio of the features at 8940 and 8948 eV varies weakly with temperature. In particular, with increasing temperature the low-energy peak originating from Yb^{2+} ion is slightly depressed, whereas the high-energy one originating from Yb^{3+} ion is enhanced, suggesting that the average valence of Yb is slightly temperature dependent and that the Yb^{3+} state is more populated at higher temperatures. Similar behavior was observed in the $YbCu_{5-x}Ga_x$ series.[39] Figure 2-10 displays both the spectra of the present phase and Yb_2O_3 at room temperature. To ensure that we are not observing spectra from oxide impurities, we also computed and compared the XAFS of $Yb_4Co_7InGe_{12}$ with that of Yb_2O_3 standard. The absence of Yb-O bonds shows that the Yb in the sample is not coordinated to oxygen, indicating that the trivalent character is intrinsic to $Yb_4Co_7InGe_{12}$, Figure 2-11.

An attempt to obtain the relative amount of Yb^{3+} and Yb^{2+} was performed by representing the normalized Yb XANES as a pair of pseudo-Voigt and modified arc-tangent functions. We estimate the amount of Yb^{3+} to be ~ 73% with an error of ~ 15%. A more accurate determination of Yb valence will require measurements of Yb^{2+} and Yb^{3+} standards (or analogs) with similar structure to the sample under study and will be a subject of future investigations.

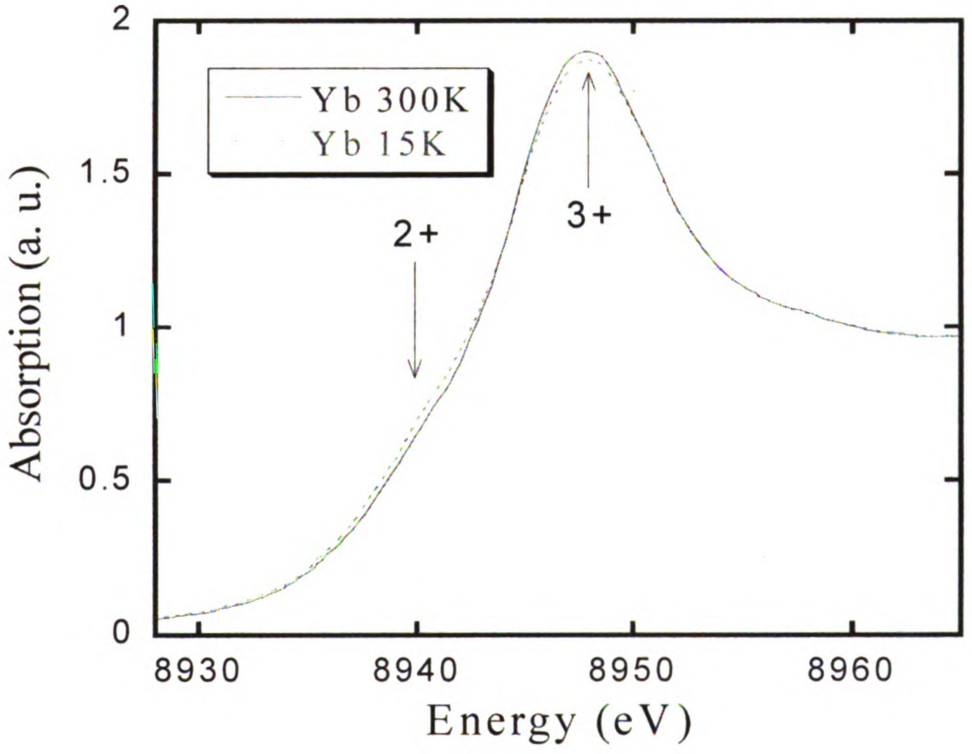

Figure 2-9. L_{III} absorption edge spectra of Yb in $Yb_7Co_4InGe_{12}$ at 15 K (dashed line) and 300 K (solid line).

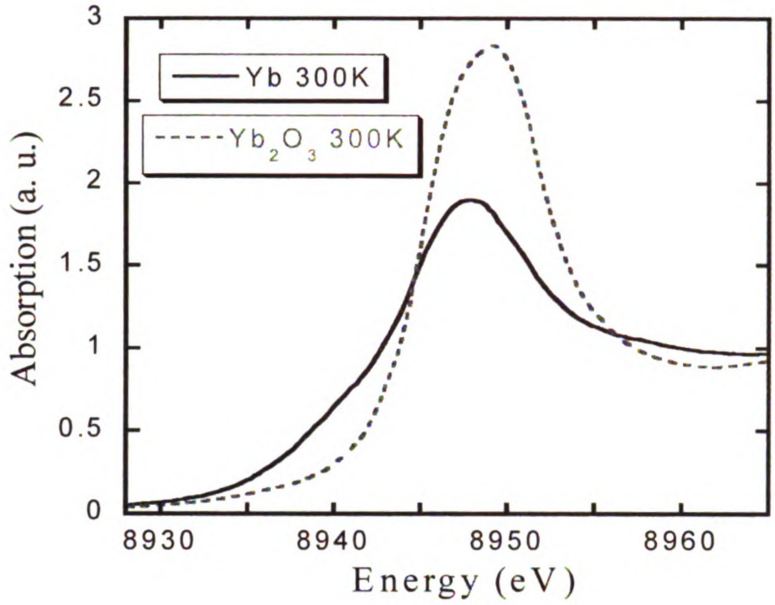

Figure 2-10. Comparison of $Yb_7Co_4InGe_{12}$ (solid line) and Yb_2O_3 (dashed line) spectra at room temperature.

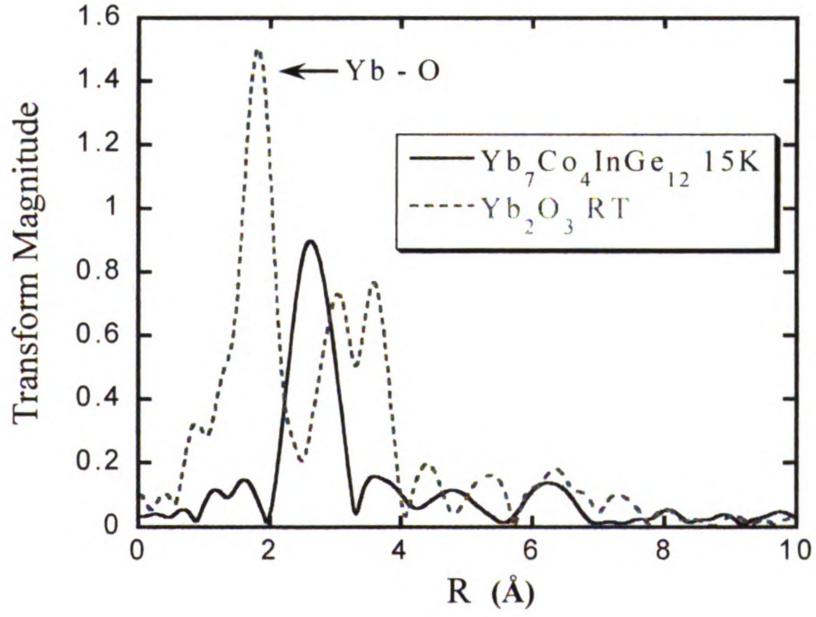

Figure 2-11. The Fourier Transform (FT) of the Yb XAFS for $Yb_4Co_7InGe_{12}$ (15 K) compared with that for Yb_2O_3 (RT). The FT's are not corrected for photo-electron phase shifts. The k-range of the FT was 3-10 $Å^{-1}$.

X-ray absorption near-edge spectroscopy (XANES) measurements at the Yb L_{III}-edge were also performed for the $Yb_4Ni_7InGe_{12}$ compound. The near-edge spectra of an $Yb_4Ni_7InGe_{12}$ sample obtained at 18 K and 295 K are given in Figure 2-12. The double-peaked structure of the spectra for both measured temperatures indicates that the Ni compound is also a mixed-valence compound. Additionally, the relative ratio of the features at 8940 and 8948 eV, originating from Yb^{2+} and Yb^{3+} ions respectively, varies weakly with temperature. Particularly the Yb^{3+} state tends to be more populated at higher temperatures, as it was also observed for the $Yb_4Co_7InGe_{12}$ compound. An attempt to estimate the relative amount of Yb^{3+} and Yb^{2+} resulted in a Yb^{3+} content of ~ 73 (5) %.

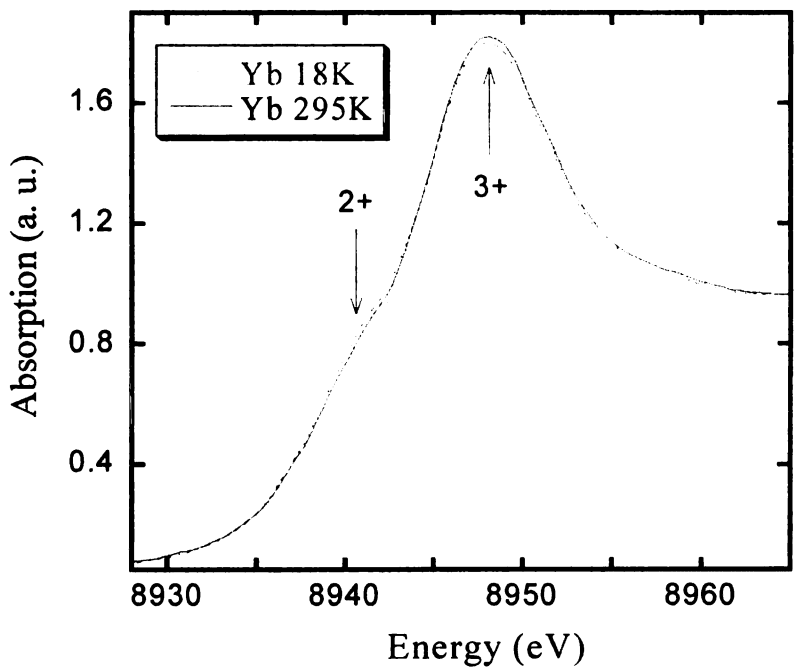

Figure 2-12. L_{III} absorption edge spectra of Yb in $Yb_7Ni_4InGe_{12}$ at 18 K (dashed line) and 295 K (solid line).

Magneto-Transport Measurements:

The temperature dependence of the resistivity (ρ) for samples of $Yb_4Co_7InGe_{12}$ with and without the application of magnetic field is shown in Figure 2-12. The resistivity data measured on single crystals along the *c*-axis and at zero applied field reveal a rather moderate metallic behavior with $\rho \sim 205\ \mu\Omega$ cm at 246 K. The inset in Figure 2-13 displays the low-temperature ρ data at a field of 0, 1 and 5 T applied perpendicular to the *c*-axis. It can be clearly seen that the material displays negative-magnetoresistance at low temperatures (i.e. the resistivity drops with increasing applied field). This behavior is frequently seen in many Kondo or Heavy Fermion systems and it is attributed to the suppression of scattering of the conduction electrons from the unpaired f-electrons in a high field.

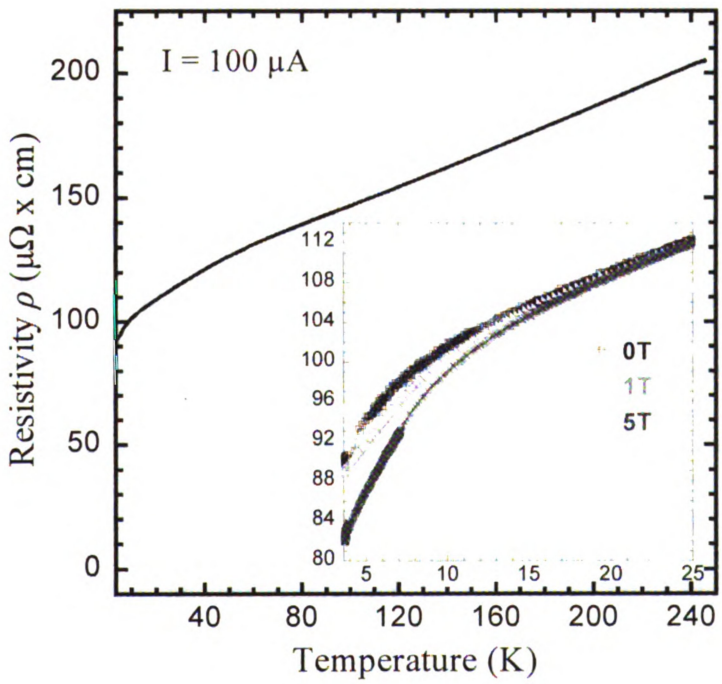

Figure 2-13. Variable temperature single-crystal resistivity data for $Yb_7Co_4InGe_{12}$ at zero field. Inset: displays the low temperature resistivity data at 0, 1 and 5 T field.

Both magnetic susceptibility and XANES measurements suggest that the $Yb_4Co_7InGe_{12}$ is a new heterogeneous mixed-valence compound, i.e., a system with both Yb^{3+} and Yb^{2+} sites with about two thirds of the Yb atoms being in the Yb^{3+} (f^{13}) state. Because there are three crystallographically distinct Yb sites, we can possibly speculate that two of them have atoms in the Yb^{3+} configuration and one in the Yb^{2+} configuration. To assign which site could possibly accommodate Yb^{2+} ions, we can compare the coordination environment of each Yb site. The nearest neighbor distances for Yb(1) are 2.9060 (Yb-Ge) and 3.0102 (Yb-Co) Å, respectively, whereas those for the Yb(2) site are 2.9575 (Yb-Ge) and 3.1323 (Yb-Co) Å, respectively. The corresponding distances for the Yb(3) site are 3.0473 (Yb-Ge) and 3.3074 (Yb-Co) Å, respectively. Because the distances around the Yb(3) sites are considerably longer than those of the other two sites, a plausible conclusion is that the Yb^{2+} ions with their larger ionic radius probably occupy the Yb(3) site.

2-4. Conclusions

Four new quaternary $RE_7TM_4InGe_{12}$ phases crystallize in molten In in the tetragonal *P4/m* space group with the $Ca_7Ni_4Sn_{13}$ structure type. The flux seems necessary to stabilize these compounds because direct combination of the elements and induction heating reactions with various stoichiometric ratios failed so far to form them. In general, when studying systems of the type RE/M/Ge in liquid In, the tendency is for In not to get incorporated into the compound. In the case of $RE_7TM_4InGe_{12}$, we observe the reactive nature of the flux where In enters the structure of the final product. The fact that only Dy, Ho and Yb form the $RE_7Co_4InGe_{12}$ and only Yb the corresponding Ni

compound (other RE atoms produced the $RE_4Ni_2InGe_4$ phase), suggests that the size of the rare-earth cations likely plays a decisive role for the formation of these compounds.

The $Yb_7Co_4InGe_{12}$ and $Yb_7Ni_4InGe_{12}$ are mixed valence compounds with a high Yb^{3+}/Yb^{2+} ratio which is slightly temperature dependent. Because of the small yields of the other two RE analogs complete property characterization could not be performed. Nevertheless, preliminary magnetic susceptibility measurements for $Dy_7Co_4InGe_{12}$ indicate ferromagnetic ordering below 21 K.

References:

1. Kanatzidis, M. G.; Pöttgen, R.; Jeitschko, W., *Angewandte Chemie-International Edition* **2005,** 44, (43), 6996-7023.

2. Chen, X. Z.; Sportouch, S.; Sieve, B.; Brazis, P.; Kannewurf, C. R.; Cowen, J. A.; Patschke, R.; Kanatzidis, M. G., *Chemistry of Materials* **1998,** 10, (10), 3202-3211.

3. Sieve, B.; Chen, X. Z.; Henning, R.; Brazis, P.; Kannewurf, C. R.; Cowen, J. A.; Schultz, A. J.; Kanatzidis, M. G., *Journal of the American Chemical Society* **2001,** 123, (29), 7040-7047.

4. Sieve, B.; Trikalitis, P. N.; Kanatzidis, M. G., *Zeitschrift Fur Anorganische Und Allgemeine Chemie* **2002,** 628, (7), 1568-1574.

5. Chen, X. Z.; Larson, P.; Sportouch, S.; Brazis, P.; Mahanti, S. D.; Kannewurf, C. R.; Kanatzidis, M. G., *Chemistry of Materials* **1999,** 11, (1), 75-83.

6. Zhuravleva, M. A.; Kanatzidis, M. G., *Zeitschrift Fur Naturforschung Section B-a Journal of Chemical Sciences* **2003,** 58, (7), 649-657.

7. Chen, X. Z.; Small, P.; Sportouch, S.; Zhuravleva, M.; Brazis, P.; Kannewurf, C. R.; Kanatzidis, M. G., *Chemistry of Materials* **2000,** 12, (9), 2520-2522.

8. Zhuravleva, M. A.; Pcionek, R. J.; Wang, X. P.; Schultz, A. J.; Kanatzidis, M. G., *Inorganic Chemistry* **2003,** 42, (20), 6412-6424.

9. Zhuravleva, M. A.; Evain, M.; Petricek, V.; Kanatzidis, M. G., *Journal of the American Chemical Society* **2007,** 129, (11), 3082-3083.

10. Salvador, J. R.; Bilc, D.; Gour, J. R.; Mahanti, S. D.; Kanatzidis, M. G., *Inorganic Chemistry* **2005,** 44, (24), 8670-8679.

11. Salvador, J. R.; Gour, J. R.; Bilc, D.; Mahanti, S. D.; Kanatzidis, M. G., *Inorganic Chemistry* **2004,** 43, (4), 1403-1410.

12. Bailey, M. S.; McGuire, M. A.; DiSalvo, F. J., *Journal of Solid State Chemistry* **2005,** 178, (11), 3494-3499.

13. Benbow, E. M.; Latturner, S. E., *Journal of Solid State Chemistry* **2006,** 179, (12), 3989-3996.

14. Klunter, W.; Jung, W., *Journal of Solid State Chemistry* **2006,** 179, (9), 2880-2888.

15. Lukachuk, M.; Galadzhun, Y. V.; Zaremba, R. I.; Dzevenko, M. V.; Kalychak, Y. M.; Zaremba, V. I.; Rodewald, U. C.; Pottgen, R., *Journal of Solid State Chemistry* **2005,** 178, (9), 2724-2733.

16. Zaremba, V. I.; Dubenskiy, V. P.; Rodewald, U. C.; Heying, B.; Pottgen, R., *Journal of Solid State Chemistry* **2006,** 179, (3), 891-897.

17. Salvador, J. R.; Kanatzidis, M. G., *Inorganic Chemistry* **2006,** 45, (18), 7091-7099.

18. Lawrence, J. M.; Riseborough, P. S.; Parks, R. D., *Reports on Progress in Physics* **1981,** 44, (1), 1-84.

19. Kindler, B.; Finsterbusch, D.; Graf, R.; Ritter, F.; Assmus, W.; Luthi, B., *Physical Review B* **1994,** 50, (2), 704-707.

20. Sheldrick, G. M. *SADABS and SAINT*, version 4; University of Gottingen: Gottingen, Germany, 1995.

21. Sheldrick, G. M. *SHELXTL, Structure Determination Program*, version 5; Siemens Analytical X-ray Instruments Inc.: Madison, WI, 1995.

22. Farrugia, L. J. *WinGX, Solution, Refinement and Analysis of Single Crystal X-Ray Diffraction Data*, version 1.70.01; University of Glasgow: Glasgow, Scotland, 1997-2005. .

23. GmbH, S. C., **2006**, D 64295 Darmstadt, Germany.

24. Bruker, *Advanced X-ray Solutions SHELXTL (Version 6.14)*, Bruker AXS Inc., Madison, WI (2003).

25. Zaremba, V. I.; Tyvanchuk, Y. B.; Stepien-Damm, J., *Zeitschrift Fur Kristallographie-New Crystal Structures* **1997,** 212, (2), 291-291.

26. Tobash, P. H.; Lins, D.; Bobev, S.; Lima, A.; Hundley, M. F.; Thompson, J. D.; Sarrao, J. L., *Chemistry of Materials* **2005,** 17, (22), 5567-5573.

27. Katoh, K.; Tsutsumi, T.; Yamada, K.; Terui, G.; Niide, Y.; Ochiai, A., *Physica B-Condensed Matter* **2006,** 373, (1), 111-119.

28. Vennos, D. A.; Badding, M. E.; Disalvo, F. J., *Journal of the Less-Common Metals* **1991,** 175, (2), 339-346.

29. Mruz, O. Y.; Belsky, V. K.; Gorelenko, Y. K.; Skolozdra, R. V.; Bodak, O. I., *Ukrainskii Fizicheskii Zhurnal* **1987,** 32, (12), 1856-1858.

30. Welter, R.; Venturini, G.; Malaman, B.; Ressouche, E., *Journal of Alloys and Compounds* **1993,** 201, 191-196.

31. Patil, N. G.; Ramakrishnan, S., *Physical Review B* **1999,** 59, (14), 9581-9589.

32. Becker, B.; Patil, N. G.; Ramakrishnan, S.; Menovsky, A. A.; Nieuwenhuys, G. J.; Mydosh, J. A., *Physical Review B* **1999,** 59, (11), 7266-7269.

33. Braun, H. F.; Yvon, K.; Braun, R. M., *Acta Crystallographica Section B-Structural Science* **1980,** 36, (OCT), 2397-2399.

34. Chung, J. S.; Cho, E. J.; Oh, S. J., *Physical Review B* **1990,** 41, (9), 5524-5528.

35. Szytula, A.; Jezierski, A.; Penc, B.; Winiarski, A.; Leithe-Jasper, A.; Kaczorowski, D., *Journal of Alloys and Compounds* **2003,** 360, (1-2), 41-46.

36. Rao, C. N. R.; Sarma, D. D.; Sarode, P. R.; Sampathkumaran, E. V.; Gupta, L. C.; Vijayaraghavan, R., *Chemical Physics Letters* **1980,** 76, (3), 413-415.

37. Hatwar, T. K.; Nayak, R. M.; Padalia, B. D.; Ghatikar, M. N.; Sampathkumaran, E. V.; Gupta, L. C.; Vijayaraghavan, R., *Solid State Communications* **1980,** 34, (8), 617-620.

38. Moreschini, L.; Dallera, C.; Joyce, J. J.; Sarrao, J. L.; Bauer, E. D.; Fritsch, V.; Bobev, S.; Carpene, E.; Huotari, S.; Vanko, G.; Monaco, G.; Lacovig, P.; Panaccione, G.; Fondacaro, A.; Paolicelli, G.; Torelli, P.; Grioni, M., *Physical Review B* **2007,** 75, (3), 035113.

39. Bauer, E.; Tuan, L.; Hauser, R.; Gratz, E.; Holubar, T.; Hilscher, G.; Michor, H.; Perthold, W.; Godart, C.; Alleno, E.; Hiebl, K., *Physical Review B* **1995,** 52, (6), 4327-4335.

CHAPTER 3

Flux Synthesis of the New Quaternary Intermetallic $Dy_4CoInGe_4$ Exhibiting Complex Magnetic Behavior

3-1. Introduction

The ternary systems of RE/TM/In and RE/TM/Ge (RE = rare earth metal and TM = transition metal) have been the subject of intensive investigations in the last few decades. These studies resulted in numerous novel intermetallic compounds with a variety of different crystal structures[1] and interesting magnetic and electrical properties.[2] Of the large number of intermetallic compounds in these systems, specifically the examination of those containing Co as the transition metal yield many phases with rich structural diversity and composition. Kalychack has made a concentrated effort to generalize and present the crystallographic characteristics of the RE/Co/In systems containing compounds with established crystal structure.[3] Additionally, both RE/Co indides and germanides have attracted much interest because they exhibit a variety of intriguing electrical and physical phenomena, which include heavy fermions, superconductivity and their coexistence, pressure induced superconductivity, Kondo lattices, magnetic ordering, mixed-valent and valence fluctuating behavior to name a few.[4-11]

Notable cobalt-containing indides include the heavy fermion superconductor at ambient pressure $CeCoIn_5$ with transition temperature T_c of 2.3 K, the discovery of which sparked an intense and continuous research of the $CeTMIn_5$ (TM = Co, Ir, Rh) family of compounds.[4-6] It was later shown in more detailed studies that $CeCoIn_5$ is an

unconventional superconductor very close to a quantum phase transition (QPT) at ambient pressure with *d*-wave symmetry below $T_c = 2.2$ K[7,12] while a magnetic quantum critical point (QCP) can be achieved by the application of a magnetic field of the order of the upper critical field $H_{c2}(0)$.[13] In the RE_2CoIn_8 systems the Ce analog is a Kondo lattice, exhibiting also heavy fermion superconductivity at ambient pressure with $T_c = 0.4$ K,[8,9] while the Dy and Ho ones display field induced ferromagnetic behavior at low temperatures.[9] On the other hand, noteworthy germanides comprise the $CeCoGe_2$ which is a heavy fermion Kondo compound with $T_K > 200$ K[10], while the non-stochiometric $CeCo_{0.89}Ge_2$ exhibits heavy-fermion and valence fluctuating behavior.[11] Interestingly, the stoichiometric CeCoGe absorbs very slowly hydrogen at 393K under a pressure $P(H_2)$ = 2MPa.[14]

Recently, it has been demonstrated that molten metal fluxes, particularly Al and Ga, are excellent preparative tools for the exploratory synthesis of intermetallic compounds.[15] Our own work in the systems RE/TM/Al/Si or Ge established that Al acts exclusively as a reactive flux producing complex quaternary phases. In contrast Ga flux, which readily leads to quaternary phases in the systems RE/TM/Ga/Ge, has a considerably reduced tendency to form quaternary compounds in the corresponding RE/TM/Ga/Si systems.[16-28]

Lately, we extended this work to include molten In as a solvent in the system RE/TM/Ge.[29-33] Indium flux, although it has been commonly used in the past for the crystal growth of primarily known binary and ternary phases[15,34-39] it has been less exploited as a synthetic tool for the discovery of new compounds compared to Al and Ga, particularly for quaternary phases, despite the most recent efforts.[40-43] Our work in the

exploratory synthesis of RE/TM/In/Ge indicates that, as in the case of Ga/Si system, it is difficult to readily produce quaternary phases and includes a limited number of quaternary phases so far. These are the $RE_4Ni_2InGe_4$[31] and $RE_7Co_4InGe_{12}$.[33]

The discovery of the RE/Co/In or Ge phases and their remarkable properties justifies the interest in the exploratory synthesis of the type RE/Co/In/Ge. Here we present the novel quaternary compound $Dy_4CoInGe_4$, grown from In flux which crystallizes as a new structure type. The synthesis and the study of the crystal structure and magnetic properties are reported. $Dy_4CoInGe_4$ seems to exhibit ferromagnetic behavior below 40 K.

3-2. Experimental Section

Reagents:

The following reagents were used as purchased without further purification: Dy, (in the form of powder ground from metal chunk, 99.9% Chinese Rare Earth Information center, Inner Mongolia, China), Co (-325 mesh 99.9% Cerac Milwaukee WI), Ge (ground from 2-5 mm pieces 99.999% Plasmaterials Livermore, CA) and In (tear drops 99.99% Plasmaterials Livermore, CA).

Synthesis:

The $Dy_4CoInGe_4$ compound was first obtained by combining 3 mmol of the dysprosium metal, 2 mmol cobalt, 3 mmol germanium and 15 mmol In in an Al_2O_3 (alumina) crucible under an inert nitrogen atmosphere inside a glove-box. The crucible was placed in a 13 mm fused silica tube, which was flame sealed under vacuum of 10^{-4}

Torr, to prevent oxidation during heating. The reactants were then heated to 1000 ^{0}C over 10 h, maintained at that temperature for 5 h to allow proper homogenization, followed by cooling to 850 ^{0}C in 2 h and held there for 48 h. Finally, the system was allowed to slowly cool down to 50 ^{0}C in 48 h. The reaction product was isolated from the excess In flux by heating at 350 ^{0}C and subsequent centrifugation through a coarse frit. Any remaining flux was removed by immersion and soniqation in glacial acetic acid for 48-72 h. The final crystalline product was rinsed with water and dried with acetone. Several crystals, which grow as metallic silver needles / rods were carefully selected for elemental analysis, structure characterization, and the physical measurements reported here. Impurity byproducts were the quaternary $Dy_7Co_4InGe_{12}$ (see Chapter 2) and small amounts of Dy_2InGe_2 and $Dy_{1.2}Ge$ (or DyGe). $Dy_4CoInGe_4$ was also prepared by combining the Dy/Co/Ge/In reagents in 6:2:5:20 and 2:1:1:5 mmol at later attempts to modify the synthesis. The remaining reaction profile was the same as described above. These reactions decreased the amount of the formed byproducts and resulted in ~ 50 – 65 % yield of the target phase of $Dy_4CoInGe_4$.

Elemental Analysis:

Semi-quantitative microprobe elemental analysis was performed on several crystals of the compound using a JEOL JSM-35C scanning electron microscope (SEM) equipped with a Noran Vantage Energy Dispersive Spectroscopy (EDS) detector. Data were acquired by applying a 25 kV accelerating voltage and an acquisition time of 40 s. A typical needle-like crystal of $Dy_4CoInGe_4$ is shown in Figure 1. The EDS analysis taken on visibly clean surfaces of the $Dy_4CoInGe_4$ crystals gave the atomic composition

of 39.98-42 % Dy, 8.83-10.90 % Co, 8.85-11.98 % In and 38.96-40.45 % Ge, which is in very good agreement with the results derived from the single crystal X-ray diffraction refinement.

X-ray Crystallography:

The X-ray intensity data were collected at room temperature using a Bruker SMART Platform CCD diffractometer with graphite monochromatized Mo Ka (λ = 0.71073 Å) radiation. The SMART software was used for data acquisition and SAINT for data extraction and reduction. An empirical absorption correction was applied using the program SADABS and the structure of $Dy_4CoInGe_4$ was solved by direct methods and refined with the SHELXTL package programs. A stable refinement was accomplished only in the monoclinic space group C12/*m*1. In the structure of $Dy_4CoInGe_4$ all atomic sites were refined anisotropically. Data collection and structure refinement details are given in Table 3-1. The final atomic positions, equivalent isotropic displacement parameters and anisotropic displacement parameters are listed in Table 3-2 and 3-3.

Table 3-1. Crystal data and structure refinement data for $Dy_4CoInGe_4$.

Empirical formula	$Dy_4CoInGe_4$	
Formula weight	4456.44	
Temperature (K)	293(2)	
Wavelength (Å)	0.71073	
Crystal system	Monoclinic	
Space group	C12/*m*1	
a (Å)	20.080(8),	α= 90°
b (Å)	4.1963(17),	β= 104.637(6)°
c (Å)	10.192(4),	γ = 90°
*V*olume ($Å^3$)	830.9(6)	
Z / Density(calculated) (Mg/m^3)	1 / 8.906	
Absorption coefficient (mm^{-1})	54.285	
F(000)	1872	
Theta range for data collection	2.07 to 28.24°	
Index ranges	-24≤h≤25 / -5≤k≤5 / -12≤l≤13	
Reflections collected / unique	4618 / 1099	
R(int)	0.0517	
Completeness to θ (%)	93.7	
Refinement method	Full-matrix least squares on F^2	
Data / restraints / parameters	1099 / 0 / 64	
Goodness-of-fit on F^2	1.111	
Final R indices [$I>2\sigma(I)$] (R_1 / wR_2)[a]	0.0301/ 0.0640	
R indices (all data) (R_1 / wR_2)[a]	0.0379/ 0.0688	
Extinction coefficient	0.00116(6)	
Largest diff. peak and hole (e. $Å^{-3}$)	1.890 and -2.897	

[a] $R_1 = \Sigma\|F_o\| - |F_c\| / \Sigma|F_o|$; $wR_2 = \left[\Sigma w\{|F_o| - |F_c|\}^2 / \Sigma w|F_o|^2\right]^{1/2}$; $w = 1/\sigma^2\{|F_o|\}$.

Table 3-2. Atomic coordinates ($\times 10^4$) and equivalent isotropic displacement parameters ($Å^2 \times 10^3$) for $Dy_4CoInGe_4$.

Atom	Wyckoff position	x	y	z	U(eq)[α]
Dy(1)	4i	2777(1)	0	6479(1)	7(1)
Dy(2)	4i	3693(1)	0	3580(1)	6(1)
Dy(3)	4i	3687(1)	0	10076(1)	5(1)
Dy(4)	4i	4600(1)	0	7300(1)	6(1)
In(1)	2a	5000	-5000	10000	10(1)
In(2)	2c	5000	-5000	5000	10(1)
Ge(1)	4i	2013(1)	0	8567(2)	6(1)
Ge(2)	4i	4340(1)	-5000	2172(2)	6(1)
Ge(3)	4i	3652(1)	-5000	8110(2)	6(1)
Ge(4)	4i	1375(1)	0	4449(2)	10(1)
Co	4i	2598(1)	-5000	8934(2)	7(1)

[α]U(eq) is defined as one third of the trace of the orthogonalized U^{ij} tensor.

Table 3-3. Anisotropic displacement parameters ($Å^2 \times 10^3$) for $Dy_4CoInGe_4$.

Atom	U^{11}	U^{22}	U^{33}	U^{23}	U^{13}	U^{12}
Dy(1)	5(1)	8(1)	6(1)	0	0(1)	0
Dy(2)	6(1)	6(1)	5(1)	0	2(1)	0
Dy(3)	6(1)	6(1)	5(1)	0	2(1)	0
Dy(4)	5(1)	7(1)	6(1)	0	1(1)	0
In(1)	7(1)	15(1)	7(1)	0	2(1)	0
In(2)	9(1)	13(1)	6(1)	0	0(1)	0
Ge(1)	7(1)	6(1)	6(1)	0	2(1)	0
Ge(2)	6(1)	6(1)	6(1)	0	0(1)	0
Ge(3)	7(1)	7(1)	5(1)	0	1(1)	0
Ge(4)	18(1)	7(1)	5(1)	0	4(1)	0
Co	6(1)	7(1)	9(1)	0	2(1)	0

The anisotropic displacement factor exponent takes the form: $-2\pi^2[h^2 a^{*2} U^{11} + ... + 2hk\, a^* b^* U^{12}]$

Magnetic Measurements:

Magnetic susceptibility measurements were carried out with a Quantum Design MPMS SQUID magnetometer. EDS-analyzed crystals were soaked in ~ 6M of HCl acid for 15-30 min, washed out with water, and dried out in a dry oven. The crystals were then randomly placed and sealed in Kapton tape envelope which was inserted into the SQUID magnetometer. Temperature dependence data were collected between 3 and 400 K, with an applied field of 100, 500 and 1000 G. Field dependent magnetic measurements were acquired at 3, 18 and 60 K with field sweeping from - 50000 to 50000 G.

3-3. Results and Discussion

Reaction Chemistry:

The compound $Dy_4CoInGe_4$ was first discovered in a reaction that was initially designed to form $Dy_7Co_4InGe_{12}$, a phase that can only be synthesized from In flux,[33] see Chapter 2. The reaction produced single and clustered crystals in the form of metallic silver needles and rods. The rod shaped crystals were first mistakenly identified as $Dy_7Co_4InGe_{12}$, but were later determined to be $Dy_4CoInGe_4$ after elemental analysis and subsequent single crystal diffraction experiments were performed. Modifications of ratios of the initial reagents improved the yield of the targeted $Dy_4CoInGe_4$ phase however small amounts of the $Dy_7Co_4InGe_{12}$ phase were still formed as well. Other impurity byproducts were small amounts of Dy_2InGe_2 and $Dy_{1.2}Ge$ (or DyGe) which due to their different crystal morphology of cubic and square pyramid respectively, they were easily removed. Attempts to synthesize $Dy_4CoInGe_4$ by direct combination reactions failed to produce the targeted phase. Figure 3-1 shows a scanning electron micrograph of a typical rod type $Dy_4CoInGe_4$ crystal.

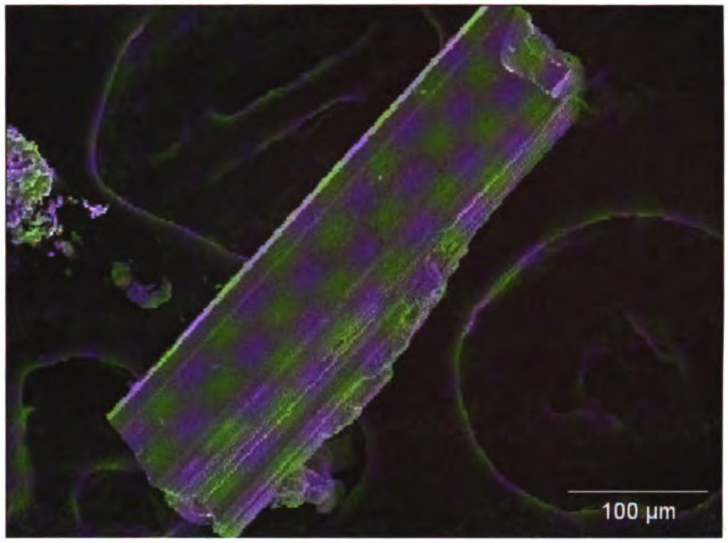

Figure 3-1. Scanning Electron micrograph (SEM) image of a flux-grown $Dy_4CoInGe_4$ rod-shaped crystal.

Structure:

$Dy_4CoInGe_4$ crystallizes in the monoclinic C12/*m*1 space group in what appears to be a new structure type. The overall structure of the compound as viewed down the *b*-axis is depicted in Figure 3-2. The bonds to the Dy atoms were omitted in order to emphasize the three dimensional [$CoInGe_4$] framework and its channels. The [$CoInGe_4$] sub-lattice is characterized by 12-membered and 5-membered channels propagating along the *b*-axis in which the Dy atoms are situated and $Co_2Ge(1)_2$ ribbons.

Figure 3-3 shows the principal building unit the repetition of which makes up the whole [$CoInGe_4$] network. It consists of pentagonal channels which are fused in groups of four that share a central column of square planar In(1) atoms. These channels consist of two different types of pentagonal rings. In one of them a Ge(3)-Ge(4) dimer is linked

to In(1) from the Ge(3) and to In(2) (also in square planar geometry) atom from the Ge(4) site correspondingly and both In atoms connect to a Co atom. Both of these pentagonal rings in the group of four, share their In(2) atom with similar pentagons of other fused groups that are on the same level, thus propagating the main building block along the *c*-axis, see Figure 3-2. The other type of pentagons consists of a Ge(1)-Ge(2) dimer which connects to a Co and an In(1) atom from the Ge(2) and Ge(1) side respectively, while a Ge(3) atom bonds to both Co and In(1) to form the second type of ring. The Co-Ge(1) side of these pentagons connects with two Co-Ge(1) bonds to the corresponding side of similar pentagons extending the structure along the *a*-axis, but which are found on a lower level down the *b*-axis, as it can be seen in the Figure 3-4 (structure view in a,b-plane with RE atoms removed to emphasize the connectivity). Dy(3) and Dy(4) are found in the center of the pentagonal channels. Similar group of four fused pentagonal channels sharing a square planar In atom is also found in the $RE_7Co_4InGe_{12}$[33] intermetallic compounds presented in Chapter 2 as well as in the family of the ternary phase RE_2InGe_2.[44] The two Ge-Ge distances of 2.630(2) and 2.595(2) Å compare well with the Ge dimmers observed in other RE germanides such as the β-$RENiGe_2$[29] compounds with Ge-Ge bonds ranging from 2.423(4) to 2.821(4) Å.

The other part of the repeating unit the $Co_2Ge(1)_2$ rhombi (Figure 3-3), are fused and form double zigzag chains (or ribbons) that run down the monoclinic *b*-axis as shown in Figure 3-4. These ribbons connect the pentagonal rings along the *b*-axis, thus forming the corresponding channels and building the 3D [$CoInGe_4$] framework. The Ge(1) atoms are in a trigonal pyramidal geometry composed of two Co and one Ge(2) atom and the Co atoms are surrounded by three Ge(1) and one Ge(3) atom forming a tetrahedral

coordination. Ge atoms in a trigonal pyramidal coordination environment forming ribbons with transition metals is found also in other intermetallic compounds as in $RE_4Ni_2InGe_4$[31] and several $RE_xCo_yIn_z$[3] phases, for example. The Co-Ge(1) bond that forms the zigzag double chains is at 2.3875(13) Å and is shorter than the Co-Ge(1) bond which fuses the chains together into a ribbon with a length of 2.468(3).

The void space left from the repetition of the main building unit, forms the highly corrugated 12-membered channels, as seen in Figure 3-5, in which the Dy(1) and Dy(2) atoms are residing. The Ge(2) and Ge(3) atoms are both in a trigonal planar bonding arrangement while the Ge(4) are in a bent geometry. There are no direct Co-Co bonds in the structure similar to $RE_7Co_4InGe_{12}$.

As mentioned above, the group of four fused pentagonal channels that share a central column of square planar In atoms is also found in the tetragonal $RE_7Co_4InGe_{12}$[33] intermetallic compounds. Additionally, the $Co_2Ge(1)_2$ ribbons resemble the $Ni_2Ge(1)_2$ ribbons found in the monoclinic $RE_4Ni_2InGe_4$[31] compounds. This suggests that the $Dy_4CoInGe_4$ structure is some kind of an "intermediate" between these two compounds. Figure 3-6 displays the structures of the *a,c*-view of $Dy_4CoInGe_4$ (*P*4/*m*, a = 10.3522(5), c = 4.1784(5)) and $Dy_4Ni_2InGe_4$ (*C*2/*m*, a = 15.420(2), b = 4.2224(7), c = 7.0191(11)) and the *a,b*-view of $Dy_7Co_4InGe_{12}$ for comparison. The fused groups of the pentagonal channels and the ribbons are highlighted.

The local coordination environments (within 4 Å) of the four crystallographically distinct Dy atoms are illustrated in Figure 3-7. Dy(1) atom is 8-coordinate, forming bonds with three Ge(4) atoms, two Ge(3) atoms, one Ge(1) atom and two Co atoms, in a way that could be described as capped "boat-like" arrangement. The Dy(1)-Ge bond distances

range from 2.9198(17) to 3.0023(14) Å while the two Dy(1)-Co bonds are at 3.3533(18) Å. The Dy(2) atom exhibits a coordination number of eight and sits in the center of a distorted tetragonal prism, made up of two Ge(1), two Ge(2), two Ge(4) and two In(2) atoms. The Dy(2)-Ge bonds vary from 2.9311(14) up to 3.1033(14) Å while the Dy(2)-In(2) distance is at 3.3865(10) Å. The Dy(3) atom is surrounded by 12 atoms which form a bicapped pentagonal prism. The prism is composed of two Ge(1), two Ge(2), two Ge(3) and two In(1) atoms and is capped by a Co and Ge(1) atom. For Dy(3) the nearest Ge atom in the pentagonal rings of the prism is at 2.8895(14) Å while the furthest one creates a bond at 3.0462(13) Å. The Dy(3)-In(1) and Dy(3)-Co bonds are equal to 3.3850(11) and 3.0419(16) Å, correspondingly. The capping Ge(1) and Co atoms are at a distance of 3.3248(19) and 3.000(2) Å, respectively. Finally, the Dy(4) atom has 10 neighbors in its immediate coordination sphere forming a pentagonal prismatic geometry with Dy(4) as the center and it is comprised of two Ge(2), Ge(3), Ge(4), In(1) and In(2) atoms. The shortest Dy(4)-Ge bond is at 2.9405(13) Å and the longest one at 3.1059(14) Å. The In(1) and In(2) atoms are found at 3.3912(11) and 3.3909(10) Å away from the RE atom correspondingly.

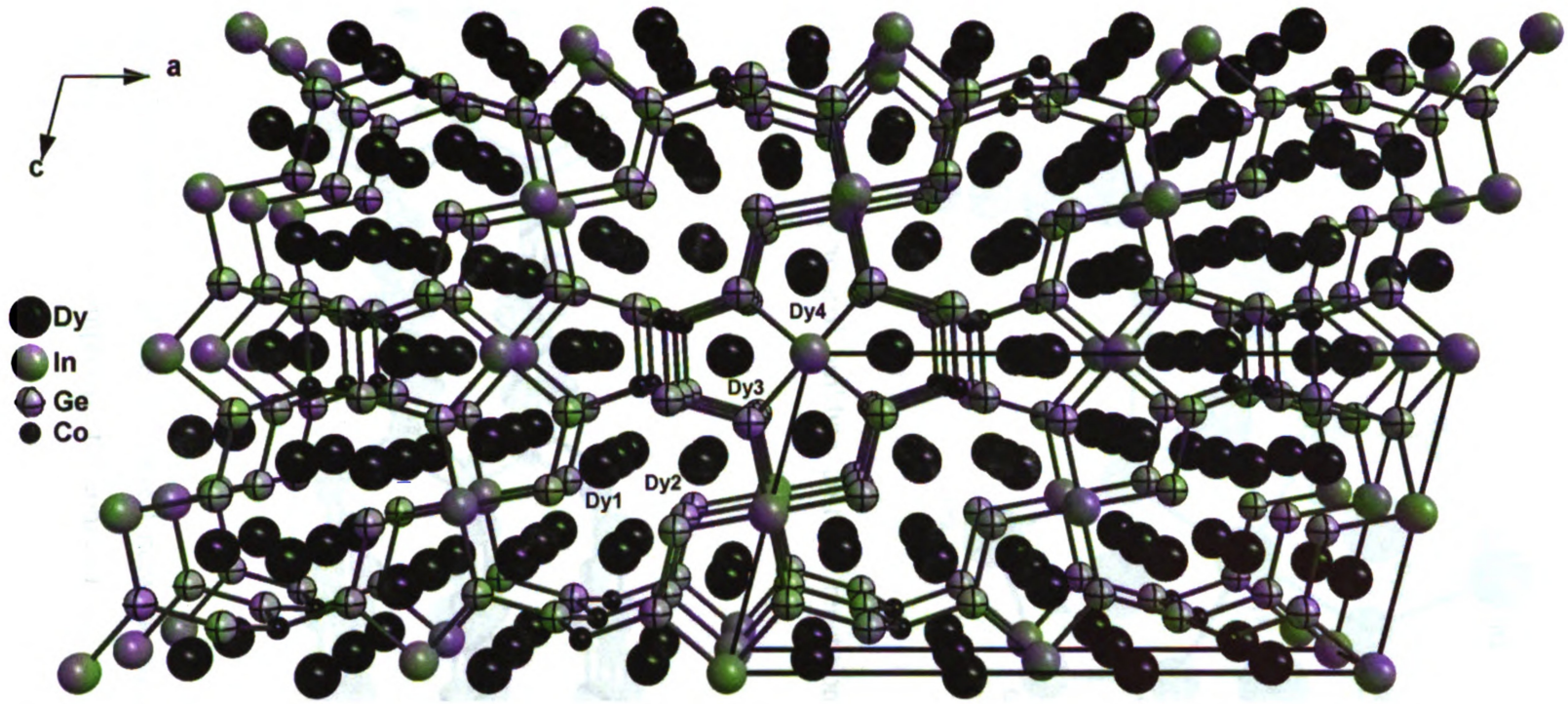

Figure 3-2. The overall structure of $Dy_4CoInGe_4$ as viewed down the *b*-axis. For clarity the bonds to the Yb atoms are not drawn.

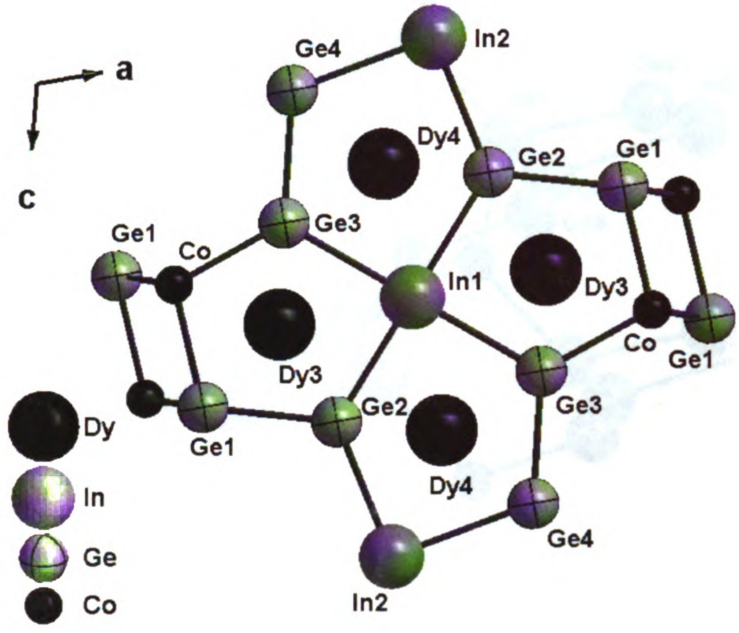

Figure 3-3. The principal building unit the repetition of which makes up the whole [$CoInGe_4$] network.

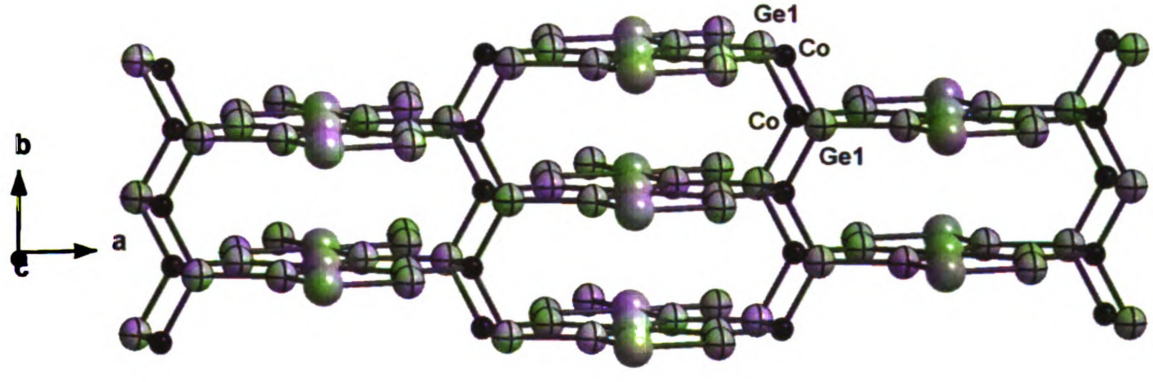

Figure 3-4. Projection of the [$CoInGe_4$] network roughly onto the *a*,*b*-plane. The RE atoms were removed to emphasize the connectivity.

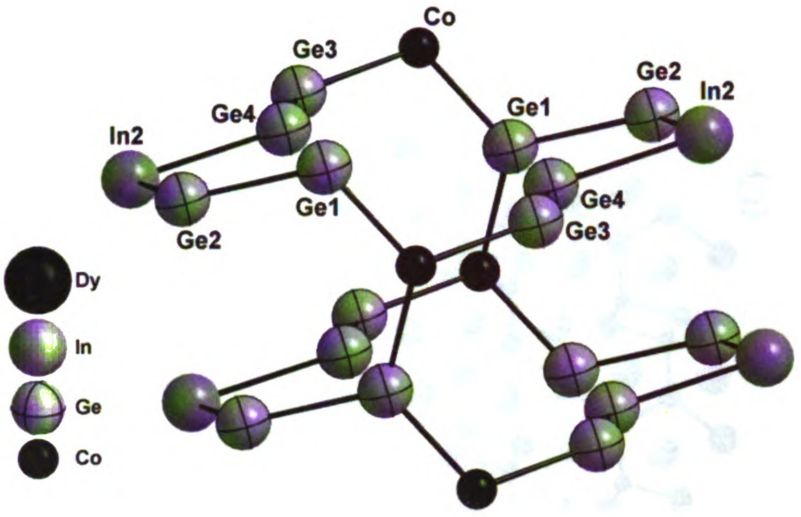

Figure 3-5. Twelve-membered rings and their interconnection to form the corrugated channels. The RE atoms were removed to emphasize the connectivity.

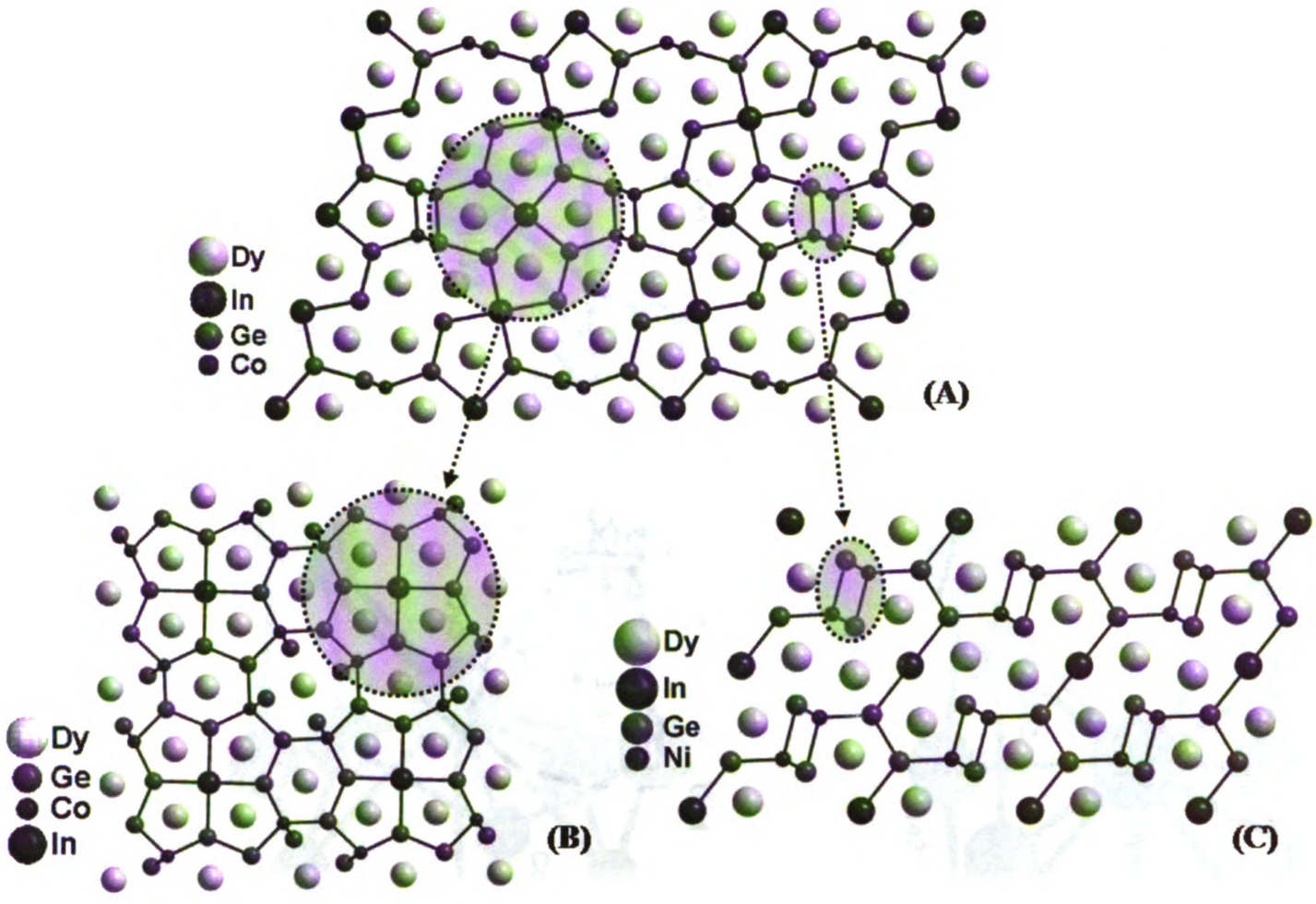

Figure 3-6. (A) Projection of the *a,c*-view of $Dy_4CoInGe_4$ (B) the *a,b*-view of $Dy_7Co_4InGe_{12}$ and (C) the *a,c*-view of $Dy_4Ni_2InGe_4$ structures are displayed for comparison.

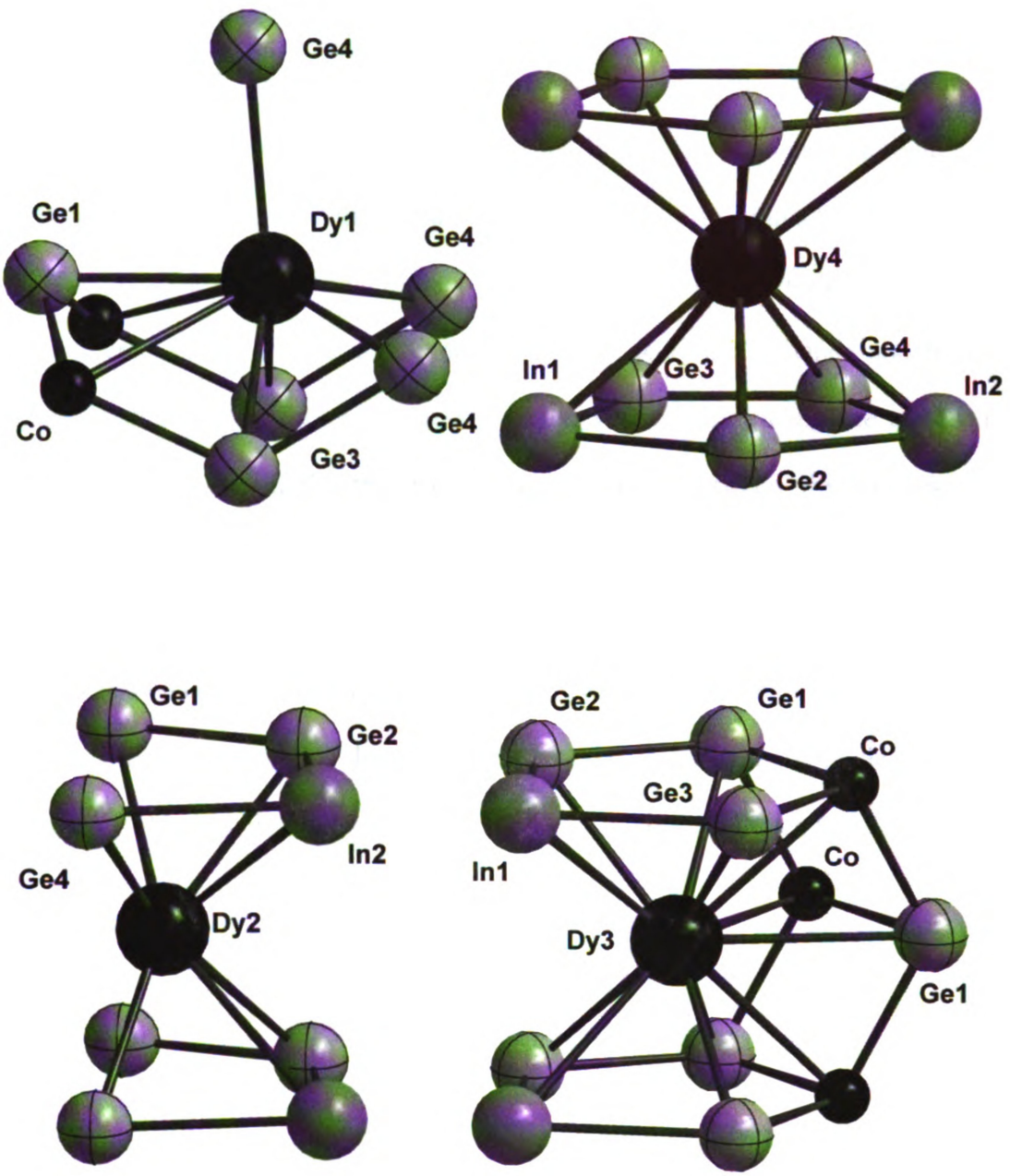

Figure 3-7. Coordination environment of the Dy(1), Dy(2), Dy(3) and Dy(4) atoms. The coordination sphere cutoff is 4.0 Å.

An alternative view of the $Dy_4CoInGe_4$ structure is in polyhedral representation. Figure 3-8 displays the structure of the title compound as Co-centered tetrahedra and In(1),In(2)-centered planar squares as viewed in the *a*,*c*-plane. Similar square planes stack along the *b*-axis while alternating In(1) and In(2) squares connect through a Ge(3)-Ge(4) bond and by corner-sharing of their Ge(2) site and form chains that run along the *c*-axis. The Dy(4) atoms are found in the trigonal channels formed within these chains. The In(1)-centered square planes also connect through Ge(1)-Ge(2) bonds and by corner-sharing of their Ge(3) sites with the Co-centered tetrahedra along the *a*-axis. Dy(3) atoms are siting within the trigonal channels formed between the squares and the tetrahedra. Finally, the Co tetrahedra form fused zigzag columns down the *b*-axis by two Ge(1)-Ge(1) edge-sharing thus building the three dimensional [$CoInGe_4$] framework, Figure 3-9. Dy(1) and Dy(2) atoms reside within the big channels created by the void space between the chains of the In squares and the fused columns made from the Co tetrahedra. Table 3-4 gives a list of selected bond distances for $Dy_4CoInGe_4$.

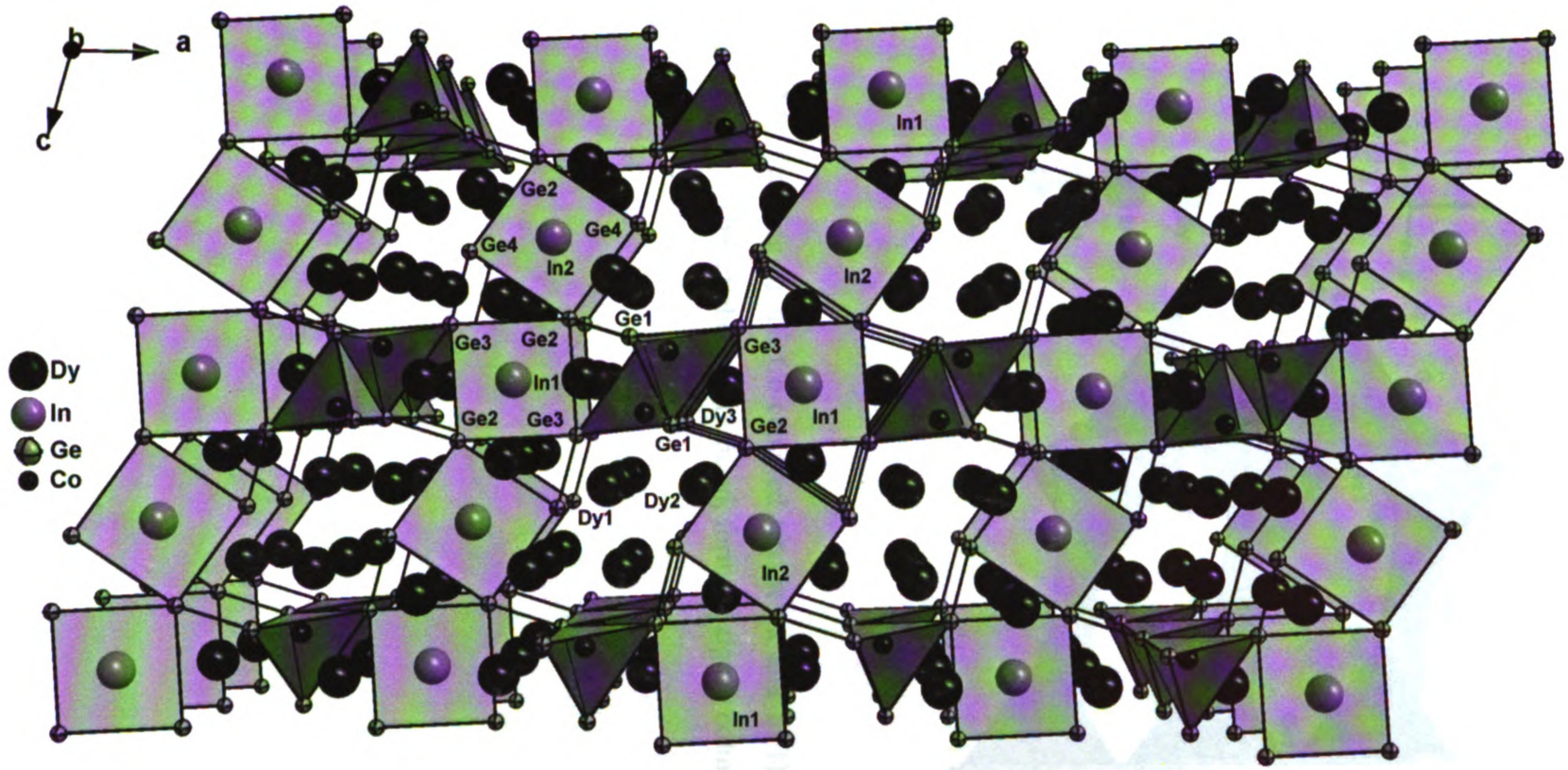

Figure 3-8. Polyhedral representation of the $Dy_4CoInGe_4$ structure featuring the connectivity of the Co-centered tetrahedra and In(1),In(2)-centered planar squares as viewed in the *a*,*c*-plane.

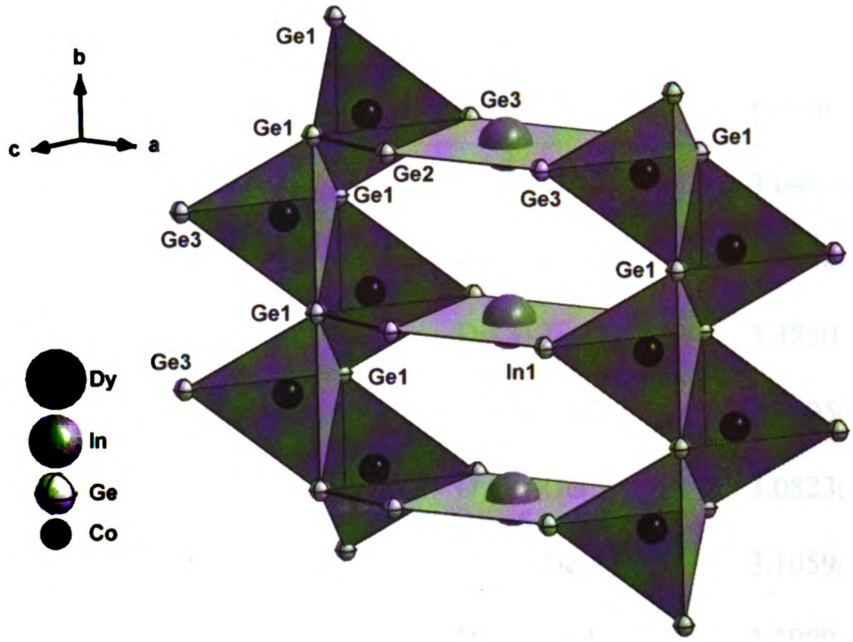

Figure 3-9. Stacking of the Co-centered tetrahedra and In(1)-centered planar squares along the *b*-axis. The tetrahedral are fused, forming zigzag columns that extend down the *b*-axis.

Table 3-4. Selected bond lengths [Å] for $Dy_4CoInGe_4$.

Bond	Length	Bond	Length
Dy(1)-Ge(1)	2.9198(17)	Dy(3)-Ge(1)	3.0462(13)
Dy(1)-Ge(3)	2.9622(13)	Dy(3)-Ge(1)	3.3248(19)
Dy(1)-Ge(4)	3.0023(14)	Dy(3)-In(1)	3.3850(11)
Dy(1)-Ge(4)	3.0429(19)	Dy(4)-Ge(2)	2.9405(13)
Dy(1)-Co	3.3533(18)	Dy(4)-Ge(3)	3.0823(13)
Dy(1)-Dy(4)	3.5427(17)	Dy(4)-Ge(4)	3.1059(14)
Dy(1)-Dy(2)	3.6081(13)	Dy(4)-In(2)	3.3909(10)
Dy(1)- Dy(1)	3.6099(15)	Dy(4)-In(1)	3.3912(11)
Dy(2)-Ge(4)	2.9311(14)	In(1)-Ge(2)	2.8530(17)
Dy(2)-Ge(2)	3.0159(13)	In(1)-Ge(3)	2.8995(17)
Dy(2)-Ge(1)	3.1033(14)	In(2)-Ge(2)	2.8517(18)
Dy(2)-Co	3.151(2)	In(2)-Ge(4)	2.9531(19)
Dy(2)-In(2)	3.3865(10)	Ge(1)-Co	2.3875(13)
Dy(2)-Dy(3)	3.5692(17)	Ge(1)-Co	2.468(3)
Dy(3)-Ge(3)	2.8895(14)	Ge(1)-Ge(2)	2.630(2)
Dy(3)-Co	3.0419(16)	Ge(3)-Co	2.465(2)
Dy(3)-Co	3.000(2)	Ge(3)-Ge(4)	2.595(2)
Dy(3)-Ge(2)	3.0446(14)		

Magnetic Measurements:

Temperature dependent molar magnetic susceptibility, $\chi_m(T)$ and inverse susceptibility, $1/\chi_m(T)$ data performed on randomly oriented single crystals of $Dy_4CoInGe_4$ are plotted in Figure 3-10. At a first glance, $Dy_4CoInGe_4$ seems to undergo a rather broad ferromagnetic transition that onsets at a Tc of ~ 20 - 25 K as indicated by a change in the slope of χ_m. As it can been clearly seen from the inset in Figure 3-10, the ZFC (zero field cooled) and FC (field cooled) data reveal considerable different behavior at the low temperature range starting slightly from ~ 40 K while separating completely at ~ 18 K. A closer look in the ZFC data reveals a maximum of the susceptibility at T_1 = 8.5 K suggesting a change in the magnetic structure. Similar multitransitional magnetic behavior has been seen in spin structures with frustrated moments as in the RNiAl intermetallic compounds.[45] The small cusp at ~ 60 K is probably due to some oxygen trapped in the sample. Above 60 K, the $1/\chi_m$ data follow the Curie-Weiss law with a resulting effective magnetic moment of 14.1 μ_B per formula unit, and a Weiss constant of Θ = - 17.5 K. The observed effective magnetic moment is quite lower than the theoretical value of 21.3 μ_B for four free Dy^{3+} ions. This difference might be ascribed to strong crystal-field effects[46] and also due to diamagnetic signal of the holder. The spins of the Dy^{3+} ions are consequently the only species contributing to the magnetic moment. The negative Weiss constant indicates antifferomagnetic interactions between the RE atoms.

In order to study the observed transitions in further detail we performed temperature dependent molar magnetic susceptibility $\chi_m(T)$ measurements on randomly oriented single crystals of $Dy_4CoInGe_4$ at three different applied fields of 100, 500 and 1000 G, see Figure 3-11. Below a ferromagnetic transition at T_c = 40 K the $\chi_m(T)$ curve

remarkably varies depending on the ZFC and the FC conditions for all three applied fields, whereas increase of the field from 100 G to 1000 G tends to suppress the divergences between the ZFC and FC curves. In Figure 3-12 the $\chi_m(T)$ data for the temperature range 0 – 100 K are given for all three fields. In the data collected at 100 G a sharp cusp appears in the ZFC curve at T_f = 40 K and irreversibility, appearing as the evident separation between the ZFC and FC curves, starts at the temperature T_s = 50 K. With increasing the magnetic field, T_s shifts towards lower temperatures, particularly it shifts to 40 K and 30 K for the fields of 500 G and 1000 G, respectively. Furthermore, the peak in the χ_{ZFC} curve loses intensity and broadens with increasing field. Additionally, more cusps appear in the lower temperature region for all curves that could mean further changes in the magnetic structure (possibly antiferromagnetic interactions). These features are characteristic to spin systems with frustrated moments and magnetic anisotropy that could lead to spin-glasses transitions.[45,47-50] In order to characterize the cusp temperature as spin-freezing transitions, further study with additional techniques is required. It should be noted here, that although in both measurements care was taken in order to place the single crystals randomly in the kapton tape folder that does not preclude the possibility of having a slightly preferred orientation of the crystals. This could create subtle differences between various measurements.

Finally, the field dependent magnetization data taken at the temperatures of 3, 18 and 60 K are displayed in Figures 3-13. The material shows metamagnetic behavior. The magnetization measured at 3 K displays roughly linear response up 12 kG with a small remnant magnetization at zero field, whereas it exhibits pronounced hysteresis loops at higher fields for both positive and negative fields, which indicates ferromagnetic ordering

of the spins. The moment does not saturate up to the highest attainable field and reaches a value of about 5.5 μ_B which is only ~ 28 % of the value expected for 4 Dy^{3+} ions, calculated from $\mu_{Dy(calc)} = gJ = 10\ \mu_B$. The metamagnetic behavior can be seen also in the curve measured at 18 K, inset in Figure 3-13. The dependence of magnetization on field is roughly linear up to 25000 G, where a spin reorientation begins to occur suggesting a more ferromagnetic arrangement of the moments while at about 35000 G a small hysteresis loop in formed. On the other hand the magnetization measured at 60 K shows linear dependence with the field indicating that $Dy_4CoInGe_4$ is paramagnetic at this temperature. Many other intermetallic compounds have shown complex spin behavior such as the quaternary phases $Dy_2AuAl_6Si_4$[25] and $DyAuAl_4Ge_2$[28] and the ternary β-$DyNiGe_2$[29] to name just a few.

The magnetic properties of the rare-earth containing intermetallic compounds have been the subject of intensive research. It is generally believed that the collective behavior of the magnetic rare-earth ions in these compounds is determined by an indirect interaction among localized *f* electrons which are coupled through the mediation of the conduction electrons according to the Ruderman-Kittel-Kasuya-Yosida (RKKY) theory.[51-53]

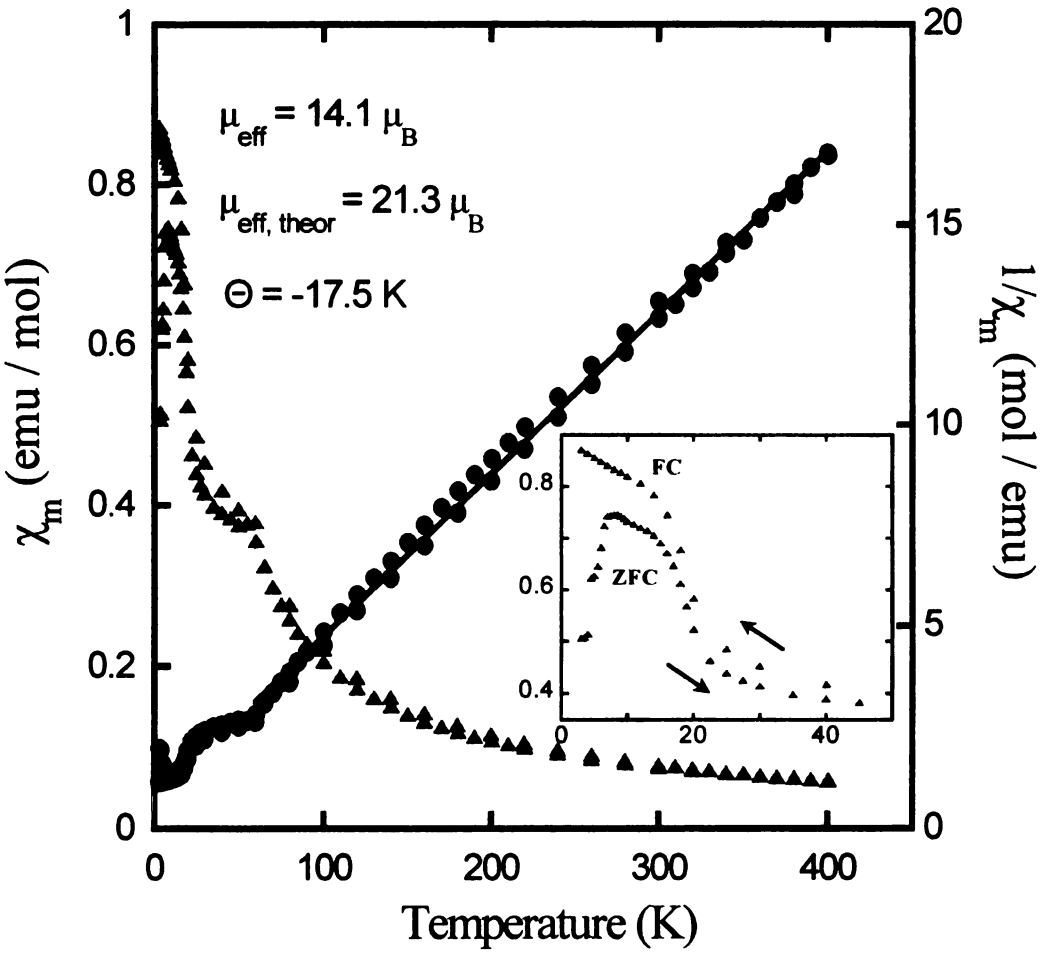

Figure 3-10. Temperature dependence of the molar susceptibility $\chi_m(T)$ and inverse susceptibility $1/\chi_m(T)$ of randomly oriented single crystals for $Dy_4CoInGe_4$ collected with an applied field of 500 G. Inset shows the low temperature data of the susceptibility $\chi_m(T)$.

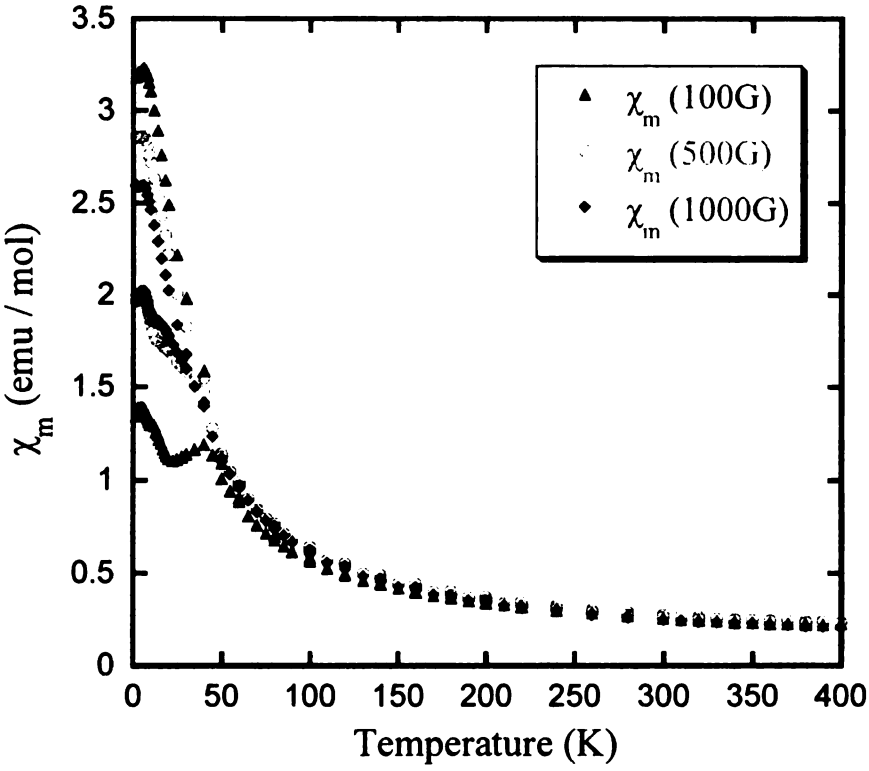

Figure 3-11. Temperature dependence of the molar susceptibility $\chi_m(T)$ of $Dy_4CoInGe_4$ on single crystals randomly oriented with applied fields of 100 G, 500 G and 1000 G.

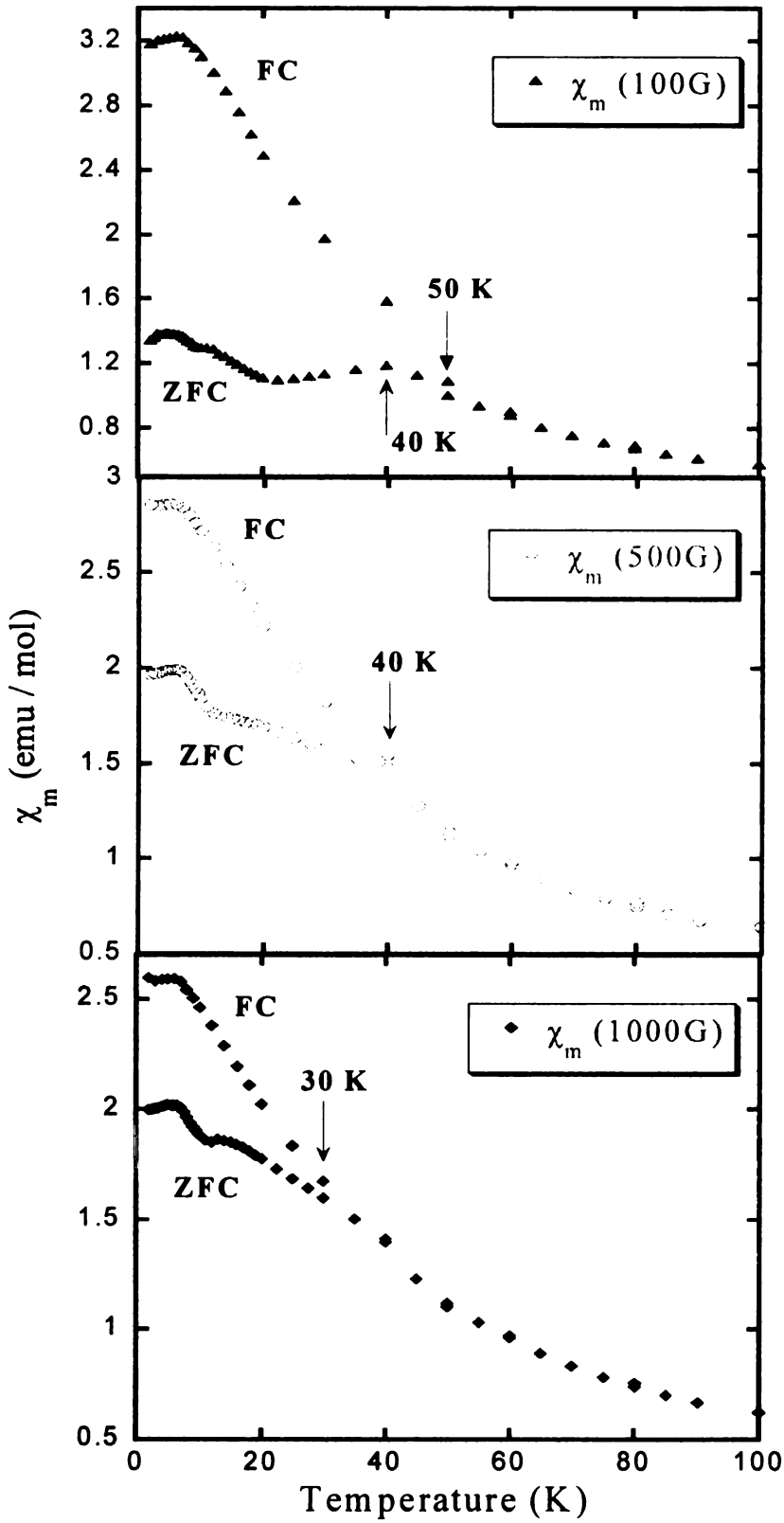

Figure 3-12. Low temperature (0 – 100 K) variation of χ_m of $Dy_4CoInGe_4$ at applied fields of 100, 500 and 1000 G in order to emphasize the magnetic transitions.

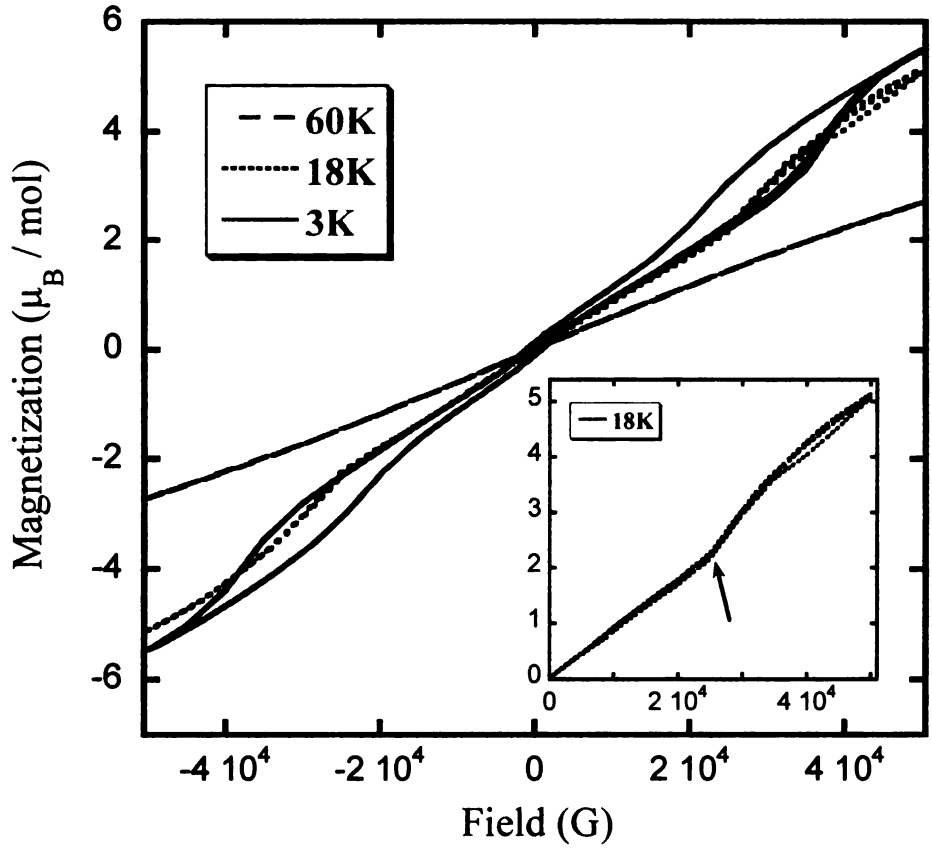

Figure 3-13. Magnetization curves of $Dy_4CoInGe_4$ collected at 3 K (solid line) 18 K (dotted line) and 60 K (dashed line). Inset shows the magnetization curve at 18 K in the positive fields area. The arrow indicates the metamagnetic transition.

3-4. Conclusions

Single-crystals of the new quaternary compound $Dy_4CoInGe_4$ were grown using an excess of indium as a flux. The flux seems necessary to stabilize this compound, since direct combination reactions failed to produce the new phase. $Dy_4CoInGe_4$ forms in the monoclinic space group $C12/m1$ as a new structure type. The synthesis of $Dy_4CoInGe_4$ is the third example of In acting as a reactive flux in the system RE/TM/Ge. This is an interesting result because, as it was stated above it is difficult to isolate quaternary phases in this system, in contrast with analogous reactions when Al or Ga are used as molten metal fluxes. The discovery of $Dy_4CoInGe_4$ which is closely related to the structure and synthetic conditions of the $RE_7Co_4InGe_{12}$ and $RE_4Ni_2InGe_4$ compounds that were also stabilized in In flux, illustrates the remarkable ability of In flux, to produce novel complex intermetallics, when coupled with the right synthetic conditions.

Magnetic susceptibility measurements of the material revealed a ferromagnetic transition with a $Tc \approx 40$ K with a complex picture below Tc that suggests the $Dy_4CoInGe_4$ could be a system with spin frustrated moments and behavior similar to spin-glasses. The magnetization measurements below and above Tc temperatures showed metamagnetic behavior and support the complex spin behavior observed in the susceptibility data. The small size of the crystals prevented the thorough investigation of its physical and electrical properties. Future work with this system should include attempts to produce bigger size crystals in order to further characterize the new material, with techniques such as ac-susceptibility, neutron diffraction and transport properties.

References:

(1) Kalychak, Ya. M. *J. Less-Common. Metals* **1997**, *262-263*, 341.

(2) Szytula, A.; Leciejewicz, J. *"Handbook of Crystal Structures and Magnetic Properties of Rare Earth Intermetallics"*; CRC Press: Boca Raton, Fl, 1994.

(3) Kalychak, Y. M. *J. Alloy. Compd.* **1999**, *291*, 80-88.

(4) Hegger, H.; Petrovic, C.; Moschopoulou, E. G.; Hundley, M. F.; Sarrao, J. L.; Fisk, Z.; Thompson, J. D. *Phys. Rev. Lett.* **2000**, *84*, 4986.

(5) Petrovic, C.; Movshovich, R.; Jaime, M.; Pagliuso, P. G.; Hundley, M. F.; Sarrao, J. L.; Fisk, Z.; Thompson, J. D. *Europhys. Lett.* **2001**, *53*, 354-359.

(6) Petrovic, C.; Pagliuso, P. G.; Hundley, M. F.; Movshovich, R.; Sarrao, J. L.; Thompson, J. D.; Fisk, Z.; Monthoux, P. *J. Phys.-Condes. Matter* **2001**, *13*, L337-L342.

(7) Izawa, K.; Yamaguchi, H.; Matsuda, Y.; Shishido, H.; Settai, R.; Onuki, Y. *Phys. Rev. Lett.* **2001**, *8705*, 4.

(8) Chen, G. F.; Ohara, S.; Hedo, M.; Uwatoko, Y.; Saito, K.; Sorai, M.; Sakamoto, I. *Journal of the Physical Society of Japan* **2002**, *71*, 2836-2838.

(9) Joshi, D. A.; Tomy, C. V.; Malik, S. K. *J. Phys.-Condes. Matter* **2007**, *19*, 0953-8984.

(10) Mun, E. D.; Lee, B. K.; Kwon, Y. S.; Jung, M. H. *Phys. Rev. B* **2004**, *69*, 5.

(11) Pecharsky, V. K.; Gschneidner, K. A. *Phys. Rev. B* **1991**, *43*, 8238-8244.

(12) Movshovich, R.; Jaime, M.; Thompson, J. D.; Petrovic, C.; Fisk, Z.; Pagliuso, P. G.; Sarrao, J. L. *Phys. Rev. Lett.* **2001**, *86*, 5152-5155.

(13) Paglione, J.; Tanatar, M. A.; Hawthorn, D. G.; Boaknin, E.; Hill, R. W.; Ronning, F.; Sutherland, M.; Taillefer, L.; Petrovic, C.; Canfield, P. C. *Phys. Rev. Lett.* **2003**, *91*, 4.

(14) Chevalier, B.; Gaudin, E.; Weill, F.; Bobet, J.-L. *Intermetallics* **2004**, *12*, 437.

(15) Kanatzidis, M. G.; Pöttgen, R.; Jeitschko, W. *Angewandte Chemie-International Edition* **2005**, *44*, 6996-7023.

(16) Chen, X. Z.; Sportouch, S.; Sieve, B.; Brazis, P.; Kannewurf, C. R.; Cowen, J. A.; Patschke, R.; Kanatzidis, M. G. *Chem. Mater.* **1998**, *10*, 3202-3211.

(17) B. Sieve; X. Z. Chen; R. Henning; P. Brazis; C. R. Kannewurf; J. A. Cowen; A. J. Schultz; Kanatzidis, M. G. *J. Am. Chem. Soc* **2001**, *123*, 7040.

(18) Sieve, B.; Trikalitis, P. N.; Kanatzidis, M. G. *Z. Anorg. Allg. Chem.* **2002**, *628*, 1568-1574.

(19) Chen, X. Z.; Larson, P.; Sportouch, S.; Brazis, P.; Mahanti, S. D.; Kannewurf, C. R.; Kanatzidis, M. G. *Chem. Mater.* **1999**, *11*, 75-83.

(20) Zhuravleva, M. A.; Kanatzidis, M. G. *Z. Naturforch B : Sec. B* **2003**, *58*, 649-657.

(21) Zhuravleva, M. A.; Pcionek, R. J.; Wang, X. P.; Schultz, A. J.; Kanatzidis, M. G. *Inorg. Chem.* **2003**, *42*, 6412-6424.

(22) Zhuravleva, M. A.; Evain, M.; Petricek, V.; Kanatzidis, M. G. *J. Am. Chem. Soc* **2007**, *129*, 3082-3083.

(23) Chen, X. Z.; Small, P.; Sportouch, S.; Zhuravleva, M. ; Brazis, P.; Kannewurf, C. R.; Kanatzidis, M. G. *Chem. Mater.* **2000**, *12*, 2520-2522.

(24) Latturner, S. E.; Bilc, D.; Mahanti, S. D.; Kanatzidis, M. G. *Chem. Mater.* **2002**, *14*, 1695-1705.

(25) Latturner, S. E.; Bilc, D.; Mahanti, S. D.; Kanatzidis, M. G. *Inorg. Chem.* **2003**, *42*, 7959-7966.

(26) Latturner, S. E.; Kanatzidis, M. G. *Inorg. Chem.* **2008**, *47*, 2089-2097.

(27) Wu, X. U.; Latturner, S. E.; Kanatzidis, M. G. *Inorg. Chem.* **2006**, *45*, 5358-5366.

(28) Wu, X. N.; Kanatzidis, M. G. *J. Solid State Chem.* **2005**, *178*, 3233-3242.

(29) Salvador, J. R.; Gour, J. R.; Bilc, D.; Mahanti, S. D.; Kanatzidis, M. G. *Inorg. Chem.* **2004**, *43*, 1403-1410.

(30) Salvador, J. R.; Bilc, D.; Gour, J. R.; Mahanti, S. D.; Kanatzidis, M. G. *Inorg. Chem.* **2005**, *44*, 8670-8679

(31) Salvador, J. R.; Kanatzidis, M. G. *Inorg. Chem.* **2006**, *45*, 7091-7099.

(32) Salvador, J. R.; Hoang, K.; Mahanti, S. D.; Kanatzidis, M. G. *Inorg. Chem.* **2007**, *46*, 6933

(33) Chondroudi, M.; Balasubramanian, M.; Welp, U.; Kwok, W.-K.; Kanatzidis, M. G. *Chem. Mater.* **2007**, *19*, 4769-4775.

(34) Canfield, P. C.; Fisk, Z. *Z. Philos. Mag. B* **1992**, *65*, 1117-1123.

(35) Bud'ko, S. l.; Islam, Z.; Wiener, T. A.; Fisher, I. R.; Lacerda, A. H.; Canfield, P. C. *J. Magn. Magn. Mater.* **1999**, *205*, 53.

(36) Fisher, I. R.; Islam, Z.; Canfield, P. C. *J. Magn. Magn. Mater.* **1999**, *202*, 1-10.

(37) Hundley, M. F.; Sarrao, J. L.; Thompson, J. D.; Movshovich, R.; Jaime, M.; Petrovic, C.; Fisk, and Z. *Phys. Rev. B* **2001**, *65*, 024401.

(38) Macaluso, R. T.; Sarrao, J. L.; Moreno, N. O.; Pagliuso, P.G.; Thompson, J. D.; Fronczek, F. R.; Hundley, M. F.; Malinowski, A.; Chan, J. Y. *Chem. Mater.* **2003**, *15*, 1394-1398.

(39) Sakamoto, I.; Shomi, Y.; Ohara, S. *Physica B* **2003**, *329-333*, 607-609.

(40) Bailey, M. S.; McCuire, M. A.; DiSalvo, and F. J. *J. Solid Sate Chem.* **2005**, *178*, 3494-3499.

(41) Benbow, E. M.; Latturner, S. E. *Inorg. Chem.* **2006**, *179*, 3989-3996.

(42) Klunter, W.; Jung, W. *J. Solid Sate Chem.* **2006**, *179*, 2880-2888.

(43) Zaremba, V. I.; Dubenskiy, V. P.; Rodewald, U. C.; Heying, B.; Pottgen, R. *J. Solid State Chem.* **2006**, *179*, 891-897.

(44) Tobash, P. H.; Lins, D.; Bobev, S.; Lima, A.; Hundley, M. F.; Thompson, J. D.; Sarrao, J. L. *Chem. Mater.* **2005**, *17*, 5567-5573.

(45) Ehlers, G.; Maletta, H. *Z. Phys. B* **1996**, *101*, 317-327.

(46) Kittel, C. *Introduction to Solid State Physics* 7th ed.; John Wiley & Sons, 1996.

(47) Yoshida, H.; Ahlert, S.; Jansen, M.; Okamoto, Y.; Yamaura, J.; Hiroi, Z. *Journal of the Physical Society of Japan* **2008**, *77*, 8.

(48) Yamamura, T.; Li, D.; Yubuta, K.; Shiokawa, Y. *J. Alloy. Compd.* **2004**, *374*, 226-229.

(49) Yamamura, T.; Li, D. X.; Shiokawa, Y. *Physica B-Condensed Matter* **2003**, *329*, 559-560.

(50) Li, D. X.; Donni, A.; Kimura, Y.; Shiokawa, Y.; Homma, Y.; Haga, Y.; Yamamoto, E.; Honma, T.; Onuki, Y. *J. Phys.-Condes. Matter* **1999**, *11*, 8263-8274.

(51) Kittel, C.; Wiley: New York, 1968; Vol. 22.

(52) Kasuya, T. *Magnetism*; Academic Press: New York, 1966; Vol. IIB.

(53) Kasuya, T. *Prog. Theoret. Phys.* **1956**, *16*, 45-57.

CHAPTER 4

Flux Synthesis of $Yb_3AuGe_2In_3$: an Ordered Variant of the YbAuIn Structure Exhibiting Mixed-Valent Yb Behavior

4-1. Introduction

Intermetallic compounds of the ternary systems RE/TM/In (M = Cu, Ag, Au) include numerous new intermetallic phases that exhibit rich structural variety[1,2] and interesting physical properties.[3] Some examples are CeAuIn,[4-8] and the families REAuIn (RE = Eu, Gd-Ho, Yb),[4,7,9-13] and $REAu_2In$.[11,14-18] In the latter family for example the members formed by light RE elements undergo a structural phase transition, while the heavy RE ones display magnetic transitions. $YbAu_2In$ is a intermediate valence (IV) compound[19] that shows pressure induced transition from IV to trivalent magnetic states.[11,15] Further examples are the RE_2Au_2In (RE = La-Gd and RE = Tm-Lu)[20] which adopt two different structure types depending on the size of the RE, Yb_2TM_2In (TM = Cu, Pd, Au),[21] and $REAg_2In$ (RE = Tb, Dy).[22] An especially interesting set of compounds are the $YbCu_{4+x}In_{1-x}$[23-26] and their Ag, Au analogs[27]. This family has shown both mixed and intermediate valency characterized by a first-order temperature-induced isostructural valence phase transition. It also shows valence fluctuation induced by pressure or alloying and it belongs to the class of "light" heavy-fermion systems.[28-30] Increase of the In ratio in the RE/Au/In system leads to $Eu_2Au_3In_4$,[31] $RE_2Au_3In_5$ (RE = Ce, Pr, Nd, Sm),[32] $REAu_2In_4$ (RE = La, Ce, Pr, Nd),[33] $EuAuIn_2$.[34]

Indium as a flux has been widely used for the crystal growth of principally known binary or ternary phases.[35-41] It has been little exploited as a synthetic medium compared to Al and Ga,[33,42-56] especially for quaternary compounds, although there is now an increasing interest in this approach.[57-62] Our work with In flux includes only a limited number of quaternary phases so far, such as the $RE_4Ni_2InGe_4$ (RE = Dy, Ho, Er, Tm)[55] and $RE_7Co_4InGe_{12}$ (RE = Dy, Ho, Yb).[56]

After the rich chemistry revealed by the thorough examination of the ternary RE/Au/In system we decided to incorporate also a tetrelide such as Ge in order to search for more complex structures and compositions. This is analogous to the RE/TM/Al /Si or Ge and RE/TM/Ga/Ge or Si systems investigated previously.[40-54] Among the rare earth compounds, the Yb-based intermetallics which are considered as the electron hole counterparts to the isostructural cerium compounds, have received considerable attention for the past few years. This interest originates from their ability to exhibit various peculiar properties such as intermediate-valence, heavy fermion or Kondo behavior and unusual magnetism.[63-65] These properties are generally believed to arise from the strong hybridization (interaction) between the localized 4f electrons and the delocalized s,p,d conduction electrons.[66,67] Here we present the new compound $Yb_3AuGe_2In_3$, grown from In flux which crystallizes as an ordered variant of the YbAuIn structure and it is the first quaternary phase reported as an extension of the rich and extensively studied RE/Au/In system. The synthesis, crystal structure, and the study of the magnetic properties, X-ray absorption near edge spectroscopy (XANES), electrical resistivity, thermoelectric power and heat capacity measurements are reported. These studies suggest that $Yb_3AuGe_2In_3$ is an intermediate or heterogeneous mixed-valence system. The results of the study of the

crystal structure refinement, magnetic properties, electrical resistivity, heat capacity and XANES experiments for the isostructural YbAuIn are also presented in an attempt to investigate the similarities and/or differences between the two compounds.

4-2. Experimental section

Reagents:

The following reagents were used as purchased without further purification: Yb, (in the form of powder ground from metal chunk, 99.9% Chinese Rare Earth Information center, Inner Mongolia, China), Au (pieces, 99.9% Alfa Aesar, Ward Hill, MA), Ge (ground from 2-5 mm pieces 99.999% Cerac, Milwaukee, WI) and In (tear drops 99.99% Plasmaterials, Livermore, CA).

Synthesis:

$Yb_3AuGe_2In_3$ was obtained by combining 3 mmol of the ytterbium metal, 2 mmol gold, 3 mmol germanium and 15 mmol In in an Al_2O_3 (alumina) crucible under an inert nitrogen atmosphere inside a glove-box. The crucible was placed in a 13 mm fused silica tube, which was flame sealed under vacuum of 10^{-4} Torr, to prevent oxidation during heating. The reactants were then heated to 1000 ^{0}C over 10 h, maintained at that temperature for 5 h to allow proper homogenization, followed by cooling to 850 ^{0}C in 2 h and held there for 48 h. Finally, the system was allowed to slowly cool to 50 ^{0}C in 48 h. The reaction product was isolated from the excess In flux by heating at 350 ^{0}C and subsequent centrifugation through a coarse frit. Any remaining flux was removed by immersion and soniqation in glacial acetic acid for 48 h. The final crystalline product was

rinsed with water and dried with acetone. This method produced the target compound with ~ 90% purity and in a yield of ~ 90 % based on the initial amount of Yb metal used in the reaction. Main side products were very small amounts of YbAuGe and unreacted In metal. Several crystals, which grow as metallic silver rods were carefully selected for elemental analysis, structure characterization, and the physical measurements reported here.

YbAuIn was prepared by direct combination of the reactant elements in their stoichiometric ratios in a Ta crucible under an inert nitrogen atmosphere inside a glove-box. The Ta tube was sealed under vacuum by Arc Welding and subsequently was sealed in a quartz tube under a vacuum of 10^{-4} Torr. The tube was then heated at 1100 °C where it stayed for 6 -24 hours and finally it was quenched from this temperature in liquid nitrogen. This method produced YbAuIn in mainly polycrystalline form but also in compact pieces of crystals in a yield of ~ 60 % and purity of ~ 97 %.

Elemental Analysis:

$Yb_3AuGe_2In_3$: Semi-quantitative microprobe elemental analysis was performed on several crystals of the compound using a JEOL JSM-35C scanning electron microscope (SEM) equipped with a Noran Vantage Energy Dispersive Spectroscopy (EDS) detector. Data were acquired by applying a 25 kV accelerating voltage and an acquisition time of 40 s. A typical rod-like crystal of $Yb_3AuGe_2In_3$ is shown in Figure 1. The EDS analysis taken on visibly clean surfaces of the $Yb_3AuGe_2In_3$ crystals gave the atomic composition of 32.95 % Yb, 10.92 % Au, 32.75 % In and 23.39 % Ge, which is in

very good agreement with the results derived from the single crystal X-ray diffraction refinement.

YbAuIn: Semi-quantitative microprobe elemental analysis was performed on several crystals of the compound using a HITACHI MODEL S-2700 Scanning Electron Microscope (SEM) equipped with a light-element window Noran System Six EDS detector. Data were acquired by applying a 20 kV accelerating voltage and an acquisition time of 1 min. For the mainly polycrystalline YbAuIn the EDS analysis gave the atomic composition of 35.37 % Yb, 33.45 % Au and 31.18 % In in fairly good agreement with the single crystal X-ray diffraction results, though some pieces gave Yb rich content suggesting they may be impurities present.

X-ray Crystallography:

The X-ray intensity data were collected at room temperature using a STOE IPDS 2T (with additional capability of 2θ swing of the detector) diffractometer with graphite-monochromatized Mo Kα (λ = 0.71073 Å) radiation. The X-AREA (and X-RED and X-SHAPE within) package suite[68] was used for data extraction and integration and to apply empirical and analytical absorption corrections. The structures of $Yb_3AuGe_2In_3$ and YbAuIn single crystals were solved by direct methods and refined with the SHELXTL package of programs.[69] A stable refinement for both compounds was accomplished only in the hexagonal space group *P*-62*m*. Data collection and structure refinement details are given in Table 4-1. The final atomic positions, equivalent isotropic displacement parameters and anisotropic displacement parameters are listed in Table 4-2 and 4-3.

To determine the phase identity and purity, powder X-ray diffractions pattern of $Yb_3AuGe_2In_3$ were collected at RT on a CPS 120 INEL X-ray diffractometer with Cu K_a radiation, equipped with a position-sensitive detector and were compared to the pattern calculated from the single crustal structure refinement. For YbAuIn RT powder X-ray diffraction analysis was carried out on a PANanalytical X'Pert Pro MPD in Bragg-Brentano geometry with Co K_a radiation and an X'celerator detector.

Table 4-1. Crystal data and structure refinement data for $Yb_3AuGe_2In_3$ and $Yb_3Au_3In_3$.

Empirical formula	$Yb_3AuGe_2In_3$	$Yb_3Au_3In_3$
Formula weight	1205.73	727.24
Temperature (K)	293(2)	293(2)
Wavelength (Å)	0.71073	0.71073
Crystal system	Hexagonal	Hexagonal
Space group	*P*-62*m*	*P*-62*m*
a, *b* (Å)	7.3153(8)	7.7127(11)
c (Å)	4.4210(5)	4.0294(8)
V (Å^3) / Z	204.89(4) / 1	207.58(6) / 1
Density$_{calc}$ (Mg/m^3)	9.772	11.635
Absorption coefficient (mm^{-1}) / F(000)	67.086 / 500	94.272 / 594
θ range for data collection (^{o})	3.22 to 28.25	5.06 to 34.27
Index ranges	$-9 \le h \le 9$ $-9 \le k \le 9$ $-5 \le l \le 5$	$-12 \le h \le 12$ $-12 \le k \le 12$ $-5 \le l \le 6$
Reflections collected / unique / R(int)	2272 / 213 / 0.0262	2949 / 363 / 0.1339
Completeness to θ (%)	99.2	99.5
Data / restraints / parameters	213 / 0 / 14	363 / 0 / 14
Refinement method	Full-matrix least- squares on F^2	
Goodness-of-fit on F^2	1.077	1.192
Final R indices [$I>2\sigma(I)$] (R_1 / wR_2)^a	0.0298 / 0.0746	0.0418 / 0.1039
R indices (all data) (R_1 / wR_2)^a	0.0298 / 0.0746	0.0432 / 0.1046
Extinction coefficient	0.0012(6)	0.0037(9)
Largest diff. peak and hole (e. Å^{-3})	1.723 and -1.777	4.004 and -2.994

$^a R_1 = \Sigma \| |F_o| - |F_c| \| / \Sigma |F_o|$; $wR_2 = \left[\Sigma w \{ |F_o| - |F_c| \}^2 / \Sigma w |F_o|^2 \right]^{1/2}$; $w = 1/\sigma^2 \{ |F_o| \}$

Table 4-2. Atomic coordinates (x 10^4) and equivalent isotropic displacement parameters ($Å^2$ x 10^3) for $Yb_3AuGe_2In_3$ and $Yb_3Au_3In_3$.

Atom	Wyckoff	x	y	z	U(eq)[a]
Yb	3*g*	4197(2)	0	5000	9(1)
Au	1*b*	0	0	5000	15(1)
Ge	2*c*	3333	-3333	0	8(1)
In	3*f*	7512(3)	0	0	13(1)
Yb	3*g*	4069(2)	0	5000	11(1)
Au(1)	1*b*	0	0	5000	12(1)
Au(2)	2*c*	3333	-3333	0	11(1)
In	3*f*	7416(3)	0	0	10(1)

[a]U(eq) is defined as one third of the trace of the orthogonalized U^{ij} tensor.

Table 4-3. Anisotropic displacement parameters ($Å^2$ x 10^3) for $Yb_3AuGe_2In_3$ and $Yb_3Au_3In_3$. The anisotropic displacement factor exponent takes the form: $-2\pi^2[h^2a^{*2}U^{11} + ... +2hka^*b^*U^{12}]$

Atom	U^{11}	U^{22}	U^{33}	U^{23}	U^{13}	U^{12}
Yb	9(1)	8(1)	8(1)	0	0	4(1)
Au	17(1)	17(1)	12(1)	0	0	8(1)
Ge	11(1)	13(1)	16(1)	0	0	6(1)
In	9(1)	9(1)	7(2)	0	0	4(1)
Yb	9(1)	10(1)	15(1)	0	0	5(1)
Au(1)	11(1)	11(1)	15(1)	0	0	5(1)
Au(2)	9(1)	9(1)	16(1)	0	0	4(1)
In	7(1)	7(1)	14(1)	0	0	4(1)

Magnetic Measurements:

Magnetic susceptibility measurements for $Yb_3AuGe_2In_3$ were carried out with a Quantum Design MPMS SQUID magnetometer at Michigan State University facilities. EDS-analyzed crystals were soaked in ~ 6M of HCl acid for 15-30 min, washed out with water, and dried out in a dry oven. The crystals were then ground in open air atmosphere and sealed in Kapton tape which was inserted into the SQUID magnetometer. Temperature dependence data were collected between 3 and 400 K, for both zero field cooled (ZFC, on warming) and field cooled mode (FC, on cooling), with an applied field of 500 G. Field dependent magnetic measurements were acquired at 3 and 150 K with field sweeping from 0 up to 50 kG. Core diamagnetic corrections were applied. In order to study the magnetic anisotropy of the material, measurements were performed on several aligned single crystals oriented with the *c*-axis parallel and normal to the applied field of 2 kG. Field dependence measurements were also performed for both orientations at 5 K between 0 and 50 kG. These measurements were conducted at Northwestern University facilities.

Additional magnetization measurements were conducted at Materials Science Division (MSD) facilities at Argonne National Laboratory (ANL) using a Quantum Design MPMS SQUID magnetometer equipped with reciprocating sample option (RSO) mode as well as a Quantum Design PPMS magnetometer. For these measurements crystals of $Yb_3AuGe_2In_3$ were soaked in glacial acetic acid and soniqated for 24 – 48 hrs, washed out with dried acetone and dried under the flow of nitrogen. Samples of YbAuIn were used without any further cleaning process. Subsequently, crystals were either ground inside a nitrogen filled glove-box or loaded randomly (or oriented) without

grounding into gelatin capsules, mounted in a plastic straw and affixed to the end of a carbon fiber rod. Multiple temperature and field dependent measurements were performed for both compounds at various fields and temperatures.

X-ray absorption near edge spectroscopy (XANES):

X-ray absorption near edge spectroscopy (XANES) experiments were performed in Sector 20, bending magnet beamline (PNC/XOR, 20-BM) of the Advanced Photon Source at the Argonne National Laboratory, IL, USA. Measurements at the Yb L_{III} edge and at ambient pressure were performed in the transmission mode using gas ionization chambers to monitor the incident and transmitted X-ray intensities. A third ionization chamber was used in conjunction with a copper foil to provide internal calibration for the alignment of the edge positions. Monochromatic X-rays were obtained using a Si (111) double crystal monochromator. The monochromator was calibrated by defining the inflection point (first derivative maxima) of Cu foil as 8980.5 eV.[70] A rhodium-coated X-ray mirror was utilized to suppress higher order harmonics. The $Yb_3AuGe_2In_3$ and YbAuIn samples were prepared both by mixing an appropriate amount of finely ground powder with BN and cold pressing them to a pellet as well as by dusting the finely ground sample on Kapton tape and stacking several layers (8-12 layers) together. Most of sample preparation procedures were carried out inside a glove box environment. Measurements were performed at a range of temperatures from 15 to 300 K using a closed cycle refrigerator. Data reduction and analysis were performed using Athena and Artemis software developed by Newville and Ravel.[71] Care was taken to minimize thickness effects in the measurements.

Resistivity:

For $Yb_3AuGe_2In_3$ electrical resistivity was determined using a six probe technique in a standard ^4He gas flow cryostat at Materials Science Division (MSD) facilities at Argonne National Laboratory (ANL). Heating was avoided by reducing the current, and hysteresis, caused by slight thermometer - sample temperature differences, was avoided by sweeping the temperature slowly. More detailed experimental description can be found elsewhere.[72] Data points were taken during the cooling cycle from 302 to 2.48 K. Typical size of the rod-shaped crystals measured for$Yb_3AuGe_2In_3$ was 0.66 x 0.12 x 0.08 mm.

For YbAuIn electrical resistivity was measured as a function of temperature on single crystals. Electrical contact was made using silver paint and Cu wire directly on the crystals surface. Measurements were made for arbitrary current directions in the *a,c*-plane using a standard four point contact geometry (AC) in a Quantum Design Physical Property Measurement System (PPMS). Data points were recorded during the heating cycle at a temperature range of 1.8 – 274.3 K.

Heat Capacity:

Specific heat measurements of single crystals of $Yb_3AuGe_2In_3$ and YbAuIn were performed by a Quantum Design PPMS commercial device, at Northwestern University facilities, in the temperature range of 1.8 – 50.3 K by relaxation method using the "Two-Tau Model".[73]

Thermoelectric Power:

Thermoelectric power was measured using a SB-100 Seebeck Measurement MMR System, at Northwestern University facilities, in the temperature range between 310 and 710 K on a single rod-shaped crystal of $Yb_3AuGe_2In_3$. The electrical contact for the thermopower measurement was made using silver paint with the sample mounted on an alumina stage.

4-3. Results and Discussion

Reaction Chemistry:

Crystals of $Yb_3AuGe_2In_3$ grow in In flux generally as metallic silver rods and in a smaller portion as thinner needles. Figure 4-1(A) shows a scanning electron micrograph of a typical rod type $Yb_3AuGe_2In_3$ crystal. Reaction byproducts were small amounts of unreacted gold which tends to wet the surface of the crystals as well as very small amounts of YbAuGe, which due to very different crystal morphology (polygonal shape) could be easily distinguished and removed when necessary. When other rare earth metals such as Ce, Sm, Eu, Dy and Pr were employed under the same reaction conditions we did not observe analogs of $Yb_3AuGe_2In_3$. Instead these reactions led to other quaternary phases which will be reported in future work. In contrast, the REAuIn family of compounds forms with most of the RE atoms including Yb.[4]

The YbAuIn compound was synthesized by direct combination of the reactants in primarily grey polycrystalline form and pieces made up from packed crystals, with the exemption of the formation of a few single silvery metallic crystals as needles. The main byproduct was recrystallized Ta from the reaction vessel. Attempts to generate the

YbAuIn phase by flux reactions failed to produce the target phase in a significant purity and yield as they are many competitive $Yb_xAu_zIn_y$ phases. Figure 4-1(B) displays an SEM image of an YbAuIn chunk.

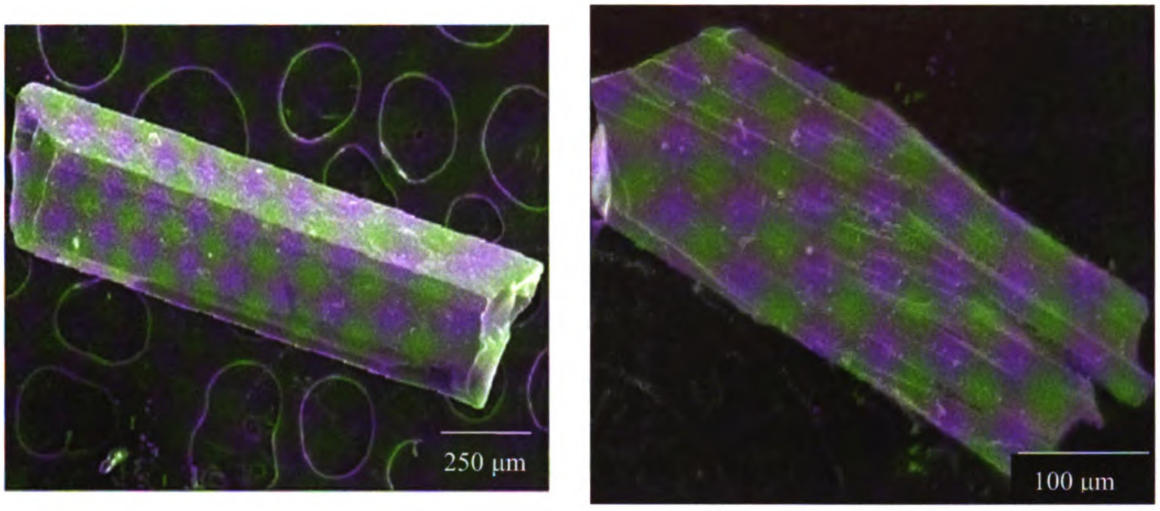

(A) **(B)**

Figure 4-1. Scanning electron micrograph (SEM) image of (A) a flux-grown $Yb_3AuGe_2In_3$ single crystal and (B) a compact piece of YbAuIn.

Structure:

$Yb_3AuGe_2In_3$ crystallizes as an ordered variant of the YbAuIn structure[4,11] which can be explained in the following manner; in the quaternary compound Ge has substituted for one of the two Au positions of the ternary compound written as $Yb_3Au_3In_3$. Both compounds adopt the ZrNiAl-type structure,[74] which itself is a ternary ordered version of Fe_2P,[75] in the hexagonal space group *P*-62*m*. The overall structure of the quaternary compound as viewed down the *c*-axis is illustrated in Figure 4-2. $Yb_3AuGe_2In_3$ can be

described as alternating layers of $[Ge_2In_3]$ and $[Yb_3Au]$ slabs that stack along the *c*-axis as it can been seen in the *a,c* view of the framework, Figure 4-3(A). Detailed descriptions of the two structural fragments are given below.

The $[Ge_2In_3]$ slabs consist of regular planar triangles built up from three In atoms and slightly distorted planar pentagons composed of one In-In dimer and four In-Ge bonds, as can be seen in the *a,b* projection of this layer, Figure 4-3(B). Every triangle is surrounded by six pentagons (two regular and four distorted) thus forming an infinite network of three- and five-membered rings that extend in the *a,b*-plane and stack along the *c*-axis. The bond between the In atoms is 3.152(4) Å which compares well to the In-In bonds found in the tetrameric segment of $REAu_2In_4$[33] ranging between 2.966(1) and 3.172(1); but it is shorter than the average In-In distance of 3.333 Å in elemental indium,[76] suggesting rather strong bonding. The In-Ge bonds at 2.7993(14) compare well to corresponding distances found in EuInGe[77] and $Ca_2LiInGe_2$[78] ranging from 2.75 to 2.876 Å, but these are shorter than the ones found in the quaternary phase $RE_7Co_4InGe_{12}$[56] (ranging from 2.9214(14) to 2.965(3) Å) or in $Ce_3In_{0.89}Ge_{1.11}$[79] where they have the value of 2.99 Å.

In the $[Yb_3Au]$ layer of the structure the Yb atoms are arranged in a flat net forming corner-sharing triangles with Yb-Yb distance of 3.7996(8) Å, see Figure 4-3(C). The Yb-Yb distance between two adjacent $[Yb_3Au]$ layers is equal to the *c*-axis at 4.4210(5) Å. The three-dimensional arrangement that the rare earth atoms adopt in this structure type leads to three exceptional features: i) The RE ions within the same layer form triangles so when it comes to antiferromagnetic coupling between nearest neighbours, this topology can cause frustration of the magnetic interactions. ii) The fact

that the magnetic RE atoms are stacked in [Yb_3Au] layers that alternate with the non-magnetic Ge-In layers, can give rise to indirect exchange interactions. iii) The crystalline electric field surrounding the lanthanide ions frequently induces strong anisotropy, which leads either to Ising or XY spin behavior.[80,81] Examples of compounds adopting this arrangement are the families of REAuIn[10-12] and RENiAl.[82,83] The Au atoms are isolated from one another and are found among the Yb triangles in the net at a Au – Au distance of 7.3153(8) Å, which is equal to the *a*-cell parameter. With respect to the [Ge_2In_3] slab the [Yb_3Au] layer is positioned so that the Yb atoms are in registry with the centers of the pentagons, while the Au atoms are in registry with the In triangles, see Figure 4-2.

The bonding environment of the Au atoms is shown in Figure 4-4. As mentioned above the Au atoms are isolated from each other forming bonds only with In and Yb atoms. Each Au atom forms six bonds to In atoms, from which three belong to the [Ge_2In_3] layer above and three to the layer below the atomic Au plane at an equal bond distance of 2.8634(13) Å, which agrees well with other reported Au-In bonds of other intermetallic compounds[31-34]. This arrangement makes for a regular trigonal prismatic geometry around the Au atoms. The rectangular faces of the gold-centered indium prism are capped by three Yb atoms in a trigonal planar mode, with Yb-Au bond equal to 3.0700(15), resulting in a coordination number (CN) of 9 for the Au atoms. A nearest neighbor environment with CN 9 is common for transition metal atoms in intermetallic compounds.

The Ge atoms are also isolated from one another and exhibit the same coordination geometry with the Au atoms, but in this case the trigonal prismatic enviroment is formed by the Yb atoms and is capped by three In atoms in a trigonal

planar manner, Figure 4-4. The In atom is eight coordinate, bonded to two other In atoms as well as to two Au, Yb and Ge atoms respectively in an arrangement that could be described as distorted tetragonal prism, Figure 4-4.

The coordination environment of the crystallographically unique Yb site is given in Figure 4-4. The rare earth atom is coordinated by 6 In atoms and 4 Ge atoms that gives rise to a pentagonal prismatic geometry, capped by a Au atom.

An alternative view of the $Yb_3AuGe_2In_3$ structure is in polyhedral representation. Figure 4-5, depicts the connectivity of the Au-centered In trigonal prisms and the Ge-centered In planar trigons, as viewed in the *a,b*-plane. The In trigonal prismatic polyhedra are fused. They share both of their trigonal faces thus forming trigonal columns that extend along the *c*-axis, see Figure 4-6. These columns are aligned parallel to each other and every such column shares each In corner, in the *a,b*-plane, with two trigonal planes which are centered by Ge atoms. Overall six such trigonal planar polyhedra surround every trigonal prismatic column to build the three-dimensional $[AuGe_2In_3]$ framework. The Yb atoms reside within the void space among the polyhedra. Table 4-4 gives a list of selected bond distances for $Yb_3AuGe_2In_3$ and YbAuIn.

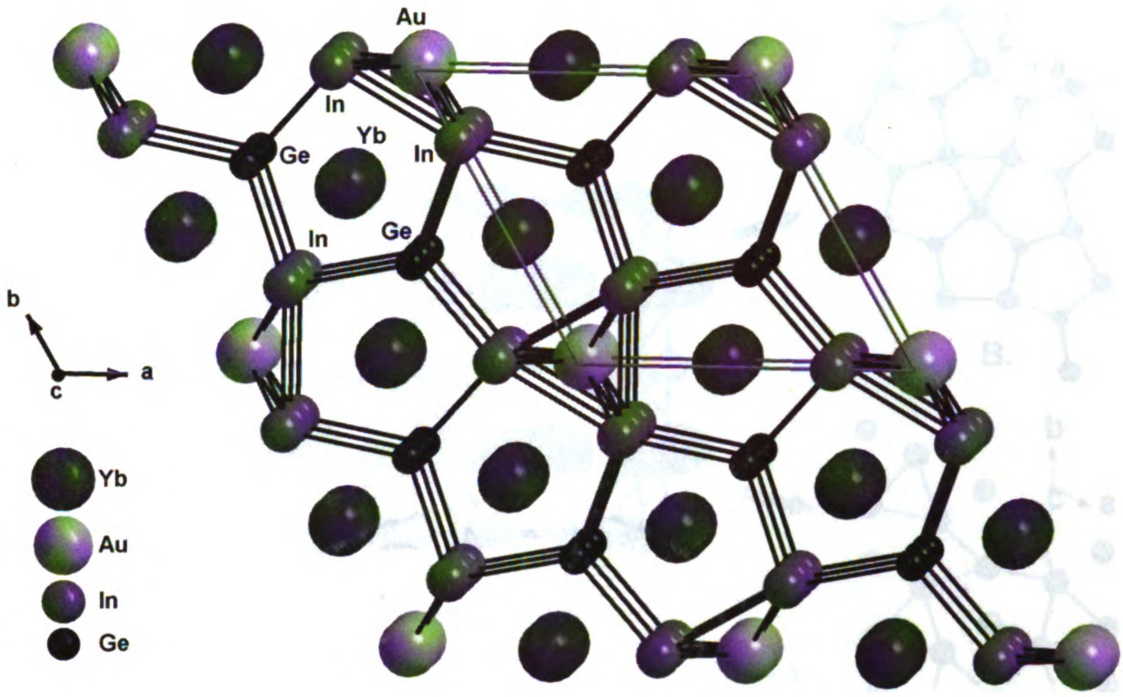

Figure 4-2. The overall structure of $Yb_3AuGe_2In_3$ as viewed onto the *a,b*-plane. For clarity the bonds to the Yb atoms are not drawn.

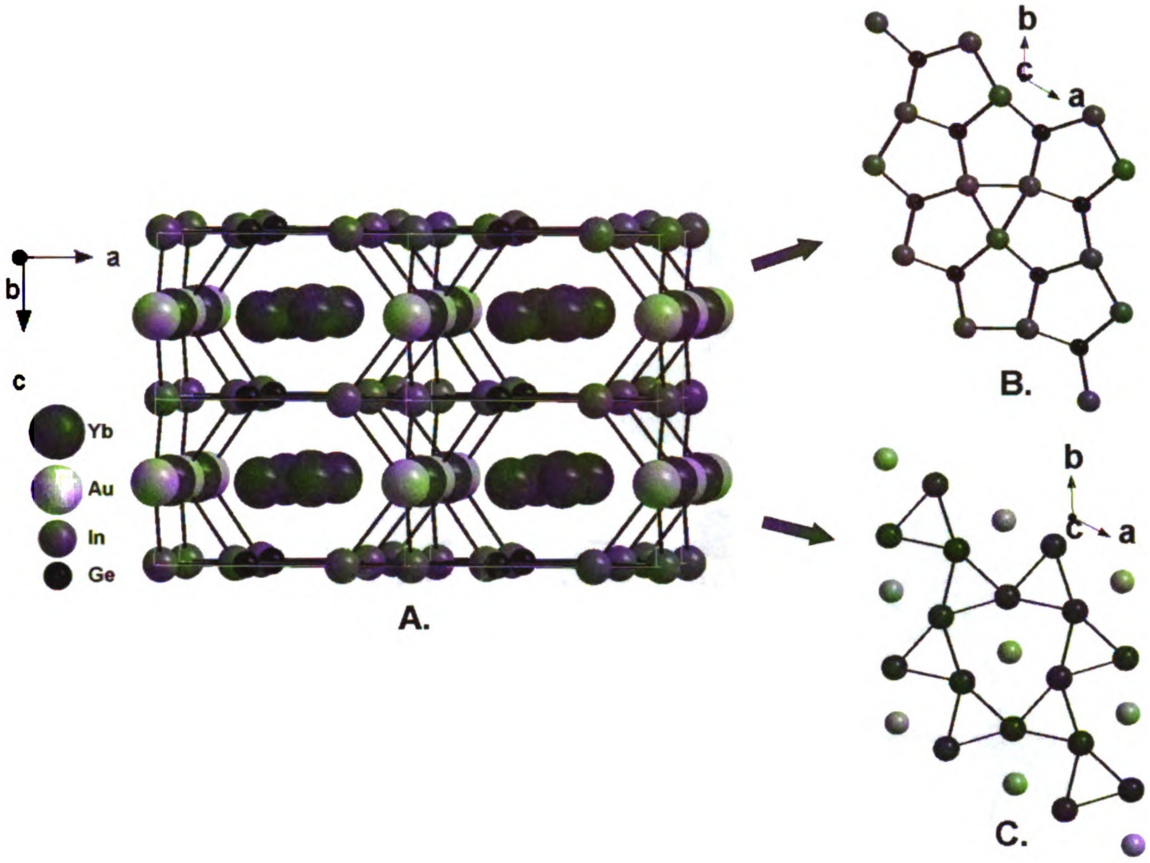

Figure 4-3. (A) Projection of the crystal structure of $Yb_3AuGe_2In_3$, viewed approximately down the *b*-axis, where the alternating layers of $[Ge_2In_3]$ and $[Yb_3Au]$ are emphasized. (B) Projection of the $[Ge_2In_3]$ layer onto the *a*,*b*-plane. (C) Projection of the $[Yb_3Au]$ layer onto the *a*,*b*-plane. The Yb atoms are connected with lines in order to emphasize the corner-sharing triangles.

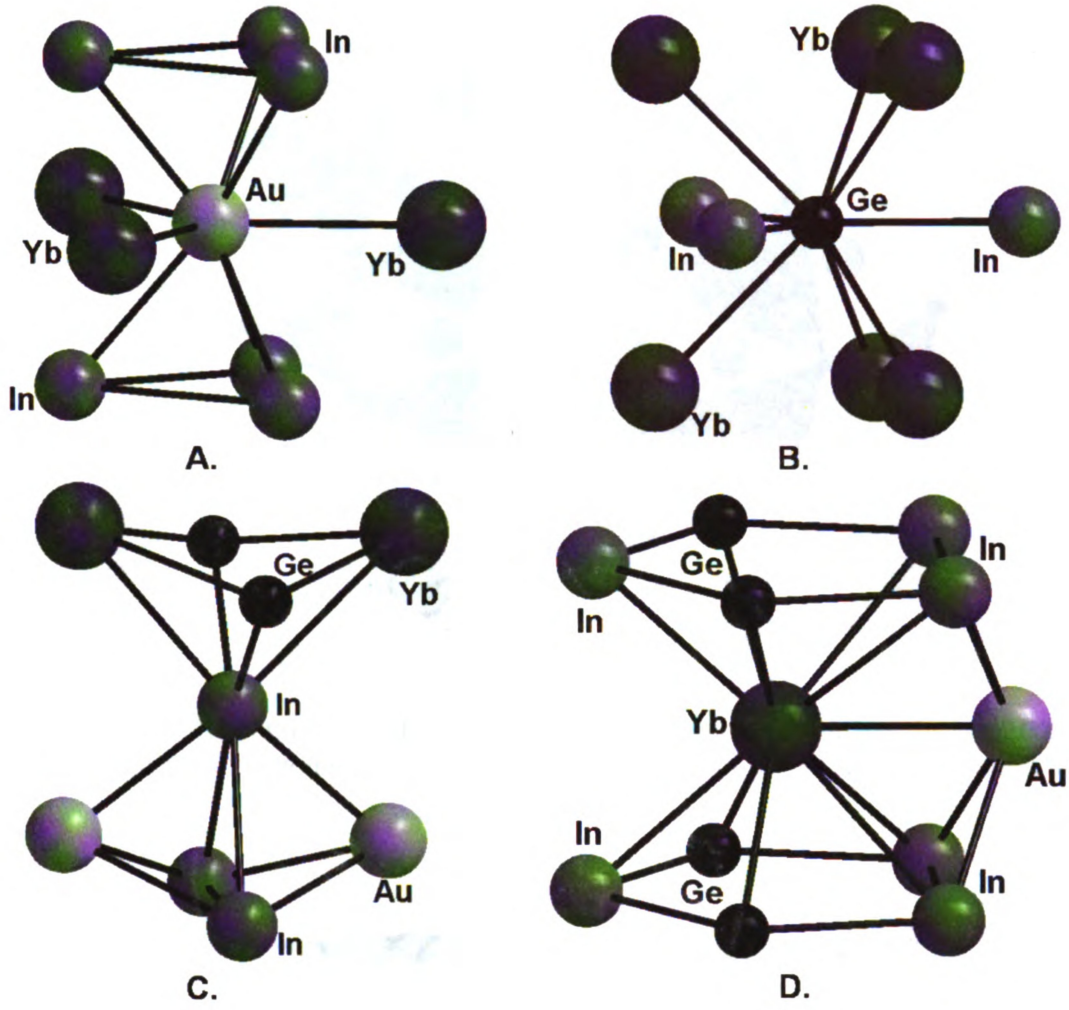

Figure 4-4. Coordination environment of the Au, Ge, In and Yb atoms. The coordination sphere cutoff is 3.5 Å.

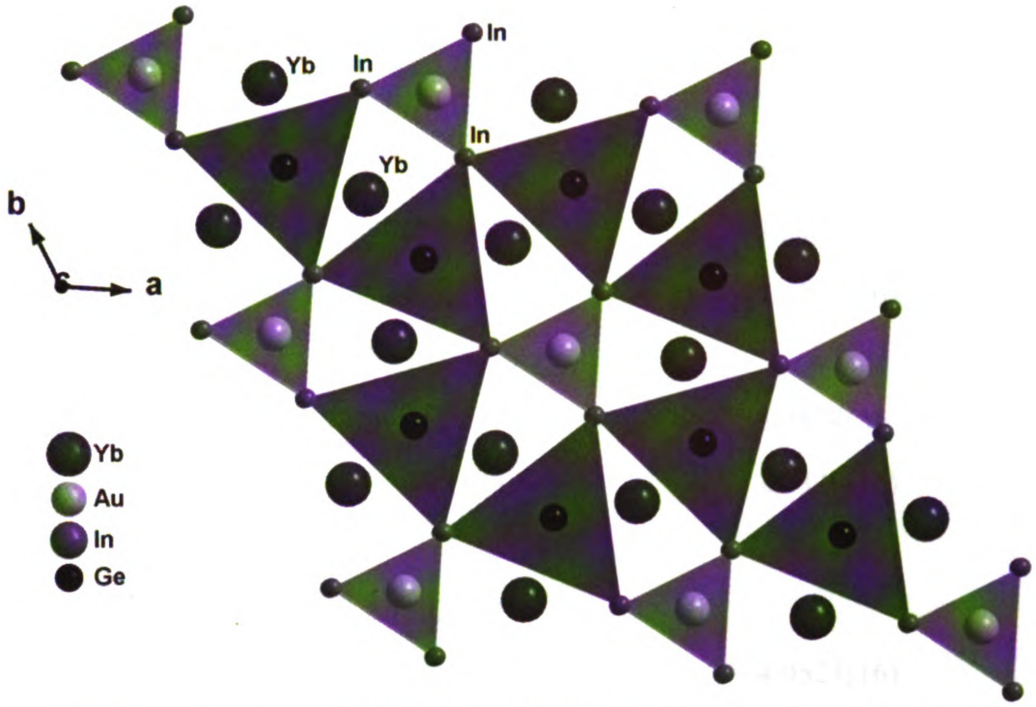

Figure 4-5. Polyhedral view of the $Yb_3AuGe_2In_3$ structure featuring the connectivity of the Au-centered In trigonal prisms and the Ge-centered In planar trigons, in the *a,b*-plane.

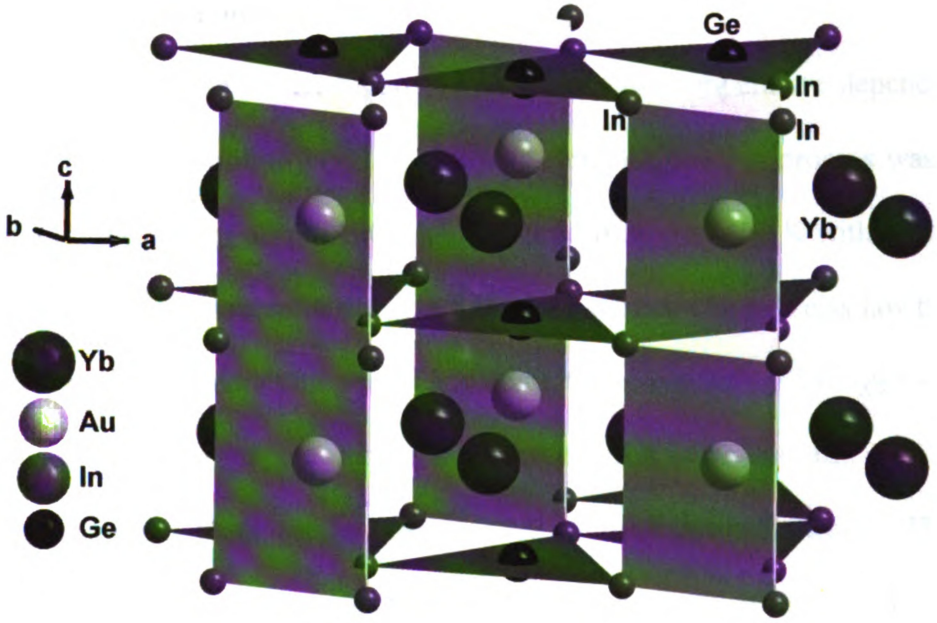

Figure 4-6. Stacking of the Ge-centered In trigonal planes and Au-centered In trigonal prisms along the *c*-axis. The In trigonal prisms are fused, forming trigonal columns that extend down the *c*-axis.

Table 4-4. Selected bond lengths (Å) for $Yb_3AuGe_2In_3$ and $Yb_3Au_3In_3$.

Bond	$Yb_3AuGe_2In_3$	$Yb_3Au_3In_3$
Yb-Au / Yb-Au(1)	3.0700(15)	3.0874(5)
Yb-In	3.2815(19)	3.275(2)
	3.4694(9)	3.4094(10)
Yb-Ge	3.1131(4)	
Yb-Au(2)		3.0874(5)
Au-In / Au(1)-In	2.8634(13)	2.8339(16)
Au(2)-In		2.9033(15)
Ge-In	2.7993(14)	
Yb-Yb	3.7966(8)	4.0521(16)

Magnetic Measurements:

Grinding in open air. Figure 4-7(A) shows the temperature dependence of the molar magnetic susceptibility (χ_m) of a ground sample (grinding process was performed in open air atmosphere) of $Yb_3AuGe_2In_3$ measured from 3 to 400 K with applied field of 500 G. The magnetic susceptibility data follow a modified Curie-Weiss law that includes a temperature independent component according to the equation $\chi(T) = \chi_0 + C / (T - \theta_p)$. χ_0 includes the sum of the temperature-independent conributions, e.g. van Vleck paramagnetism and Pauli paramagnetism (due to conduction electrons). The effective magnetic moment μ_{eff} was deduced from the Curie constant C, ($C = \mu_{eff}^2 / 8$). A nonlinear least-squares fit to this equation resulted in $\chi_0 = 3.2 \times 10^{-3}$ emu/mol of Yb atom, Curie - Weiss constant of θ_p = -1.5 K indicating antiferromagnetic interactions and an effective

moment of 0.52 μ_B / Yb atom. The inset in Figure 7(A) shows the plot of 1/ (χ - χ_0) versus temperature. The estimated effective moment of 0.52 μ_B, is only ~ 11.5 % of the value expected for the free-ion Yb^{3+}, 4.54 μ_B. This indicates that the compound contains both Yb^{2+} and Yb^{3+} atoms. In order to confirm the presence of Yb^{3+} species in the title compound we performed XANES studies that are discussed below.

The field dependence of the magnetization $M(H)$ for $Yb_3AuGe_2In_3$ ground sample at 3 and 150 K can be found in Figure 4-7(B). The data measured at 3 K exhibit linear behavior up to about 12 kG at which point the slope changes continuously until about 33 kG, where it becomes linear again but with a much shallower slope. No signs of saturation up to highest attainable field of 50 kG were observed. The magnetization curve taken at 150 K shows a very different picture. There is a strong field dependent response up to ~ 1.2 kG, which saturates at ~ 11 kG, while above that field $M(H)$ becomes linear up to the highest obtainable field. This suggests that, there is probably a small ferromagnetic component in the $Yb_3AuGe_2In_3$ compound which is part of the structure itself and not an extrinsic impurity component. It is possible that although the majority of the Yb atoms are in the Yb^{2+} state, there are small regions in the structure that are occupied by Yb atoms having a non integer valence $Yb^{2+/3+}$ or even Yb^{3+} giving rise to a small number of magnetic moments. This small ferromagnetic component could explain the hysteresis that appears between the ZFC and FC magnetic susceptibility data in the temperature range of ~ 15 – 260 K an effect that is fully reproducible.

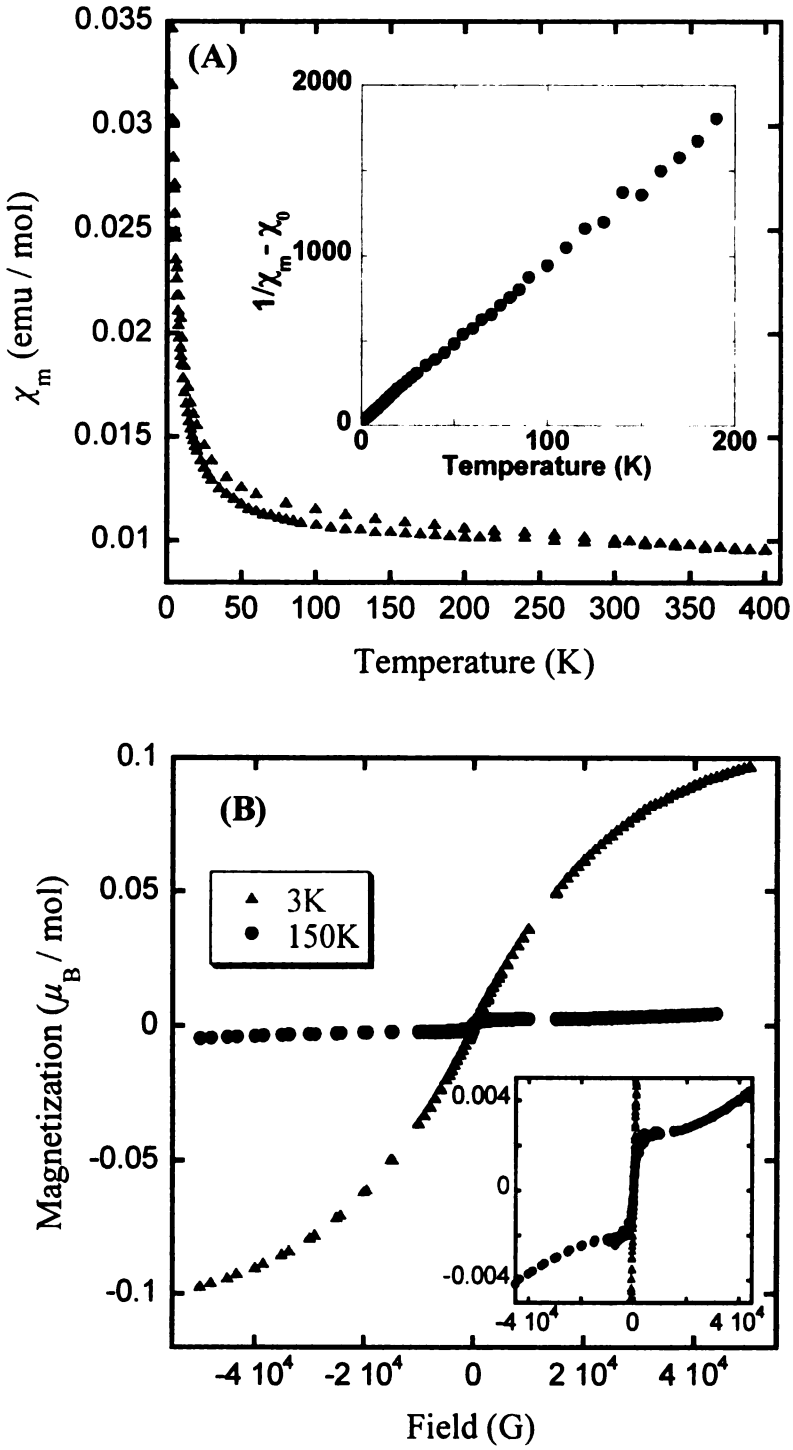

Figure 4-7. (A) Temperature dependence of the molar susceptibility χ_m of $Yb_3AuGe_2In_3$ (ground samples) with an applied field of 500 G. The inset shows the plot of $1/(\chi_m - \chi_0)$ versus temperature. (B) Magnetization data of $Yb_3AuGe_2In_3$ collected at 3 and 150K.

Unground, randomly oriented crystals. We also performed temperature dependent molar magnetic susceptibility (χ_m) measurements for $Yb_3AuGe_2In_3$ for a sample of randomly oriented crystals (placed in a kapton tape envelope, unground) measured between 3 and 400 K with an applied field of 1 kG, Figure 4-8. The data exhibit similar qualitative behavior. There is an apparent hysteresis between ZFC and FC data, at the temperature range of 15 – 340 K, but the χ_m values are smaller. A least-squares fit of the FC data with the modified Curie-Weiss law $\chi(T) = \chi_0 + C / (T - \theta_p)$, resulted in $\chi_0 = 1.8 \times 10^{-4}$ emu/mol of Yb atom, Curie - Weiss constant of $\theta_p = -0.86$ K indicating antiferromagnetic interactions and an effective moment of only 0.13 μ_B / Yb atom. We see that the estimated effective moment is much smaller than the one found from the ground sample. This suggests that in the single crystal form $Yb_3AuGe_2In_3$ has a smaller portion of Yb^{3+} moments.

The inset in Figure 4-8 shows the field dependence of the magnetization $M(H)$ for the single crystal sample of $Yb_3AuGe_2In_3$ collected at 3K. The magnetic moment shows some strong dependence on the lower fields, roughly saturates between 24 and 37 kG, while the moment after 40 kG starts decreasing. This decrease at higher fields is probably due to the weak overall response of the paramagnetic moment and that the diamagnetic signal (from the background) at the higher field values becomes more significant. The magnetization data confirm the small portion of the Yb^{3+} moments in the sample.

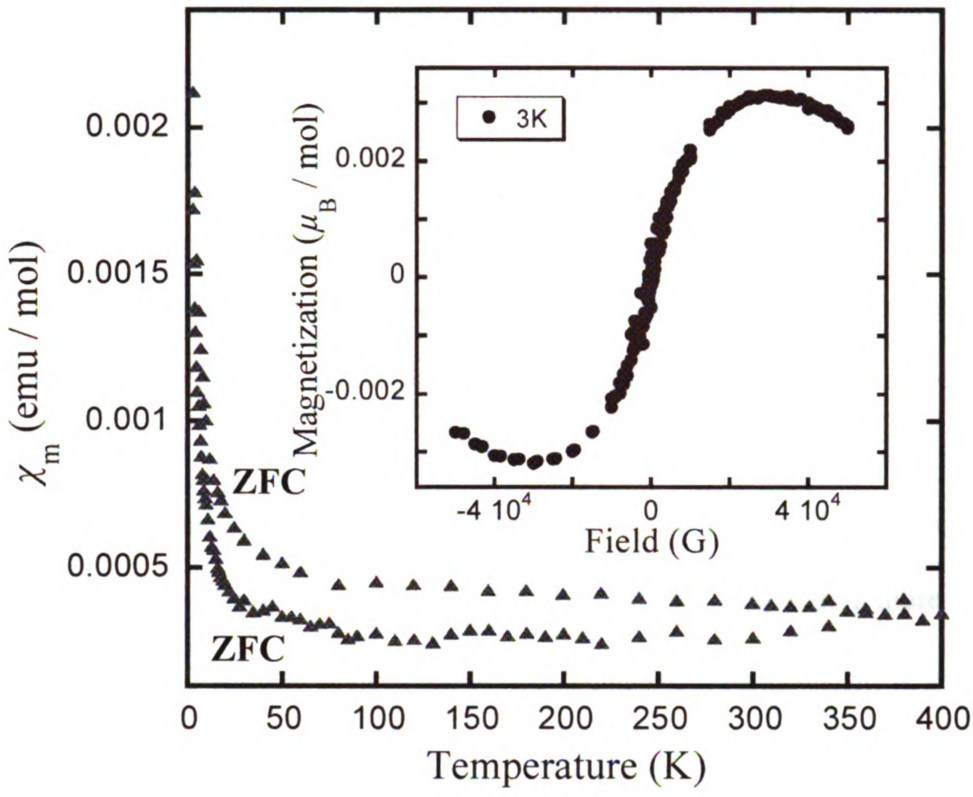

Figure 4-8. Temperature dependence of the molar susceptibility χ_m of $Yb_3AuGe_2In_3$ (sample of randomly riented crystals) with an applied field of 1 kG. The inset shows the magnetization data of the same sample collected at 3 K and with fields sweeps from -50 to 50 kG.

Magnetic anisotropy – unground, oriented crystals. Because the 3D arrangement of the RE atoms in the ZrNiAl-structure type often induces strong anisotropy, that could lead to interesting phenomena such as Ising or XY spin behavior,[10,82] we measured the magnetic susceptibility parallel and normal to the *c*-axis of crystals of $Yb_3AuGe_2In_3$. Several single crystals were aligned together so their *c*-axes were nearly parallel. From Figure 4-9 it's obvious that the material is indeed magnetically

anisotropic. When the *c*-axis is oriented parallel to the applied field the material appears nearly diamagnetic above 60 K while when it is aligned normal to the field it exhibits almost temperature independent (pauli paramagnetic like) behavior which tends to a small increase towards higher temperatures.

The magnetization curve measured at 5 K, see Figure 4-10, for the parallel orientation, shows linear dependence up to 22 kG. Beyond this point the slope starts to change with no saturation up to 50 kG. Finally, the magnetization with the field normal to *c*-axis is higher in magnitude and exhibits linear response up to 2 kG, followed by a change in slope at ~ 4 kG. The moment at 50 kG is 0.08 μ_B / mol more than the corresponding one of the parallel orientation.

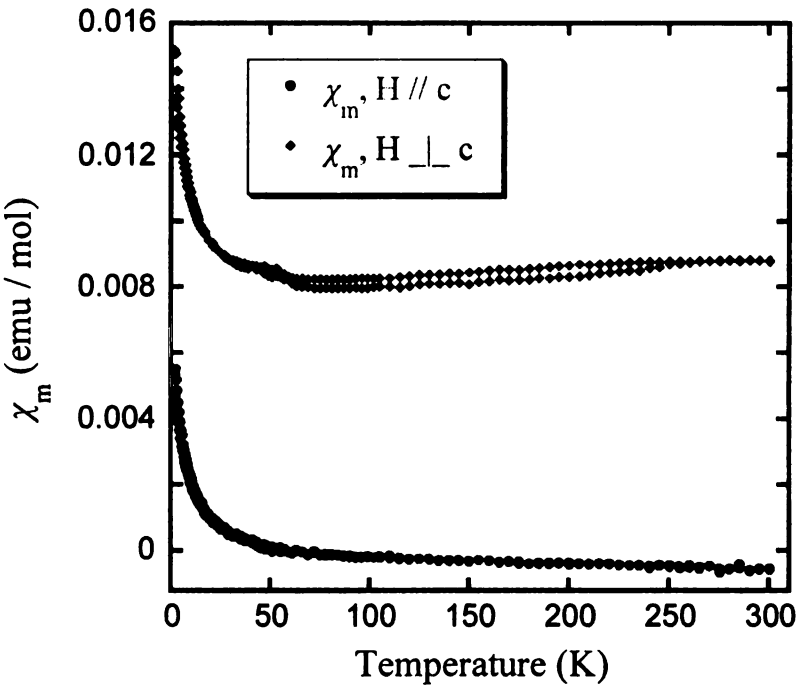

Figure 4-9. Temperature dependence of the molar susceptibility χ_m of $Yb_3AuGe_2In_3$ on single crystals, oriented with the *c*-axis parallel (circles) and normal (rhombi) to the applied field of 2 kG.

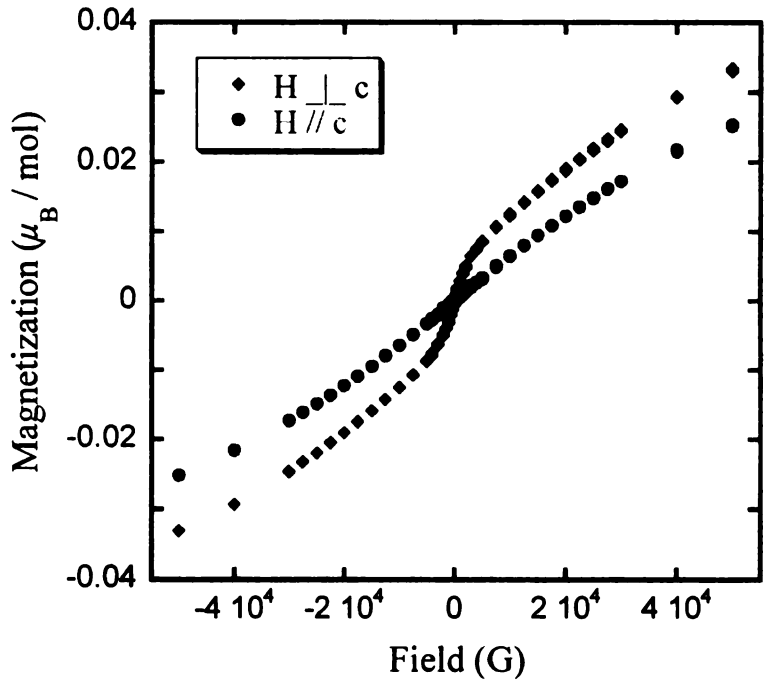

Figure 4-10. Field dependence magnetization measurements for both parallel and normal orientations measured at 5 K between -50 and 50 kG of applied fields.

Magnetic Measurements under Variation of Experimental Parameters:

In our efforts to further explore the magnetic properties we tried to study the magnetic behavior of $Yb_3AuGe_2In_3$ with measurements where various experimental parameters were adjusted. Our first attempt was to study the magnetic response of a sample initially consisted of randomly oriented crystals and subsequently after the crystals were ground in a inert atmosphere inside a N_2 filled glove-box. The grinding process in a inert atmosphere was incorporated in order to avoid possible oxidation of the sample especially of the Yb species. We additionally changed the cleaning process of the crystals before the measurements, since the initially used HCl acid is considered a rather harsh and strong acid. In the following measurements the selected crystals were further

treated with glacial acetic acid and soniqation for ~ 24 – 48 days and then consequently washed with dried acetone and dried out under N_2 atmosphere. Another experimental parameter that was tested was the temperature rate (K / min) of the initial cooling from room temperature down to lowest temperature of 2 K as well as the rate during data collection.

Unground single crystals – fast cooling. Figure 4-11(A) shows the temperature dependence of the magnetic susceptibility (χ_m) of an $Yb_3AuGe_2In_3$ sample of single crystals loaded randomly in a gel-cup and measured between 2 and 280 K with an applied field of 0.5 kG. The sample was zero field cooled from RT down to 2 K with a rate of 10 K / min (fast cooling) and the data were collected with the same rate (and settle mode). The data show again a hysteresis between the ZFC and FC at a temperature range of 60 - 280 K, see inset. A least-squares fit of the data with the modified Curie-Weiss law $\chi_m(T) = \chi_0 + C / (T - \theta_p)$, resulted in $\chi_0 = 1 \times 10^{-4}$ emu/mol of Yb atom, Curie - Weiss constant of $\theta_p = -1.7$ K indicating antiferromagnetic interactions and an effective moment of 0.21 μ_B / Yb atom. This gives a 4.7 % of the theoretical value for Yb^{3+}.

Ground inside N_2 glove-box crystals – fast cooling. The molar magnetic susceptibility $\chi_m(T)$ data of the $Yb_3AuGe_2In_3$ sample after it was ground inside a glove-box, are given in Figure 4-11(B). As it can be seen, the magnetic data exhibit a remarkably different behavior. At ~ 145 - 150 K there is a sharp change in the slope, suggesting the onset of a ferromagnetic transition, while a divergence between the ZFC and FC data starts to occur. Additionally, the ZFC curve exhibits a crossover of the FC curve between 150 and 80 K. Below 80 K the divergence between ZFC and FC mode becomes maximum. An additional feature of a small cusp centered at ~ 180 K also

appears. This behavior was fully reproducible for ground samples were the grinding process was performed inside glove-box.

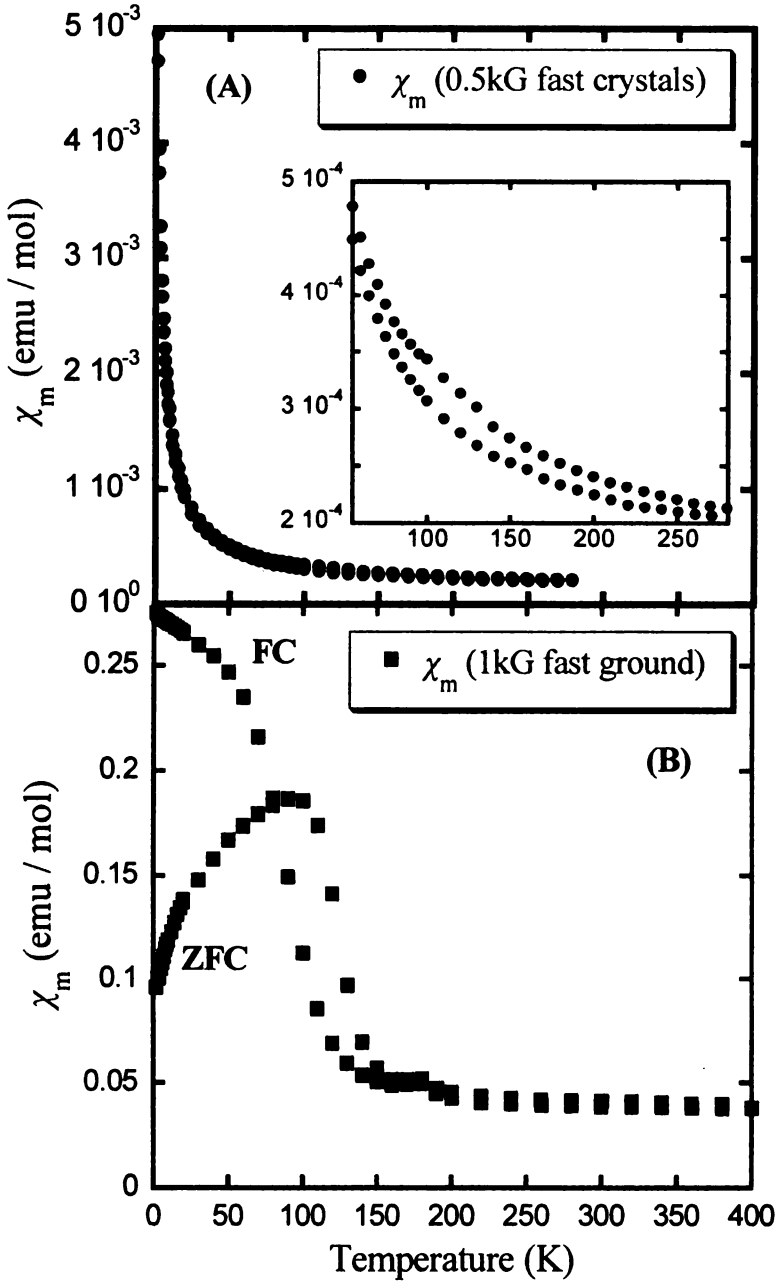

Figure 4-11. (A) Temperature dependence of the molar susceptibility χ_m of $Yb_3AuGe_2In_3$ with an applied field of 0.5 kG and with a temperature rate of 10 K / min for both initial cooling down from RT and collecting data (A) for a sample of randomly oriented crystals. Inset shows higher temperature data and (B) $\chi_m(T)$ of the same sample after grinding it inside a nitrogen filled glove-box.

The field dependence of the magnetization $M(H)$ data for both samples of $Yb_3AuGe_2In_3$, single crystals and ground, are given in Figures 4-12(A) and (B) respectively. Both curves were measured at 2 K, after the FC data were collected with a temperature rate of 10 K / min, and with field sweeping from -55 kG up to 55 kG. The magnetization curve for the sample of single crystals exhibits a stronger dependence at lower fields, while after roughly 0.9 kG the slope continuously changes and becomes shallower. There is no sign of saturation up to the highest attainable field of 55 kG.

The corresponding magnetization $M(H)$ curve for the ground sample shows a very different picture. The moment shows a very strong field dependent response for very small fields while the slope immediately changes sharply and the material goes through a metamagnetic like transition that takes place only in increasing field data, see arrow in Figure 4-12(C). This jump disappears in the decreasing filed data. In both increasing and decreasing field curves though there are apparent hysteresis loops for both positive and negative fields, indicating a ferromagnetic ordering of the spins. This reinforces the results obtained already from the susceptibility $\chi_m(T)$ data where it was seen that even though $Yb_3AuGe_2In_3$ when measured as single crystals exhibits weakly temperature dependent paramagnetic behavior above 50 K while a hysteresis between the ZFC and FC data starts to arise; however, when the crystals are ground in an inert atmosphere $Yb_3AuGe_2In_3$ exhibits a ferromagnetic transition. This suggests that the material goes into a different magnetic state with a much higher magnetic moment. Further measurements are needed at this point to explain this behavior.

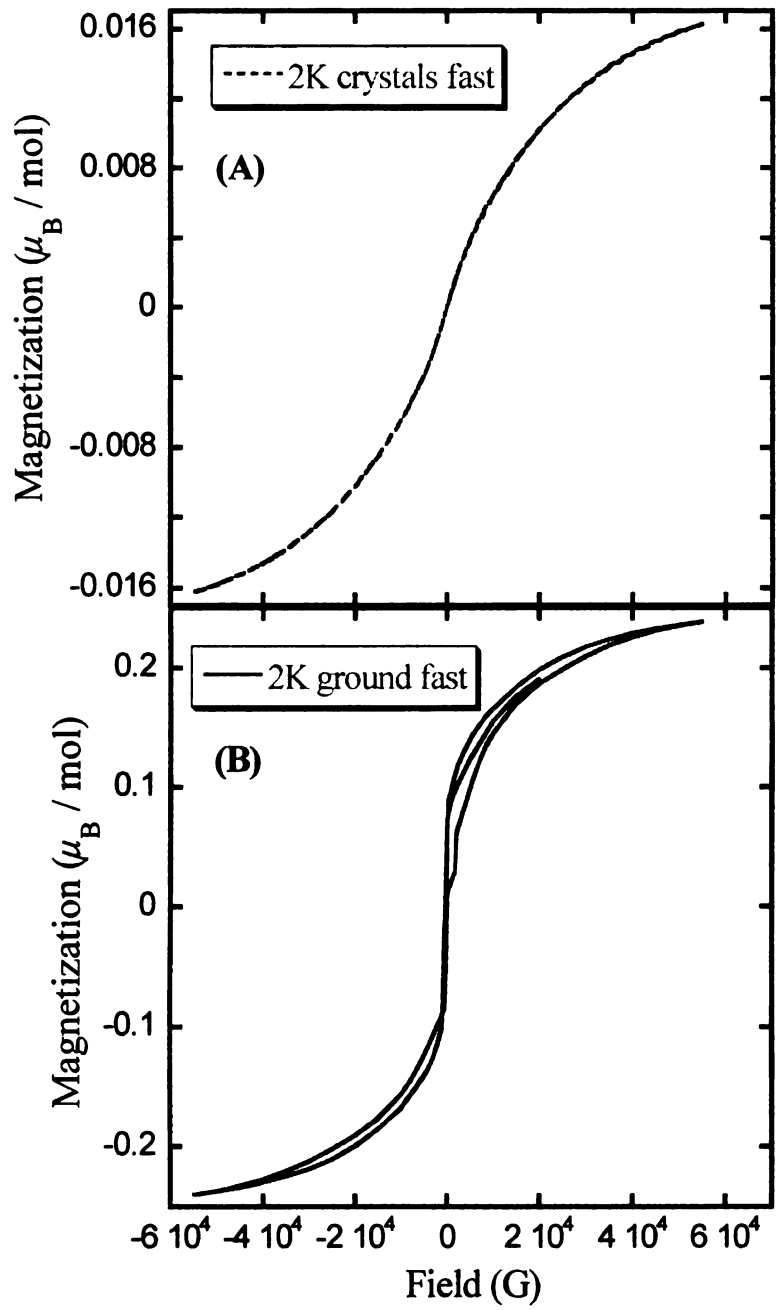

Figure 4-12. Magnetization data of $Yb_3AuGe_2In_3$ collected at 2 K and field sweeps between -55 and 55 kG (A) for a sample of randomly oriented crystals and (B) same sample after grinding inside a N_2 filled glove-box. Inset shows low field data, where arrow indicates a metamagnetic like transition.

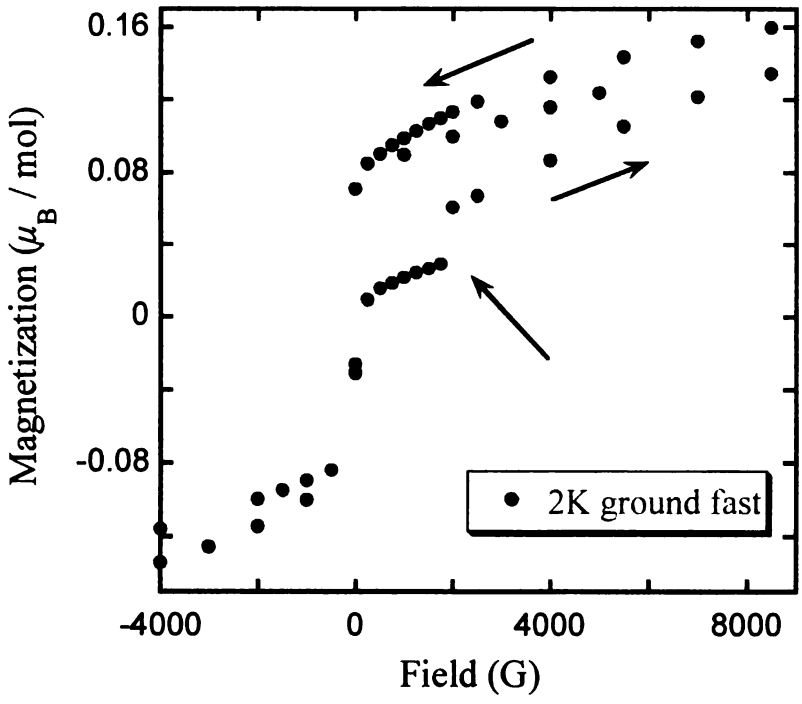

Figure 4-12. (C) Low field magnetization data of the ground inside the glove box $Yb_3AuGe_2In_3$ sample. The arrow indicates a metamagnetic like transition.

Slow cooling. In a next step, we tried to investigate the magnetic response of both single crystals and ground samples of $Yb_3AuGe_2In_3$ with a slow cooling rate. Since the material seems to undergo a magnetic transition we wanted to explore the effect of giving the system more time for this transition to take place. For the following measurements the temperature was decreased from 300 K to 200 K with a rate of 10 K / min, and finally down to 2 K with 1 K / min. During data collection the settle mode was used with a temperature change of 1 K / min (that accounts for a very slow overall measurement).

Unground, single crystals – slow cooling. Figure 4-13(A) shows the thermal variation of the molar magnetic susceptibility (χ_m) of an $Yb_3AuGe_2In_3$ sample of single

crystals loaded randomly in a gel-cup and measured between 2 and 300 K with an applied field of 1 kG. The material shows similar behavior with the fast cooling measurement. There is a profound hysteresis between the ZFC and FC at a temperature range of 30 - 300 K and weak temperature dependence above ~ 50 K. A least-squares fit of the data with the modified Curie-Weiss law $\chi(T) = \chi_0 + C / (T - \theta_p)$, resulted in $\chi_0 = 5.3 \times 10^{-4}$ emu/mol of Yb atom, Curie - Weiss constant of $\theta_p = -4$ K indicating antiferromagnetic interactions and an effective moment of 0.28 μ_B / Yb atom. This gives a 6.2 % of the theoretical value for Yb^{3+}. In overall, comparing to the fast cooling data the slow cooling one results in bigger irreversibility between ZFC and FC curves and in a slightly increased Yb^{3+} amount.

Ground inside N_2 glove-box crystals – very slow cooling. The molar magnetic susceptibility $\chi_m(T)$ data of the same $Yb_3AuGe_2In_3$ sample after it was ground inside a glove-box with applied fields of 0.5 and 1 kG (open trigons and solid circles, respectively), are given in Figure 4-13(B). The material exhibits again a ferromagnetic ordering, as in the case of the ground sample, after fast cooling. However, under a very slow overall measurement we observe that the transition has moved to a higher temperature, from ~ 150 to ~ 240 K, (almost 100 K difference) and has become sharper and more clear, in that the ZFC curve does not crossover the FC curve anymore, but simply diverges considerably below ~ 220 K. A possible interpretation of this could be that, whatever transition the material goes through when it is in the ground form, prolonged initial cooling time as well as collection time, allows it to develop to a higher degree.

Remeasurement of the ground inside glove-box sample after the course of 44 days. In order to check whether the system relaxes back to the initial state (before the grinding), stays the same or even keeps changing the same ground sample was measured again after the period of ~ 44 days and under very slow temperature rate again. The molar magnetic susceptibility $\chi_m(T)$ data of this measurement with an applied field of 0.5 kG (v. slow 2, open squares) are also given in Figure 4-13(B). Comparing with the previous measurement (0.5 kG, v. slow, solid circles) the data, with the exception of a small difference in the ZFC curve below the transition temperature, did not show any significant change. This means that the system remained stable during the period of ~ 44 days (stored under nitrogen flow). That could possibly mean that the transition had been already completed in the course of the first measurement.

Ground inside glove box sample after fast cooling and pressing it into a pellet. Figure 4-13(B) also displays the $\chi_m(T)$ data of two additional measurements of the same sample as above. One after fast cooling (solid rhombi) and one after the sample was pressed into a pellet (open circles, only a small portion of the pellet was used). For both measurements same rate profile was used: from 300 K to 10 K with 10 K /min and then with 1 K / min down to 2 K and a sweep mode with 1 K / min rate during data collection. The only significant difference that we see is a gradual decrease of the absolute $\chi_m(T)$ value going from one to another data set.

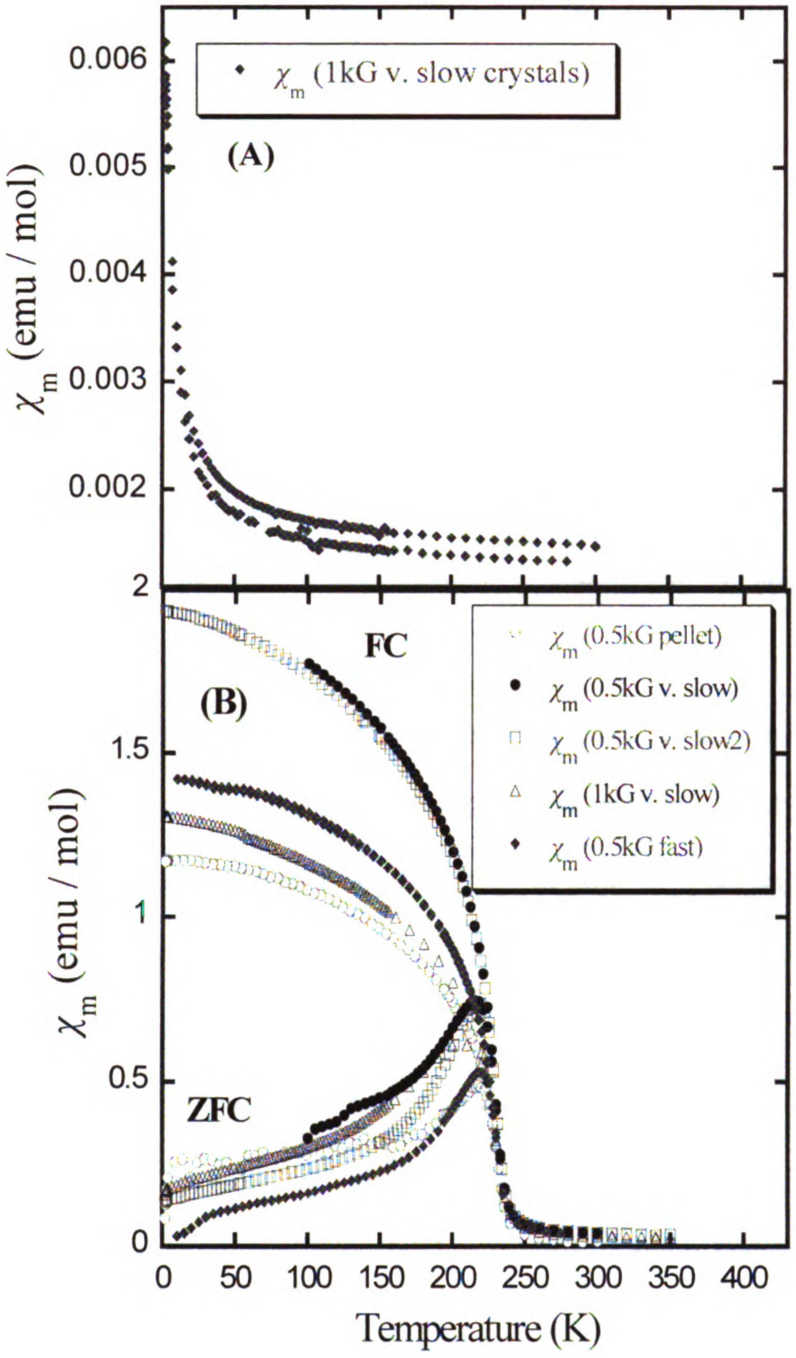

Figure 4-13. Temperature dependence of the molar susceptibility χ_m of $Yb_3AuGe_2In_3$ with an applied field of 0.5 and 1 kG and temperature rates of 10 K / min (fast cooling) and 1 K / min (very slow cooling) (A) for a sample of randomly oriented crystals (B) same sample after grinding inside a nitrogen filled glove-box.

Unground single crystals - slow cooling. The field dependence of the magnetization $M(H)$ data for both samples of $Yb_3AuGe_2In_3$, single crystals and ground and under slow cooling, are given in Figures 4-14(A) and (B) respectively. For the magnetization data of the single crystals sample the temperature of 65 K was chosen in order to study the magnetic response in a temperature where the ZFC and FC data exhibit hysteresis in the $\chi_m(T)$ data. The magnetic moment shows a linear response to the field up to ~ 20 kG. At higher fields there is a hysteresis loop up to about 50 kG, at which point the magnetization curve becomes linear again. This suggests that at 65 K where the ZFC and FC differ there is probably a ferromagnetic component in the system already before the crystals are ground.

Ground crystals inside glove-box – slow cooling. Figure 4-14(B) shows the magnetization $M(H)$ data after the grinding of the sample measured at 2 K and 200 K. The curve at 2 K exhibits a clear hysteresis loop for both negative and positive values of the field, which is a typical magnetic response for ferromagnetic systems. Above the field of ~ 27 kG the hysteresis loop disappears the moment starts to saturate. At the highest applied field of 60 kG, the moment reaches a value of 0.45 μ_B / mol which is only 7 % of the theoretical value for three Yb^{3+} atoms. In the $M(H)$ data measured at 200 K (dashed line) the slope of the curve continuously changes and becomes linear at ~ 30 kG. At the field of 55 kG the moment has a value of 0.37 μ_B / mol, which is consisted with decreased saturation moment expected at higher temperatures. The inset shows the low field region data. The magnetization data support the assumption that there is a higher amount of Yb^{3+} species in the ground form of the sample and that the system goes through a magnetic phase transition that seems to be of ferromagnetic nature.

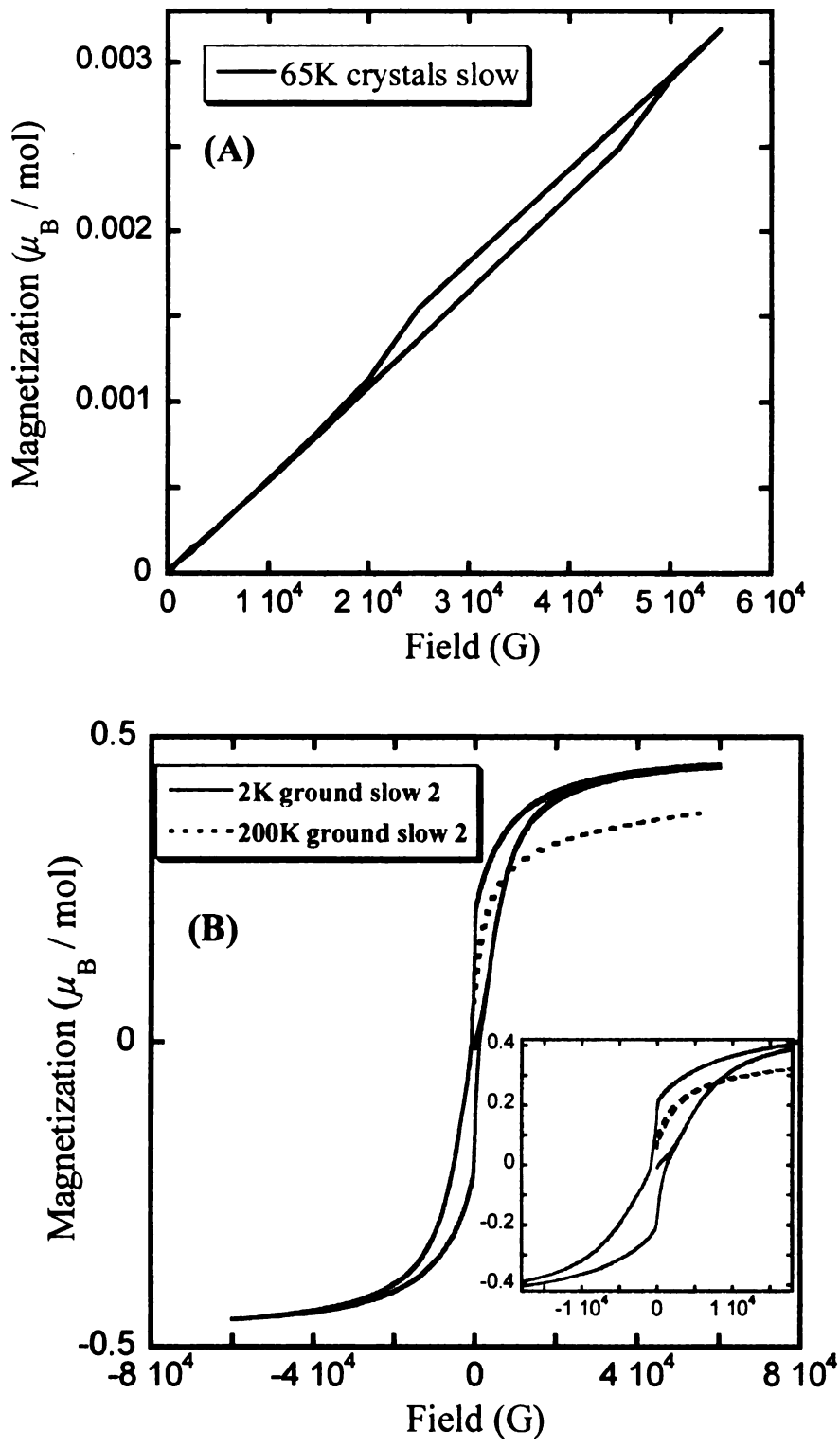

Figure 4-14. Magnetization data of $Yb_3AuGe_2In_3$ collected at 2, 65 and 200 K and with a temperature rate of 1 K / min (A) for a sample of randomly oriented crystals (B) same sample after grinding inside a nitrogen filled glove-box. Inset shows low fields region.

We also tried to investigate the magnetism of the YbAuIn compound under similar experimental conditions applied for the $Yb_3AuGe_2In_3$ compound, hoping that it will help us in a better understanding of the intriguing results that we got from the study of the magnetic properties of the quaternary phase. Under this scope, measurements of both single crystals (or compact pieces of crystals) and ground samples (in open air and inside a glove-box) were used for fast as well as slow cooling temperature rates.

Ground crystals in open air. Figure 4-15 shows the temperature dependence of the molar magnetic susceptibility (χ_m) of a ground sample (grinding process was performed in open air atmosphere) of YbAuIn measured from 2 to 400 K and with an applied field of 1.8 kG. Qualitative the $\chi_m(T)$ data display similar behavior with the ground in open air sample of the isostructural $Yb_3AuGe_2In_3$, in that there is no transition but instead there is a small hysteresis between ZFC and FC (not apparent in the plot due to the scale of the low temperature region) roughly at the region of 15 – 250 K and above ~ 50 K the moment is only weakly temperature dependent. A nonlinear least-squares fit to this equation of the FC data up to 175 K (higher temperature data were excluded due to increased noise) resulted in $\chi_0 = 5 \times 10^{-4}$ emu/mol, Curie - Weiss constant of $\theta_p = -3.5$ K indicating antiferromagnetic interactions and an effective moment of 0.68 μ_B / Yb atom, which is about 15 % of the theoretical value for a free Yb^{3+} atom.

The isothermal magnetization for the same ground sample of YbAuIn measured at 2 K can be found in the inset of Figure 4-15. The magnetization increases gradually with applied external field, which is characteristic of the paramagnetic state; and no sign of saturation is observed up to maximum applied field of 55 kG. Both susceptibility and low temperature magnetization measurements for a ground in open air atmosphere sample of

YbAuIn exhibit similar behavior with the corresponding ground sample in open air of $Yb_3AuGe_2In_3$. Both materials exhibit paramagnetic behavior with no observed magnetic ordering but with a distinct, reproducible hysteresis between ZFC and FC data.

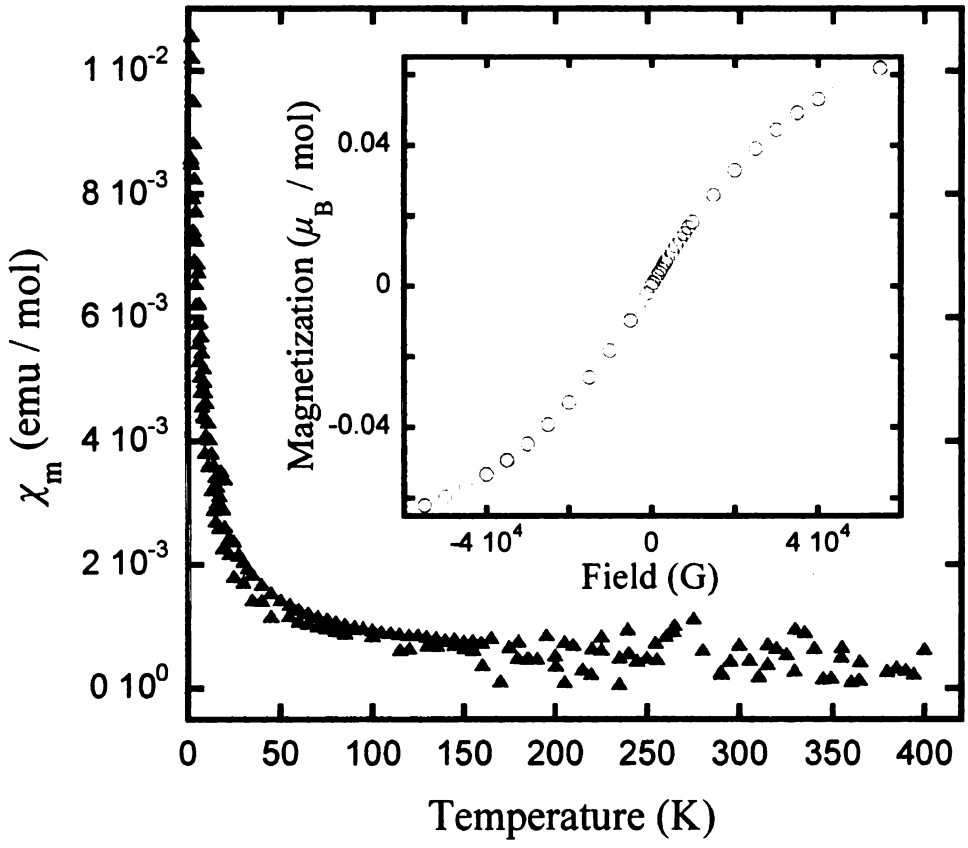

Figure 4-15. Temperature dependence of the molar susceptibility χ_m of a ground in open air YbAuIn sample, with an applied field of 1.8 kG. The inset shows the magnetization data of the same sample collected at 2 K and with field sweeps from -55 to 55 kG.

Ground crystals inside glove-box. In Figure 4-16 two samples of YbAuIn are examined, one where crystals and compact pieces of crystals where ground inside a N_2 filled glove-box and one where bigger pieces where just broken into much smaller ones by slightly hitting with a pestle in a mortar (in open air). Both samples were cooled from room temperature down to 2 K with the fast (10 K / min) temperature rate and the same rate was used during data collection.

Ground inside glove box sample – fast cooling. The thermal variation of the susceptibility $\chi_m(T)$ of the ground sample (open rhombi) of YbAuIn measured with 1 kG applied field, given in Figure 4-16(A), differs remarkably from the ground in open air sample, in a similar way observed for the quaternary phase. The system seems to also undergo a ferromagnetic transition that onsets at ~ 145 - 150 K, as is evident by the steep change in the slope, which also coincides with the beginning of the ZFC and FC data divergences, as well as with the crossover of the ZFC curve of the FC curve that continues until 80 K. Below 80 K the difference becomes maximum as the ZFC curve after a peak starts going down, while the FC curves keeps rising to higher χ_m values. The additional feature of a small cusp centered at ~ 180 K is also present.

Crashed pieces – fast cooling. The susceptibility $\chi_m(T)$ of the sample consisting of crashed pieces (solid triangles) displays quite similar behavior, see Figure 4-16(A). Even though the overall increase of the moment is much smaller than in the ground sample, it still goes through a ferromagnetic transition. In this case, the transition is much broader and it starts at ~ 135 - 140 K, while the ZFC curve crosses over the FC curve until ~ 90 K (see inset). The biggest difference from the ground sample is in the ZFC curve behavior below 90 K. The ZFC data instead of going down towards smaller

susceptibility values, after the crossover they show a plateau until ~ 35 K and then they continue rising up to higher susceptibility values, even though they still diverge from the corresponding FC data. A very small cusp at 180 K also still appears.

The isothermal magnetization for both ground (solid line) and crashed pieces (dashed line) samples of YbAuIn measured at 2 K, are given in Figure 4-16(B). For the ground sample the moments are rapidly aligned with the application of very small fields while hysteresis loops appear for both negative and positive fields, confirming the ferromagnetic state of the material. The highest applied field of 55 kG is not enough to saturate the spins and the moment reaches only a value of 0.1 μ_B / mol. The magnetization of the crashed pieces sample (dashed line) displays also a stronger field response at very small fields and a very small hysteresis at higher ones, but at the maximum applied field the moment is very small.

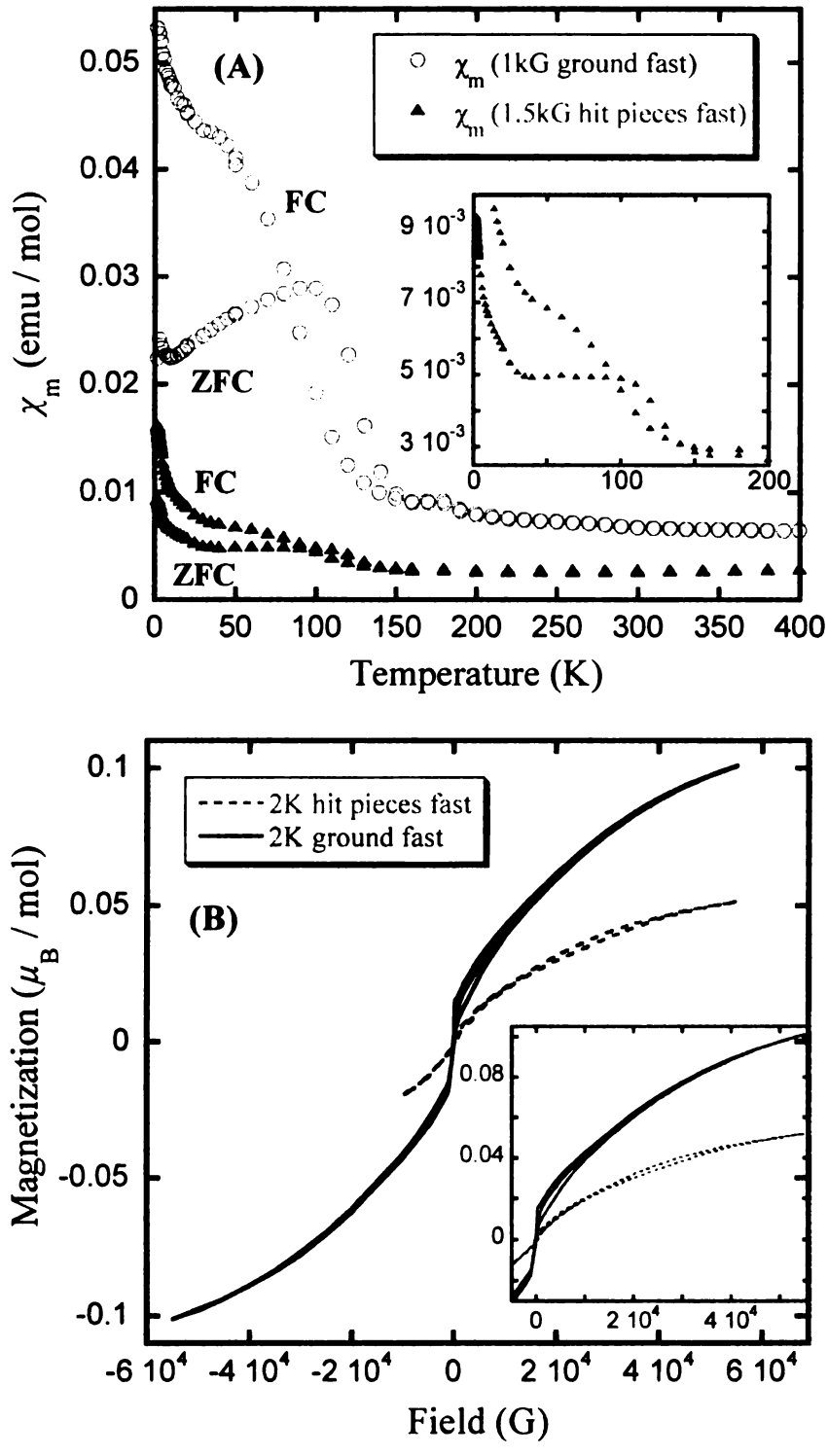

Figure 4-16. (A) Temperature dependence of the molar susceptibility χ_m of YbAuIn of a ground sample and hit pieces one, with applied fields of 1 and 1.5 kG, respectively and fast cooling. Inset shows low temperature data for pieces sample (B) Magnetization data of both samples collected at 2 K and field sweeps between -55 and 55 kG. Inset shows low positive fields region.

In the next measurements we tried to study the difference in the magnetic response of a sample consisted of random compact pieces of YbAuIn crystals as they came out of the reaction vessel without any grinding or crushing and after the pieces were ground in an inert atmosphere of a glove-box. Measurements were performed for both fast cooling (300 to 10 K with 10 - 12 K / min and down to 2 K with 1 K / min rate) and slow cooling (300 to 2 K with 1 K / min rate). During data collection the sweep mode was used with 1 K / min temperature change. The measurements were performed with a PPMS magnetometer (generally smaller sensitivity compare to SQUID measurements.

Unground randomly oriented pieces, slow / fast cooling. Figure 4-17 shows the temperature dependence of the molar susceptibility χ_m of YbAuIn for the sample of randomly oriented pieces for fast (open circles) and slow (solid trigons) cooling rates. For both rates the sample seems to appear as paramagnetic, similar to the behavior for random single crystals of the $Yb_3AuGe_2In_3$ compound, with a much more distinct hysteresis for the fast cooling data.

Light ground crystals inside glove-box, slow / fast cooling. The susceptibility $\chi_m(T)$ data measured again for both fast and slow cooling after the same sample was slightly ground inside a glove-box, are displayed in Figure 4-18. The sample for both cooling rates shows practically the same behavior and exhibits the ferromagnetic transition that was seen in the previous ground samples (inside the glove-box) but some new features are also observed. Comparing to the data given in Figure 4-16(A) (measured at a SQUID), the hysteresis between the ZFC and FC data starts at 180 K, which coincides with the cusp found in the previous measurements and is followed by the ZFC curve crossing over the FC one at ~ 135 K until ~ 90 K. Below this temperature the

curves follow the same behavior as in the ground sample in Figure 4-16(A). Furthermore, we notice a jump in the susceptibility for both cooling rates measurements at about 235 – 240 K, which coincides with the sharp and clear ferromagnetic transition that the ground sample of the $Yb_3AuGe_2In_3$ phase showed when it was measured at very slow cooling as well as data collection temperature rate (Figure 4-13(B)).

Stronger grinding. In order to examine if the strength of the grinding process has any effect on the observed transition, we reground the previous lightly ground sample described in the previous paragraph but this time harder and for longer time. The susceptibility $\chi_m(T)$ data of the reground sample (solid squares) are also presented in Figure 4-18. The reground sample measured under slow cooling rate gave the same qualitative behavior but the susceptibility was increased.

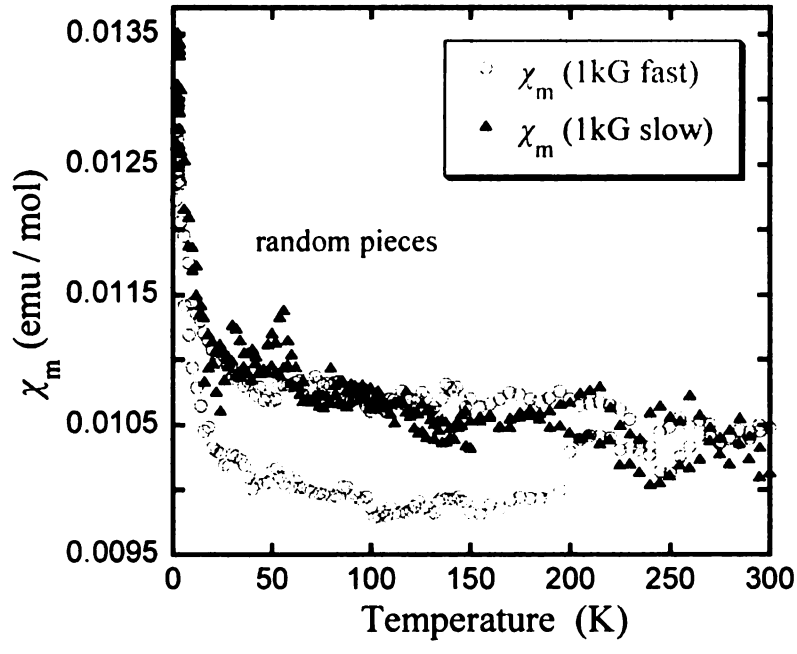

Figure 4-17. Temperature dependence of the molar susceptibility of a sample consisting of randomly oriented pieces for fast and slow cooling rates with 1 kG applied field.

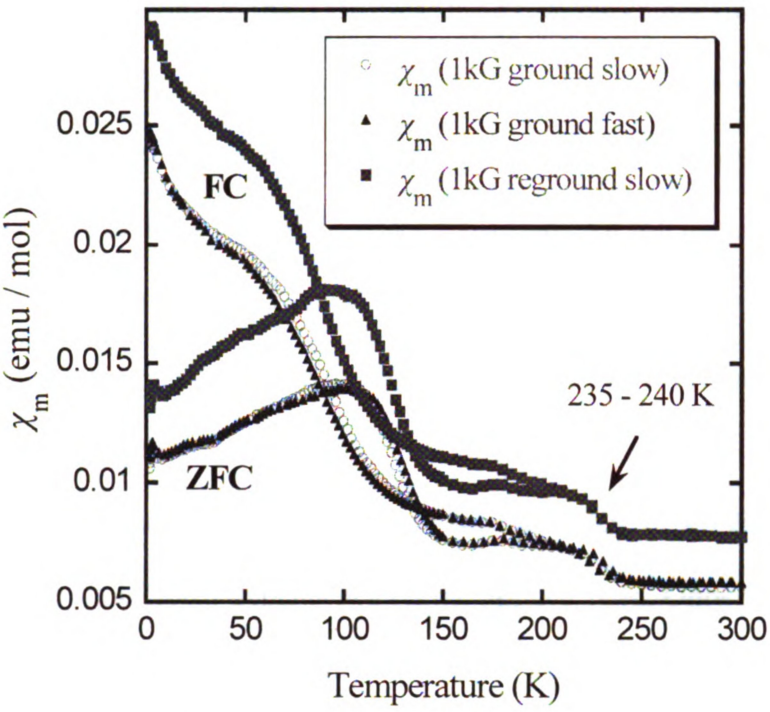

Figure 4-18. Temperature dependence of the molar susceptibility χ_m of YbAuIn sample after it was ground once (slightly) for fast and slow cooling and reground for second time (harder) for slow cooling. The applied field was 1 kG for all measurements.

All ZFC-FC measurements presented up to this point were conducted with initial cooling from room temperature down to 2 K without the application of a field, and then after the field was turned on the ZFC data were collected on warming and the FC data on a consecutive cooling. In the following measurements given in Figure 4-19 and 4-20, we added an additional cycle where data were collected after the FC mode on warming again and these are the field cooled data on warming (FCW).

ZFC, FC, FCW modes. Figure 4-19(A) shows the temperature dependent molar susceptibility $\chi_m(T)$ of the previous reground sample (given in Figure 4-18) of YbAuIn for a cycle consisting of ZFC, FC and FCW data collected with 1 kG applied field and for both slow and fast cooling rates. The ZFC and FC curves remained the same as in the

previous measurement (Figure 4-18). However, the FCW curve does not coincide with the FC one for the whole temperature range but instead displays some irreversibility between ~ 30 and 150 K which is indicative of 1^{st} order transition. So the ferromagnetic ordering is accompanied by a sort of 1^{st} order transition. An interesting observation is also the fact that comparing the ZFC and FCW data both measured on warming there is no crossover of the curves anymore and a hysteresis appears starting at ~ 200 - 210 K when the high temperature hump ends.

Field variation on ground inside glove box samples. In a subsequent step we tried to examine the transition's dependence on the applied field. Only the FC and FCW modes were measured for this experiment with applied fields of 50, 150, 250 and 500 G, Figure 4-19(B). The previous data measured at 1 kG are also plotted again. The data collected at 50 G are generally noisy with very weak moment and there is no obvious transition besides a small hump in between roughly 50 and 150K. When the external field was increased to 150 G, seemed to be enough to induce the main, 1^{st} order type, transition at the temperature range of ~ 30 -150 K. Furthermore, the high temperature feature at 200 – 235 K appears more enhanced comparing to the data collected at 1 kG and the overall susceptibility values are larger. The data measured with 250 G field gave the same picture with a slightly increased χ_m values. When the field was raised to 500 G however, both features at 30 – 150 K and at 200 -235 K started losing in intensity. And then finally, at 1 kG the overall susceptibility is much lower. From this experiment we conclude that both features seem to be field induced and they depend on the strength of the applied field.

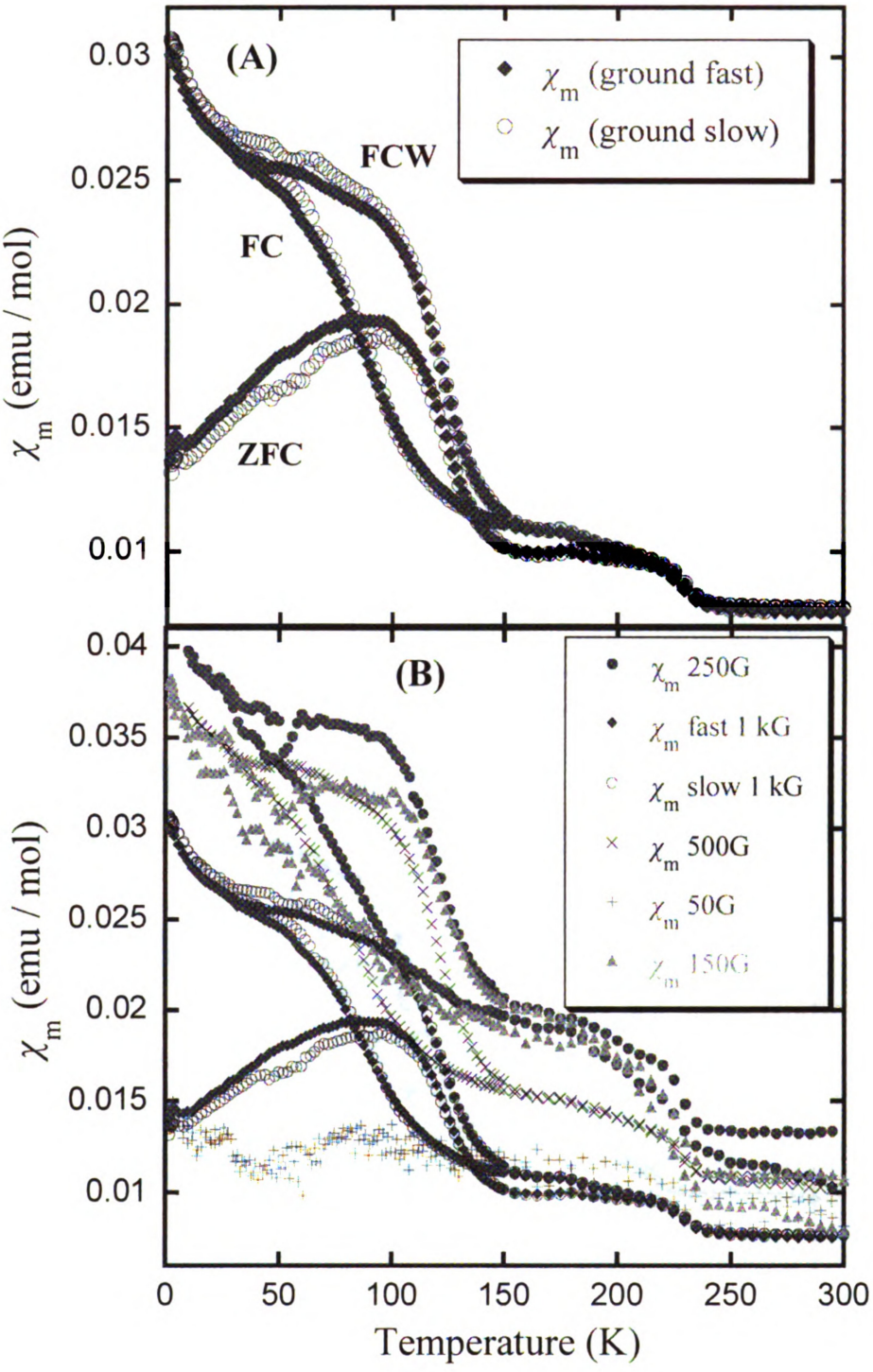

Figure 4-19. Temperature dependence of the molar susceptibility χ_m of a ground sample of YbAuIn of (A) ZFC, FC and FCW modes at 1 kG field (slow / fast cooling) and (B) curves in (A) and additional FC / FCW modes at 50, 150, 250 and 500 G fields.

Pressed pellet. The last measured ground sample was also pressed into a pellet and part of the pellet was measured with 1 kG applied field and with fast cooling rate. The thermal variation of the susceptibility of the pellet is given in Figure 4-20. The corresponding 1 kG data from Figure 4-19 are also plotted for comparison. As in the case of the pellet sample for the $Yb_3AuGe_2In_3$ compound (Figure 4-13), besides the decrease in the susceptibility values, there was no significant change in behavior, comparing to the data before the sample was pressed into pellet. The only qualitative difference that can be observed is that the ZFC curve does not crossover the FC curve significantly any more.

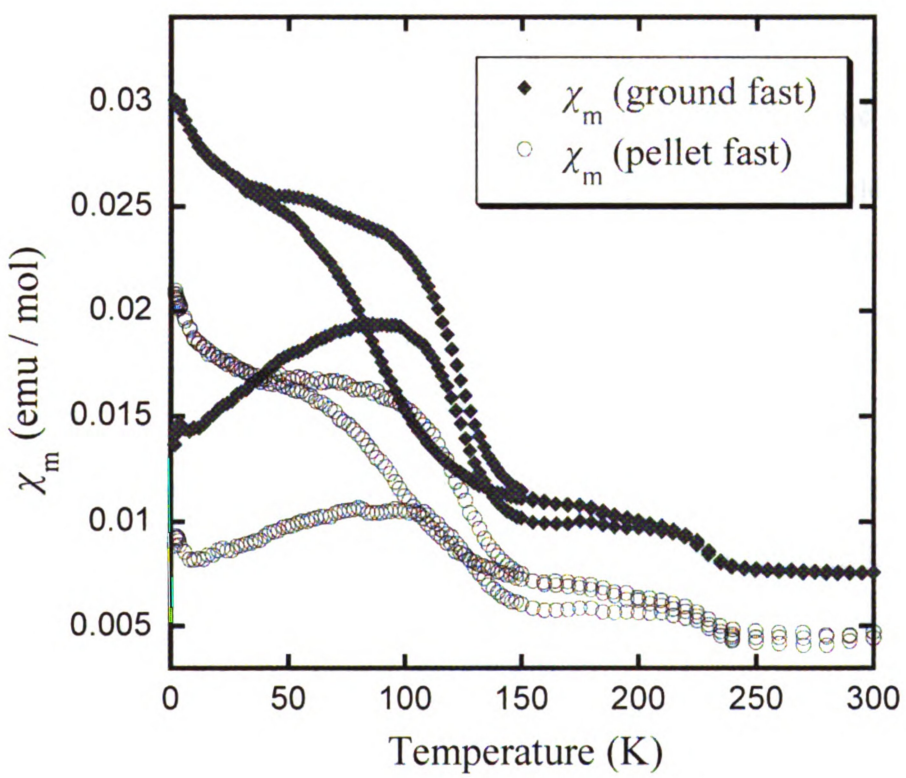

Figure 4-20. Temperature dependence of the molar susceptibility χ_m of a ground sample of YbAuIn and after pressing it into a pellet for ZFC, FC and FCW modes at 1 kG applied field and after fast cooling.

Unground specific oriented pieces. After investigating the magnetic behavior of YbAuIn for ground samples (outside and inside the glove-box) and random pieces the next logical step was to try to align some pieces into a specific orientation. For the following measurements a big compact piece was chosen as a base, and a few more crystals were placed on top of it with the help of a thin layer of high vacuum grease. The pieces were oriented so that the *c*-axis was parallel to the applied field. It should be noted here, that even though care was taken so that the selected compact pieces were consisted of mainly parallel aligned crystals, however within those pieces some variation of the crystals orientation did exist. In other words, the chosen orientation was achieved only in an approximation. Additionally, although the whole composite of the big and smaller pieces was tightly packed inside a gelatin-cup, small movement of the smaller pieces during the various measurements cannot be completely excluded. Magnetic susceptibility measurements for the composite sample were performed for various fields, as well as magnetization measurements at multiple temperatures for both fast and slow cooling rates. These conditions were the same as for the ones described for the previous measurements included in Figures 4-17 – 420.

Slow / fast cooling. Figure 4-21 shows the temperature dependence of the molar magnetic susceptibility $\chi_m(T)$ of the YbAuIn oriented pieces with applied fields of 1 and 5 kG for both fast and slow cooling profiles. Both ZFC and FC modes were measured. As it can be seen more clear in the inset, which contains only the low temperature data, an apparent ferromagnetic like transition appears only for the slow cooling rate for both measured fields of 1 and 5 kG, that starts at ~ 70 and 80 K, respectively. Significant divergence between the ZFC and FC data also occurs after the onset of the transition. The

1 kG data under fast cooling, even though they exhibit a small hysteresis between the ZFC and FC curves below ~ 65 K there is no obvious and sharp transition. A possible weak and broad transition that could start taking place at 65 K could be hindered by the peak at 60 K, which also appears in all the measurements, and is due to an artifact of the PPMS magnetometer used for the experiment.

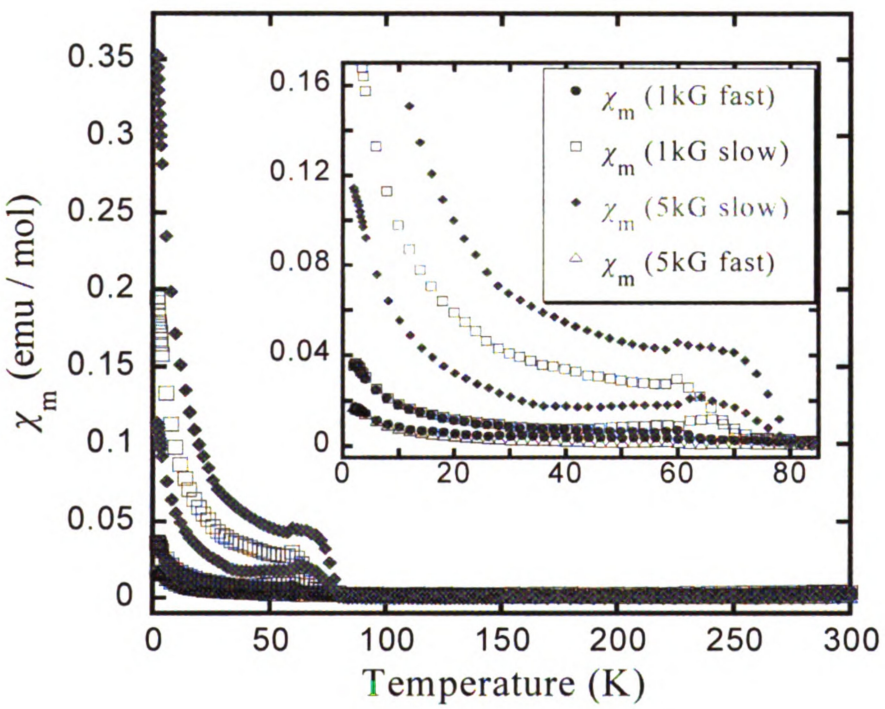

Figure 4-21. Temperature dependence of the molar susceptibility χ_m of YbAuIn of a sample of compact pieces with crystals approximately oriented with *c*-axis parallel to the applied fields of 1 and 5 kG for fast and slow cooling temperature rates.

Magnetization at various temperatures for slow / fast cooling. Magnetization measurements for the same sample at various temperatures and for both slow / fast cooling are given in Figure 4-22. For the temperatures of 2 and 65 K that are measured for both cooling rates we see different response of the moment with the field for each cooling rate. The slow cooling magnetization curve at 2 K increases gradually with the applied field and does not seem to saturate up to 50 kG, where it reaches a magnetization value of 0.25 μ_B / mol. On the other hand in the fast cooling corresponding curve, we see a decrease in the overall moment value and much weaker field dependence, while a field of about 40 kG is enough to start saturating the moments. At 50 kG the magnetization reaches the very small value of 0.068 μ_B / mol. The fast cooling curve at 40 K, which is below the ferromagnetic transition seen in the susceptibility data, shows a small increase of the moment until ~ 2.5 kG and then it stays roughly unchanged with a very small overall moment. Similar picture is observed for the fast cooling data at 100 K, which is above the transition. A weak field dependence until 2 kG is followed by a slightly decreasing moment, which after 5 kG it has a negative value. The slow cooling magnetization data at 65 K, which is within the transition temperature range, exhibits an evident hysteresis loop confirming the ferromagnetic transition observed in the susceptibility data. Additionally, in the increasing field cycle only there seems to be a metamagnetic like transition at ~ 16 kG where the moment starts showing a stronger field dependence, with no signs of saturation up to the highest attainable field, where it reaches a value of 0.23 μ_B / mol. In the fast cooling data at 65 K even though the overall magnetization is much smaller than the slow cooling one, there is still a hysteresis loop

between increasing and decreasing field curves. The magnetization at 50 kG is only 0.039 μ_B / mol, with no observed saturation.

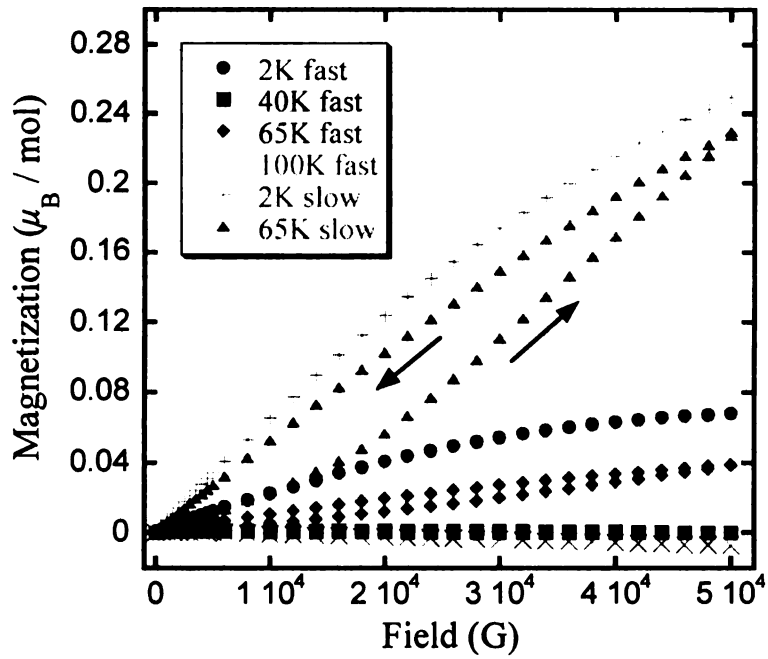

Figure 4-22. Comparison of fast/slow cooling magnetization data at various temperatures for the YbAuIn sample of compact pieces with crystals approximately oriented with *c*-axis parallel.

Magnetization at various temperatures for slow cooling. Complementary field dependent magnetization measurements for the same sample were performed for only the slow cooling rate at additional temperatures, see Figure 4-23. The 2 K data show again a gradual increase of the moment with the field and no saturation up to 70 kG, where it reaches a value of 1.4 μ_B / mol. At 10 K the magnetization increase linearly with the

applied external field and reaches a value of 0.52 μ_B / mol at 56 kG. The magnetization measured at 20 K even though it still responds linearly to the field, surprisingly it reaches higher overall values with almost 1 μ_B / mol at 56 kG. The magnetization curves at the next two temperatures of 30 and 40 K show very small positive or negative values of moment and stay roughly stable, within the sensitivity of the instrument, up to the highest applied field. When the temperature was raised to 50 K, the magnetization started reaching higher positive values with linear response to the field and got a value of 0.38 μ_B / mol at 56 kG of applied field. At 65 K data were collected for a complete cycle, with the field going from positive values to negative ones (not all data included in the plot) and then back to positive. At this temperature a hysteresis loop appears for the positive region of fields, while noticeably after the negative fields region when the field was switched back to positive values the magnetization data did not coincide with the ones collected the first time of positive applied fields. It is worth mentioning at this point, when comparing with the data plotted in Figure 4-22 for the same temperatures the absolute magnetization values are not the same for the same applied fields. This could be possibly due to some sort of a "memory effect" that could arise from the history preceding every measurement, meaning the temperature, the cooling rate and the highest applied field that was used.

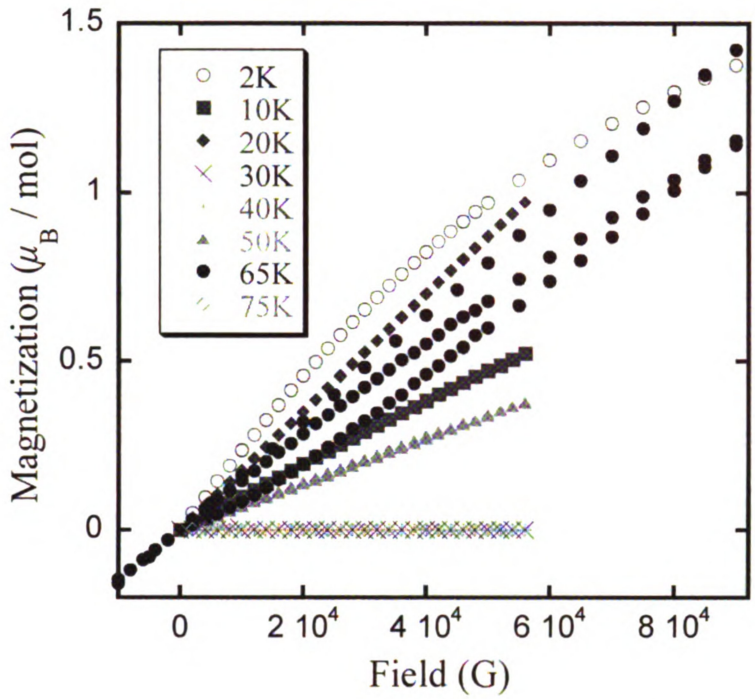

Figure 4-23. Comparison of slow cooling magnetization data at various temperatures for YbAuIn sample of compact pieces with crystals roughly oriented with *c*-axis parallel to applied fields.

From all the measurements described above, we have seen some intriguing features in the magnetic properties of both $Yb_3AuGe_2In_3$ and YbAuIn compounds. For both compounds there are some remarkable differences in the magnetic response among samples consisting of random or oriented crystals and ground samples for which the grounding process was carried out in the open air or in a inert atmosphere of N_2 filled glove-box. The open air ground samples seem to be paramagnetic with a characteristic hysteresis between ZFC and FC data. On the other hand, the inside the glove-box ground

samples exhibit surprisingly a ferromagnetic transition and for most samples the onset of the transition is followed by an unusual ZFC curve crossover of the FC one. This behavior is fully reproducible and it has been observed by measurements performed in various samples and instruments. Furthermore, the strength of the grinding process seems to play a role in the overall amount of the measured magnetic moment. Additionally, the temperature rate of the initial cooling from room temperature down to 2 K as well as during collection time proved to play a decisive role in some cases for the occurrence of the ferromagnetic transition or the temperature that takes place. Unfortunately, at this point we are not able to fully understand and explain the magnetic behavior of the two compounds. Further study of this behavior, with the help of additional experimental techniques are necessary in order to clarify the observed properties.

However, we could perhaps speculate on two possible explanations. In one of them, the two Yb-based compounds would exhibit a flexible and fluctuating Yb valence state, and the application of strain and/or pressure by the grinding process could perhaps induce an increase in the Yb^{3+}/Yb^{2+} ratio that would lead to a new magnetic phase. Alternatively, the two systems could be some sort of dilute spin systems, in which the few existing spins intrinsically are dispersed throughout the crystal and they are not able to see each other, in order to lead in any kind of magnetic ordering, thus behaving as paramagnets. In this case the application of strain and/or pressure could not necessarily lead to an increase of the Yb^{3+} component, but instead force the spins to accumulate in small areas, forming small ferromagnetic domains. In those domains the more concentrated spins could perhaps be able to see each other with the application of a field,

thus leading to a ferromagnetic ordering. Figure 4-24, gives a hypothetical schematic picture for the second suggested theory.

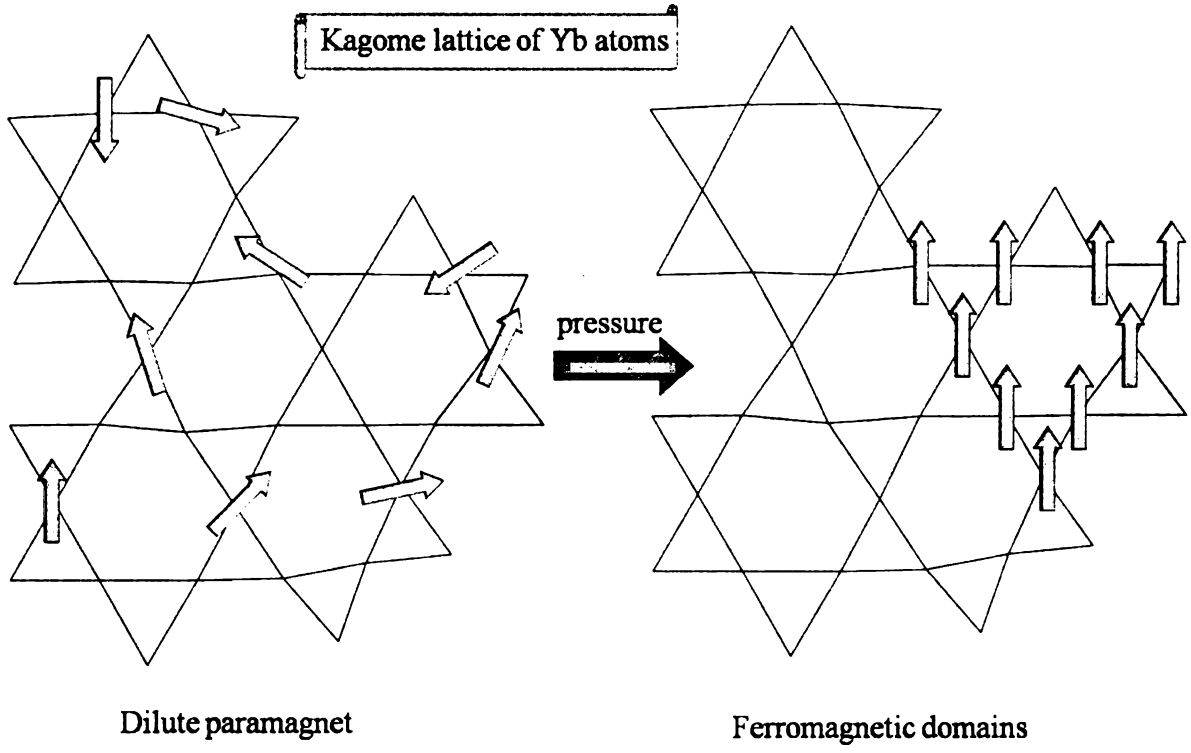

Figure 4-24. Schematic picture of the hypothetical accumulation of spins forming small ferromagnetic domains.

Tables 4-5 and 4-6 summarize the main features observed in the magnetic measurements for $Yb_3AuGe_2In_3$ and YbAuIn, correspondingly.

Table 4-5. Summary of the magnetic behavior for various samples of $Yb_3AuGe_2In_3$.

Sample type	**ZFC / FC hysteresis**	**Magnetic behavior**	**Slow / fast cooling rate effect**	**Grinding strength**
ground in open air	yes	Para-	not tested	not tested
ground in glove-box	yes, below transition	Ferro-	very slow rate higher transition T	stronger grinding → higher moment
random crystals	yes	Para-	Slow → higher μ_{eff}	
oriented crystals (H//c)	no	Para- (low T) Diam- (high T)	not tested	
oriented crystals (H_|_c)	yes	Para-	not tested	

Table 4-6. Summary of the magnetic behavior for various samples of YbAuIn.

Sample type	**Magnetic behavior**	**Slow / fast cooling rate effect**	**Grinding strentgh**
ground in open air	Para-	not tested	not tested
ground in glove-box	Ferro-	Not big difference	stronger grinding → higher moment
random crystals	Para-	Not big difference	
oriented crystals (H // c)	Ferro- Para-	Only slow shows clear transition & big difference in magnetization data	

XANES Measurements at Ambient Pressure:

To further probe the Yb valence state in $Yb_3AuGe_2In_3$ and YbAuIn we performed X-ray absorption measurements at the Yb L_{III}-edge. The near-edge spectra for both compounds obtained at temperatures of ~15 - 18 K and 300 K and at ambient pressure showed no significant difference between the two temperatures, suggesting that the Yb valence remained stable in the measured temperature range. The spectra at 295 and 300 K (room temperature) for $Yb_3AuGe_2In_3$ and YbAuIn, respectively, are given in Figure 4-25. The main absorption peak (white line resonance) of the spectrum for both spectra is centered at ~8941.5 eV, which is attributed to divalent Yb atoms.[84-86] The spectra also revealed the presence of weaker feature (shoulder) at ~8949.5 eV, indicating that some trivalent Yb is also present.[84-86] Since in both compounds under study there is only one unique crystallographic Yb site (as determined by the time scale of diffraction), there could be two plausible scenarios; one in which $Yb_3AuGe_2In_3$ and YbAuIn could be classified as an intermediate valence (*IV*) compounds with all Yb atoms having a non-integer valence, and a second where the materials are heterogeneous mixed-valence (*MV*) compound, in which the Yb atoms alternate between 2+ and 3+ state in various unit cells in the lattice.

The relative amounts of the two electronic configurations were determined by decomposing the normalized Yb XANES into a pair of arc-tangents (representing the edge step) and Lorentzians functions (representing the white line resonance). Fitting of the data with the above technique for $Yb_3AuGe_2In_3$, resulted in ~ 85.2% of Yb^{2+} and ~ 14.8% of Yb^{3+} which leads to an average Yb valence of ~ 2.15. For YbAuIn, similar analysis led to an average Yb valence of ~ 2.22. In the case of the YbAuIn however,

while majority of the Yb is present in the intermetallic state, a careful inspection and analysis of the EXAFS indicates that the sample might also contain ~ 3 - 5% trivalent oxide impurity component. Taking into account the possible presence of an oxide component we determine the intrinsic valence of Yb in YbAuIn to be ~ 2.17. Within the accuracy of the EXAFS technique the $Yb_3AuGe_2In_3$ sample did not show any noticable oxide component. We estimate the uncertainty in the absolute valence to be ~ 5%, arising mainly from correlations between parameters used to represent the edge-step and white line resonances. The Yb^{3+} fraction for $Yb_3AuGe_2In_3$ is consistent with that estimated independently from the magnetic measurements described above.

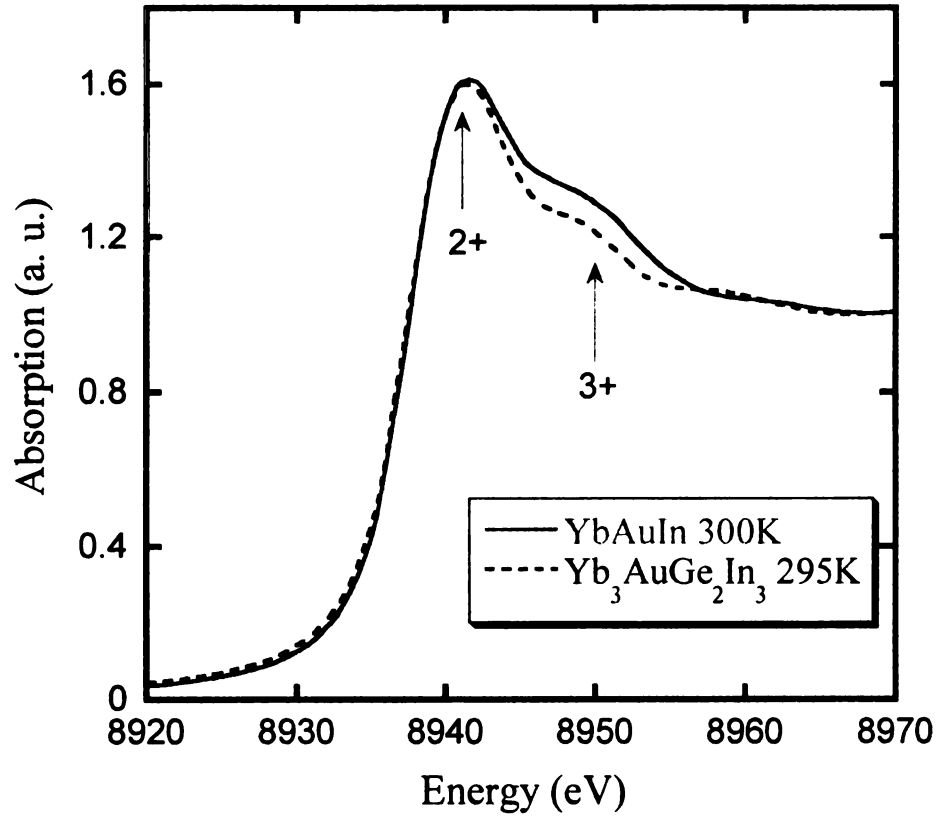

Figure 4-25. L_{III} absorption edge spectra of Yb in $Yb_3AuGe_2In_3$ at 295 K (dashed line) and in YbAuIn at 300 K (solid line).

Magnetotransport measurements:

The $Yb_3AuGe_2In_3$ compound is clearly metallic. The temperature variation of the electrical resistivity $\rho(T)$ of $Yb_3AuGe_2In_3$ between 2.48 and 302.3 K is presented in Figure 4-26. The resistivity data measured on single crystals along the *c*-axis and at zero applied field reveal metallic conductivity with a room temperature resistivity value ρ(300K) of 39.6 $\mu\Omega$ cm. When a magnetic field of 6 Tesla was applied the compound showed no magnetoresistance as it can be seen from the inset in Figure 4-26. In the measured temperature range, the resistivity of $Yb_3AuGe_2In_3$ can be well described by the Bloch – Grüneisen – Mott formula:[91]

$$\rho(T) = \rho_0 + 4R\Theta_D\left(\frac{T}{\Theta_D}\right)^5 \int_0^{\frac{\Theta_D}{T}} \frac{x^5\,dx}{(e^x - 1)(1 - e^{-x})} - KT^3 \qquad (1)$$

where ρ_0 is the residual resistivity, the second term represents electron-phonon scattering, and the third term accounts for Mott's s-d interband electron scattering. The least-squares fitting procedure of (1) yielded the parameters ρ_0 = 29.08 $\mu\Omega$ cm and a Debye temperature Θ_D = 166 K, which is in good agreement with the Θ_D value that was estimated from the specific heat results (see below). The relatively low Θ_D is consistent with the presence of heavy atoms in the structure and suggests a soft lattice.

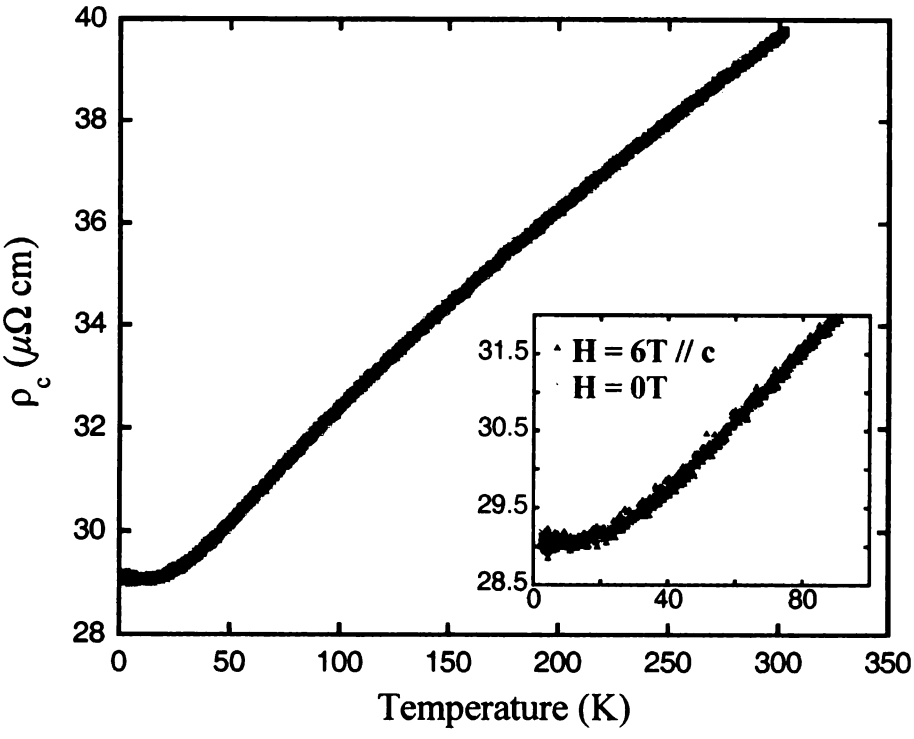

Figure 4-26. Temperature variation of the electrical resistivity $\rho(T)$ of $Yb_3AuGe_2In_3$ from 2.48 to 302.3 K. The dashed line is a fit of the experimental data (squares) to the Bloch – Grüneisen – Mott formula (2). The inset displays the $\rho(T)$ data for zero applied field (empty squares) and for 6 T applied field (solid trigons) for T < 100 K.

The temperature dependent data of the electrical resistivity $\rho(T)$ of YbAuIn measured between 4.2 and 274.3 K and at zero applied field, are given in Figure 4-27. The resistivity data measured on crystals along the *c*-axis reveal a rather moderate metallic behavior with resistivity value ρ(274.3K) of ~ 433 $\mu\Omega$ cm. Attempts to describe the $\rho(T)$ data of YbAuIn with the Bloch – Grüneisen – Mott formula (1) did not result in a successful fit, in contrast with the $Yb_3AuGe_2In_3$. An extra term to the formula perhaps could be required to achieve a good description of the resistivity data for YbAuIn.

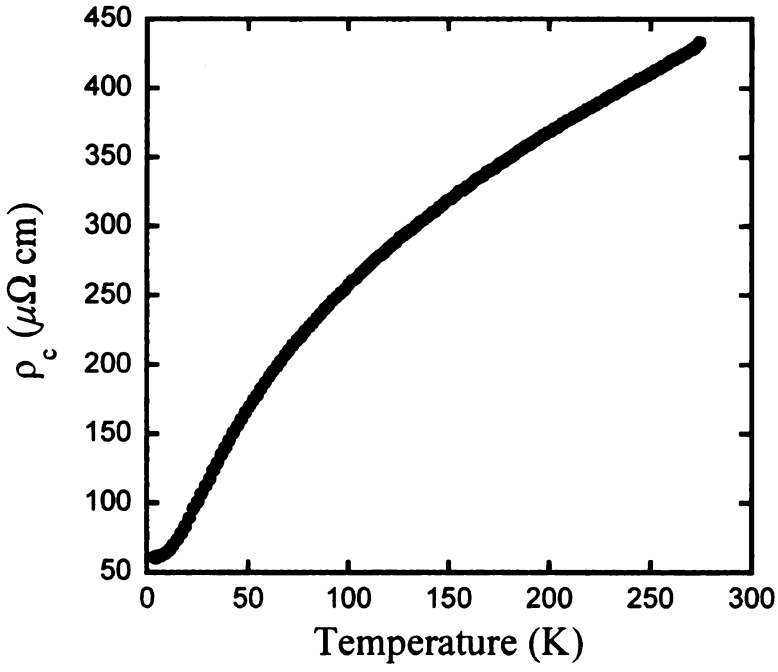

Figure 4-27. Temperature variation of the electrical resistivity $\rho(T)$ of YbAuIn from 4.2 to 274.3 K and at zero applied field.

The temperature dependence of the thermoelectric power (TEP) of $Yb_3AuGe_2In_3$ was measured in the temperature range of 310 – 700 K, Figure 4-28. During the whole temperature range TEP has negative value with a magnitude of -3 μV / K at room temperature (310 K). The negative sign of thermopower, is suggestive of the intermediate valence state of the Yb atoms in $Yb_3AuGe_2In_3$ and agrees with the negative TEP observed in most of the Yb-containing mixed- or intermediate-valent compounds as in YbCuGa[92] and $YbNi_4Si$[93] for example.

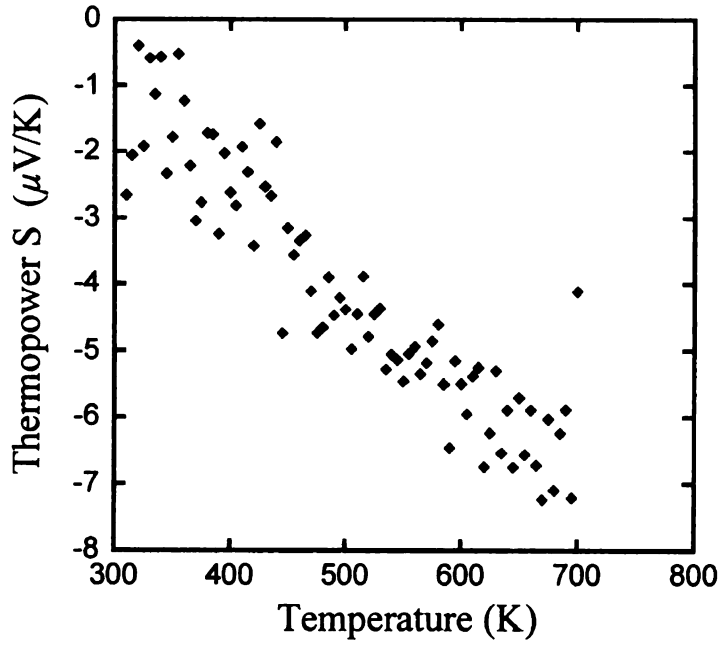

Figure 4-28. The temperature dependence of the thermoelectric power (TEP) of $Yb_3AuGe_2In_3$ measured in the temperature range of 310 – 700 K

Heat Capacity Measurements:

The temperature dependent specific heat from 1.8 to 50 K for $Yb_3AuGe_2In_3$ is shown in Figure 4-29. The data can be described well by a Debye function (2) where the first and second term correspond to the electronic and the phonon contribution, respectively. N is the number of the atoms in the formula unit and $x = \hbar\omega/k_BT$.

$$C_p(T) = \gamma T + 9NR\left(\frac{T}{\Theta_D}\right)^3 \int_0^{\frac{\Theta_D}{T}} \frac{x^4\,dx}{(e^x-1)^2} - KT^3 \qquad (2)$$

A fit to the experimental points resulted in a Debye temperature Θ_D of about 178 K, and an electronic specific heat coefficient $\gamma \approx 31$ mJ / mol K^2, which was determined

from $\gamma (= C_p / T)_{T \to 0}$ at low temperatures. Therefore the compound does not appear to be a heavy-fermion material according to the arbitrary classification of these compounds into "light", "moderate" and classical heavy-fermions with γ values lying in the range of ~ 50-60, 100-400 and > 400 mJ / mol K^2 respectively. Nevertheless, this value of electronic specific heat compares well with the ones found in other mixed valent or intermediate compounds such as the $YbAl_2$,[94] $YbAl_3$,[95] $YbMgCu_4$,[30] $YbNi_4Si$,[93] and $YbInAu_2$[96] in which γ ranges at 15 – 62 mJ / mol K^2.

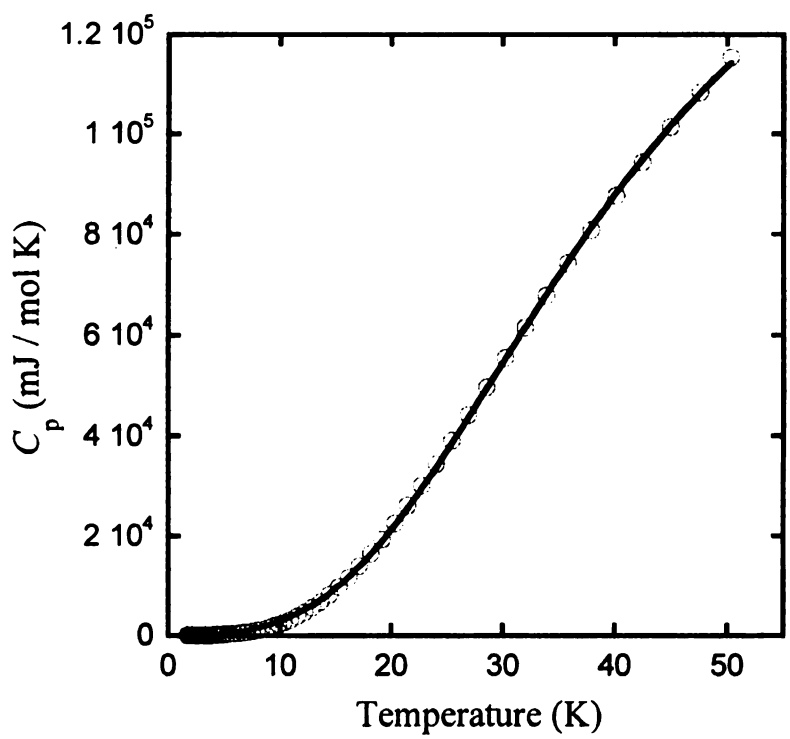

Figure 4-29. Heat capacity (C_p) of $Yb_3AuGe_2In_3$ measured from 1.8 to 50.3K. The experimental data (circles) are fitted with Debye formula (2) (solid line).

The temperature dependent specific heat data measured at a temperature range of 1.8 to 50 K for YbAuIn are shown in Figure 4-30. The data can be also described well by the Debye function (2). A least-square fit to the experimental points resulted in a Debye temperature Θ_D of about 156 K, and an electronic specific heat coefficient $\gamma \approx 84$ mJ / mol K^2, which was determined from $\gamma (= C_p / T)_{T \to 0}$ at low temperatures. According to the arbitrary classification of the heavy-fermion compounds mentioned above, YbAuIn could be classified as "light" heavy-fermion material.

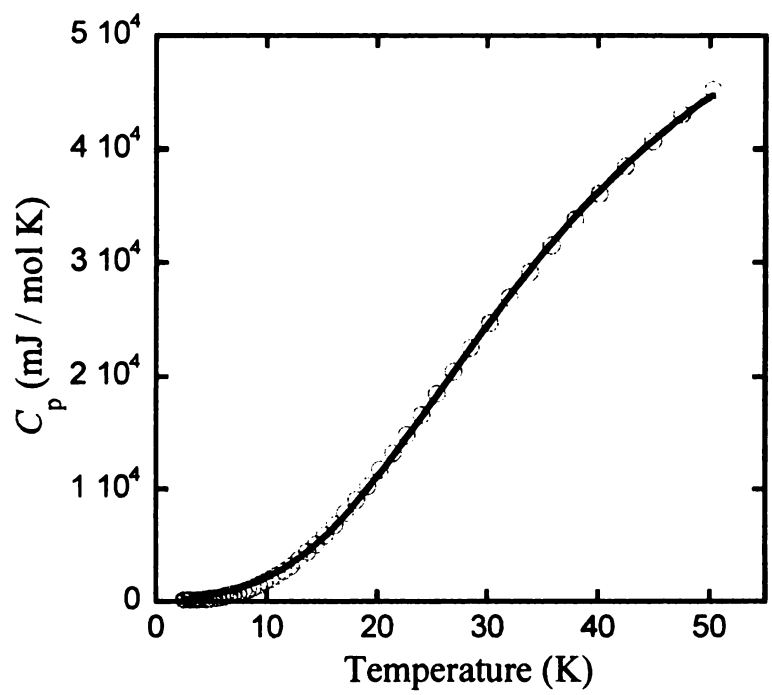

Figure 4-30. Heat capacity (C_p) of YbAuIn measured from 1.8 to 50.3K. The experimental data (circles) are fitted with Debye formula (2) (solid line).

4-4. Conclusions

Single-crystals of the new Yb based quaternary compound, namely $Yb_3AuGe_2In_3$ were grown using an excess of indium as a flux. The flux seems necessary to stabilize this compound since direct combination reactions failed to produce the new phase. $Yb_3AuGe_2In_3$ forms in the hexagonal space group *P*-62*m* as an ordered variant of the YbAuIn structure. YbAuIn was also synthesized for comparison of the structure and measured properties. A modified Curie-Weiss fit to the magnetic susceptibility data gave an estimated effective moment of 0.52 μ_B which is ~ 11% of the value expected for the free-ion Yb^{3+}, 4.54 μ_B. This indicates that the compound contains both Yb^{2+} and Yb^{3+} atoms. In order to clarify this XANES studies were also performed which resulted in 85.2% of Yb^{2+} and 14.8% of Yb^{3+} leading to an average Yb valence of 2.15. The unique crystallographic Yb site in the structure suggests two hypotheses in which $Yb_3AuGe_2In_3$ could be an (*IV*) compound with all Yb atoms having a non-integer valence or that the material is a heterogeneous (*MV*) compound, in which the Yb atoms alternate between 2+ and 3+ state in various unit cells in the lattice. As already stated above, magnetic measurements on various types of samples for both compounds, exhibited significant dependence on the form of the measured sample and other experimental conditions. Random or oriented single crystals samples and samples ground in open air or inside a glove-box, differ remarkably in their magnetic response and vary from being paramagnetic to exhibit ferromagnetic ordering. The intriguing magnetic properties observed for the two compounds are not yet fully understood, although two possible explanations have been suggested. Future work with additional experimental techniques such as neutron diffraction experiments and detailed magnetic measurements under

pressure, are required to further elucidate the reason behind these properties. Nevertheless, our magnetotransport measurements revealed a metallic nature of the compound and negative thermopower which is a common feature of mixed valence Yb compounds. Finally, the heat capacity measurements excluded a heavy-fermion behavior of the material.

References:

(1) Villars, P.; Calvert, L. D. *"Pearson's Handbook of Crystallographic Data for Intermetallic Phases", 2nd ed.; American Society for Metals* OH 44073, 1991.

(2) Kalychak, Ya. M. *J. Alloys Compd.* **1997**, *341*, 262.

(3) Szytoula, A.; Leciejewicz, J. *"Handbook of Crystal Structures and Magnetic Properties of Rare Earth Intermetallics"*; CRC Press: Boca Raton, Fl, 1994.

(4) Rossi, D.; Ferro, R.; Contardi, V.; Marazza, R. *Zeitschrift fuer Metallkunde* **1977**, *68*, 493.

(5) Fujii, H.; Uwatoko, Y.; Akayam, M.; Satch, K.; Maeno, Y.; Fujita, T.; Sakurai, J.; Kamimura, H.; Okamoto, T. *Jpn. J. Appl. Phys.* **1987**, *26*, 549.

(6) Szytula, A.; Penc, B.; Gondek, L. *Acta Physica Polonica A* **2007**, *111*, 475.

(7) Gondek, L.; Szytula, A.; Penc, B.; al, et *J. Magn. Magn. Mater.* **2003**, *262*, L1XX.

(8) Gondek, L.; Penc, B.; Szytula, A.; al., et *Acta Physica Polonica B* **2003**, *34*, 1209.

(9) Mullmann, R.; Mosel, B. D.; Eckert, H.; Kotzyba, G.; Pottgen, R. *J. Solid State Chem.* **1998**, *137*, 174.

(10) Szytula, A.; Bazela, W.; Gondek, L.; Jaworska-Golab, T.; Penc, B.; Stusser, N.; Zygmunt, A. *J. Alloys Compd.* **2002**, *336*, 11.

(11) Zell, W.; Pott, R.; Roden, B.; Wohlleben, D. *Solid State Commun.* **1981**, *40*, 751.

(12) Bauchspiess, K. R.; Boksch, W.; Holland-Moritz, E.; Launois, H.; Pott, R.; Wohlleben, D. *Proc. Int. Conf. on Valence Fluctuations in Solids, St. Barbara, U.S.A.* **1981**.

(13) Pottgen, R. *J. Mater. Chem* **1996**, *6*, 63.

(14) Oesterreicher, H.; Parker, F. T. *Phys. Rev. B* **1977**, *16*, 5009.

(15) Fuse, A.; Nakamoto, G.; Ishimatsu, N.; Kurisu, M. *J. Appl. Phys.* **2006**, *100*, 043712

(16) M. J. Besnus, J. P. Kappler, A. Meyer, J. Sereni, E. Siaud, R. Lahiouel and J. Pierre *J. Physica B, C* **1985** *130B.*

(17) Besnus, M. J.; al, et *J. Less-Common Met.* **1986**, *120*, 101.

(18) Kurisu, M.; Fuse, A.; Nobata, T.; Nakamoto, G. *Physica B* **2000**, *281 & 282*, 147.

(19) Muller, D.; Hussain, S.; Cattaneo, E.; Schneider, H.; Schlabitz, W.; Wohlleben, D. *"Valence Instabilities" edited by P. Wachter and H. Boppart (North-Holland), Amsterdam,* **1982**, 463.

(20) Pottgen, R. *Z. Naturforch B : Chem. Sci* **1994**, *49B*, 1525.

(21) M. Giovannini, E. Bauer, H. Michor, G. Hilscher, A. Galatanu, A. Saccone and P. Rogl *Intermetallics* **2001**, *9.*

(22) ANDRE G, BAZELA W, OLES A, SZYTULA A *JOURNAL OF MAGNETISM AND MAGNETIC MATERIALS* **1992**, *109.*

(23) Felner, I.; Nowik, I. *Phys. Rev. B* **1986**, *33*, 617.

(24) Felner, I.; Nowik, I.; Vaknin, D.; Potzel, U.; Moser, J.; Kalvius, G. M.; Wortmann, G.; Schmiester, G.; Hilscher, G.; Gratz, E.; Schmitzer, C.; Pillmayr, N.; Prasad, K. G.; Waard, H. de; Pinto, H. *Phys. Rev. B* **1987**, *35*, 6956.

(25) Nowik, I.; Felner, I.; Voiron, J.; Beille, J.; Najib, A.; Lachiesserie, E. du Temolet de; Gratz, E. *Phys. Rev. B* **1988**, *37*, 5633.

(26) Sarrao, J. L. *Physica B* **1999**, *259-261*, 128.

(27) Sarrao, J. L.; Immer, C. D.; Fisk, Z.; Booth, C. H.; Figueroa, E.; Lawrence, J. M.; Modler, R.; Cornelius, A. L.; Hundley, M. F.; Kwei, G. H.; Thompson, J. D. *Phys. Rev. B* **1999**, *59*, 6855.

(28) Mushnikov, N. V.; Goto, T.; Rozenfeld, E. V.; Yoshimura, K.; Zhang, W.; Yamada, M.; Kageyama, H. *J. Phys.: Condens. Matter* **2003**, *15*, 2811.

(29) Junhui, H.E.; Tsujii, N.; Yoshimura, K.; Kosuge, K.; Goto, T. *J. Phys. Soc. Jpn* **1997**, *66*, 2481.

(30) Golubkov, A. V.; Parfen'eva, L. S.; Smirnov, I. A.; Misiorek, H.; Mucha, J. *Physics of the Solid State* **2007**, *49*, 2038-2041.

(31) Hoffmann, R.-D.; Pottgen, R.; Rosenhahn, C.; Mosel, B. D.; Kunnen, B.; Kotzyba, G. *J. Solid Sate Chem.* **1999**, *145*, 283.

(32) Galadzhun, Y. V.; Hoffmann, R.-D.; Pottgen, R.; Adam, M. *J. Solid Sate Chem.* **1999**, *148*, 425

(33) Salvador, J. R.; Hoang, K.; Mahanti, S. D.; Kanatzidis, M. G. *Inorg. Chem.* **2007**, *46*, 6933

(34) Hoffmann, R. D.; Pottgen, R.; Zaremba, V. I.; Kalychak, Y. M. *Z. Naturforch B : Chem. Sci* **2000**, *55*, 834.

(35) Kanatzidis, M. G.; Pottgen, R.; Jeitschko, W. *Angewandte Chemie-International Edition* **2005**, *44*, 6996-7023.

(36) Canfield, P. C.; Fisk, Z. *Z. Philos. Mag. B* **1992**, *65*, 1117-1123.

(37) Bud'ko, S. l.; Islam, Z.; Wiener, T. A.; Fisher, I. R.; Lacerda, A. H.; Canfield, P. C. *J. Magn. Magn. Mater.* **1999**, *205*, 53-78.

(38) Fisher, I. R.; Islam, Z.; Canfield, P. C. *J. Magn. Magn. Mater.* **1999**, *202*, 1-10.

(39) Nicklas, M.; Sidorov, V. A.; Borges, H. A.; Pagliuso, P. G.; Petrovic, C.; Fisk, Z.; Sarrao, J. L.; Thompson, and J. D. *Physical Review B* **2004**, *67*, 020506.

(40) Hundley, M. F.; Sarrao, J. L.; Thompson, J. D.; Movshovich, R.; Jaime, M.; Petrovic, C.; Fisk, and Z. *Phys. Rev. B* **2001**, *65*, 024401.

(41) Macaluso, R. T.; Sarrao, J. L.; Moreno, N. O.; Pagliuso, P.G.; Thompson, J. D.; Fronczek, F. R.; Hundley, M. F.; Malinowski, A.; Chan, J. Y. *Chem. Mater.* **2003**, *15*, 1394-1398.

(42) Chen, X. Z.; Sportouch, S.; Sieve, B.; Brazis, P.; Kannewurf, C. R.; Cowen, J. A.; Patschke, R.; Kanatzidis, M. G. *Chem. Mater.* **1998**, *10*, 3202-3211.

(43) B. Sieve; X. Z. Chen; R. Henning; P. Brazis; C. R. Kannewurf; J. A. Cowen; A. J. Schultz; Kanatzidis, M. G. *J. Am. Chem. Soc* **2001**, *123*, 7040.

(44) Chen, X. Z.; Larson, P.; Sportouch, S.; Brazis, P.; Mahanti, S. D.; Kannewurf, C. R.; Kanatzidis, M. G. *Chem. Mater.* **1999**, *11*, 75-83.

(45) Zhuravleva, M. A.; Kanatzidis, M. G. *Z. Naturforch B : Sec. B* **2003**, *58*, 649-657.

(46) Zhuravleva, M. A.; Pcionek, R. J.; Wang, X. P.; Schultz, A. J.; Kanatzidis, M. G. *Inorg. Chem.* **2003**, *42*, 6412-6424.

(47) Zhuravleva, M. A.; Evain, M.; Petricek, V.; Kanatzidis, M. G. *J. Am. Chem. Soc* **2007**, *129*, 3082-3083.

(48) Chen, X. Z.; Small, P.; Sportouch, S.; Zhuravleva, M. ; Brazis, P.; Kannewurf, C. R.; Kanatzidis, M. G. *Chem. Mater.* **2000**, *12*, 2520-2522.

(49) Latturner, S. E.; Bilc, D.; Mahanti, S. D.; Kanatzidis, M. G. *Inorg. Chem.* **2003**, *42*, 7959-7966.

(50) Wu, X. U.; Latturner, S. E.; Kanatzidis, M. G. *Inorg. Chem.* **2006**, *45*, 5358-5366.

(51) Latturner, S. E.; Kanatzidis, M. G. *Inorg. Chem.* **2008**, *47*, 2089-2097.

(52) Latturner, S. E.; Bilc, D.; Mahanti, S. D.; Kanatzidis, M. G. *Chem. Mater.* **2002**, *14*, 1695-1705.

(53) Salvador, J. R.; Gour, J. R.; Bilc, D.; Mahanti, S. D.; Kanatzidis, M. G. *Inorg. Chem.* **2004**, *43*, 1403-1410.

(54) Salvador, J. R.; Bilc, D.; Gour, J. R.; Mahanti, S. D.; Kanatzidis, M. G. *Inorg. Chem.* **2005**, *44*, 8670-8679

(55) Salvador, J. R.; Kanatzidis, M. G. *Inorg. Chem.* **2006**, *45*, 7091-7099.

(56) Chondroudi, M.; Balasubramanian, M.; Welp, U.; Kwok, W.-K.; Kanatzidis, M. G. *Chem. Mater.* **2007**, *19*, 4769-4775.

(57) Bailey, M. S.; McCuire, M. A.; DiSalvo, and F. J. *J. Solid Sate Chem.* **2005**, *178*, 3494-3499.

(58) Benbow, E. M.; Latturner, S. E. *Inorg. Chem.* **2006**, *179*, 3989-3996.

(59) Klunter, W.; Jung, W. *J. Solid Sate Chem.* **2006**, *179*, 2880-2888.

(60) Zaremba, V. I.; Dubenskiy, V. P.; Rodewald, U. C.; Heying, B.; Pottgen, R. *J. Solid State Chem.* **2006**, *179*, 891-897.

(61) Lukachuk, M.; Galadzhun, Y. V.; Zaremba, R. I.; Dzevenko, M. V.; Kalychak, Y. M.; Zaremba, V. I.; Rodewald, U. C.; Pottgen, R. *J. Solid State Chem.* **2005**, *178*, 2724-2733.

(62) Macaluso, R. T.; Sarrao, J. L.; Pagliuso, P.G.; Moreno, N. O.; Goodrich, R. G.; Browne, D. A.; Fronczek, F. R.; Chan, J. Y. *J. Solid Sate Chem.* **2002**, *166*, 245-250.

(63) Kindler, B.; Finsterbusch, D.; Graf, R.; Ritter, F. *Phys. Rev. B* **1994**, *50*, 704.

(64) Bauer, E. *Adv. Phys.* **1991**, *40*, 417.

(65) Wachter, P. *Handbook on the Physics and Chemistry of Rare Earths* **1994**, *(Elsevier Science, Amsterdam)*, 177.

(66) Lawrence, J. M.; Riseborough, P. S.; Park, R. D. *Rep. Progr. Phys.* **1981**, *44*, 1.

(67) Fisk, Z.; Hess, D. W.; Pethick, C. J.; Pines, D.; Smith, J. L.; Thomson, J. D.; Willis, J. O. *Science* **1988**, *239*, 33.

(68) GmbH, STOE & Cie **2006**, D 64295 Darmstadt, Germany.

(69) Bruker *Advanced X-ray Solutions SHELXTL (Version 6.14)*, Bruker AXS Inc., Madison, WI (2003).

(70) Kraft, S.; Stumpel, J.; Becker, P.; Kuetgens, U. *Rev. Sci. Instrum.* **1996**, *67*, 681.

(71) Ravel, B.; Newville, M. *J. Synchrotron Rad.* **2005**, *12:4*, 537-541.

(72) Li, Qing'An; Gray, K. E.; Mitchell, J. F. *Phys. Rev. B* **1999**, *59*, 9357 - 9361.

(73) *Advanced Heat Capacity with Helium-3 Application Note. Physical Property Measurement System Brochure* **1999**.

(74) Yoshida, M.; Akiba, E.; Shimojo, Y.; Morii, Y.; Izumi, F. *J. Alloys Compd.* **1995**, *231*, 755.

(75) S. B. Hendricks and P. R. Kosting *Z. Krist.* **1930**, *74*, 511.

(76) Donohue, J. *"The structures of the elements"*; Wiley: New York, 1974.

(77) Mao, J.-G.; Goodey, J.; Guloy, A.M. *Inorg. Chem.* **2002**, *41*, 931-937.

(78) Mao, J.-G.; Xu, Z.; Guloy, A.M. *Inorg. Chem.* **2001**, *40*, 4472-4477.

(79) Nychyporuk, G.;Zaremba, V.;Kalychak, Ya.M.;Stepien-Damm, J.;Pietraszko, A. *Journal of Alloys Compd.* **2000**, *312*, 154.

(80) Kawamura, H. *J. Phys.: Condens. Matter* **1998**, *10*, 4707-4754.

(81) Yoshida, H.; Ahlert, S.; Jansen, M.; Okamoto, Y.; Yamaura, J.-I.; Hiroi, Z. *J. Phys. Soc. Jpn* **2008**, *77*, 074719.

(82) Ehlers, G.; Maletta, H. *Z. Phys. B* **1996**, *101*, 317 - 327.

(83) Javorsky, P.; Tuan, N.C.; Divis, M.; Havela, L.; Svoboda, P.; Sechovsky, V.; Hilscher, G. *J. Magn. Magn. Mater.* **1995**, *140-144*, 1139.

(84) Rao, C. N. R.; Sarma, D. D.; Sarode, P. R.; Sampathkumaran, E. V.; Gupta, L. C.; Vijayaraghavan, R. *Chemical Physics Letters* **1980**, *76*, 413-415.

(85) Hatwar, T. K.; Nayak, R. M.; Padalia, B. D.; Ghatikar, M. N.; Sampathkumaran, E. V.; Gupta, L. C.; Vijayaraghavan, R. *Solid State Communications* **1980**, *34*, 617-620.

(86) Moreschini, L.; Dallera, C.; Joyce, J. J.; Sarrao, J. L.; Bauer, E. D.; Fritsch, V.; Bobev, S.; Carpene, E.; Huotari, S.; Vanko, G.; Monaco, G.; Lacovig, P.; Panaccione, G.; Fondacaro, A.; Paolicelli, G.; Torelli, P.; Grioni, M. *Physical Review B* **2007**, *75*.

(87) Johansson, B.; Rosengren, A. *Phys. Rev. B* **1975**, *11*, 2836.

(88) Dallera, C.; Wessely, O.; Colarieti-Tosti, M.; Eriksson, O.; Ahuja, R.; Johansson, B.; Katsnelson, M. I.; Annese, E.; Rueff, J. P.; Vanko, G.; Braicovich, L.; Grioni, M. *Physical Review B* **2006**, *74*, 4.

(89) Lubbers, R.; Dumschat, J.; Wortmann, G.; Bauer, E. *J. Phys. IV France* **1997**, *7*, C2-1021.

(90) Dallera, C.; Annese, E.; Rueff, J. P.; Palenzona, A.; Vanko, G.; Braicovich, L.; Shukla, A.; Grioni, M. *J. Electron Spectrosc. Relat. Phenom.* **2004**, *137-40*, 651-655.

(91) Mott, N. F.; Jones, H. *"The Theory of the Properties of Metals and Alloys"* Oxford University Press: New York, 1958; Vol. p. 240.

(92) Androja, D. T.; Malik, S. K.; Padalia, B. D.; Bhatia, S. N.; Walia, R.; Vijayaraghvan, R. *Phys. Rev. B* **1990**, *42*, 2700.

(93) Kowalczyk, A.; Falkowski, M.; Tolinski, T.; Tran, V. H.; Miiller, W.; Reiffers, M.; Timko, M. *Materials Research Bulletin* **2008**, *43*, 185.

(94) Gorlach, T.; Pfleiderer, C.; Grube, K.; Lohneysen, H.v. *Phys. Rev. B* **2005**, *71*, 033101.

(95) Klaasse, J. C. P.; Boer, F. R. de; Chatel, P. F. de *Phys. B* **1981**, *106*, 178.

(96) Tsujii, N.; Yoshimura, K; Kosuge, K. *J. Phys.: Condens. Matter* **2003**, *15*, 1993.

EXPLORATORY SYNTHESIS OF COMPLEX INTERMETALLIC GERMANIDES AND INDIDES USING MOLTEN INDIUM AS A FLUX

VOLUME II

By

Maria Chondroudi

A DISSERTATION

Submitted to
Michigan State University
in partial fulfillment of the requirements
for the degree of

DOCTOR OF PHILOSOPHY

Chemistry

2009

CHAPTER 5

CeAuGeIn and $EuAuGeIn_2$: New Quaternary Intermetallics Grown from Indium flux

PART I. Synthesis and Characterization of CeAuGeIn: Exhibiting Complicated Magnetic Structure

5-I-1. Introduction

Intermetallic compounds of the ternary systems RE/TM/X (*RE* = rare earth metal, *TM* = transition metal and *X* = *p*-block element) include numerous new intermetallic phases that exhibit rich structural variety[1,2] and interesting physical properties[3] and have been extensively investigated in the last few decades. Particularly, intermetallics of Ce, Yb and sometimes Eu continue to attract much experimental and theoretical interest owing to a large variety of unusual ground states that often lead to remarkable electrical and physical properties.[3,4] It is generally believed that, the stability of different ground states depends strongly on the hybridization (interaction) strength between the magnetic 4*f* electrons and the conduction band electrons.[5-7] The intriguing physical phenomena that particularly Ce-based compounds often exhibit include heavy fermion (*HF*) systems,[7-14] superconductivity and their coexistence,[15] ambient and pressure induced superconductivity,[16-20] kondo lattices,[15,21] magnetic ordering with low[8,21] and anomalously high ordering temperatures,[22] mixed valence (*MV*) or valence fluctuating behavior,[23-26] and non-Fermi-liquid (NFL) behavior.[27,28] A recent review includes a series of experiments performed on strongly correlated electron phenomena in f-electrons materials in the past few decades.[29]

The reason for such diversity in ground states that lead to these phenomena is a delicate interplay between two competing mechanisms: the long range Ruderman-Kittel-Kasuya-Yosida (RKKY) indirect interactions and the Kondo effect.[29-32] These two mechanisms are mainly governed by the strength of the $4f$ - conduction electrons hybridization, measured by the exchange integral J_{KF}. For low J_{KF} values, the RKKY interaction dominates and thus long-range magnetic ordering (*LMO*) of the localized Ce magnetic moments can occur (with magnetic ground state (*GS*) characterized by the temperature T_{RKKY}). For higher J_{KF} values on the other hand, the Kondo interaction leads to the suppression of Ce 4f moments resulting in a nonmagnetic (*GS*), with a characteristic temperature T_K. Finally, for large J_{KF}, an intermediate-valence (*IV*) state is expected, in which the f electrons are only partially localized. Heavy-fermion (*HF*) behavior is often observed at the borderline between the (*LMO*) and (*IV*) regions.

In a recent review, it has been demonstrated that molten metal fluxes, particularly Al and Ga, are excellent preparative tools for the exploratory synthesis of new intermetallic compounds.[33] After our own successful work with Al and Ga fluxes in the systems RE/TM/Al/Si or Ge and RE/TM/Ga/Ge or Si,[34-43] we have lately extended this work to include molten In as a solvent in analogous systems.[44-48] Our early investigations in the scheme RE/TM/In/Ge indicated that, as in the case of Ga/Si system, it is difficult to readily produce quaternary phases. However, under careful control of the experimental conditions we have been able to isolate a number of novel quaternary phases which include the $RE_4Ni_2InGe_4$,[45] $RE_7Co_4InGe_{12}$,[48] $Dy_4CoInGe_4$ and $Yb_3AuGe_2In_3$ which are described in Chapters 3 and 4, respectively.

After the rich chemistry revealed by the thorough examination of the ternary RE/Au/In system[49] and in combination with the intriguing magnetic properties exhibited by the $Yb_3AuGe_2In_3$ compound (P-62m space group, YbAuIn structure type, see Chapter 4) and the various remarkable physical phenomena observed in many Ce and Eu intermetallics, we explored the systems Ce(Eu)/Au/Ge/In. Interestingly, none of them resulted in an analog of the $Yb_3AuGe_2In_3$ phase, but instead the substitution of the Yb metal by Ce and Eu led to the new quaternary phases of CeAuGeIn and $EuAuGeIn_2$. Each of the two new compounds crystallizes in a different structure type, however as it will be described below are closely related. Here we present the CeAuGeIn, grown from In flux which crystallizes in the orthorhombic space group *Cmcm* with the $CeNiSi_2$ structure type.[50,51] The synthesis, crystal structure, and the study of the magnetic properties, electrical resistivity and X-ray absorption near edge spectroscopy (XANES) are reported. These studies suggest that in CeAuGeIn the Ce atom exists in a trivalent state that leads to both antiferromagnetic and ferromagnetic ordering of the Ce^{3+} magnetic moments. The synthesis and characterization of $EuAuGeIn_2$ will be described in the second part of this chapter.

5-I-2. Experimental section

Reagents:

The following reagents were used as purchased without further purification: Ce, (in the form of powder ground from metal lump, 99.9% Atlantic Equipment Engineers, Bergenfield, N.J.), Au (pieces, 99.9% Alfa Aesar, Ward Hill, MA), Ge (~100 mesh,

99.999% , Cerac, Milwaukee, WI) and In (tear drops 99.99% Plasmaterials, Livermore, CA).

Synthesis:

Method A. CeAuGeIn was obtained by combining 3 mmol of the cerium metal, 2 mmol gold, 3 mmol germanium and 15 mmol In in an Al_2O_3 (alumina) crucible under an inert nitrogen atmosphere inside a glove-box. The crucible was placed in a 13 mm fused silica tube, which was flame sealed under vacuum of 10^{-4} Torr, to prevent oxidation during heating. The reactants were then heated to 1000 ^{0}C over 12 h, maintained at that temperature for 5 h to allow proper homogenization, followed by cooling to 850 ^{0}C in 2 h and held there for 48 h. Finally, the system was allowed to slowly cool to 50 ^{0}C in 48 h. The reaction product was isolated from the excess In flux by heating at 350 ^{0}C and subsequent centrifugation through a coarse frit. Any remaining flux was removed by immersion and soniqation in glacial acetic acid for 48 - 72 h. The final crystalline product was rinsed with water and dried with acetone. This method produced the target compound with ~ 85 – 90 % purity and in a yield of ~ 85 % based on the initial amount of Ce metal used in the reaction. Main side products were small amounts of $CeAu_2In_4$[46] compound and unreacted In metal. CeAuGeIn crystals form as sort of compressed on one direction rectangular prisms (or cuboids), with some elongated into a rod-like shape, and in the majority they tend to grow together in layers forming irregular shaped disk-like (or platelet-like) compact pieces, see Figure 5-I-1. Several pieces and single crystals were carefully selected for elemental analysis, structure characterization, and the physical measurements reported here.

Method B. CeAuGeIn was also obtained by combining 6 mmol of the cerium metal, 2 mmol gold, 4 mmol germanium and 20 mmol In in an Al_2O_3 (alumina) crucible under an inert nitrogen atmosphere inside a glove-box. The crucible was placed in a 15 mm fused silica tube, which was flame sealed under vacuum of 10^{-4} Torr, to prevent oxidation during heating. The reactants were then heated to 1000 ^{0}C over 12 h, maintained at that temperature for 24 h to allow proper homogenization, followed by cooling to 850 ^{0}C in 2 h and held there for 48 h. Finally, the system was allowed to slowly cool to 50 ^{0}C in 48 h. Under the same heating profile reactions with the reactants ratio used in method A were also performed. This method produced more rod-shaped crystals (and slightly longer) but the yield in the target phase was reduced since additional byproducts were found. Besides the $CeAu_2In_4$ compound, additional phases were formed which EDS analysis gave as roughly $Ce_{1.8}Au_4Ge_1In_{4.6}$ needles and very small amounts of $AuIn_2$ polyhedra and $Ce_xAu_yGe_z$ thin plates.

Elemental Analysis:

Semi-quantitative microprobe elemental analysis was performed on several crystals of the compound using a HITACHI MODEL S-2700 Scanning Electron Microscope (SEM) equipped with a light-element window Noran System Six EDS detector, at the Materials Science Division (MSD) facilities at Argonne National Laboratory (MSD). Data were acquired by applying a 20 kV accelerating voltage and an acquisition time of 1 min. The EDS analysis gave an average atomic composition of 23 % Ce, 23 % Au, 28 % Ge and 26 % In, which is in very good agreement with the single crystal X-ray diffraction results.

X-ray Crystallography:

The X-ray intensity data were collected at room temperature using a STOE IPDS 2T (with additional capability of 2θ swing of the detector) diffractometer with graphite-monochromatized Mo Kα (λ = 0.71073 Å) radiation. The X-AREA (and X-RED and X-SHAPE within) package suite[52] was used for data extraction and integration and to apply empirical and analytical absorption corrections. The structure of CeAuGeIn single crystals were solved by direct methods and refined with the SHELXTL package of programs.[53] A stable refinement was accomplished only in the hexagonal space group *Cmcm*. The initial refinement resulted in R_1 / wR_2 values (all data) of 0.0429 / 0.08854 which suggest satisfactory refinement, but the U^{22} anisotropic displacement parameter was too low for all atoms, with values of 0(1) / 1(1) / 2(1) / 0(1) for Au / Ce / In / Ge, correspondingly. Additional crystal symmetry was not suggested when the PLATON-Addsym application of the WinGX package software,[54] was performed. Attempts to perform only analytical absorption corrections (without face indexed absorption corrections) through XABS application of WinGX package software did not help the U^{22} parameters. The U^{22} values improved when some small, probably wrong faces were removed from the crystal description and consecutively successful face indexed absorption corrections were applied. The face corrections resulted in better R_1 / wR_2 and U^{22} values in the following tables. The final data collection and structure refinement details are given in Table 5-I-1. The final atomic positions, equivalent isotropic displacement parameters and anisotropic displacement parameters are listed in Tables 5-I-2 and 5-I-3.

Table 5-I-1. Crystal data and structure refinement data for CeAuGeIn.

Empirical formula	CeAuGeIn	
Formula weight	1048.99	
Temperature (K)	293(2)	
Wavelength (Å)	0.71073	
Crystal system	Orthorhombic	
Space group	*Cmcm*	
a (Å)	4.3215(9)	$\alpha = 90^{o}$
b (Å)	19.176(4)	$\beta = 90^{o}$
c (Å)	4.4259(9)	$\gamma = 90^{o}$
V (Å^3) / Z	366.77(13) / 2	
Density$_{calc}$ (Mg/m^3)	9.498	
Absorption coefficient (mm^{-1}) / F(000)	66.101 / 872	
θ range for data collection (^{o})	4.84 to 34.38	
Index ranges	$-6 \le h \le 6$ $-30 \le k \le 29$ $-7 \le l \le 6$	
Reflections collected / unique / *R*(int)	2332 / 463 / 0.0893	
Completeness to θ (%)	98.7	
Data / restraints / parameters	463 / 0 / 18	
Refinement method	Full-matrix least- squares on F^2	
Goodness-of-fit on F^2	1.231	
Final R indices [$I>2\sigma(I)$] (R_1 / wR_2)^a	0.0372 / 0.0736	
R indices (all data) (R_1 / wR_2)^a	0.0386 / 0.0740	
Extinction coefficient	0.00124(17)	
Largest diff. peak and hole (e. Å^{-3})	4.010 and -4.224	

$$^{a}R_1 = \Sigma\left\|F_o\right| - \left|F_c\right\| / \Sigma\left|F_o\right|;\ wR_2 = \left[\Sigma w\left\{\left|F_o\right| - \left|F_c\right|\right\}^2 / \Sigma w\left|F_o\right|^2\right]^{1/2};\ w = 1/\sigma^2\left\{\left|F_o\right|\right\}$$

Table 5-I-2. Atomic coordinates (x 10^4) and equivalent isotropic displacement parameters ($Å^2$ x 10^3) for CeAuGeIn.

Atom	Wyckoff	x	y	z	U(eq)[a]
Ce	4c	-5000	948(1)	-2500	7(1)
Au	4c	0	1597(1)	2500	9(1)
In	4c	0	2484(1)	-2500	8(1)
Ge	4c	0	310(1)	2500	12(1)

[a]U(eq) is defined as one third of the trace of the orthogonalized U^{ij} tensor.

Table 5-I-3. Anisotropic displacement parameters ($Å^2$ x 10^3) for CeAuGeIn. The anisotropic displacement factor exponent takes the form: $-2\pi^2[h^2a^{*2}U^{11} + ... +2hka^*b^*U^{12}]$

Atom	U^{11}	U^{22}	U^{33}	U^{23}	U^{13}	U^{12}
Ce	6(1)	7(1)	9(1)	0	0	0
Au	10(1)	6(1)	11(1)	0	0	0
In	6(1)	9(1)	8(1)	0	0	0
Ge	19(1)	5(1)	10(1)	0	0	0

Magnetic Measurements:

Magnetization measurements for CeAuGeIn were conducted using a Quantum Design PPMS magnetometer at Materials Science Division (MSD) facilities at Argonne National Laboratory (ANL). For these measurements crystals of CeAuGeIn were soaked in glacial acetic acid and soniqated for 24 – 48 hrs, washed out with dried acetone and dried under the flow of nitrogen. Subsequently, crystals were loaded randomly without grounding into gelatin capsules, mounted in a plastic straw and affixed to the end of a carbon fiber rod. Temperature dependence data were collected between 2 and 300 K, for both zero field cooled (ZFC) and field cooled mode (FC) with applied fields of 0.3 and 1 kG. A typical measurement consists of initial cooling from room temperature (300 K) down to 2 K with no applied field, then the selected field is turned on and the ZFC data are collected on warming, followed with the collection of the FC data on cooling back to 2 K and with the applied field still on. Field dependent magnetic measurements were acquired at 2, 8, 11 and 60 K with field sweeping from 0 up to 62 kG.

Additional low field magnetic measurements were performed with a commercial Low field SQUID magnetometer,[55] located also in the MSD facilities of ANL, in the temperature range of 1.3 - 35 K, with applied fields of 5 and 50 G for ZFC and FC modes. In a typical measurement the temperature from 35 K is cooled down to 1.3 K under zero field. Then the field is turned on and the ZFC data are collected on warming. Consecutively, the temperature is cooled down to 1.3 K with the field on and then the FC data are also measured on warming. For these measurements, a piece consisting of parallel in approximation grown crystals was aligned with the *b*-axis parallel and normal

sy

Re

in

Ar

hy

by

fou

K.

X-ra

in Se

Sour

and a

cham

rays w

was ca

eV.[" A

The Ce

and stac

to the external applied field to examine possible magnetic anisotropy in the measured system.

Resistivity:

For CeAuGeIn electrical resistivity was determined using a four probe technique in a standard ^{4}He gas flow cryostat, at Materials Science Division (MSD) facilities at Argonne National Laboratory (ANL). Heating was avoided by reducing the current, and hysteresis, caused by slight thermometer - sample temperature differences, was avoided by sweeping the temperature slowly. More detailed experimental description can be found elsewhere.[56] Data points were taken during the cooling cycle from 108 K to 1.58 K.

X-ray absorption near edge spectroscopy (XANES):

X-ray absorption near edge spectroscopy (XANES) experiments were performed in Sector 20, bending magnet beamline (PNC/XOR, 20-BM) of the Advanced Photon Source at the Argonne National Laboratory, IL, USA. Measurements at the Ce L_{III}-edge and at ambient pressure were performed in the transmission mode using gas ionization chambers to monitor the incident and transmitted X-ray intensities. Monochromatic X-rays were obtained using a Si (111) double crystal monochromator. The monochromator was calibrated by defining the inflection point (first derivative maxima) of Cr foil as 5989 eV.[57] A rhodium-coated X-ray mirror was utilized to suppress higher order harmonics. The CeAuGeIn samples were prepared by dusting finely ground samples on Kapton tape and stacking around 4 layers together. Sample preparation procedures were carried out

inside a glove box environment. Measurements were performed at a range of temperatures from 16 K to 300 K using a closed cycle refrigerator. Data reduction and analysis were performed using the Athena software developed by Newville and Ravel.[58] Care was taken to minimize thickness effects in the measurements.

5-I-3. Results and Discussion

Reaction Chemistry:

The compound CeAuGeIn was first discovered in a reaction that was initially designed to form the Ce analog of the $Yb_3AuGe_2In_3$ phase, described in Chapter 4. This result, reinforces and generalizes the suggestion made in Chapter 2 where we saw that only a few RE atoms formed the $RE_7Co_4InGe_{12}$ phase that, the size of the rare-earth cations likely plays a decisive role for the formation of generally quaternary phases in the system RE/TM/Ge/In, when the In-flux method is used. Furthermore, the synthesis of CeAuGeIn is yet another example which demonstrates the ability of liquid In to act as a reactive flux in reactions containing group 14 elements. Nevertheless, CeAuGeIn crystals form as a sort of compressed rectangular prisms (or cuboids), with some being elongated into a rod-like shape, and in the majority they tend to grow together in layers forming irregular shaped disk-like (or platelet-like) compact pieces. Main reaction byproducts were unreacted In flux and small amounts of mainly clustered needles of $CeAu_2In_4$ compound[46] which, due to their very different crystal morphology were easily distinguishable. Figure 5-I-1 shows scanning electron micrographs of typical single crystals as well as aggregates of CeAuGeIn crystals.

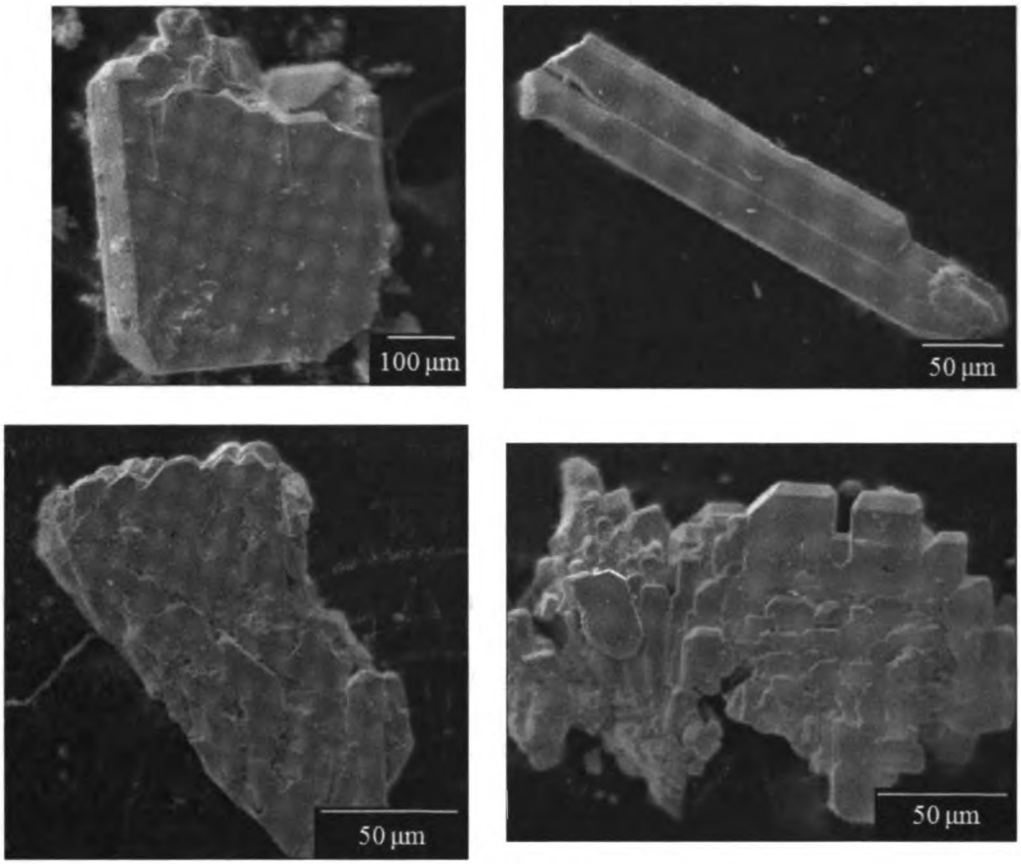

Figure 5-I-1. Scanning Electron micrograph (SEM) images of flux-grown single crystals as well as aggregates of CeAuGeIn crystals.

Structure:

The new intermetallic CeAuGeIn compound, crystallizes in the orthorhombic space group *Cmcm* with the $CeNiSi_2$ structure type.[50,51] CeAuGeIn is an ordered quaternary variant of this ternary phase, with the Ce and Au atoms occupying the Ce and Ni positions, respectively, and In and Ge adopting the Si sites. The overall structure of CeAuGeIn as viewed down the *a*-axis is illustrated in Figure 5-I-2. The bonds to the Ce

its

lay

In-

Cr

for

tw

tetr

she

alte

ove

at 2

thar

inter

Au-

desc

emp

interr

respe

along

longer

atoms were omitted to emphasize the three-dimensional (3D) [AuGeIn] framework and its channels. In CeAuGeIn, all of the Ce, Au, In and Ge atoms are located in alternating layers stacked along the along *b*-axis in the sequence: Ce-Au-In-Au-Ce-Ge-Ge-Ce-Au-In-Au-Ce. The structure can also be described as an intergrowth of distorted PbO- and CrB-type layers,[59-62] (see Figure 5-I-2) with the Ce atoms residing within the channels formed by the connection of the two layers, see Figure 5-I-3. Detailed descriptions of the two structural fragments are given below.

The distorted PbO-type slab contains the Au and In atoms. In this, the tetrahedrally coordinated (by 4 Au atoms) In atoms form a 2-dimensional (2D) quadratic sheet that extends in the *ac*-plane (see Figure 5-I-4(A),(C)) and is capped by Au atoms alternatively above and below this plane (Figure 5-I-(C)), thus forming a puckered overall layer, see Figure 5-I-4(B). There are two different Au-In bonds. The longer one is at 2.7912(8) Å and the shorter one is at 2.7884(8) Å. Both distances are slightly shorter than the sum of the covalent radii of 2.85 Å (R_{Au} + R_{In}),[63] indicating strong Au-In interactions within the layer. The Au-In bonds in CeAuGeIn seem to be stronger than the Au-In bonds (at 2.8634(13) Å) found in the quaternary $Yb_3AuGe_2In_3$ compound, described in chapter 4, and which was formed under similar reaction conditions when the employed RE was Yb. The Au-In bonds however, agree well with other Ce containing intermetallic compounds as in $Ce_2Au_3In_5$[64] and $CeAu_2In_4$[46] for example.

The CrB-type layer is composed of Ce and Ge atoms in the Cr and B positions, respectively. In this, the Ge atoms form one dimensional (1D) zigzag chains propagating along the *c*-axis, Figure 5-I-2. The Ge – Ge bonds are at 2.5127(16) Å which is slightly longer than the Ge – Ge distances found in the elemental diamond-like Ge structure (2.45

int

RE

Ce

Au

con

ther

laye

aton

1 Au

inte

3.65

to A

arra

All (

comp

R_{XJ}.[6]

Å). Nevertheless, this distance compares well to other Ge – Ge bonds found in intermetallics as the ones in β-$RENiGe_2$,[44] which average at 2.495 Å and in $RE_4Ni_2InGe_4$[45] at 2.490 Å but they are shorter than the ones found in the isostructural $CeNiGe_2$[65] which range at 2.543 - 2.984 Å.

The In square sheets and Ge zigzag chains, described above, are bridged by the Au atoms along the *b*-axis thus building the 3D [AuGeIn] open framework. The connection of the two layers creates channels that extend down the *c*-axis, and each of them accommodates a pair of Ce columns, see Figure 5-I-3. The connection of the two layers with Au – Ge bonds at 2.4672(17) Å, makes for a 5 coordinate (4 In and 1 Ge atom) distorted square pyramidal geometry for the Ni atoms, and 3 coordinate (2 Ge and 1 Au atom) trigonal planar arrangement for the Ge atoms. This is a common geometry in intermetallic compounds when one neglects the RE contacts.[3]

The coordination environment for the crystallographically unique Ce site out to 3.65 Å, is given in Figure 5-I-5. The rare earth atom is 12-coordinate, forming four bonds to Au atoms, four bonds to Ge atoms and two bonds to In atoms at longer distances. This arrangement gives rise to a distorted pentagonal prismatic geometry around the Ce atoms. All Ce – X (X = Au, In and Ge) distances ranging at 3.2384 – 3.6538 Å, are quite longer comparing to the sum of the corresponding covalent radii of 2.938 – 3.155 Å (R_{Ce} + R_X),[63] indicating rather weak interactions among the Ce and the surrounding atoms.

Figure

plane.

Figure 5

axis. For

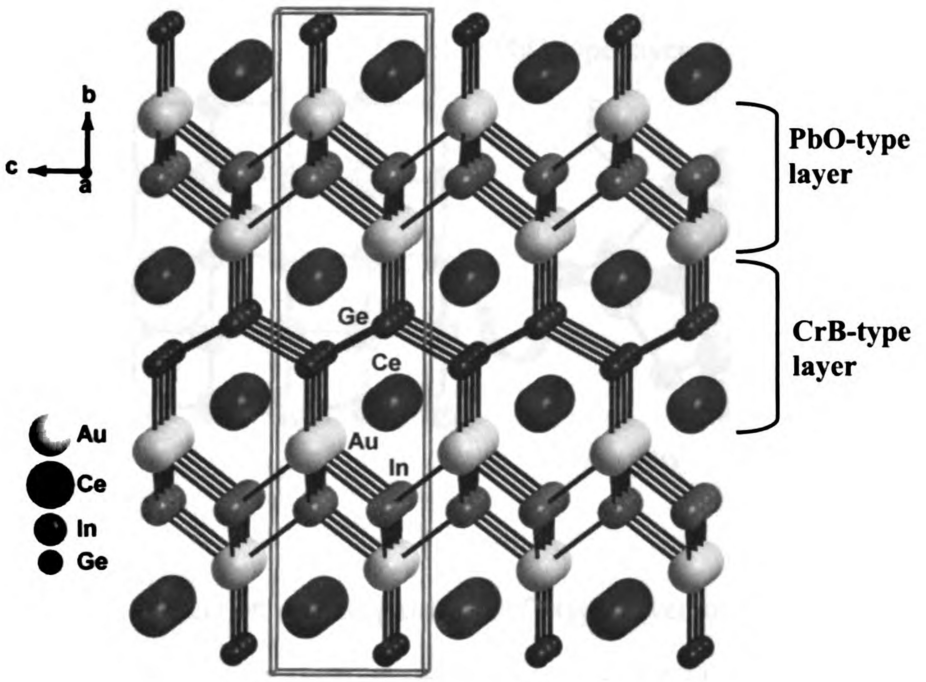

Figure 5-I-2. The overall structure of CeAuGeIn as viewed approximately onto the *b,c*-plane. For clarity the bonds to the Ce atoms are not drawn.

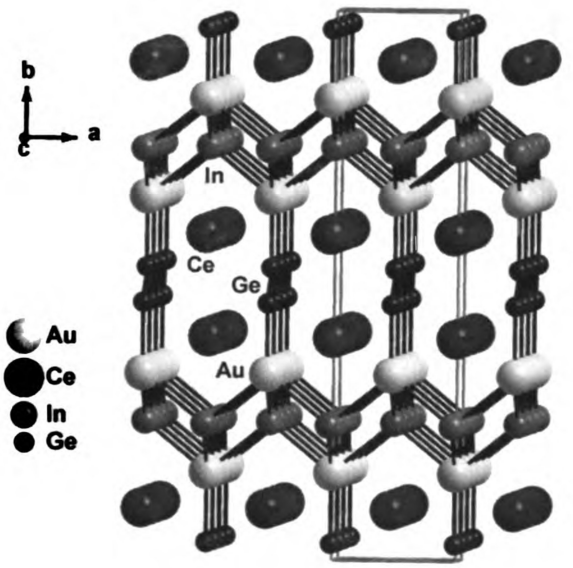

Figure 5-I-3. The overall structure of CeAuGeIn as viewed approximately down the *c*-axis. For clarity the bonds to the Ce atoms are not drawn.

c

Figu

rotat

Figur

high

Figure

coordina

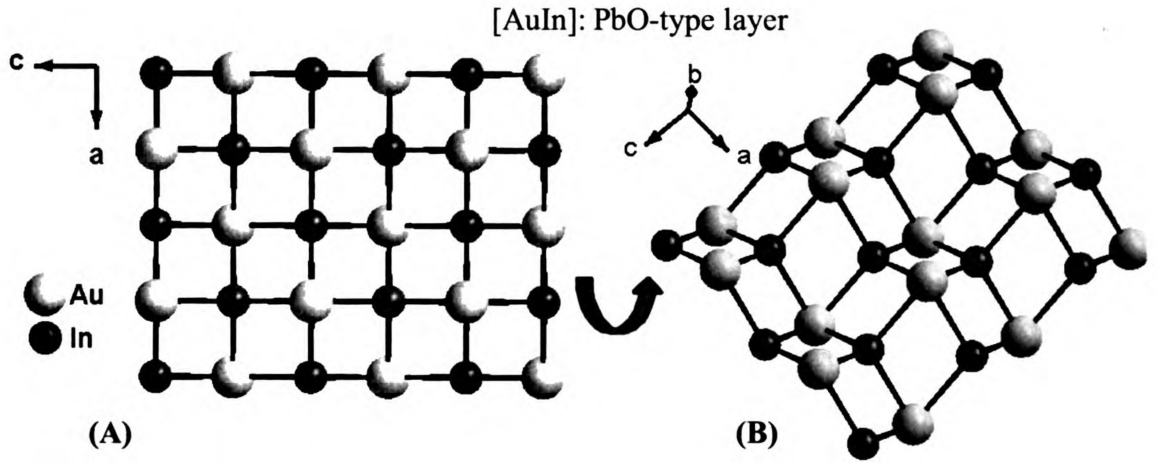

Figure 5-I-4. (A) Projection of the [AuIn]: PbO-type layer onto the *a*,*c*-plane, (B) a rotated view of the [AuIn] slab where the puckered form of the layer is emphasized.

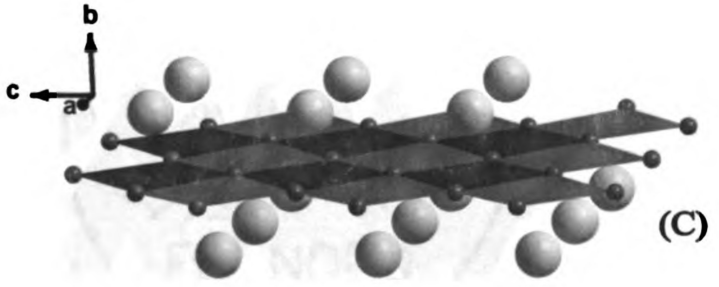

Figure 5-I-4. (C) an alternative view of [AuIn] layer where the square Ge sheets are highlighted.

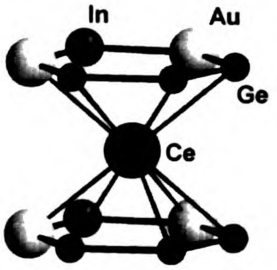

Figure 5-I-5. Coordination environment of the crystallographically unique Ce atom. The coordination sphere cutoff is 3.65 Å.

An alternative view of the CeAuGeIn structure is in polyhedral representation. Figure 5-I-6(A), depicts the connectivity of the Au-centered distorted square pyramids and Ge zigzag chains, as viewed in the *b,c*-plane. The Au-centered square pyramids, which are composed of 4 In and 1 Ge atom, are condensed via common In-In edges, thereby generating two-dimensional layers parallel to the *a,c*-plane, Figure 5-I-6(A) and 5-I-6(B). The tops of the pyramids of adjacent layers form zigzag chains, running along the *c*-direction. This arrangement of Au, In and Ge atoms results to a three-dimensional network without any Au –Au contacts. The void space within this framework creates distorted channels which are occupied by the Ce atoms. Table 5-I-4 gives a list of selected bond distances for CeAuGeIn.

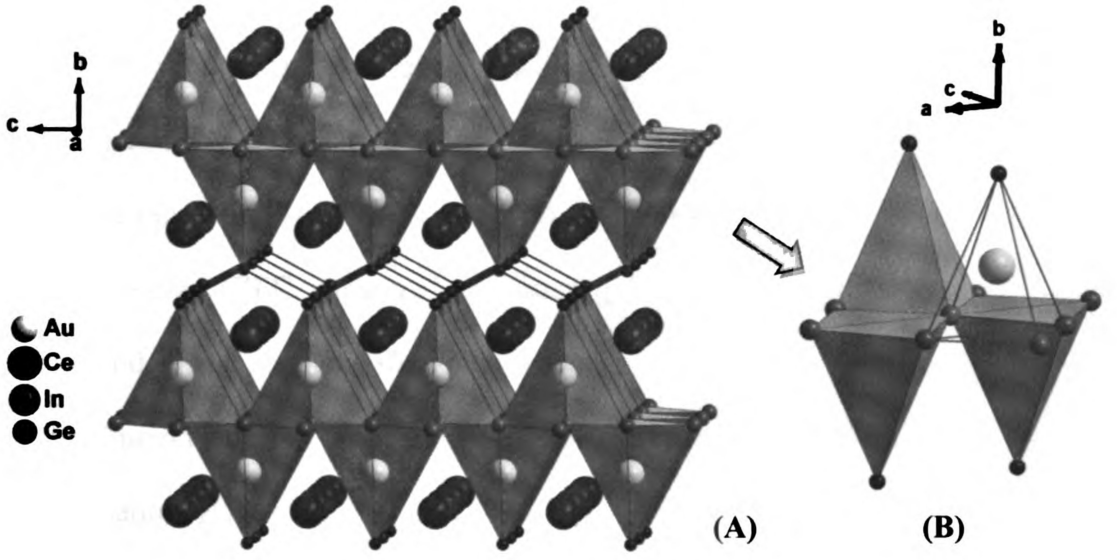

Figure 5-I-6. (A) Polyhedral *b,c*-view of the CeAuGeIn structure, featuring the three-dimensional network of condensed distorted Au-centered In_4Ge square pyramids and Ge zigzag chains and (B) details of the pyramids connectivity. One pyramid polyhedron has clear faces for clarity.

Table 5-I-4. Selected bond lengths (Å) for CeAuGeIn.

Bond	Length	Bond	Length
Ce - Au	3.3342(6)	Au - Ge	2.4672(17)
Ce - Ge	3.2383(14)	Au - In	2.7884(8)
Ce - Ge	3.3255(8)	Au - In	2.7912(8)
Ce - In	3.6538(12)	In - In	3.0935(5)
Ce - In	3.7341(12)	Ge- Ge	2.5127(16)

Magnetic Measurements:

Figure 5-I-7 shows the temperature dependence of the molar magnetic susceptibility $\chi_m(T)$ of a CeAuGeIn sample of single crystals loaded randomly in a gel-cup measured between 2 and 300 K with an applied field of 1 kG and measured for the temperature range of 2 – 61 K for 300 G of applied field. Data were collected for both zero field cooled (ZFC, measured on warming) and field cooled (FC, measured on cooling) modes. The magnetic susceptibility data for 1 kG field and above 15 K, follow a modified Curie-Weiss law that includes a temperature independent component according to the equation $\chi(T) = \chi_0 + C / (T - \theta_p)$. χ_o includes the sum of the temperature-independent contributions, e.g. van Vleck paramagnetism, Pauli paramagnetism (due to conduction electrons) and core-electron diamagnetic contributions. The effective magnetic moment μ_{eff} was deduced from the Curie constant C, ($C = \mu_{eff}^2 / 8$). A nonlinear least-squares fit to this equation resulted in $\chi_0 = 2.2 \times 10^{-3}$ emu / mol of Ce atom, Curie -

Weiss constant of θ_p = 9.8 K suggesting ferromagnetic interactions and an effective moment of 2.3 μ_B / Ce atom. The estimated experimental μ_{eff} value is somewhat reduced with respect to that expected for a free Ce^{3+} ion (2.54 μ_B), but close enough to suggest a principally trivalent valence state for the Ce atom. As emphasized in the inset of Figure 5-I-7, at a Néel temperature of ~ T_N = 11 K the compound orders antiferromagnetically, indicated by the distinct peak in both 1kG and 300 G $\chi_m(T)$ data. Additionally, at a temperature of 5 K there is a sharp change in the $\chi_m(T)$ curves which is indicative of ferromagnetic phase transition. The magnetic susceptibility measured at 0.3 and 1 kG did not show any significant difference in the magnetic behavior.

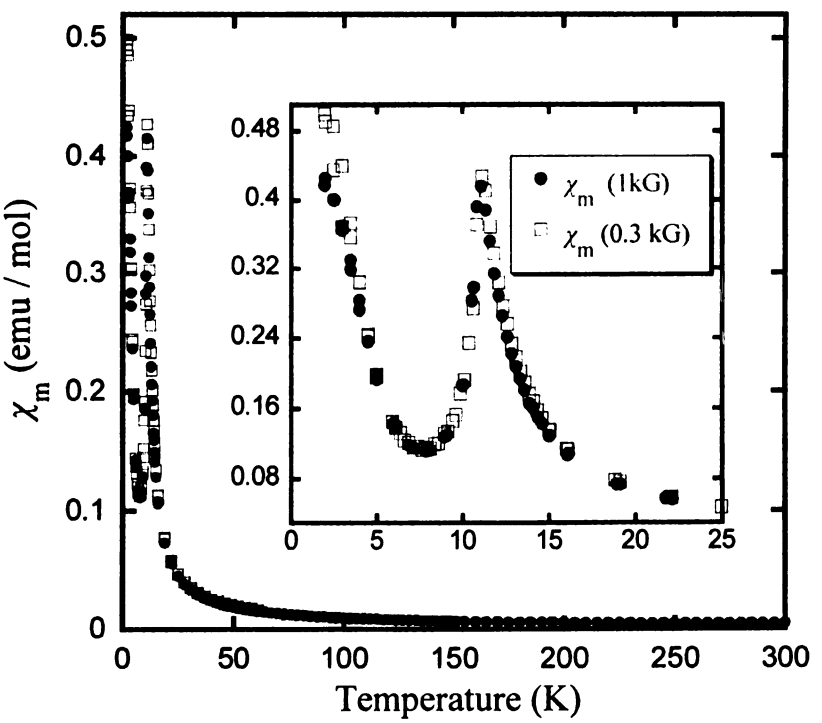

Figure 5-I-7. Temperature dependence of the molar susceptibility $\chi_m(T)$ of CeAuGeIn measured on single crystals randomly oriented with applied fields of 0.3 kG and 1 kG.

The field variation of the magnetization $M(H)$ for the same CeAuGeIn sample of crystals measured at 2, 8, 11 and 60 K can be found in Figure 5-I-8(A). The magnetization curves at both 2 and 8 K exhibit a characteristic metamagnetic behavior as is emphasized in Figure 5-I-8(B), which shows only the 8 K magnetization data at the lower fields region. The metamagnetic transition in CeAuGeIn occurs at the critical field of ~ H_C = 3 kG, indicated by the arrow in Figure 5-I-8(B). The magnetization at 8 K shows weak and linear (indicated by the solid line in Figure 5-I-8(B) field dependence at low fields and at 3 kG there is a reorientation of the spins, where the moment exhibits stronger filed dependence and an apparent hysteresis loop after ~ 5 kG. This metamagnetic transition corroborates the antiferromagnetic and ferromagnetic nature of the two transitions observed in the susceptibility measurements. Similar behavior is observed for the lowest measured data at 2 K, where at about 37 kG the moment starts to saturate and at 62 kG of applied field it reaches a value of 1.5 μ_B / Ce. This value is about 70 % of the theoretical saturation moment for Ce^{3+} of 2.14 μ_B / Ce (calculated by $\mu_{sat} = g_J J$). Saturation moments in the range of 1 μ_B / Ce atom are frequently observed for cerium-based intermetallic compounds. These small values of the μ_{sat} are due to crystal field splitting effects on the J = 5/2 ground state of the Ce^{3+} ion. The experimentally determined moments per cerium atom are 0.75 – 0.9 μ_B for $CeRhSn_2$,[66,67] 1.09 μ_B for CeAuGe,[68] 1.01 μ_B for $CePd_{0.63}Ge_{1.37}$[69] and 0.9 μ_B for $CeCuBi_3$[70] to name a few.

The magnetization at 11 K exhibits linear response up to ~ 7 kG of applied field, while at higher fields the slope of the curve continuously changes and a very small difference between increasing and decreasing field data still exists. The moment does not show signs of saturation up to the highest attainable field of 50 kG. Finally, the data

collected at 60 K, which is well above the two observed magnetic transitions, show linear field dependence up to 50 kG with a considerably reduced moment, indicative of the paramagnetic nature of the material at this temperature.

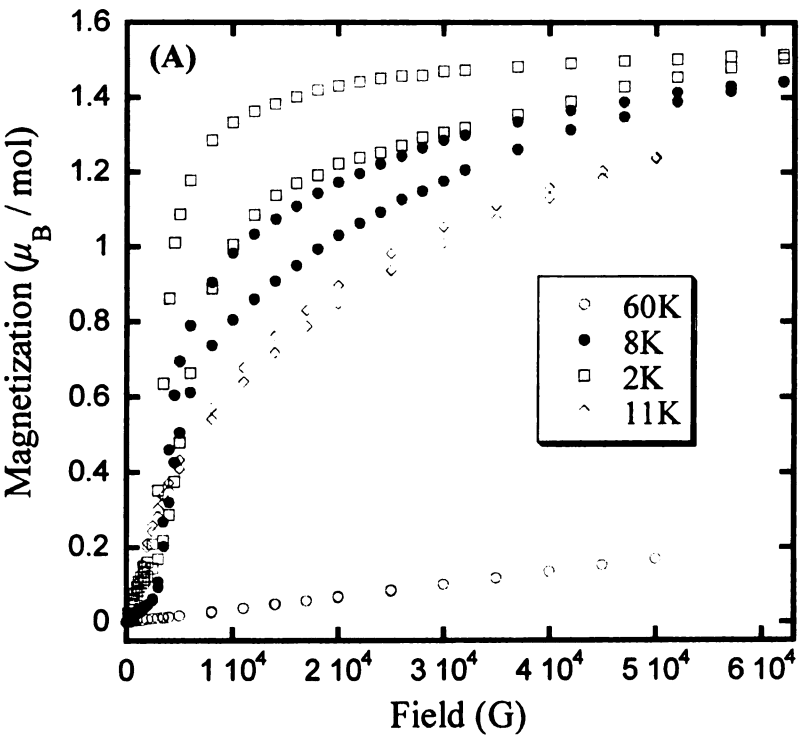

Figure 5-I-8. (A) Field variation of the magnetization of CeAuGeIn collected at 2, 8, 11 and 60 K.

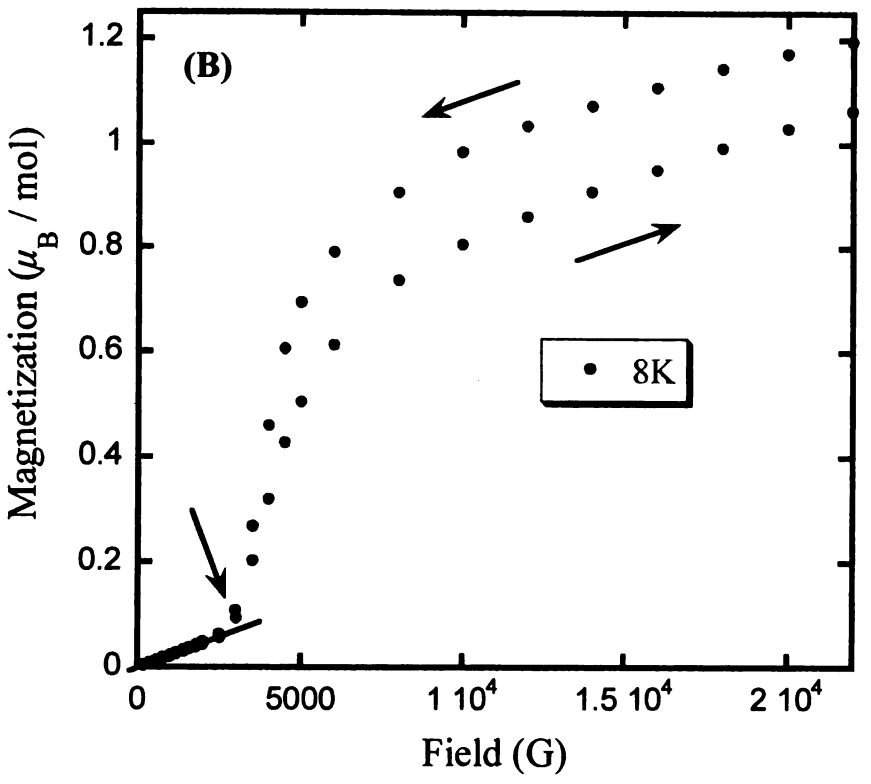

Figure 5-I-8. (B) Magnetization curve at 2 K at low fields (0 – 22 kG) emphasizing the metamagnetic transition, indicated by the arrow. The solid line indicates a linear behavior of $M(H)$ below the metamagnetic transition at $H_C = 3$ kG.

Additional magnetic measurements were carried out on a low field SQUID magnetometer on a piece consisting of aggregated aligned crystals, for 1.3 K < T < 35 K, and with applied fields of 5 and 50 G. Measurements were performed with the piece oriented with the *b*-axis parallel and perpendicular to the external field. Figure 5-I-9(A) shows the magnetic susceptibility (M/H) data for both ZFC and FC configurations for 5 G applied field parallel to the *b*-axis. As it has been observed in the higher field measurements described above, CeAuGeIn first undergoes an antiferromagnetic

transition with a Néel temperature of ~ T_N = 11 K and then a ferromagnetic one with a Curie temperature of ~ T_C = 5 K. At this low field and orientation though, we see some additional features. At ~ 23 K there is a rather broad change in the slope of the FC curve and a significant hysteresis between ZFC and FC data starts to occur. Furthermore, at ~ 2.7 K there is another transition that appears as peaks for both ZFC and FC curves. Low-temperature neutron diffraction measurements could shed light on the subtleties of the multiple magnetic transitions. A FC measurement at 50 G and with the same orientation, also presented in Figure 5-I-9(A), exhibited almost the same behavior with the one measured at 5 G, with the exemption of the disappearance of the upturn in the slope observed at ~ 23 K in the 5 G of applied field corresponding data.

When the field of 5 G was applied normal to the *b*-axis the low temperature behavior remained the same and both the ferromagnetic ordering at 5 K and the peak at 2.7 K, were observed, Figure 5-I-9(B). Nevertheless, the picture at the higher temperature range changed. The distinct peak of the antiferromagnetic ordering at 11 K disappeared and instead a change in the slope occurred at about 20 K, followed by a broad curvature until the T_c of 5 K for the FC curve and a more intense hump until 10 K for the ZFC curve. The hysteresis between ZFC and FC configurations started at ~ 15 K in this case. When the field was raised to 50 G the FC data showed no curvature change at 20 K. However, there was a very small peak at ~ 11 K, followed by the two transitions at 5 and 2.7 K. This orientation dependent behavior implies that CeAuGeIn is magnetically anisotropic. Other Ce based compounds that have be shown to undergo complex magnetic ordering at low generally temperatures include the $CeAu_4Si_2$,[71] the family of compounds Ce_5CuX_3 (X = Sn, Pb and Bi),[72,73] and $CeCoGe_3$.[74-76]

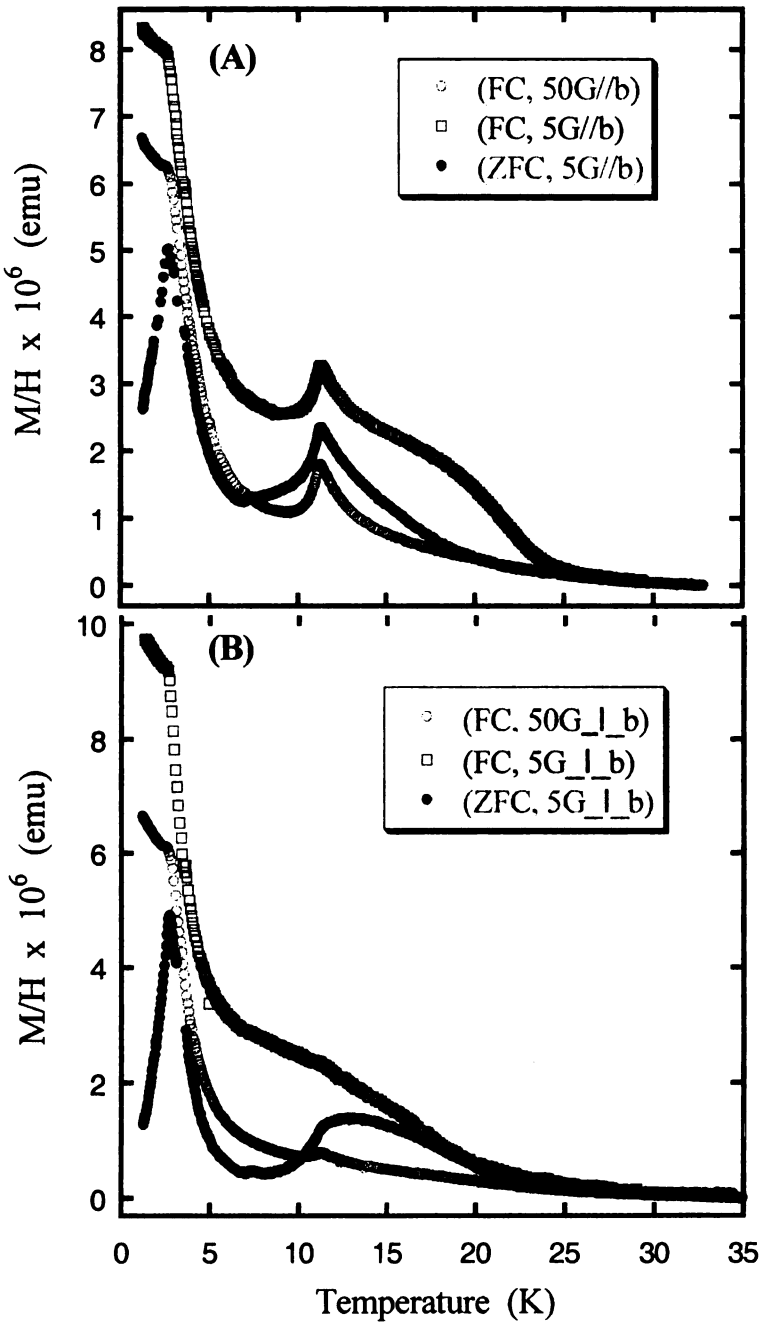

Figure 5-I-9. Temperature dependence of the susceptibility M/H of CeAuGeIn measured on a compact piece composed of several crystals oriented with applied fields of 5 and 50 G (A) parallel to *b*-axis and (B) perpendicular to *b*-axis.

Magnetotransport measurements:

The temperature variation of the electrical resistivity $\rho(T)$ of CeAuGeIn measured between 1.58 and 35 K with applied fields of 0 – 4 T, are given in Figure 5-I-10. The inset in Figure 5-I-10 displays the zero applied field $\rho(T)$ data up to 108 K. The temperature dependence of $\rho(T)$ above 15 K suggests metallic character ($\rho(T)$ decreases with decreasing temperature) of the material. The resistivity data measured on crystals along the *b*-axis below 15 K and at 0 Tesla revealed a shoulder-like feature at ~ 10 – 14 K. When a magnetic field of 1 Tesla was applied the shoulder was significantly reduced. With the application of even higher fields the feature at 10 – 14 K became even smaller and finally at 4 T applied field it completely disappeared. The reducing intensity of the shoulder-like feature at 10 – 14 K with the application of higher magnetic fields suggests possible antiferromagnetic transition, which agrees with the antiferromagnetic-like peak, observed at 11 – 12 K in the magnetic susceptibility measurements, described above.

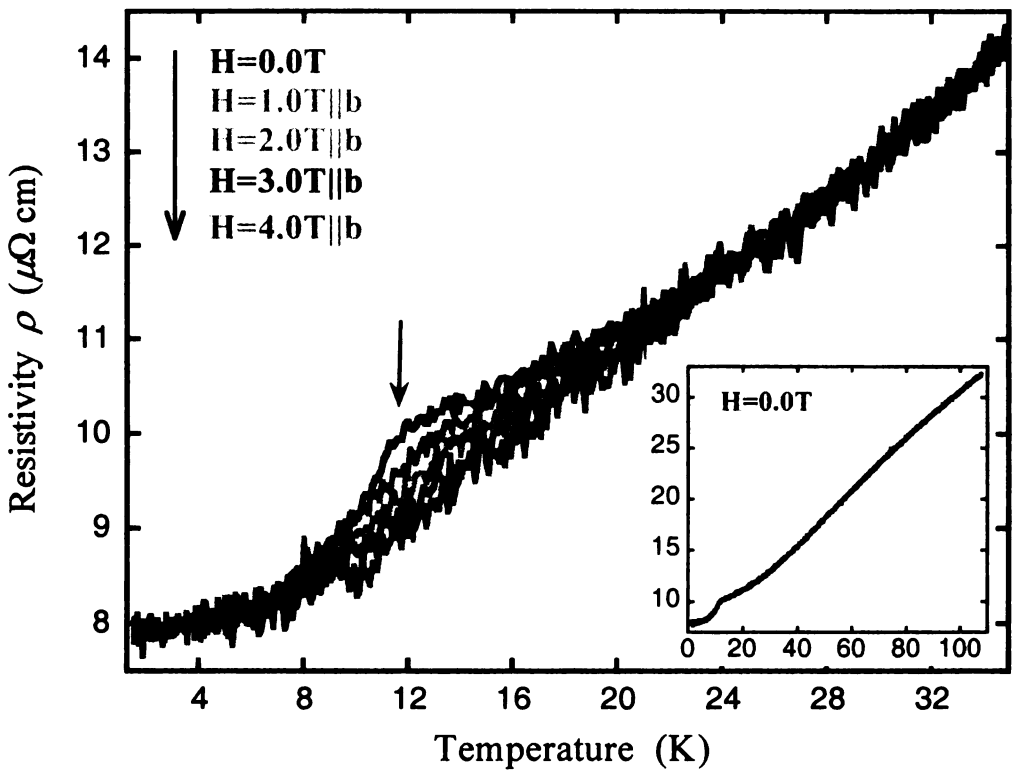

Figure 5-I-10. Temperature variation of the electrical resistivity $\rho(T)$ of CeAuGeIn from 1.58 to 35 K with applied fields of 0, 1, 2, 3 and 4 Tesla along the *b*-axis. The inset displays the $\rho(T)$ data for zero applied field for a temperature range of 1.58 – 108 K.

XANES Measurements:

To further probe the Ce valence state in CeAuGeIn we performed X-ray absorption measurements at the Ce L_{III}-edge. The XANES on Ce L_{III}-edge represents the excitation of an electron from the $2p_{3/2}$ core level into the conduction band so that it probes directly the electronic structure of the unoccupied valence band.[77] The energy variation of the normalized X-ray absorption at the Ce L_{III} threshold obtained at temperatures of 16 and 300 K and at ambient pressure is depicted in Figure 5-I-11. The

spectrum of the tetravalent Ce in CeO_2 measured at 16 K is also presented for comparison. The measured near-edge spectra did not present any considerable difference between the two temperatures, suggesting that the Ce valence remained stable in the measured temperature range. Nevertheless, in the presence of both $4f^1$ and $4f^0$ final states, the L_{III}-edge is comprised by two main structures (double peak) approximately separated by 10 eV.[78,79] As it can be seen in Figure 5-I-11, both spectra show a single dominant absorption peak (white line resonance), centered at ~ 5726 eV. A singly peaked edge structure in this energy region is attributed to trivalent Ce atoms, [6,80-82] (due to a $2p_{3/2} \rightarrow (4f^1)5d$ electron transition). On the other hand, the tetravalent Ce in CeO_2 gives a double peaked spectrum. Other intermetallic compounds where Ce (IV) is present also exhibit double peak structure.[6,80-82] The presence of single peaked spectrum reveals that Ce is present exclusively in the trivalent state in CeAuGeIn. Thus, the XANES experiments do not provide any evidence for the existence of valence fluctuations and support the analysis of the magnetic properties of this compound. Examples of Ce-based intermetallic compounds exhibiting similar XANES spectra include the ternary compounds $CePt_4Ni$,[6] CePtSn,[80] $CeRu_2Si_2$,[77] CeAuIn and $CeAu_2In$[82] to name just a few.

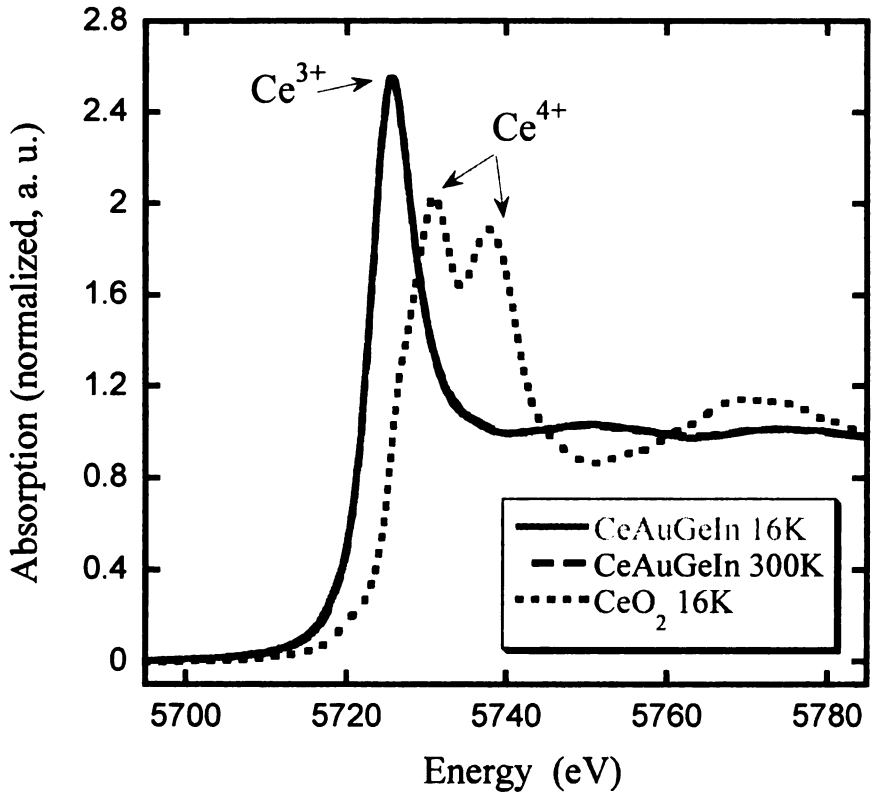

Figure 5-I-11. L_{III}-edge absorption spectra of Ce in CeAuGeIn at 16 K (solid line) and 300 K (dashed line). The spectrum of CeO_2 at 16 K (dotted line) is also given for comparison.

5-I-4. Conclusions:

The novel intermetallic compound of CeAuGeIn crystallizes in molten In with the orthorhombic *Cmcm* space group as an ordered quaternary variant of the ternary $CeNiSi_2$ structure type. This is another example were liquid In acts as a reactive flux in reactions containing group 14 elements, despite the general tendency for In not to get incorporated into the compound when used in systems of the type RE/M/Ge. The formation of the title

compound when Ce was employed under similar reaction conditions as in the $Yb_3AuGe_2In_3$ phase, reinforces and generalizes the suggestion made in Chapter 2 where we saw that only a few RE elements formed the $RE_7Co_4InGe_{12}$ phase that, the size of the RE cations plays a crucial role for the formation of quaternary phases in the system RE/TM/Ge/In, when the In-flux method is used.

The magnetic susceptibility data suggests the Ce^{3+} atoms are in a +3 state. Additionally, the magnetic measurements revealed that the material undergoes both an antiferromagnetic transition with a Néel temperature of ~ T_N = 11 K as well as a ferromagnetic one with a Curie temperature of ~ T_C = 5 K. Orientation dependent magnetic susceptibility experiments showed magnetically anisotropic behavior for CeAuGeIn. The antiferromagnetic transition was also observed in electrical resistivity measurements. Finally, when temperature XANES measurements on Ce L_{III}-edge were performed at 16 and 300 K, both spectra gave a singly peaked edge structure which confirms the suggestion of the Ce atom being as Ce^{3+} in CeAuGeIn compound. Future work for this material could include attempts to grow bigger single crystals in order to facilitate more detailed magnetic measurements. Neutron diffraction experiments could be also helpful to elucidate possible additional magnetic structures seen in the low field magnetic measurements.

CHAPTER 5

PART II. Synthesis and Characterization of $EuAuGeIn_2$

5-II-1. Introduction

The intermetallic compounds with a general formula of $RE(TM,X)_4$ (*RE* = rare earth metal, *TM* = transition metal and *X* = *p*-block element) according to a classification constituted by Krypyakevich, belong to the class N9 characterized by a tetragonal antiprism coordination environment around the smallest atoms. Depending on the specific composition of each phase they crystallize in several structure types. For one of the most common compositions of 1:2:2, more than 1000 intermetallics adopt the $BaAl_4$ structure (*I*4/*mmm* space group), or the ternary ordered variants of $ThCr_2Si_2$ structure (*I*4/*mmm* space group), $CaBe_2Ge_2$ (*P*4/*nmm* space group), $LaPt_2Ge_2$ ($P2_1$ space group) and $CeNi_{2+x}Sb_{2-x}$ (*Imm* space group). The ternary $RE_2TM_3Si_5$ compounds crystallize in $Sc_2Fe_3Si_5$ (*P*4/*mnc*), $U_2Co_3Si_5$ (*Ibam* space group) and $Lu_2Co_3Si_5$ (*C*2/*c* space group). Finally for the ternary $RETMX_3$ compounds the structures of $BaNiSn_3$ (*I*4*mm* space group) and $ScNiSi_3$ (*Cmmm* space group) have been commonly reported in the literature. The These structures are included in a concentrated effort made by Szytoula and Leciejewicz in categorizing the various ternary rare earth intermetallics structures and magnetic properties.[3] The structures $ThCr_2Si_2$,[83] $CaBe_2Ge_2$ and $BaNiSn_3$[84] constitute ternary derivatives of the $BaAl_4$ structure types, representing a large number of the observed RE/TM/X intermetallic systems.

As it was stated in part I of this Chapter, after the rich chemistry revealed by the thorough examination of the ternary RE/Au/In system[49] and in combination with the

intriguing magnetic properties exhibited by the $Yb_3AuGe_2In_3$ compound and the various remarkable physical phenomena observed in many Ce and Eu based intermetallics (also presented in part I), we explored the system Eu/Au/Ge/In. Interestingly, it did not result in an analog of the $Yb_3AuGe_2In_3$ phase, but instead the substitution of the Yb metal with Eu metal led to $EuAuGeIn_2$. The new compound crystallizes in a different structure type, however as it will be described below are closely related. The synthesis and characterization of CeAuGeIn were reported in part I of this chapter. Here we present the new compound $EuAuGeIn_2$, grown from In flux which crystallizes in the tetragonal space group *I4mm* with the $BaNiSn_3$ structure type. [84] The synthesis, crystal structure, and a preliminary study of the magnetic properties are reported.

5-II-2. Experimental section

Reagents:

The following reagents were used as purchased without further purification: Eu, (in small pieces cut from metal chunks, 99.99% HEFA Rare Earth Canada Co. Ltd), Au (pieces, 99.9% Alfa Aesar, Ward Hill, MA), Ge (~100 mesh, 99.999% Cerac, Milwaukee, WI) and In (tear drops 99.99% Plasmaterials, Livermore, CA).

Synthesis:

$EuAuGeIn_2$ was synthesized by combining 3 mmol of the europium metal, 2 mmol gold, 3 mmol germanium and 15 mmol In in an Al_2O_3 (alumina) crucible under an inert nitrogen atmosphere inside a glove-box. The crucible was placed in a 15 mm fused silica tube, which was flame sealed under vacuum of 10^{-4} Torr, to prevent oxidation

during heating. The reactants were then heated to 1000 ^{0}C over 12 h, maintained at that temperature for 5 h to allow proper homogenization, followed by cooling to 850 ^{0}C in 2 h and held there for 48 h. Finally, the system was allowed to slowly cool to 50 ^{0}C in 48 h. The reaction product was isolated from the excess In flux by heating at 350 ^{0}C and subsequent centrifugation through a coarse frit. Any remaining flux was removed by immersion and soniqation in glacial acetic acid for 48 - 72 h. The final crystalline product was rinsed with water and dried with acetone. $EuAuGeIn_2$ crystals grow as thick rods with rectangular faces and a rather rough silvery surface. Main side products were small amounts of $Eu_2AuGe_{2.5\text{-}3.5}$ thin plates, as defined only from EDS analysis, and unreacted In metal. Several single crystals were carefully selected for elemental analysis, structure characterization, and magnetic measurements reported here.

Elemental Analysis:

Semi-quantitative microprobe elemental analysis was performed on several crystals of the compound using a HITACHI MODEL S-2700 Scanning Electron Microscope (SEM) equipped with a light-element window Noran System Six EDS detector. Data were acquired by applying a 20 kV accelerating voltage and an acquisition time of 1 min. The EDS analysis gave an average atomic composition of 19.9 % Eu, 20.62 % Au, 18.96 % Ge and 40.52 % In, which is in very good agreement with the final single crystal X-ray diffraction refinement results.

X-ray Crystallography:

The X-ray intensity data were collected at room temperature using a STOE IPDS 2T (with additional capability of 2θ swing of the detector) diffractometer with graphite-monochromatized Mo Kα (λ = 0.71073 Å) radiation. The X-AREA (and X-RED and X-SHAPE within) package suite[52] was used for data extraction and integration and to apply empirical and analytical absorption corrections. The structure of $EuAuGeIn_2$ single crystals were solved by direct methods and refined with the SHELXTL package of programs.[53] A structure refinement for $EuAuGeIn_2$ was initially performed for the tetragonal noncentrosymmetric space group of *I4mm*. A second refinement was also attempted for the tetragonal centrosymmetric space group of *I4/mmm* after it was suggested by the PLATON-Addsym application of the WinGX package software,[54] which gave a composition of $Eu_{0.82}Au_{0.28}Ge_{1.72}In_2$ for the title compound. Both refinements resulted in comparable R_1 / wR_2 values. For comparison reasons, additional structure refinement was also attempted in the *I*4 space group (data not provided here) which has the lowest symmetry. The agreement in the chemical composition of $EuAuGeIn_2$ from both *I4mm* and *I*4 space group refinements and the EDS analysis and the fact that the refinement in the *I4mm* S.P. can be considered as showing less atomic site disorder, led us to choose the tetragonal *I4mm* S.G. as the better one to describe the final structure. The final data collection and structure refinement details for both space group refinements are given in Table 5-II-1. The final atomic positions, equivalent isotropic displacement parameters and anisotropic displacement parameters are listed in Tables 5-II-2,3 and 5-II-4,5.

Table 5-II-1. Crystal data and structure refinement data for $EuAuGeIn_2$ in *I4mm* and *I4/mmm* space groups.

Empirical formula	$EuAuGeIn_2$	$Eu_{0.82}Au_{0.28}Ge_{1.72}In_2$
Formula weight	651.16	535.63
Temperature (K)	293(2)	293(2)
Wavelength (Å)	0.71073	0.71073
Crystal system	Tetragonal	Tetragonal
Space group	*I4mm*	*I4/mmm*
a (Å)	4.4996(6)	4.4996(6)
b (Å)	4.4996(6)	4.4996(6)
c (Å)	11.799(2)	11.799(2)
V (Å^3) / Z	238.88(7) / 2	238.88(7) / 2
$Density_{calc}$ (Mg/m^3)	9.053	7.447
Absorption coefficient (mm^{-1}) / F(000)	59.059 / 544	39.370 / 455
θ range for data collection (^{o})	4.85 to 34.38	4.85 to 34.38
Index ranges	-7<=h<=6 -7<=k<=5 -18<=l<=18	-7<=h<=6 -7<=k<=5 -18<=l<=18
Reflections collected / unique / *R*(int)	1532 / 322 / 0.1238	1532 / 168 / 0.1350
Completeness to θ (%)	92.3	92.3
Data / restraints / parameters	322 / 1 / 18	168 / 0 / 10
Refinement method	Full-matrix least- squares on F^2	
Goodness-of-fit on F^2	1.133	1.194
Final R indices [$I>2\sigma(I)$] (R_1 / wR_2)^a	0.0435 / 0.1083	0.0431 / 0.1140
R indices (all data) (R_1 / wR_2)^a	0.0437 / 0.1088	0.0433 / 0.1142
Extinction coefficient	0.014(3)	0.032(6)
Largest diff. peak and hole (e. Å^{-3})	2.552 and -3.025	2.185 and -4.166

$$^{a}R_1 = \Sigma\left||F_o|-|F_c|\right| / \Sigma|F_o|;\ wR_2 = \left[\Sigma w\{|F_o|-|F_c|\}^2 / \Sigma w|F_o|^2\right]^{1/2};\ w = 1/\sigma^2\{|F_o|\}$$

Table

param

Atom
Eu
In
Au
Ge
Au
Ge

Tab

para

At
Eu
In
Au
Ge

[a] Un

Table 5-II-2. Atomic coordinates (x 10^4) and equivalent isotropic displacement parameters ($Å^2$ x 10^3) for $EuAuGeIn_2$ in *I4mm* space group.

Atom	Wyckoff	x	y	z	U(eq)[a]	S.O.F
Eu	2a	-5000	-5000	5669(1)	11(1)	1
In	4b	0	-5000	3167(3)	10(1)	1
Au(1)	2a	0	0	4603(1)	12(1)	0.46
Ge(1)	2a	0	0	4603(1)	12(1)	0.54
Au(2)	2a	0	0	6753	7(1)	0.536
Ge(2)	2a	0	0	6753	7(1)	0.464

Table 5-II-3. Atomic coordinates (x 10^4) and equivalent isotropic displacement parameters ($Å^2$ x 10^3) for $EuAuGeIn_2$ in *I4/mmm* space group.

Atom	Wyckoff	x	y	z	U(eq)[a]	S.O.F
Eu	2a	0	0	0	11(1)	0.82
In	4e	-5000	-5000	-1078(1)	9(1)	1
Au	4d	-10000	-5000	-2500	9(1)	0.142
Ge	4d	-10000	-5000	-2500	9(1)	0.858

[a]U(eq) is defined as one third of the trace of the orthogonalized U^{ij} tensor.

Table 5-II-4. Anisotropic displacement parameters ($Å^2$ x 10^3) for $EuAuGeIn_2$ in *I4mm* space group.

Atom	U^{11}	U^{22}	U^{33}	U^{23}	U^{13}	U^{12}
Eu	11(1)	11(1)	11(1)	0	0	0
In	9(1)	9(1)	11(1)	0	0	0
Au(1)	13(1)	13(1)	11(1)	0	0	0
Ge(1)	13(1)	13(1)	11(1)	0	0	0
Au(2)	9(1)	9(1)	5(1)	0	0	0
Ge(2)	9(1)	9(1)	5(1)	0	0	0

Table 5-II-5. Anisotropic displacement parameters ($Å^2$ x 10^3) for $EuAuGeIn_2$ in *I4/mmm* space group.

Atom	U^{11}	U^{22}	U^{33}	U^{23}	U^{13}	U^{12}
Eu	11(1)	11(1)	10(1)	0	0	0
In	10(1)	10(1)	7(1)	0	0	0
Au	8(1)	8(1)	10(1)	0	0	0
Ge	8(1)	8(1)	10(1)	0	0	0

The anisotropic displacement factor exponent takes the form: $-2\pi^2[h^2a^{*2}U^{11} + \ldots + 2hka^*b^*U^{12}]$

Magnetic Measurements:

Low field magnetic measurements on randomly oriented crystals were performed with a commercial Low Field SQUID magnetometer,[55] located also in the MSD facilities of ANL, in the temperature range of 1.3 - 65 K, with applied fields of 1 and 10 G for the ZFC and the FC mode run, respectively. In a typical measurement the temperature from 40 K is cooled down to 1.3 K under zero field. Then the field is turned on and the ZFC data are collected on warming. Consecutively, the temperature is cooled down to 1.3 K with the field on and then the FC data are also measured on warming.

5-II-3. Results and Discussion

Reaction Chemistry:

The compound $EuAuGeIn_2$ was first discovered in a reaction that was initially designed to form the Eu analog of the $Yb_3AuGe_2In_3$ phase, described in Chapter 4. As in the case of the CeAuGeIn compound, when Yb was substituted by Eu metal a different compound was formed. Interestingly, the Eu analog did not form the CeAuGeIn phase either, but instead it crystallized in another structure type which as it will be demonstrated below is closely related to the CeAuGeIn structure type. This result is another example of where the size of the rare-earth cation plays a decisive role for the formation of a specific quaternary phase in the system RE/TM/Ge/In, when the In-flux method is used. Furthermore, the synthesis of $EuAuGeIn_2$ is yet another example which demonstrates the ability of liquid In to act as a reactive flux in reactions containing group 14 elements. Nevertheless, $EuAuGeIn_2$ crystals form as thick rods with rectangular faces

and a rather rough silvery surface. Figure 5-II-1 shows scanning electron micrographs of typical single crystals of the $EuAuGeIn_2$ compound.

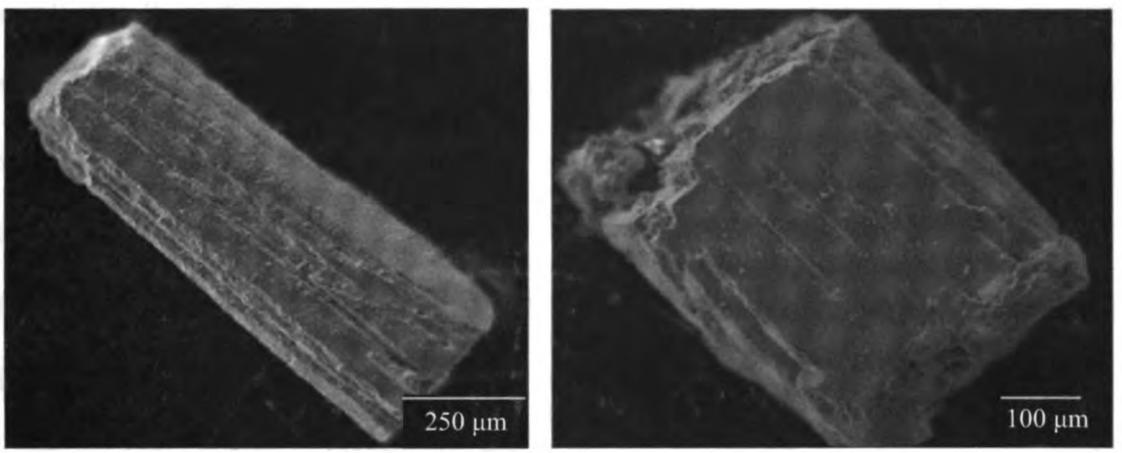

Figure 5-II-1. Scanning Electron micrograph (SEM) images of flux-grown $EuAuGeIn_2$ crystals.

Structure:

According to the data in Tables 5-II-1-3 in the refinement under the centrosymmetric *I*4/*mmm* S.P., the title compound adopts the $ThCr_2Si_2$ type structure[83] with partial occupancy of 82 % for the Th (2a) site by the Eu atom, full occupancy for the Si (4e) site by the In atom while the Cr (4d) position is randomly occupied by Au and Ge atoms. For the latter position there is stronger preference of 86 % to be occupied by the Ge atom. This arrangement resulted in R_1 / wR_2 values (all data) of 0.0433 / 0.1142 and a final composition of $Eu_{0.82}$ $Au_{0.28}Ge_{1.72}In_2$ which did not agree with the results obtained from the EDS analysis, given above. On the other hand when the refinement is performed

under the non-centrosymmetric *I*4*mm* S.P., the present compound adopts the $BaNiSi_3$ type structure[84] with fully occupied Ba (2a) and Sn(2) (4b) sites by Eu and In atoms, respectively. The Ni and Sn(1) positions of the prototype on the other hand, are shared almost equally between the Au and Ge atoms. The refinement with the *I*4*mm* S.G. resulted in R_1 / wR_2 values (all data) of 0.0437 / 0.1088, comparable to the corresponding values of the *I*4/*mmm* S.P., and a final composition of $EuAuGeIn_2$ which agrees very well with the results obtained from the EDS analysis. Additionally, structure refinement was also attempted in the *I*4 space group (data not provided here) which has lowest symmetry for comparison reasons. This attempt led to the same chemical composition of $EuAuGeIn_2$, as in the refinement with the *I*4*mm* space group. The agreement in the chemical composition of $EuAuGeIn_2$ from both *I*4*mm* and *I*4 space group refinements and the EDS analysis and the fact that the refinement in the *I*4*mm* space group can be considered as showing less atomic site disorder; suggests that the $BaNiSn_3$ type represents a better alternative for the crystal structure of the title compound than the $ThCr_2Si_2$ type. A similar case has been reported for the $CeCuAl_3$ compound where after trial refinements were performed for both $ThCr_2Si_2$ type and $BaNiSn_3$ type structures, the $BaNiSn_3$ was proved to be a better model to describe the structure because it resulted in a lower atomic site disorder.[85] Therefore, in the structure description presented below for $EuAuGeIn_2$ compound we chose the tetragonal space group of *I*4*mm*, as a disordered variant of the $BaNiSn_3$ structure type.

The overall structure of $EuAuGeIn_2$ as viewed down the *b*-axis is depicted in Figure 5-II-2. For clarity only one of the Au/Ge atoms is presented for each of the two mixed-occupied sites. For the representation, Ge(1) atom was chosen for the Au(1)/Ge(1)

position and the Au(2) atom for the Au(2)/Ge(2) site as the atoms with the slightly higher occupation factor for each site, correspondingly. Additionally, the bonds to the Eu atoms were omitted to emphasize the three-dimensional (3D) [$AuGeIn_2$] framework and its channels. In $EuAuGeIn_2$, similar to the CeAuGeIn, all of the Eu, Au, In and Ge atoms are located in alternating layers stacked along the long *c*-axis in the sequence: Eu-Au-In-Ge-Eu-Au-In-Ge-Eu. The structure can also be described in terms of alternating [$AuGeIn_2$] and Eu atoms layers (see Figure 5-II-2). Detailed descriptions of the two structural fragments are given below.

The [Au(2)Ge(1)In_2] slab can be described as a distorted PbO-type layer, which was also seen in the [AuIn] layer in CeAuGeIn structure. In [Au(2)Ge(1)In_2], the tetrahedrally coordinated ($Au(2)_2Ge(1)_2$) In atoms form a 2-dimensional (2D) quadratic sheet that extends in the *ab*-plane (see Figure 5-II-3(A),(B)) and is capped by Au(2) atoms above and Ge(1) atoms below this plane, thus forming a puckered overall layer, see Figure 5-II-3(B). The Au-In bond has a length of 2.801(1) Å which is slightly shorter than the sum of the covalent radii of 2.85 Å ($R_{Au} + R_{In}$),[63] indicating strong Au – In interactions within the layer. Nevertheless, the Au(2) – In distance compares well with the corresponding bonds found in CeAuGeIn at 2.7912(8) Å and 2.7884(8) Å as well as with those found in other intermetallic compounds as in $EuAuIn_2$,[86] for example. The In – Ge(1) bond has a length of 2.817(3) Å, which in this case, is longer than the sum of the covalent radii of 2.667 Å ($R_{Ge} + R_{In}$).[63] but are well within the range reported for other intermetallic compounds as the ones in $RE_7Co_4InGe_{12}$ which range at 2.9214 – 2.965 Å.[48]

Adjacent [Au(2)Ge(1)In_2] layers connect through Au(2) – Ge(1) bonds at 2.5362(18) Å which is shorter than the sum of the covalent radii of 2.636 Å ($R_{Au} + R_{Ge}$),[63]

indicating strong Au – Ge interactions between neighboring layers. This bond is longer than the Au – Ge bond at 2.4672(17) Å which is connecting the two different types of layers in the CeAuGeIn compound. The [Au(2)Ge(1)In_2] layers interconnection makes for a distorted square pyramidal geometry around each of the Au(2) and Ge(1) atoms, with 4 In atoms as the base for both, while Ge(1) and Au(2) occupy the top of the pyramids for Au(2) and Ge(1), respectively. The layers interconnection also creates fused tubes that run along both the *a*- and *b*-axes, and host the Eu atoms.

In the Eu layers, the Eu atoms form planar 2D nets of squares extending parallel to the *a,b*-plane, see Figure 5-II-4. The Eu – Eu intralayer distance is equal to the *a,b*-axis at 4.4996 Å while the Eu – Eu distance between neighboring layers is at a longer distance of 6.7028(24) Å. Adjacent Eu nets are stacked in a staggered way along the *c*-axis, while every other layer is aligned with each other. Finally, there is a 16-fold coordination polyhedron around each Eu atom, see Figure 5-II-4(B). All the Eu – X distances ranging at 3.4209(10) – 3.7112(31) Å are rather long to be considered bonding.

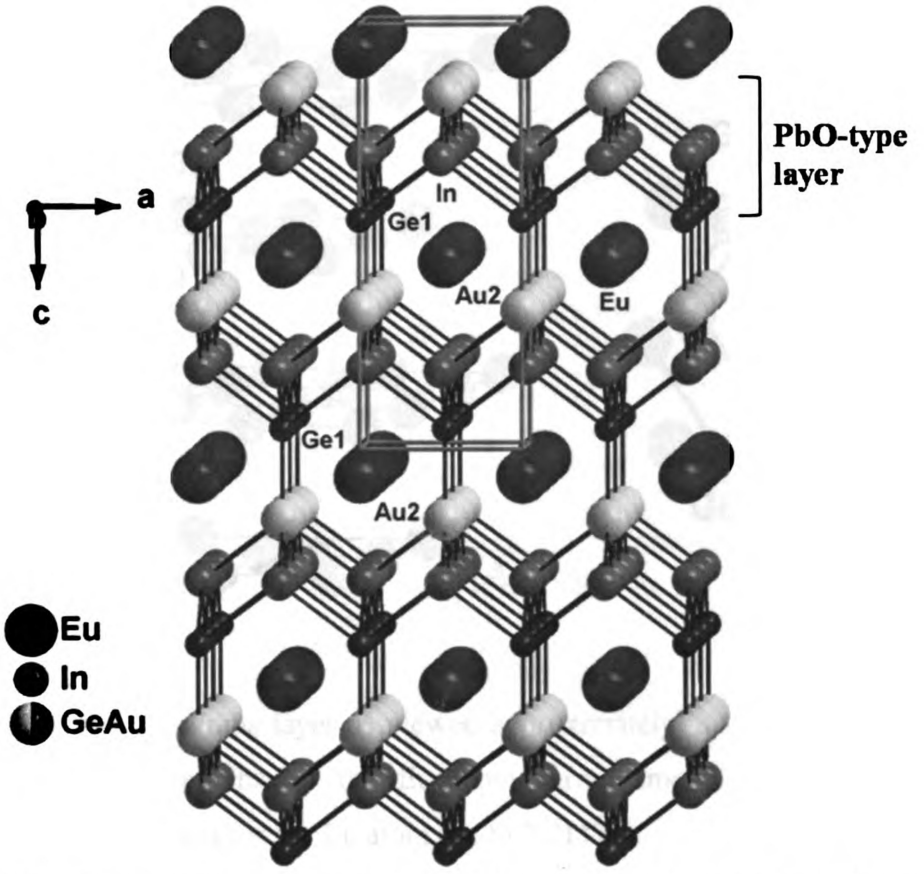

Figure 5-II-2. The overall structure of $EuAuGeIn_2$ as viewed approximately onto the *a,c*-plane. For clarity the bonds to the Eu atoms are not drawn, and only Ge(1) and Au(2) are shown for the two mixed-occupied sites of Au(1)/Ge(1) and Au(2)/Ge(2), respectively.

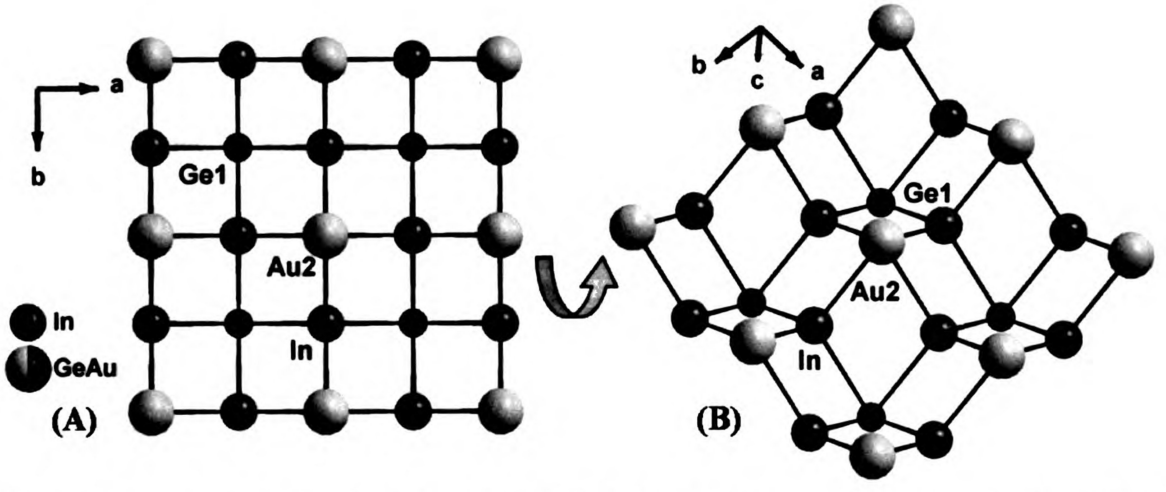

Figure 5-II-3. (A) Projection of the $[AuGeIn_2]$: PbO-type layer onto the *a,b*-plane, (B) a rotated view of the $[AuGeIn_2]$ slab where the puckered form of the layer is emphasized.

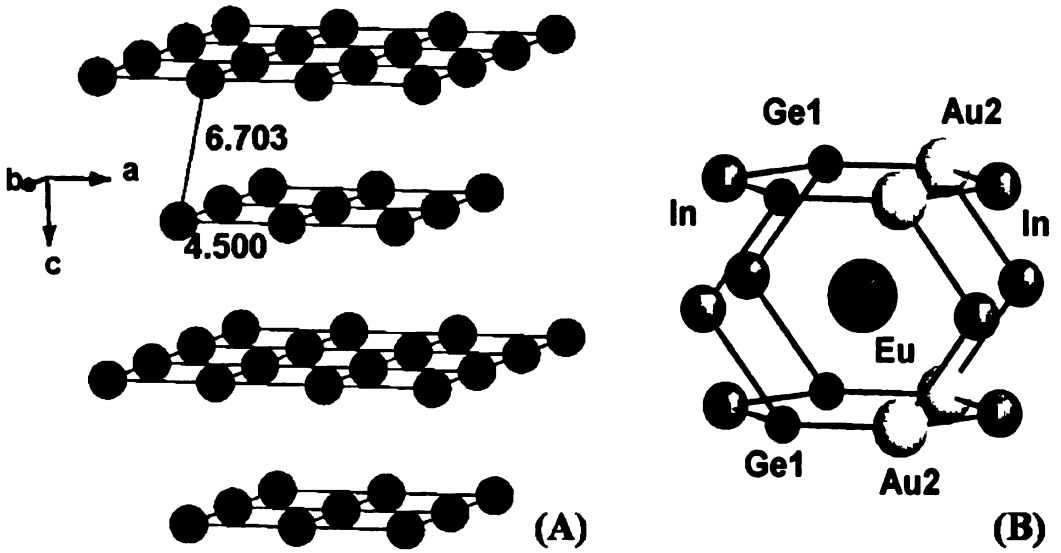

Figure 5-II-4. (A) Eu atoms layer as viewed approximately in the *a,c*-direction. Eu-Eu bonds are drawn to emphasize the Eu atoms arrangement within the layers. (B) Coordination environment for the Eu atom out to 3.7112 Å.

An alternative view of the $EuAuGeIn_2$ structure is in polyhedral representation. Figure 5-II-5, depicts the connectivity of the In-centered distorted tetrahedra, as viewed in the *a,c*-plane. The In-centered tetrahedra, which are composed of 2 Au(2) and 2 Ge(1) atom are condensed via common Au(2)-Ge(1) edges, thereby generating two-dimensional layers parallel to the *a,b*-plane. The Au(2) and Ge(1) vertices of each such layer are connected with the Ge(1) and Au(2) vertices, respectively, of adjacent layers through Au(2) – Ge(1) bonds along the *c*-direction. This arrangement of Au(2), In and Ge(1) atoms results to a three-dimensional network. The void space within this framework hosts the Eu atoms. Table 5-II-6 gives a list of selected bond distances for CeAuGeIn.

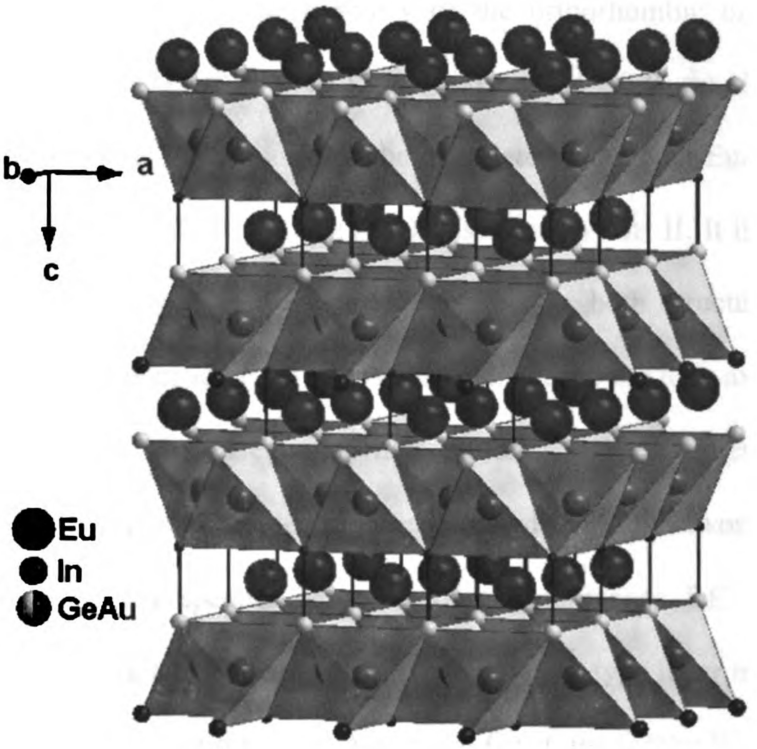

Figure 5-II-5. Polyhedral *a,c*-view of the $EuAuGeIn_2$ structure featuring the interconnection of layers consisting of condensed In-centered $Au(2)_2Ge(1)_2$ tetrahedra.

Table 5-II-6. Selected bond lengths (Å) for $EuAuGeIn_2$.

Bond	Length
Eu - Au(2)	3.4293(7)
Eu - Ge(1)	3.4209(10)
Ge(1) - In	2.817(3)
Au(2) - In	2.801(2)
In - In	3.1817(4)

Figure 5-II-6 illustrates the *b,c*-view of the orthorhombic ordered CeAuGeIn structure (*Cmcm*, a = 3.3215(9), b = 19.176(4) and c = 4.4259(9) Å), described in Part I of this chapter, as well as the *a,c*-view of the disordered tetragonal $EuAuGeIn_2$ structure (*I*4mm, a,b = 19.176(4) and c = 4.4259(9) Å), described in Part II. It is obvious that the two structures can be considered as closely related. In both structures, coordination polyhedra with Au atoms inside form layers perpendicular to the long axis. The layers are interconnected through Au – Ge bonds thus building a three dimensional [AuInGe] framework. The RE atoms are located in large holes within this network. Both structures can be described with a specific sequence of atomic planes RE, Au, Ge, and In perpendicular to the long axis. Both of them contain a PbO-type layer made of Au and In atoms for the CeAuGeIn compound and Au, In and Ge atoms for the $EuAuGeIn_2$.

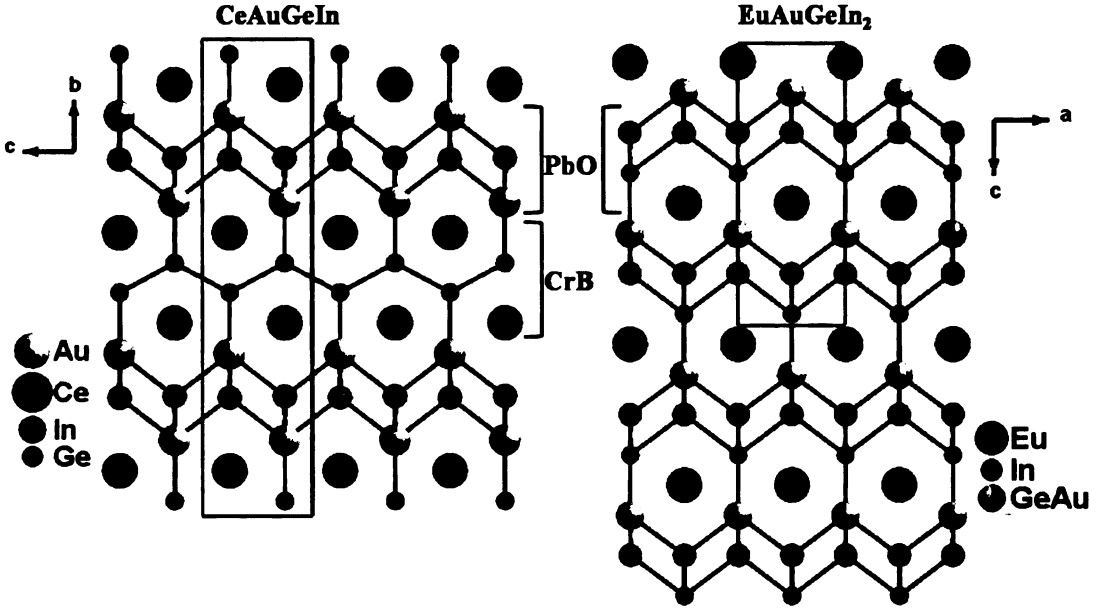

Figure 5-II-6. The overall structure of CeAuGeIn as viewed onto the *b,c*-plane and the overall structure of $EuAuGeIn_2$ as viewed onto the *a,c*-plane.

Magnetic Measurements:

Figure 5-II-7 shows the magnetic susceptibility (M/H) data for ZFC mode measurement with 1 G of applied field and for FC mode at 5 G of applied field. Both measurements were performed on randomly oriented crystals. As it can be seen more clearly in the inset of Figure 5-II-7 which depicts the lower temperature data, the system seems to undergo an antiferromagnetic transition at a temperature of ~ 11 -12 K as indicated by the cusp in both ZFC and FC measurements. Successively, the material exhibits a ferromagnetic ordering at a temperature of ~ 5 K, where there is change in the slope. Furthermore, at ~ 2.6 - 2.7 K there is another feature appearing as peaks for both

ZFC and FC curves, with the ZFC decreasing towards lower moment values and the FC data increasing to a higher moment. Low-temperature neutron diffraction measurements could shed light on the subtleties of the multiple magnetic transitions. $EuAuGeIn_2$ magnetic behavior is very similar to the corresponding CeAuGeIn behavior since both compounds seem to exhibit both anti- and ferromagnetic transition at the same temperature ranges and possible additional features at lower temperatures.

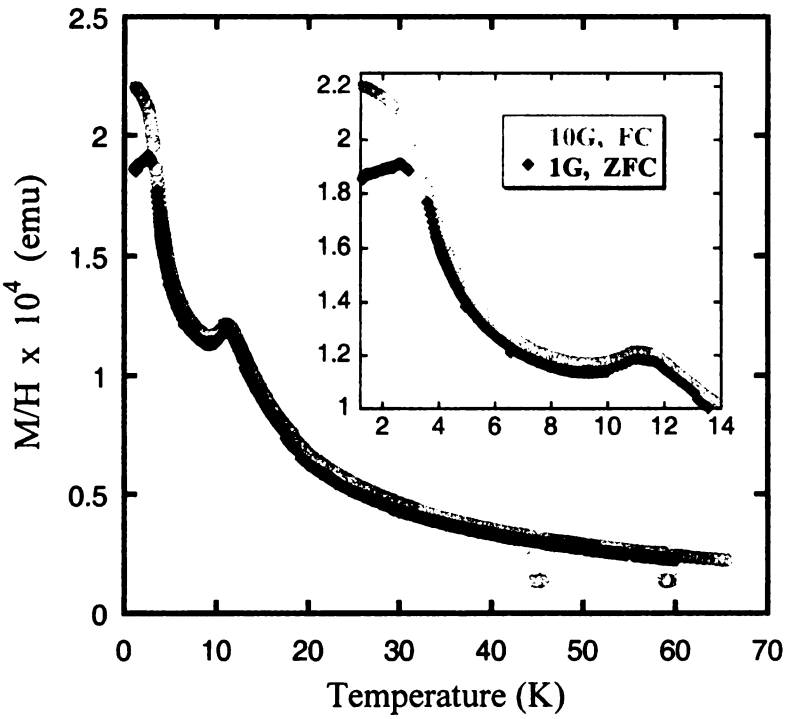

Figure 5-II-7. Temperature dependence of the susceptibility M/H of $EuAuGeIn_2$ measured on randomly oriented crystals with applied fields of 1 G for the ZFC mode (solid rhombi) and 10 G for the FC mode (open circles).

5-II-4. Conclusions

We have shown that the $BaNiSn_3$ type structure in the tetragonal *I4mm* space group, represents a better alternative for describing the crystal structure of the novel intermetallic compound of $EuAuGeIn_2$ than the $ThCr_2Si_2$-type structure in tetragonal *I4/mmm* space group. This conclusion was drawn because the refinement under *I4mm* space group offers the possibility of lower atomic site disorder and results in a stoichiometric composition that is in excellent agreement with the atomic ratio obtained by the EDS analysis.

The formation of $EuAuGeIn_2$ is another example in which liquid In acts as a reactive flux in reactions containing group 14 elements, despite the general tendency for In not to get incorporated into the compound when used in systems of the type RE/M/Ge. This also shows the great potential of metallic fluxes for exploratory solid state synthesis.

Additionally, our exploratory synthesis with In metal as a solvent in the system RE/Au/Ge with RE = Yb, Ce, Eu (Yb was employed in the work presented in the preceding chapter) under similar experimental conditions resulted in the three different intermetallic compounds of $Yb_3AuGe_2In_3$, CeAuGeIn and $EuAuGeIn_2$. Each of the three new compounds crystallizes under different structure type. This suggests that the size of the rare-earth cations likely plays a crucial role for the formation of quaternary phases in the system RE/TM/Ge/In, when the In-flux method. The detailed study of such systems can contribute in further understanding of the stoichiometry-structure-properties relationships which is a requirement for the development of new solid state materials.

Finally, preliminary low field magnetic measurements revealed a rather complex magnetic structure for the title compound as the material undergoes both an

antiferromagnetic transition with a Néel temperature of ~ T_N = 11 K as well as a ferromagnetic one at a temperature of 5 K. Future work on this compound is needed and could include attempts to grow bigger single crystals in higher yields in order to facilitate more detailed magnetic measurements and electrical conductivity. Neutron diffraction experiments could be also helpful to elucidate possible additional magnetic structures seen in the low field magnetic measurements. XANES measurements could also be useful for the probing the Eu valence configuration, as many Eu based intermetallics have shown mixed valence or valence fluctuating behavior.

References:

(1) Villars, P.; Calvert, L. D. *"Pearson's Handbook of Crystallographic Data for Intermetallic Phases", 2nd ed.; American Society for Metals* OH 44073, 1991.

(2) Kalychak, Ya. M. *J. Alloys Compd.* **1997**, *341*, 262.

(3) Szytula, A.; Leciejewicz, J. *"Handbook of Crystal Structures and Magnetic Properties of Rare Earth Intermetallics"*; CRC Press: Boca Raton, Fl, 1994.

(4) Sereni, J.G. *J. Phys. Soc. Jpn* **1998**, *67*, 1767.

(5) Lawrence, J.; Chen, Y.-Y.; Thompson, J. *Theoretical and Experimental Aspects of Valence Fluctuations and Heavy Fermions*; Plenum: New York and London, 1987.

(6) Pikul, A. P.; Kaczorowski, D.; Bukowski, Z.; Gofryk, K.; Burkhardt, U.; Grin, Y.; Steglich, F. *Phys. Rev. B* **2006**, *73*, 092406.

(7) Stewart, G. R. *Rev. Mod. Phys.* **1984**, *56*, 755.

(8) Nikiforov, V. N.; Kovacik, V.; Grischenko, I. O.; Velikhovski, A. A.; Mirkovic, J.; Shapiev, B. I.; Bodak, O. I.; Seropegin, Y. D. *Physica B* **1993**, *186-188*, 514.

(9) Moreno, N. O.; Hundley, M. F.; Pagliuso, P. G.; Movshovich, R.; Nicklas, M.; Thompson, J. D.; Sarrao, J. L.; Fisk, Z. *Physica B* **2002**, *312&313*, 241.

(10) Moreno, N. O.; Hundley, M. F.; Pagliuso, P. G.; Movshovich, R.; Nicklas, M.; Thompson, J. D.; Sarrao, J. L.; Fisk, Z. In *Physical properties of Ce-2(Rh,Ir)(1-x)CoxIn8* 2002, p 274-276.

(11) Mun, E. D.; Lee, B. K.; Kwon, Y. S.; Jung, M. H. *Phys. Rev. B* **2004**, *69*, 085113.

(12) Hong, J.B.; Park, T.; Kwon, Y.S. *J. Korean Phys. Soc.* **2005**, *47*, 479.

(13) Cornelius, A. L.; Pagliuso, P. G.; Hundley, M. F.; Sarrao, J. L. *Phys. Rev. B* **2001**, *6414*, 144411.

(14) Shim, J.H.; Haule, K.; Kotliar, G. *Science* **2007**, *318*, 1615.

(15) Joshi, D. A.; Tomy, C. V.; Malik, S. K. *J. Phys.: Condens. Matter* **2007**, *19*, 0953-8984.

(16) Hegger, H.; Petrovic, C.; Moschopoulou, E. G.; Hundley, M. F.; Sarrao, J. L.; Fisk, Z.; Thompson, J. D. *Phys. Rev. Lett.* **2000**, *84*, 4986.

(17) Petrovic, C.; Pagliuso, P. G.; Hundley, M. F.; Movshovich, R.; Sarrao, J. L.; Thompson, J. D.; Fisk, Z.; Monthoux, P. *J. Phys.: Condens. Matter* **2001**, *13*, L337-L342.

(18) Movshovich, R.; Jaime, M.; Thompson, J. D.; Petrovic, C.; Fisk, Z.; Pagliuso, P. G.; Sarrao, J. L. *Phys. Rev. Lett.* **2001**, *86*, 5152-5155.

(19) Izawa, K.; Yamaguchi, H.; Matsuda, Y.; Shishido, H.; Settai, R.; Onuki, Y. *Phys. Rev. Lett.* **2001**, *8705*, 4.

(20) Paglione, J.; Tanatar, M. A.; Hawthorn, D. G.; Boaknin, E.; Hill, R. W.; Ronning, F.; Sutherland, M.; Taillefer, L.; Petrovic, C.; Canfield, P. C. *Phys. Rev. Lett.* **2003**, *91*, 4.

(21) Jung, M. H.; N.Harrison; H.Lacerda, A.; Nakotte, H.; Pagliuso, P. G.; Sarrao, J. L.; Thompson, J. D. *Phys. Rev. B* **2002**, *66*, 054420.

(22) Malik, S. K.; Adroja, D.T. *Phys. Rev. B* **1991**, *43*, 6295.

(23) Lawrence, J. M.; Riseborough, P. S.; Park, R. D. *Rep. Progr. Phys.* **1981**, *44*, 1.

(24) Edelstein, A.S. *J. Magn. Magn. Mater.* **2003**, *256*, 430.

(25) Mun, E. D.; Kwon, Y. S.; Jung, M. H. *Phys. Rev. B* **2003**, *67*, 033103.

(26) Adroja, D.T.; Rainford, B.D. *J. Magn. Magn. Mater.* **1993**, *119*, 54.

(27) Adroja, D. T.; Hillier, A. D.; Park, J. G.; Kockelmann, W.; McEwen, K. A.; Rainford, B. D.; Jang, K. H.; Geibel, C.; Takabatake, T. *Phys. Rev. B* **2008**, *78*, 11.

(28) Lohneyson, H.v. *J. Magn. Magn. Mater.* **1999**, *200*, 532.

(29) Maple, M. B. *J. Phys. Soc. Jpn* **2005**, *74*, 222.

(30) Grewe, N.; Steglich, F. *Handbook on the Physics and Chemistry of Rare Earths* Elsevier Science Publishers B. V. : Amsterdam, 1994; Vol. 19, p 383.

(31) Doniach, S. *Physica B & C* **1977**, *91*, 231.

(32) Kittel, C. *Introduction to Solid State Physics* 7th ed.; John Wiley & Sons, 1996.

(33) Kanatzidis, M. G.; Pottgen, R.; Jeitschko, W. *Angewandte Chemie-International Edition* **2005**, *44*, 6996-7023.

(34) Chen, X. Z.; Small, P.; Sportouch, S.; Zhuravleva, M. ; Brazis, P.; Kannewurf, C. R.; Kanatzidis, M. G. *Chem. Mater.* **2000**, *12*, 2520.

(35) B. Sieve; X. Z. Chen; R. Henning; P. Brazis; C. R. Kannewurf; J. A. Cowen; A. J. Schultz; Kanatzidis, M. G. *J. Am. Chem. Soc* **2001**, *123*, 7040.

(36) Sieve, B.; Trikalitis, P. N.; Kanatzidis, M. G. *Z. Anorg. Allg. Chem.* **2002**, *628*, 1568-1574.

(37) Zhuravleva, M. A.; Pcionek, R. J.; Wang, X. P.; Schultz, A. J.; Kanatzidis, M. G. *Inorg. Chem.* **2003**, *42*, 6412.

(38) Zhuravleva, M. A.; Kanatzidis, M. G. *Z. Naturforch B : Sec. B* **2003**, *58*, 649.

(39) Latturner, S. E.; Bilc, D.; Mahanti, S. D.; Kanatzidis, M. G. *Inorg. Chem.* **2003**, *42*, 7959.

(40) Latturner, S. E.; Kanatzidis, M. G. *Inorg. Chem.* **2008**, *47*, 2089.

(41) Zhuravleva, M. A.; Evain, M.; Petricek, V.; Kanatzidis, M. G. *J. Am. Chem. Soc* **2007**, *129*, 3082.

(42) Wu, X. N.; Kanatzidis, M. G. *J. Solid State Chem.* **2005**, *178*, 3233.

(43) Wu, X. U.; Latturner, S. E.; Kanatzidis, M. G. *Inorg. Chem.* **2006**, *45*, 5358.

(44) Salvador, J. R.; Gour, J. R.; Bilc, D.; Mahanti, S. D.; Kanatzidis, M. G. *Inorg. Chem.* **2004**, *43*, 1403-1410.

(45) Salvador, J. R.; Kanatzidis, M. G. *Inorg. Chem.* **2006**, *45*, 7091-7099.

(46) Salvador, J. R.; Hoang, K.; Mahanti, S. D.; Kanatzidis, M. G. *Inorg. Chem.* **2007**, *46*, 6933

(47) Salvador, J. R.; Bilc, D.; Gour, J. R.; Mahanti, S. D.; Kanatzidis, M. G. *Inorg. Chem.* **2005**, *44*, 8670

(48) Chondroudi, M.; Balasubramanian, M.; Welp, U.; Kwok, W.-K.; Kanatzidis, M. G. *Chem. Mater.* **2007**, *19*, 4769-4775.

(49) *for related references see chapter four.*

(50) Bodak, O. I.; Gladyshevskii, E. I. *Kristallografiya* **1969**, *14*, 990.

(51) Bodak, O. P.; Gladyshe.Ei *Soviet Physics Crystallography, Ussr* **1970**, *14*, 859.

(52) GmbH, STOE & Cie In *X-RED - Data Reduction Program, X-SHAPE - Crystal Optimization for Numerical Absorption Correction* D 64295 Darmstadt, Germany, 2006.

(53) Bruker *Advanced X-ray Solutions SHELXTL (Version 6.14)*, Bruker AXS Inc., Madison, WI (2003).

(54) Farrugia, L. J. In *WinGX, Solution, Refinement and Analysis of Single Crystal X-Ray Diffraction Data*; version 1.70.01 ed. University of Glasgow, 1997-2005.

(55) Vandervoort, K.; Griffith, G.; Claus, H.; Crabtree, G. W. *Rev. Sci. Instrum.* **1991**, *62*, 2271.

(56) Li, Qing'An; Gray, K. E.; Mitchell, J. F. *Phys. Rev. B* **1999**, *59*, 9357 - 9361.

(57) Kraft, S.; Stumpel, J.; Becker, P.; Kuetgens, U. *Rev. Sci. Instrum.* **1996**, *67*, 681.

(58) Ravel, B.; Newville, M. *J. Synchrotron Rad.* **2005**, *12:4*, 537-541.

(59) Boher, P.; Garnier, P.; Gavarri, J.R.; Hewat, A.W. *J. Solid State Chem.* **1985**, *57*, 343.

(60) Boher, P.; Garnier, P.; Gavarri, J.R.; Hewat, A.W. *Phase Trans.* **1992**, *38*, 127.

(61) Okada, S.; Atoda, T.; Higashi, I. *J. Solid State Chem.* **1987**, *68*, 61.

(62) Okada, S.; Atoda, T.; Higashi, I. *Acta Chemica Scandinavica* **1949**, *3*, 595.

(63) Pauling, L.; Kamb, B. *Proc. Natl. Acad. Sci. U. S. A.* **1986**, *83*, 3569-3571.

(64) Galadzhun, Y. V.; Hoffmann, R.-D.; Pottgen, R.; Adam, M. *J. Solid State Chem.* **1999**, *148*, 425

(65) Schobinger-Papamantellos, P.; Krimmel, A.; Grauel, A.; Buschow, K.H.J. *J. Magn. Magn. Mater.* **1993**, *125*, 151.

(66) Niepmann, D.; Pottgen, R.; Kunnen, B.; Kotzyba, G.; Rosenhahn, C.; Mosel, B. D. *Chem. Mat.* **1999**, *11*, 1597-1602.

(67) Hossain, Z.; Gupta, L. C.; Geibel, C. *J. Phys.: Condens. Matter* **2002**, *14*, 9687-9691.

(68) Pottgen, R.; Borrmann, H.; Kremer, R. K. *J. Magn. Magn. Mater.* **1996**, *152*, 196.

(69) Jones, C. D. W.; Gordon, R. A.; DiSalvo, F. J.; Pottgen, R.; Kremer, R. K. *J. Alloys Comp.* **1997**, *50*, 260.

(70) Tran, V. H.; Gamza, M.; Slebarski, A.; Miiller, W.; Jarmuska, J. *J. Alloys Comp.* **2008**, *451*, 457-460.

(71) Sefat, A. S.; Palasyuk, A. M.; Bud'ko, S. L.; Corbett, J. D.; Canfield, P. C. *J. Solid State Chem.* **2008**, *181*, 282.

(72) Tran, V.H. *Phys. Rev. B* **2004**, *70*, 094424.

(73) Tran, V.H.; Jarmulska, J.; Miiller, W. *Mater. Sci. Poland*, in press.

(74) V. K. Pecharsky, et al *Phys. Rev. B* **1995**, *47*, 11839.

(75) S.L. Bud'ko, et al *Physica B* **1999**, *259-261*, 118.

(76) Das, A.; Nigam, A.K. *J. Phys.: Condens. Matter* **2000**, *12*, 1315.

(77) Materlik, G.; Muller, J. E.; Wilkins, J.W. *Phys. Rev. Lett.* **1983**, *50*, 267.

(78) Malterre, D. *Phys. Rev. B* **1991**, *43*, 1391.

(79) Rohler, J.; Wohlleben, D.; Kappler, J. P.; Krill, G. *Phys. Let.* **1984**, *103A*, 220.

(80) Janousova, B.; Wilhelm, F.; Jaouen, N.; Rogalev, A.; Sechovsky, V.; Elsevier Science Bv: 2005, p 127-129.

(81) C Giorgetti, et al *Phys. Rev. B* **1993**, *48*, 12732.

(82) In *Valence Fluctuations in Solids*; Falikov, L. M., Hanke, W., Malpe, M. P., Eds.; North-Holland Publishing Company, Amsterdam, New York, Oxford: Santa Barbara, Ca, 1981.

(83) Ban, Z.; Sikirica, M. *Acta Crystallogr.* **1965**, *18*, 594.

(84) Doerrscheidt, W.; Schaefer, H. *J. Less-Common Met.* **1978**, *58*, 209.

(85) Moze, O.; Buschow, K.H.J. *J. Alloys Comp.* **1996**, *245*, 112.

(86) Hoffmann, R. D.; Pottgen, R.; Zaremba, V. I.; Kalychak, Y. M. *Z. Naturforch B : Chem. Sci* **2000**, *55*, 834.

CHAPTER 6

Yb_4TMGe_8 (TM = Fe, Cr and Co) an In Flux Grown Intermetallic: Exhibiting Temperature Induced Yb Valence Fluctuation and Anomalous Thermal Expansion below ~ 100 K

6-1. Introduction

A large number of the ternary intermetallic compounds with the $RETMxTt_2$ composition,[1,2] where RE is a rare earth metal, TM is a transition metal (Mn, Fe, Ni, Co, Cu, Ru, Rh, Re, Ir, Pd, Pt) and Tt is a tetrelide element (Si, Ge, Sn) crystallize in the orthorhombic structure of $CeNiSi_2$-type (*Cmcm*).[3,4] The main characteristics of this structure are the slightly deformed square pyramidal coordination of the TM atoms while the Tt atoms define a flat square net. Some of them crystallize with the ideal composition ($x = 1$)[3,5,6] whereas the majority form a range of solid solutions ($0 < x < 1$) characterized by different degrees of TM deficiency.[7-14] At the present time, the origin of the vacancies on the TM-site has been little understood and structural studies of most systems have been performed primarily with X-ray powder diffraction techniques. The limited single crystal X-ray diffraction studies have given indications for superstructure existence in some cases, but have not been successfully resolved yet.[15,16] Single crystal X-ray and electron diffraction studies of the Tb_4FeGe_8 (or $TbFe_{0.25}Ge_2$) compound[14] revealed a strongly modulated square net of the Ge atoms. Additionally, for $SrAuSn_2$ where the RE has been substituted by Sr a commensurately modulated structure of the $CeNiSi_2$-type has been described.[17] It is thus of particular importance to synthesize high-quality single crystals of this type of systems in order to perform a more thorough structural

investigation, that could also shed further light on the nature of the observed TM deficiency and/or the possible distortion of the Tt atoms square sheets in some cases.

Among these rare earth-systems particularly the $CeTM_xTt_2$ compounds have been the focus of continuous interest as they exhibit a wealth of interesting physical phenomena such as magnetically ordered Kondo lattice behavior in $CeRhSn_2$[18,19] and $CeNiGe_2$,[20] heavy-fermion Kondo behavior in $CeCoGe_2$[6] and heavy-fermion valence fluctuating behavior in $CeCo_{0.89}Ge_2$[21] valence fluctuating behavior in $CeRhSi_2$[22] and $CeNiSi_2$[23,24] and heavy- fermion behavior in $CePtSi_2$.[25] These properties are associated with the presence of an unstable electronic 4*f*-shell, as Ce ion shows two electronic configurations that are closely spaced in energy: the magnetic Ce^{3+} ($4f^1$) and the nonmagnetic Ce^{4+} ($4f^0$). It is generally believed that, the stability of the different ground states depends strongly on the hybridization (interaction) strength between the magnetic 4*f* electrons and the *s*, *p*, and *d* conduction electrons.[26-28] It is interesting to add that Yb can also exhibit two energetically similar electronic configurations: the magnetic Yb^{3+} ($4f^{13}$) and the nonmagnetic Yb^{2+} ($4f^{14}$) one. Due to this feature Yb is usually considered as the "*f*-hole" analogue of Ce. Under this consideration, the roles of the 4*f* electron and 4*f* hole can be interchanged and many similar phenomena such as intermediate valence, Kondo effect or heavy-fermion behavior, are observed in Ce and Yb counterparts.[29-33] However, the Ce-based intermetallic compounds have been more extensively studied comparing to the Yb-based compounds due to the inherent difficulties in sample preparation (high vapor pressure of Yb metal). Even though today there is a significant number of structurally and physically characterized Yb compounds that exhibit many of the above intriguing properties[26,34-37] there have not been any reports of thorough

investigations of $YbTM_xTt_2$ compounds that adopt the $CeNiGe_2$-type or a variation, up to our knowledge. Consequently, it is of great interest to explore the crystallographic and physical properties of $YbTM_xTt_2$ systems.

In a recent review, it has been demonstrated that molten metal fluxes are excellent alternative to the conventional synthetic methods for the exploratory synthesis of new rare earth intermetallic compounds.[38] After our own successful investigations with Al and Ga fluxes in the systems RE/TM/Al/Si or Ge and RE/TM/Ga/Si or Ge which resulted in a numerous ternary and quaternary phases,[39-47] we have recently started employing molten In metal as a solvent in analogous systems. Within this work we have been able to isolate the germanides $RE_2Zn_3Ge_6$[48] and the β-$RENiGe_2$[49] where In acts as a non-reactive flux, as well as a number of intermetallic compounds in which In gets incorporated into the products including $RE_4Ni_2InGe_4$,[50] $RE_7Co_4InGe_{12}$,[51] $Dy_4CoInGe_4$, $Yb_3AuGe_2In_3$, CeAuGeIn and $EuAuGeIn_2$ (described in Chapters 3-5) and $REAu_2In_4$.[52] Interestingly, CeAuGeIn crystallizes as an ordered quaternary variant of the $CeNiSi_2$ structure. Here we report the In-flux synthesis and crystal growth of Yb_4TMGe_8 (TM = Cr, Fe and Co) compounds. We have successfully elucidated their superstructure by single crystal X-ray diffraction and (3+1) dimensional crystallography. The single crystal X-ray diffraction, magnetic properties for Yb_4TMGe_8 (TM = Cr, Fe), temperature dependent X-ray absorption near edge spectroscopy (XANES), heat capacity (for Yb_4CrGe_8) and electrical resistivity (for Yb_4CrGe_8) are reported. All Yb_4TMGe_8 compounds exhibit Yb mixed-valence behavior with the valence constantly changing with the temperature. Additionally, the compounds exhibit anomalous thermal expansion behavior below ~ 100

K and the Cr analog has an enhanced electronic specific heat coefficient γ suggesting possible heavy-fermion behavior.

6-2. Experimental section

Reagents:

The following reagents were used as purchased without further purification: Yb, (in the form of powder ground from metal lump, 99.99% HEFA Rare Earth Canada Co. Ltd), Fe (-100, +200 mesh, 99.9% Cerac, Milwaukee, WI), Cr (~200 mesh, 99.95% Cerac, Milwaukee, WI), Co (~100 mesh, 99.9% ESPI Metals, Ashland, OR), Ge (~100 mesh, 99.999% Cerac, Milwaukee, WI) and In (tear drops 99.99% Plasmaterials, Livermore, CA).

Synthesis:

Method A. Yb_4TMGe_8 (TM = Cr, Fe and Co) were obtained by combining 4 mmol of the ytterbium metal, 1 mmol transition metal, 4 mmol germanium and 30 mmol In in an Al_2O_3 (alumina) crucible under an inert nitrogen atmosphere inside a glove-box. The crucible was placed in a 15 mm fused silica tube, which was flame sealed under vacuum of 10^{-4} Torr, to prevent oxidation during heating. The reactants were then heated to 1000 ^{0}C over 12 h, maintained at that temperature for 5 h to allow proper homogenization, followed by cooling to 850 ^{0}C in 2 h and held there for 144 h. Finally, the system was allowed to slowly cool to 50 ^{0}C in 74 h. The reaction product was isolated from the excess In flux by heating at 350 ^{0}C and subsequent centrifugation through a coarse frit. Any remaining flux was removed by immersion and soniqation in glacial

acetic acid for 48 - 72 h. The final crystalline product was rinsed with water and dried with acetone. All three Yb_4TMGe_8 compounds form mainly as platelet-like silvery metallic rods while some crystals grow in an irregular shape. Main side product for all three compounds was the ternary Yb_2InGe_2 compound[53,54] (long rods) and small amounts of the binaries $YbIn_3$ (cubes) and $YbGe_{1.5-3}$ (cubes), as given by the EDS analysis. Additionally, for the Co analog crystals of $Yb_7Co_4InGe_{12}$ (needles) and $YbCoGe_2$ (plates) were also observed. Several crystals were carefully selected for elemental analysis, structure characterization, and the physical measurements reported here.

Method B. Yb_4CrGe_8 and Yb_4FeGe_8 were also obtained by combining 4 mmol of the ytterbium metal, 2 mmol gold, 8 mmol germanium and 30 mmol In in an Al_2O_3 (alumina) crucible under an inert nitrogen atmosphere inside a glove-box and Yb_4CoGe_8 was also obtained by combining 4 mmol of the ytterbium metal, 1 mmol cobalt, 6 mmol germanium and 30 mmol In in an Al_2O_3 (alumina) crucible under an inert nitrogen atmosphere inside a glove-box The crucible was placed in a 15 mm fused silica tube, which was flame sealed under vacuum of 10^{-4} Torr, to prevent oxidation during heating. The reactants were then heated with the same heating profile used in method A. This method reduced the amount of the main byproduct Yb_2InGe_2 and increased the yield in the target compounds.

Elemental Analysis:

Semi-quantitative microprobe elemental analysis was performed on several crystals of the compound using a HITACHI MODEL S-2700 Scanning Electron Microscope (SEM) equipped with a light-element window Noran System Six EDS

detector. Data were acquired by applying a 20 kV accelerating voltage and an acquisition time of 1 min. The EDS analysis gave an average atomic composition of 30.23 % Yb, 7.77 % Cr, 62 % Ge which is in excellent agreement with the final single crystal X-ray diffraction refinement results. Similar ratio resulted for the Fe and Co analogs.

X-ray Crystallography:

Yb_4CrGe_8. X-ray intensity data were initially collected at room temperature using a Bruker SMART Platform CCD diffractometer with graphite monochromatized Mo Ka (λ = 0.71073 Å) radiation. The SMART software was used for data acquisition and SAINT for data extraction and reduction.[55] An empirical absorption correction was applied using the program SADABS[55] and the structure of Yb_4CrGe_8 was solved by direct methods and refined with the SHELXTL package programs.[56] A stable refinement was accomplished in the orthorhombic space group *Cmcm,* and a total of four atomic positions were identified (all at 4*c* Wyckoff position). Data collection and structure refinement details are given in Table 6-1. The final atomic positions, equivalent isotropic displacement parameters and anisotropic displacement parameters are listed in Table 6-2 and 6-3. The site occupancy of the Cr atom was found to be reduced to only ¼ whereas the rest sites were found to be fully occupied. Additionally, the anisotropic displacement parameters U_{11} and U_{33} (directed along the *a* and *c*-axis, respectively) of Ge(2) atom were enlarged. The observed deficiency on the Cr site, unusual thermal displacement parameters and shortened Cr-Ge bond distances (2.133(2) Å) raised suspicion for the existence of a superstructure. For this reason, we recollected data on a STOE diffractometer with longer exposure time and we noticed that extra weak reflections were

revealed that were missed the first time of data collection with the CCD. This indicated the existence of a long range superstructure the solution and refinement of which is described below. The initial data collection (substructure) resulted in a very good refinement (R1 / wR2 = 0.0175 / 0.0439). However, this was misleading as it was later found that the initial substructure solution did not include all the diffraction information and thus did not fully describe the Yb_4CrGe_8 modulated superstructure.

Yb_4TMGe_8. The X-ray intensity data were collected at 100 K using a STOE IPDS 2T diffractometer with graphite-monochromatized Mo Kα (λ = 0.71073 Å) radiation, at Northwestern University (NU) facilities and at Materials Science Division (MSD) facilities at Argonne National Laboratory (ANL).The modulated structures were solved by our group member Dr. Christos Malliakas (Northwestern University). The X-AREA package suite was used for data reduction and analytical absorption corrections. The subcell (average structure) of Yb_4TMGe_8 (TM = Cr, Fe, Co) was solved by direct methods using the SHELXTL package. The superstructures were refined with JANA2000 software.[57] The length determination and refinement of the q-vectors was performed with the Peaklist 1.06 software part of the X-Area 1.39 suite[58] using a least square refinement algorithm.

In the (3+1)D crystallographic approach, the distortion (positional or temperature parameter) of a given atomic parameter x_4 in the subcell can be expressed by a periodic modulation function $p(x_4)$ in a form of a Fourier expansion:

$$p(k+x_4)=\sum_{n=1}^{m} A_{sn}\sin[2\pi\bar{q}_n(k+x_4)]+\sum_{n=1}^{m} A_{cn}\cos[2\pi\bar{q}_n(k+x_4)]$$

where A_{sn} is the sinusoidal coefficient of the given Fourier term, A_{cn} the cosine coefficient, n the number of modulation waves used for the refinement and k the lattice translation $\bar{q}_n = \sum_{i=1}^{d} \alpha_{ni} q_i$ where α_{ni} integer numbers for the linear combination of the incommensurate modulation vectors q_i.

Satellite reflections of first order were observed at 100 K and used for the refinement. One modulation wave for positional, temperature parameters and occupational (TM = Cr, Fe, Co) distortions were used. Only the symmetry allowed Fourier terms were refined. Data collection and structure refinement details, atomic coordinates, equivalent isotropic displacement parameters and atomic thermal parameters along with Fourier components of the corresponding modulations and finally the bond lengths distributions are given in Table 6-4 – 6-18(II).

All the temperature dependent measurements of the cell parameters were performed on the same single crystal for each analogue using both STOE IPDS 2T diffractometers at the ANL (MSD) and NU facilities. For Yb_4CrGe_8 and Yb_4CoGe_8 crystals the temperature range of 15 – 90 K was measured with the STOE at ANL while the higher temperatures were collected at NU. The temperature dependent data for the Yb_4FeGe_8 crystal were obtained at NU for the whole temperature range.

Table 6-1. Initial crystal data and substructure refinement data for Yb_4CrGe_8.

Empirical formula	Yb_4CrGe_8
Formula weight	1324.88
Temperature (K)	293(2)
Wavelength (Å)	0.71073
Crystal system	Orthorhombic
Space group	*Cmcm*
Unit cell dimensions (Å)	a = 4.0994(5)
	b = 15.582(2)
	c = 3.9869(5)
Volume ($Å^3$) / Z	254.67(6) / 1
Density (calculated) (Mg/m^3)	8.639
Absorption coefficient (mm^{-1})	60.479
F(000)	560
θ range for data collection (°)	2.61 to 28.12
Index ranges	$-5 \le h \le 5$, $-19 \le k \le 19$, $-5 \le l \le 5$
Reflections collected	1363
Independent reflections	195 [R(int) = 0.0347]
Completeness to theta = 28.12°	96.5 %
Refinement method	Full-matrix least-squares on F^2
Data / restraints / parameters	195 / 0 / 18
Goodness-of-fit on F^2	1.188
Final R indices [I>2sigma(I)]	R_1 = 0.0172, wR_2 = 0.0438
R indices (all data)	R_1 = 0.0175, wR_2 = 0.0439
Extinction coefficient	0.0040(4)
Largest diff. peak and hole ($e.Å^{-3}$)	1.032 and -1.270

$$^{a} R_1 = \Sigma \| F_o | - | F_c \| / \Sigma | F_o |; wR_2 = \left[\Sigma w \{ | F_o | - | F_c | \}^2 / \Sigma w | F_o |^2 \right]^{1/2}; w = 1/\sigma^2 \{ | F_o | \}.$$

Table 6-2. Atomic coordinates (x 10^4) and equivalent isotropic displacement parameters ($Å^2$ x 10^3) for Yb_4CrGe_8.

Atom	Wyck.	x	y	z	U(eq)[a]	Occup.(%)
Yb	4*c*	0	3974(1)	2500	9(1)	1
Ge(1)	4*c*	0	533(1)	2500	14(1)	1
Ge(2)	4*c*	0	7523(1)	2500	31(1)	1
Cr	4*c*	0	1990(3)	2500	4(1)	0.25

[a]U(eq) is defined as one third of the trace of the orthogonalized U^{ij} tensor.

Table 6-3. Anisotropic displacement parameters ($Å^2$ x 10^3) for Yb_4CrGe_8.

Atom	U^{11}	U^{22}	U^{33}	U^{23}	U^{13}	U^{12}
Yb(1)	9(1)	12(1)	7(1)	0	0	0
Ge(1)	9(1)	27(1)	6(1)	0	0	0
Ge(2)	35(1)	14(1)	45(1)	0	0	0
Cr(1)	3(1)	9(2)	0(2)	0	0	0

Table 6-4. Crystal data and structure refinement data for Yb_4CrGe_8 at 100.0(3) K.

Empirical formula	Yb_4CrGe_8
Formula weight	1324.9
Temperature (K)	100.0(3)
Wavelength (Å)	0.70926
Crystal system	Triclinic
Space group	$C1(\alpha\beta\gamma)0$
Unit cell dimensions (Å)	$a = 4.0919(5)$ $\alpha = 90°$ $b = 15.531(2)$ $\beta = 90°$ $c = 3.9745(5)$ $\gamma = 90°$
q-vector(1)	$1/4a^* + 1/4c^*$
Volume ($Å^3$) / Z	252.59(5) / 1
$Density_{calc}$ (Mg/cm^3)	8.7069(19)
Absorption coefficient (mm^{-1}) / F(000)	60.408 / 561
Crystal size (mm^3)	0.46 x 0.21 x 0.12
θ range for data collection (°)	4.03 to 32.9
Index ranges	$-5 \le h \le 6$, $-23 \le k \le 23$, $-5 \le l \le 6$, $-1 \le m \le 1$
Reflections collected	4743
Independent reflections	4011 [$R_{int} = 0.0591$]
Completeness to $\theta = 25.72°$	95%
Refinement method	Full-matrix least-squares on F^2
Data / restraints / parameters	4011 / 0 / 173
Goodness-of-fit on F^2	2.08
Final R indices [$I>3\sigma(I)$]	$R_{obs} = 0.0556$, $wR_{obs} = 0.1353$
R indices (all data)	$R_{all} = 0.0730$, $wR_{all} = 0.1402$
Final R main indices [$I>3\sigma(I)$]	$R_{obs} = 0.0469$, $wR_{obs} = 0.1192$
R main indices (all data)	$R_{all} = 0.0477$, $wR_{all} = 0.1196$
Final R 1st order satellites [$I>3\sigma(I)$]	$R_{obs} = 0.0893$, $wR_{obs} = 0.1717$
R 1st order satellites (all data)	$R_{all} = 0.1283$, $wR_{all} = 0.1791$
Extinction coefficient	0.041(5)
T_{min} and T_{max} coefficients	0.0056 and 0.0774
Largest diff. peak and hole ($e.Å^{-3}$)	4.33 and -4.90

$R = \Sigma||F_o|-|F_c|| / \Sigma|F_o|$, $wR = \{\Sigma[w(|F_o|^2 - |F_c|^2)^2] / \Sigma[w(|F_o|^4)]\}^{1/2}$ and $w=1/(\sigma^2(I)+0.0016I^2)$

Table 6-5. Atomic coordinates ($x10^4$), Fourier components of the displacive modulation ($x10^4$) and equivalent isotropic displacement parameters ($Å^2x10^4$) for Yb_4CrGe_8 at 100.0(3) K with estimated standard deviations in parentheses.

Atom	Wave	x	y	z	Occupancy	U(eq)
Yb(1a)	0	0	-3974	2549	1	5(1)
	sin, 1	15	29(1)	-37(5)		
	cos, 1	-65(4)	8(2)	77(4)		
Yb(1b)	0	-2(1)	3974(1)	7500(1)	1	5(1)
	sin, 1	-16(4)	23(1)	17(5)		
	cos, 1	73(4)	7(2)	-76(3)		
Ge(1a)	0	33(9)	-536(2)	2548(6)	1	6(1)
	sin, 1	-15(10)	84(2)	15(8)		
	cos, 1	39(10)	13(5)	-29(7)		
Ge(1b)	0	31(9)	523(2)	7556(6)	1	6(1)
	sin, 1	-12(10)	94(2)	-67(9)		
	cos, 1	-12(10)	14(6)	70(8)		
Ge(2a)	0	22(10)	-7525(2)	2635(8)	1	17(1)
	sin, 1	20(19)	-19(2)	195(20)		
	cos, 1	-204(12)	-1(3)	-351(16)		
Ge(2b)	0	16(11)	7517(2)	7646(10)	1	22(1)
	sin, 1	-85(30)	-17(2)	-165(20)		
	cos, 1	452(15)	-4(3)	260(16)		
Cr(1a)	0	-165(60)	-2059(12)	1995(60)	0.345(12)	1(1)
	sin, 1	215(70)	80(16)	765(70)		
	cos, 1	75(40)	21(9)	185(60)		
Cr(1b)	0	115(30)	2023(6)	7875(30)	0.182(10)	1(1)
	sin, 1	145(40)	69(9)	345(30)		
	cos, 1	25(50)	27(11)	155(40)		

Table 6-6. Fourier components of the atomic thermal parameters modulation ($x10^3$) for Yb_4CrGe_8 at 100.0(3) K with estimated standard deviations in parentheses.

Atom	Wave	U_{11}	U_{22}	U_{33}	U_{12}	U_{13}	U_{23}
Yb(1a)	0	4(1)	6(1)	5(1)	0(1)	2(1)	0(1)
	sin, 1	2(1)	0(1)	0(1)	1(1)	0(1)	3(1)
	cos, 1	-1(1)	-2(1)	4(1)	3(1)	-2(1)	-3(1)
Yb(1b)	0	4(1)	6(1)	5(1)	0(1)	2(1)	0(1)
	sin, 1	0(1)	-5(1)	1(1)	1(1)	0(1)	2(1)
	cos, 1	2(1)	-1(1)	-3(1)	0(1)	2(1)	2(1)
Ge(1a)	0	5(1)	12(1)	2(1)	1(1)	1(1)	2(1)
	sin, 1	-2(2)	0(2)	1(1)	3(1)	3(1)	1(1)
	cos, 1	0(2)	3(1)	-1(1)	0(1)	1(1)	1(1)
Ge(1b)	0	5(1)	12(1)	2(1)	1(1)	1(1)	2(1)
	sin, 1	-3(2)	-1(2)	-1(1)	2(1)	3(1)	1(1)
	cos, 1	0(2)	1(1)	2(1)	2(1)	2(1)	-2(1)
Ge(2a)	0	21(2)	5(1)	26(2)	4(1)	-11(1)	-3(1)
	sin, 1	22(2)	2(1)	-41(2)	0(1)	-4(1)	4(1)
	cos, 1	12(3)	4(1)	-1(3)	5(1)	1(2)	-4(1)
Ge(2b)	0	19(2)	10(1)	37(2)	-2(1)	-15(1)	9(1)
	sin, 1	-28(3)	2(1)	55(2)	0(1)	-2(2)	3(1)
	cos, 1	-16(3)	-3(1)	8(4)	-4(1)	-7(2)	0(1)

Table 6-7. Fourier components of the occupational modulation for Yb_4CrGe_8 at 100.0(3) K with estimated standard deviations in parentheses.

Atom	Wave	Occupational component
Cr(1a)	sin, 1	0.39(2)
	cos, 1	0.09(3)
Cr(1b)	sin, 1	-0.430(18)
	cos, 1	-0.12(3)

Table 6-8(I). Bond lengths distributions [Å] for Yb_4CrGe_8 at 100.0(3) K with estimated standard deviations in parentheses.

Atom	Average Distance	Minimum Distance	Maximum Distance
Yb(1a) - Ge(1a)	3.166(8)	3.101(7)	3.231(7)
Yb(1a) - Ge(1a)	3.182(8)	3.119(7)	3.246(7)
Yb(1a) - Ge(1b)	2.934(8)	2.914(8)	2.954(8)
Yb(1a) - Ge(1b) x 2	2.966(7)	2.919(8)	3.009(8)
Yb(1a) - Ge(1b)	2.982(8)	2.940(7)	3.024(7)
Yb(1a) - Ge(2a) x 2	3.041(8)	3.011(9)	3.071(8)
Yb(1a) - Ge(2b)	3.019(7)	2.989(7)	3.054(7)
Yb(1a) - Ge(2b)	3.095(7)	3.027(7)	3.159(7)
Yb(1a) - Cr(1a)	3.00(3)	2.94(3)	3.06(3)
Yb(1a) - Cr(1b) x 2	3.17(2)	3.09(2)	3.23(2)
Yb(1a) - Cr(1b)	3.24(2)	3.16(2)	3.37(2)
Yb(1a) - Cr(1b)	3.29(2)	3.20(2)	3.44(2)
Yb(1b) - Ge(1a)	2.930(7)	2.906(7)	2.956(7)
Yb(1b) - Ge(1a) x 2	2.958(7)	2.923(7)	2.988(8)
Yb(1b) - Ge(1a)	2.975(7)	2.952(7)	3.001(7)
Yb(1b) - Ge(1b)	3.150(8)	3.068(7)	3.235(7)
Yb(1b) - Ge(1b)	3.168(9)	3.097(8)	3.241(7)
Yb(1b) - Ge(2a)	3.029(7)	2.969(6)	3.091(6)
Yb(1b) - Ge(2a)	3.096(7)	3.010(7)	3.184(7)
Yb(1b) - Ge(2b) x 2	3.050(10)	2.963(9)	3.142(9)
Yb(1b) - Cr(1a)	3.39(3)	3.15(4)	3.70(3)
Yb(1b) - Cr(1a)	3.21(3)	3.18(3)	3.23(3)
Yb(1b) - Cr(1a)	3.31(3)	3.12(4)	3.58(3)
Yb(1b) - Cr(1a)	3.15(3)	2.96(4)	3.31(4)
Yb(1b) - Cr(1b)	3.069(19)	3.00(2)	3.108(17)
Ge(1a) - Ge(1b) x 2	2.579(8)	2.524(8)	2.632(8)
Ge(1a) - Ge(2b)	3.600(9)	3.409(8)	3.793(8)
Ge(1a) - Ge(2b)	3.644(9)	3.485(8)	3.803(8)
Ge(1a) - Cr(1a)	2.38(3)	2.35(2)	2.43(3)
Ge(1b) - Ge(2a)	3.612(9)	3.374(7)	3.845(7)
Ge(1b) - Ge(2a)	3.646(9)	3.462(8)	3.825(8)
Ge(1b) - Ge(2b) x 2	3.719(11)	3.495(9)	3.939(10)

Table 6-8(II). Bond lengths distributions [Å] for Yb_4CrGe_8 at 100.0(3) K with estimated standard deviations in parentheses (continue from part I).

Atom	Average Distance	Minimum Distance	Maximum Distance
Ge(1b) - Cr(1b)	2.35(2)	2.31(2)	2.369(18)
Ge(2a) - Ge(2b) x 4	2.848(13)	2.467(12)	3.237(12)
Ge(2a) - Cr(1a)	2.26(3)	2.18(3)	2.34(3)
Ge(2a) - Cr(1a)	2.16(3)	2.02(3)	2.31(4)
Ge(2a) - Cr(1b)	2.14(2)	1.80(2)	2.32(2)
Ge(2a) - Cr(1b)	2.22(2)	2.10(2)	2.29(2)
Ge(2b) - Cr(1a)	2.31(3)	2.13(4)	2.57(4)
Ge(2b) - Cr(1a)	1.94(3)	1.49(4)	2.30(4)
Ge(2b) - Cr(1b) x 2	2.25(3)	1.96(3)	2.41(2)
Cr(1a) - Cr(1b)	2.88(4)	2.80(4)	2.97(4)
Cr(1a) - Cr(1b)	3.32(4)	3.27(4)	3.43(4)
Cr(1a) - Cr(1b)	3.18(4)	2.97(4)	3.29(4)

Table 6-9. Crystal data and structure refinement data for Yb_4FeGe_8 at 100.0(3) K.

Empirical formula	Yb_4FeGe_8
Formula weight	1328.7
Temperature (K)	100.0(3)
Wavelength (Å)	0.70926
Crystal system	Triclinic
Space group	$C1(\alpha\beta\gamma)0$
Unit cell dimensions (Å)	$a = 4.0770(9)$ $\alpha = 90°$ $b = 15.395(4)$ $\beta = 90°$ $c = 3.9537(8)$ $\gamma = 90°$
q-vector(1)	$0.225(2)a^* + 0.269(2)c^*$
Volume ($Å^3$) / Z	248.15(9) / 1
$Density_{calc}$ (Mg/cm^3)	8.889(3)
Absorption coefficient (mm^{-1}) / F(000)	61.831 / 567
Crystal size (mm^3)	0.22 x 0.12 x 0.03
θ range for data collection (^{o})	3.92 to 31.63
Index ranges	$-6 \le h \le 6$, $-22 \le k \le 22$, $-6 \le l \le 5$, $-1 \le m \le 1$
Reflections collected	3863
Independent reflections	3460 [$R_{int} = 0.0601$]
Completeness to $\theta = 19.96°$	93%
Refinement method	Full-matrix least-squares on F^2
Data / restraints / parameters	3460 / 0 / 168
Goodness-of-fit on F^2	2.08
Final R indices [$I>3\sigma(I)$]	$R_{obs} = 0.0633$, $wR_{obs} = 0.1359$
R indices (all data)	$R_{all} = 0.1307$, $wR_{all} = 0.1824$
Extinction coefficient	1.08(17)
T_{min} and T_{max} coefficients	0.0065 and 0.1300
Largest diff. peak and hole ($e.Å^{-3}$)	8.66 and -12.46

$R = \Sigma||F_o|-|F_c|| / \Sigma|F_o|$, $wR = \{\Sigma[w(|F_o|^2 - |F_c|^2)^2] / \Sigma[w(|F_o|^4)]\}^{1/2}$ and

$w = 1/(\sigma^2(I)+0.0016I^2)$

Table 6-10. Atomic coordinates ($x10^4$), Fourier components of the displacive modulation ($x10^4$) and equivalent isotropic displacement parameters ($Å^2x10^4$) for Yb_4FeGe_8 at 100.0(3) K with estimated standard deviations in parentheses.

Atom	Wave	x	y	z	Occupancy	U(eq)
Yb(1a)	0	0	-3974	2549	1	5(1)
	sin, 1	15	12(2)	9(13)		
	cos, 1	-46(7)	8(3)	-61(8)		
Yb(1b)	0	1(2)	3984(1)	7502(3)	1	5(1)
	sin, 1	-11(8)	11(2)	-26(16)		
	cos, 1	57(6)	4(3)	85(9)		
Ge(1a)	0	10(17)	-551(4)	2559(19)	1	8(1)
	sin, 1	37(18)	66(7)	-5(20)		
	cos, 1	44(17)	30(11)	65(20)		
Ge(1b)	0	13(16)	531(4)	7558(18)	1	8(1)
	sin, 1	-40(15)	43(6)	-45(20)		
	cos, 1	-8(16)	18(8)	-15(20)		
Ge(2a)	0	33(17)	-7486(3)	2635(20)	1	18(1)
	sin, 1	25(30)	7(6)	25(40)		
	cos, 1	-145(20)	-29(6)	185(30)		
Ge(2b)	0	22(18)	7572(4)	7625(20)	1	18(1)
	sin, 1	-45(50)	-79(10)	-25(80)		
	cos, 1	265(20)	-56(12)	-475(30)		
Fe(1a)	0	-45(30)	-2041(13)	2265(50)	0.37(2)	6(2)
	sin, 1	35(60)	44(19)	185(80)		
	cos, 1	-65(50)	5(16)	-85(80)		
Fe(1b)	0	65(70)	2135(20)	7815(90)	0.22(2)	6(2)
	sin, 1	105(90)	215(20)	585(100)		
	cos, 1	115(90)	65(40)	55(140)		

Table 6-11. Fourier components of the atomic thermal parameters modulation ($x10^3$) for Yb_4FeGe_8 at 100.0(3) K with estimated standard deviations in parentheses.

Atom	Wave	U_{11}	U_{22}	U_{33}	U_{12}	U_{13}	U_{23}
Yb(1a)	0	1(1)	8(1)	5(1)	1(1)	0(1)	5(1)
	sin, 1	-3(1)	1(1)	4(1)	-4(1)	0(1)	-1(1)
	cos, 1	3(1)	2(1)	-3(2)	2(1)	1(1)	-1(1)
Yb(1b)	0	1(1)	8(1)	5(1)	1(1)	0(1)	5(1)
	sin, 1	0(1)	1(1)	4(1)	-1(1)	1(1)	-1(1)
	cos, 1	-1(1)	0(1)	0(2)	0(1)	-1(1)	2(1)
Ge(1a)	0	1(1)	17(1)	6(1)	1(1)	1(1)	7(1)
	sin, 1	-7(2)	11(4)	5(4)	-11(2)	-6(2)	1(3)
	cos, 1	3(3)	8(4)	-12(4)	2(3)	-1(2)	1(3)
Ge(1b)	0	1(1)	17(1)	6(1)	1(1)	1(1)	7(1)
	sin, 1	-4(3)	-2(3)	7(4)	-6(3)	-5(2)	0(3)
	cos, 1	-4(2)	-1(3)	11(3)	-14(2)	-3(2)	-1(3)
Ge(2a)	0	17(1)	8(1)	28(2)	1(1)	6(1)	2(1)
	sin, 1	9(3)	-2(3)	-22(4)	-14(3)	2(3)	4(3)
	cos, 1	4(4)	-2(3)	0(7)	-6(3)	-13(3)	6(4)
Ge(2b)	0	17(1)	8(1)	28(2)	1(1)	6(1)	2(1)
	sin, 1	-9(4)	13(3)	29(6)	1(3)	7(3)	20(5)
	cos, 1	-10(4)	12(3)	21(6)	3(2)	11(3)	27(4)

Table 6-12. Fourier components of the occupational modulation for Yb_4FeGe_8 at 100.0(3) K with estimated standard deviations in parentheses.

Atom	Wave	Occupational component
Fe(1a)	sin, 1	0.22(3)
	cos, 1	0.06(4)
Fe(1b)	sin, 1	-0.44(3)
	cos, 1	-0.06(8)

Table 6-13. Bond lengths distributions [Å] for Yb_4FeGe_8 at 100.0(3) K with estimated standard deviations in parentheses.

Atom	Average Distance	Minimum Distance	Maximum Distance
Yb(1a) - Ge(1a) x 2	3.167(16)	3.084(15)	3.250(15)
Yb(1a) - Ge(1b) x 2	2.921(14)	2.887(14)	2.958(14)
Yb(1a) - Ge(1b) x 2	2.952(14)	2.938(14)	2.967(14)
Yb(1a) - Ge(2a) x 2	3.060(15)	3.045(15)	3.076(14)
Yb(1a) - Ge(2b)	3.07(2)	2.98(2)	3.15(2)
Yb(1a) - Ge(2b)	3.13(2)	2.92(2)	3.33(2)
Yb(1a) - Fe(1a)	2.98(3)	2.93(4)	3.03(4)
Yb(1a) - Fe(1b) x 4	3.21(6)	3.20(5)	3.26(6)
Yb(1b) - Ge(1a) x 2	2.912(15)	2.874(15)	2.950(15)
Yb(1b) - Ge(1a) x 2	2.942(15)	2.929(15)	2.956(15)
Yb(1b) - Ge(1b) x 2	3.132(15)	3.085(14)	3.178(14)
Yb(1b) - Ge(2a)	2.973(14)	2.942(15)	3.002(15)
Yb(1b) - Ge(2a)	3.039(14)	2.987(12)	3.094(12)
Yb(1b) - Ge(2b) x 2	2.98(2)	2.88(2)	3.08(2)
Yb(1b) - Fe(1a) x 2	3.32(3)	3.19(3)	3.45(4)
Yb(1b) - Fe(1a) x 2	3.21(3)	3.19(3)	3.22(3)
Yb(1b) - Fe(1b)	2.99(6)	2.69(7)	3.18(5)
Ge(1a) - Ge(1b) x 2	2.585(18)	2.545(18)	2.627(19)
Ge(1a) - Ge(2a)	3.606(19)	3.434(18)	3.776(19)
Ge(1a) - Ge(2b) x 2	3.49(2)	3.19(2)	3.79(2)
Ge(1a) - Fe(1a)	2.30(4)	2.24(4)	2.35(4)
Ge(1b) - Ge(2a)	3.621(17)	3.478(16)	3.766(16)
Ge(1b) - Fe(1b)	2.35(6)	2.20(5)	2.61(7)
Ge(2a) - Ge(2b) x 4	2.86(3)	2.79(2)	2.92(2)
Ge(2a) - Fe(1a)	2.19(3)	2.15(4)	2.23(4)
Ge(2a) - Fe(1a)	2.13(3)	2.04(3)	2.21(3)
Ge(2a) - Fe(1b) x 2	2.15(6)	1.80(6)	2.35(6)
Ge(2b) - Fe(1a)	2.21(4)	2.11(4)	2.30(4)
Ge(2b) - Fe(1a)	1.94(4)	1.65(4)	2.22(4)
Ge(2b) - Fe(1b) x 2	2.25(5)	2.04(5)	2.40(5)
Fe(1a) - Fe(1b) x 2	3.06(6)	2.81(6)	3.22(6)
Fe(1a) - Fe(1b) x 2	3.24(7)	3.19(7)	3.28(6)

Table 6-14. Crystal data and structure refinement data for Yb_4CoGe_8 at 100.0(3) K.

Empirical formula	Yb_4CoGe_8
Formula weight	1331.8
Temperature (K)	100.0(3)
Wavelength (Å)	0.71069
Crystal system	Triclinic
Space group	$C1(\alpha\beta\gamma)0$
Unit cell dimensions (Å)	$a = 4.0542(7)$ $\alpha = 90°$ $b = 15.515(3)$ $\beta = 90°$ $c = 3.9402(6)$ $\gamma = 90°$
q-vector(1)	$0.2276(6)a^* + 0.2572(6)c^*$
Volume ($Å^3$) / Z	247.84(7) / 1
$Density_{calc}$ (Mg/cm^3)	8.920(3)
Absorption coefficient (mm^{-1}) / F(000)	62.722 / 567
Crystal size (mm^3)	0.34 x 0.12 x 0.02
θ range for data collection (°)	4.01 to 29.13
Index ranges	$-5 \le h \le 5$, $-20 \le k \le 21$, $-5 \le l \le 5$, $-1 \le m \le 1$
Reflections collected	3473
Independent reflections	2974 [$R_{int} = 0.024$]
Completeness to $\theta = 24.68°$	92%
Refinement method	Full-matrix least-squares on F^2
Data / restraints / parameters	2974 / 0 / 162
Goodness-of-fit on F^2	1.80
Final R indices [$I>3\sigma(I)$]	$R_{obs} = 0.0612$, $wR_{obs} = 0.2004$
R indices (all data)	$R_{all} = 0.0780$, $wR_{all} = 0.2210$
Extinction coefficient	0.0160(5)
T_{min} and T_{max} coefficients	0.0245 and 0.2373
Largest diff. peak and hole ($e.Å^{-3}$)	8.17 and -7.77

$R = \Sigma||F_o|-|F_c|| / \Sigma|F_o|$, $wR = \{\Sigma[w(|F_o|^2 - |F_c|^2)^2] / \Sigma[w(|F_o|^4)]\}^{1/2}$ and

$w=1/(\sigma^2(I)+0.0063999998I^2)$

Table 6-15. Atomic coordinates ($x10^4$), Fourier components of the displacive modulation ($x10^4$) and equivalent isotropic displacement parameters ($Å^2x10^4$) for Yb_4CoGe_8 at 100.0(3) K with estimated standard deviations in parentheses.

Atom	Wave	x	y	z	Occupancy	U_{eq}
Yb(1a)	0	0	-3974	2549	1	4(1)
	sin, 1	15	6(1)	18(5)		
	cos, 1	-32(3)	3(1)	-47(3)		
Yb(1b)	0	2(2)	3970(1)	7489(2)	1	4(1)
	sin, 1	-15(3)	5(1)	-18(5)		
	cos, 1	32(2)	3(1)	51(3)		
Ge(1a)	0	32(9)	-543(3)	2598(7)	1	9(1)
	sin, 1	-2(8)	37(2)	-6(7)		
	cos, 1	11(8)	15(4)	37(6)		
Ge(1b)	0	39(9)	523(3)	7606(7)	1	9(1)
	sin, 1	-8(8)	42(3)	7(7)		
	cos, 1	-10(8)	16(4)	-33(7)		
Ge(2a)	0	35(9)	-7521(2)	2752(7)	1	9(1)
	sin, 1	74(12)	-28(2)	-96(10)		
	cos, 1	-88(11)	1(3)	77(11)		
Ge(2b)	0	37(9)	7536(2)	7686(8)	1	9(1)
	sin, 1	-83(15)	-36(2)	125(20)		
	cos, 1	128(12)	-2(4)	-200(13)		
Co(1a)	0	-15(20)	-1947(5)	2615(20)	0.3928	2(1)
	sin, 1	35(20)	8(6)	25(20)		
	cos, 1	-39(19)	-2(5)	-58(15)		
Co(1b)	0	-505(110)	2045(30)	8015(100)	0.1962	2(1)
	sin, 1	-635(130)	75(40)	455(130)		
	cos, 1	-175(90)	18(18)	215(70)		

Table 6-16. Fourier components of the atomic thermal parameters modulation ($x10^3$) for Yb_4CoGe_8 at 100.0(3) K with estimated standard deviations in parentheses.

Atom	Wave	U_{11}	U_{22}	U_{33}	U_{12}	U_{13}	U_{23}
Yb(1a)	0	5(1)	1(1)	6(1)	0(1)	1(1)	0(1)
	sin, 1	0(1)	0(1)	1(1)	0(1)	1(1)	0(1)
	cos, 1	0(1)	0(1)	-1(1)	-1(1)	-1(1)	0(1)
Yb(1b)	0	5(1)	1(1)	6(1)	0(1)	1(1)	0(1)
	sin, 1	1(1)	0(1)	0(1)	0(1)	0(1)	0(1)
	cos, 1	0(1)	0(1)	1(1)	1(1)	1(1)	1(1)
Ge(1a)	0	10(1)	10(1)	7(1)	1(1)	0(1)	-1(1)
	sin, 1	6(1)	3(2)	0(1)	-3(1)	1(1)	-2(1)
	cos, 1	4(2)	-2(1)	0(1)	0(1)	1(1)	0(1)
Ge(1b)	0	10(1)	10(1)	7(1)	1(1)	0(1)	-1(1)
	sin, 1	5(1)	1(2)	2(1)	-3(1)	3(1)	-2(1)
	cos, 1	1(2)	2(1)	0(1)	-5(1)	-1(1)	-1(1)
Ge(2a)	0	10(1)	10(1)	7(1)	1(1)	0(1)	-1(1)
	sin, 1	3(2)	1(2)	-7(1)	0(1)	-1(1)	-1(1)
	cos, 1	2(2)	-1(1)	-3(1)	4(1)	3(1)	4(1)
Ge(2b)	0	10(1)	10(1)	7(1)	1(1)	0(1)	-1(1)
	sin, 1	-4(2)	2(2)	5(1)	1(1)	0(1)	-2(1)
	cos, 1	-2(2)	2(1)	5(2)	1(1)	-3(1)	5(1)

Table 6-17. Fourier components of the occupational modulation for Yb_4CoGe_8 at 100.0(3) K with estimated standard deviations in parentheses.

Atom	Wave	Occupational component
Co(1a)	sin, 1	0.190(11)
	cos, 1	0.07(2)
Co(1b)	sin, 1	-0.240(14)
	cos, 1	-0.09(3)

Table 6-18(I). Bond lengths distributions [Å] for Yb_4CoGe_8 at 100.0(3) K with estimated standard deviations in parentheses.

Atom	Average Distance	Minimum Distance	Maximum Distance
Yb(1a) - Ge(1a) x 2	3.159(9)	3.122(8)	3.198(8)
Yb(1a) - Ge(1b)	2.894(8)	2.880(8)	2.908(8)
Yb(1a) - Ge(1b)	2.950(8)	2.936(8)	2.965(8)
Yb(1a) - Ge(1b)	2.916(8)	2.899(8)	2.933(8)
Yb(1a) - Ge(1b)	2.972(8)	2.957(8)	2.985(8)
Yb(1a) - Ge(2a)	3.025(9)	2.973(8)	3.076(8)
Yb(1a) - Ge(2a)	3.043(9)	3.023(9)	3.064(8)
Yb(1a) - Ge(2b)	3.016(7)	2.942(7)	3.089(7)
Yb(1a) - Ge(2b)	3.111(7)	3.069(7)	3.152(7)
Yb(1a) - Co(1a)	3.146(12)	3.138(12)	3.155(12)
Yb(1a) - Co(1b) x 2	3.22(6)	3.11(7)	3.39(7)
Yb(1a) - Co(1b)	3.41(6)	3.15(7)	3.74(6)
Yb(1a) - Co(1b)	3.04(6)	2.81(6)	3.22(7)
Yb(1b) - Ge(1a)	2.889(8)	2.872(8)	2.906(8)
Yb(1b) - Ge(1a)	2.947(8)	2.933(8)	2.961(8)
Yb(1b) - Ge(1a)	2.906(8)	2.893(8)	2.920(8)
Yb(1b) - Ge(1a)	2.963(8)	2.948(8)	2.979(8)
Yb(1b) - Ge(1b)	3.140(9)	3.094(9)	3.186(8)
Yb(1b) - Ge(1b)	3.159(9)	3.120(8)	3.198(8)
Yb(1b) - Ge(2a)	2.973(5)	2.925(5)	3.021(5)
Yb(1b) - Ge(2a)	3.107(5)	3.099(5)	3.115(5)
Yb(1b) - Ge(2b)	3.002(9)	2.938(9)	3.066(9)
Yb(1b) - Ge(2b)	3.022(9)	2.988(9)	3.054(9)
Yb(1b) - Co(1a) x 2	3.142(13)	3.094(13)	3.190(14)
Yb(1b) - Co(1a) x 2	3.199(13)	3.192(13)	3.206(13)
Yb(1b) - Co(1b)	3.04(6)	2.97(7)	3.10(7)
Ge(1a) - Ge(1b) x 2	2.570(7)	2.554(7)	2.587(7)
Ge(1a) - Ge(2b)	3.555(9)	3.449(8)	3.657(8)
Ge(1a) - Ge(2b)	3.593(9)	3.458(8)	3.726(8)
Ge(1a) - Co(1a)	2.178(14)	2.126(14)	2.229(14)

Table 6-18(II). Bond lengths distributions [Å] for Yb_4CoGe_8 at 100.0(3) K with estimated standard deviations in parentheses (continue from part I).

Atom	Average Distance	Minimum Distance	Maximum Distance
Ge(1b) - Co(1b)	2.35(6)	2.31(7)	2.44(7)
Ge(2a) - Ge(2b) x 2	2.847(11)	2.831(11)	2.864(11)
Ge(2a) - Ge(2b) x 2	2.809(11)	2.635(11)	2.984(11)
Ge(2a) - Co(1a)	2.236(16)	2.185(16)	2.288(16)
Ge(2a) - Co(1a)	2.196(16)	2.161(16)	2.229(16)
Ge(2a) - Co(1b) x 2	2.08(6)	1.83(5)	2.27(6)
Ge(2b) - Co(1a)	2.158(13)	2.063(14)	2.253(14)
Ge(2b) - Co(1a)	2.099(13)	2.030(13)	2.167(13)
Ge(2b) - Co(1b)	2.35(6)	2.24(7)	2.52(6)
Ge(2b) - Co(1b)	2.05(6)	1.74(7)	2.29(7)
Co(1a) - Co(1b) x 2	3.27(6)	3.24(7)	3.33(7)
Co(1a) - Co(1b)	3.40(6)	3.22(7)	3.66(6)
Co(1a) - Co(1b)	3.10(6)	2.77(6)	3.35(7)

Magnetic Measurements:

Magnetization measurements for Yb_4CrGe_8 and Yb_4FeGe_8 were conducted using a Quantum Design MPMS SQUID magnetometer equipped with reciprocating sample option (RSO) mode as well as a Quantum Design PPMS magnetometer at Materials Science Division (MSD) facilities at Argonne National Laboratory (ANL), IL, USA. For these measurements crystals were soaked in glacial acetic acid and soniqated for 24–48 hrs, washed out with dried acetone and dried under the flow of nitrogen. Subsequently, crystals were loaded randomly without grounding into gelatin capsules, mounted in a plastic straw and affixed to the end of a carbon fiber rod. Temperature dependence data were collected for both zero field cooled (ZFC) and field cooled mode (FC) between 2 and 400 K, with applied fields of 1 kG and 600 G for Yb_4CrGe_8 and Yb_4FeGe_8, respectively. A typical measurement consists of initial cooling from room temperature (300 K) down to 2 K with no applied field, then the selected field is turned on and the ZFC data are collected on warming, followed with the collection of the FC data on cooling back to 2 K and with the applied field still on. Field dependent magnetic measurements were acquired at 5 K with field sweeping from – 30 kG up to 60 kG for Yb_4CrGe_8 and at 2 K with field sweeping from 0 G up to 62 kG for Yb_4FeGe_8. The raw data were corrected for the sample holder (straw) contribution. There were not magnetic measurements performed for Yb_4CoGe_8 up to this point.

X-ray absorption near edge spectroscopy (XANES):

X-ray absorption near edge spectroscopy (XANES) experiments were performed in Sector 20, bending magnet beamline (PNC/XOR, 20-BM) of the Advanced Photon Source at the Argonne National Laboratory, IL, USA. Measurements at the Yb L_{III}-edge and at ambient pressure were performed in the transmission mode using gas ionization chambers to monitor the incident and transmitted X-ray intensities. A third ionization chamber was used in conjunction with a copper foil to provide internal calibration for the alignment of the edge positions. Monochromatic X-rays were obtained using a Si (111) double crystal monochromator. The monochromator was calibrated by defining the inflection point (first derivative maxima) of Cu foil as 8980.5 eV.[59] A rhodium-coated X-ray mirror was utilized to suppress higher order harmonics. The Yb_4FeGe_8, Yb_4CrGe_8, Yb_4CoGe_8 samples were prepared by mixing an appropriate amount of finely ground powder of each sample with BN powder (to minimize self-absorption) and cold pressing them into a pellet. Most of sample preparation procedures were carried out inside a glove box environment. Measurements were performed at a range of temperatures from 15 K to 300 K using a closed cycle refrigerator. Data reduction and analysis were performed using Athena and Artemis software developed by Newville and Ravel.[60] Care was taken to minimize thickness effects in the measurements.

Heat Capacity:

Specific heat measurements of single crystals of Yb_4CrGe_8 were performed at Northwestern University facilities with a Quantum Design PPMS commercial device in the temperature range 2.96 – 50.8 K by relaxation method using the "Two-Tau Model".[61]

Resistivity:

For Yb_4FeGe_8 electrical resistivity was determined using a six probe technique in a standard ^4He gas flow cryostat, at Materials Science Division (MSD) at Argonne National Laboratory (ANL). A current of 1 mA was applied along the length of a platelet-like rod shaped crystal. Heating was avoided by reducing the current, and hysteresis, caused by slight thermometer - sample temperature differences, was avoided by sweeping the temperature slowly. More detailed experimental description can be found elsewhere.[62] Data points were taken during the cooling cycle from 301.75 K to 2.29 K.

6-3. Results and Discussion

Reaction Chemistry:

The compound Yb_4CoGe_8 was first discovered in a reaction that was initially designed to optimize the In flux synthesis of the $Yb_7Co_4InGe_{12}$ phase, described in Chapter 2, while Yb_4CrGe_8 was found in an attempt to form the Cr analog of $Yb_7Co_4InGe_{12}$. After a synthesis method was established for Yb_4CoGe_8 and Yb_4CrGe_8 other 1st row transition metals were also employed in similar reactions in order to produce more members in the Yb_4TMGe_8 series. When Fe, Ni and Mn substituted for Cr or Co only Fe formed the targeted Yb_4FeGe_8 compound. Additionally, attempts were made to synthesize the Cr and Co members with Sn and Ga as fluxes instead of In in order to bypass the formation of the main impurity product of Yb_2InGe_2.[53,54] Both alternative fluxes did not succeed in producing the corresponding Yb_4TMGe_8 compounds. Furthermore, Yb was substituted for Lu but another phase was formed which will be reported in a future work. All three title ternary Yb_4TMGe_8 compounds stabilize in In

flux, but in contrary to the systems presented in chapters 2-5, in this case In acts as a non-reactive flux in reactions of the type Yb/TM/Ge/In and does not get incorporated into the targeted product. Nevertheless, Yb_4TMGe_8 compounds form mainly as platelet-like silvery metallic rods while some crystals grow in an irregular shape. From the three analogs usually Yb_4CrGe_8 crystals grow in larger size. Figure 6-1 gives scanning electron micrographs of some typical Yb_4TMGe_8 crystals.

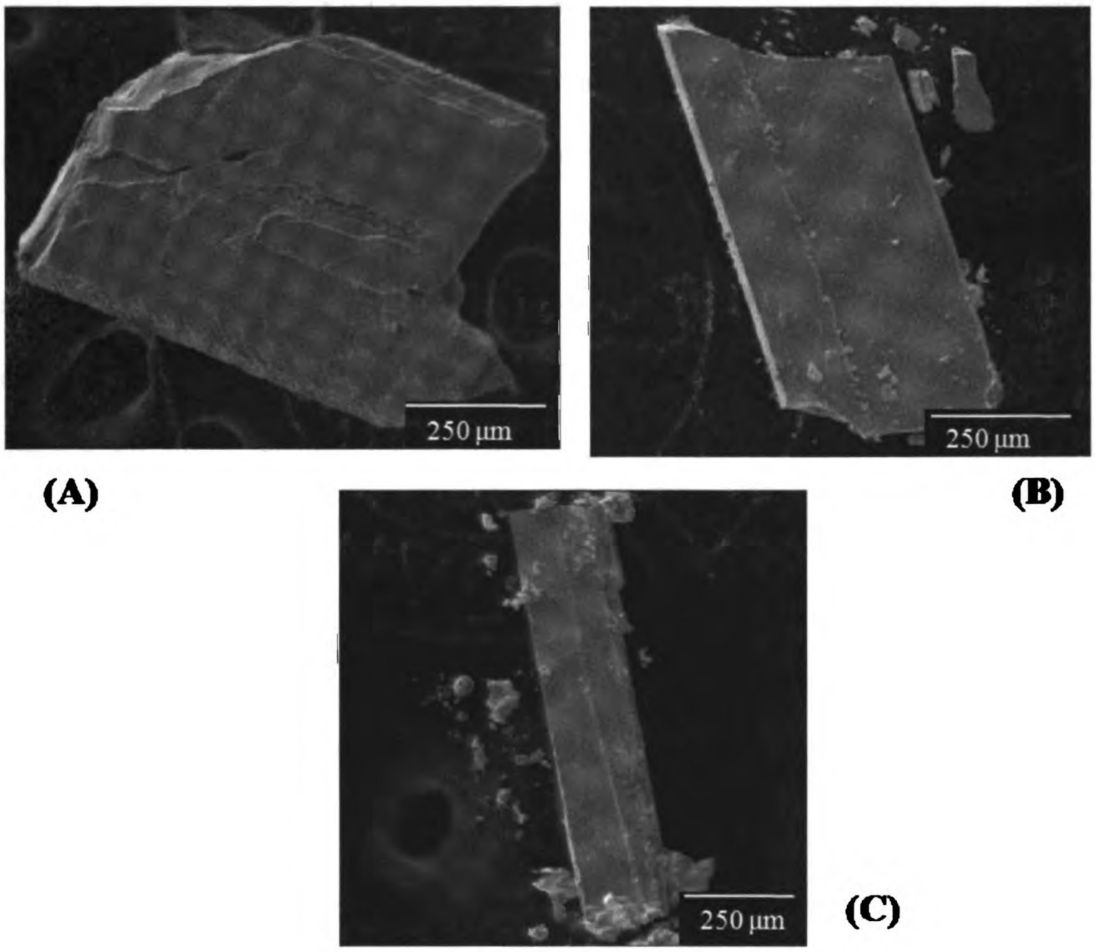

Figure 6-1. Scanning Electron micrograph (SEM) images of flux-grown crystals of (A) Yb_4CrGe_8, (B) Yb_4FeGe_8 and (C) Yb_4CoGe_8.

Structure:

(A) Substructure

The new intermetallic Yb_4TMGe_8 (TM = Cr, Fe and Co) average structure is closely related to the $CeNiSi_2$ structure type (orthorhombic *Cmcm* space group), with the Yb and Ge atoms occupying the Ce and Ge positions, respectively, and TM adopting the Ni sites with the difference that in the title compounds the TM is only partially occupied while in the prototype there is no deficiency on the corresponding Ni site. Due to the similar substructure of all three title compounds only the Yb_4CrGe_8 one is described. The overall substructure of Yb_4CrGe_8 (or $YbCr_{0.25}Ge_2$) as viewed down the *a*-axis is illustrated in Figure 6-2. The bonds to the Yb atoms were omitted to emphasize the three-dimensional (3D) $[Cr_{1/4}Ge(2)_2]$ framework and its channels. In Yb_4CrGe_8, all of the Yb, Cr and Ge atoms are located in alternating layers stacked along the long *b*-axis in the sequence: Yb-Cr-Ge(2)-Cr-Yb-Ge(1)-Ge(1)-Yb-Cr-Ge(2)-Cr-Yb. The structure can also be described as an intergrowth of distorted PbO- and CrB-type layers[63-66] (see Figure 6-2) with the Yb atoms residing within the channels formed by the connection of the two layers, see Figure 6-3. Detailed descriptions of the two structural fragments are given below.

The distorted PbO-type slab contains the Cr and Ge(2) atoms. In this, the tetrahedrally coordinated (by 4 Cr atoms) Ge(2) atoms form a 2-dimensional (2D) quadratic sheet that extends in the *ac*-plane (Figure 6-4(A)) and is capped by Cr atoms alternatively above and below this plane, thus forming a puckered overall layer, see Figure 6-4(B). The CrB-type layer on the other hand, is composed of Yb and Ge(1) atoms in the Cr and B positions, respectively. In this, the Ge(1) atoms form one dimensional

(1D) infinite zigzag chains propagating along the *c*-axis, Figure 6-2. The Ge(2) square sheets and Ge(1) zigzag chains, described above, are bridged by the Cr atoms along the *b*-axis thus building the 3D $[Cr_{1/4}Ge(2)_2]$ open framework. The connection of the two layers creates channels that extend down the *c*-axis, and each of them accommodates a pair of Yb columns, see Figure 6-3. The connection of the two layers with Cr – Ge(1) bonds makes for a 5 coordinate (4 Ge(2) and 1 Ge(1) atom) distorted square pyramidal geometry for the Cr atoms, and 3 coordinate (2 Ge(1) and 1 Cr atom) trigonal planar arrangement for the Ge(1) atoms. This is a common geometry in intermetallic compounds when one neglects the RE contacts.

(B) Superstructure

Supercell reflections were observed in the reciprocal space due to the modulation of the Ge atoms in the extended square net. A superspace crystallographic approach was necessary since most of the distortions were incommensurate in respect to the underline lattice. The Yb_4TMGe_8 (TM = Cr, Fe, Co) family adopts the $C1(\alpha\beta\gamma)0$ superspace group. The q-vector for $Yb_4Cr_{1-x}Ge_8$ is commensurate and along the *ac*-plane in the form 1/4a* + 1/4c*. The q-vectors for $Yb_4Fe_{1-x}Ge_8$ and $Yb_4Co_{1-x}Ge_8$ are incommensurate with lengths $0.225(2)a^* + 0.269(2)c^*$ and $0.2276(6)a^* + 0.2572(6)c^*$ respectively. Interestingly, the refinement suggested that the resulted vacancies in the *a,c*-layer of Yb_4TMGe_8 due to the occupational modulation, are long range ordered (Tables 6-7, 6-12 and 6-17), see Figures 6-5(A), 6-6(A) and 6-7(A) for Yb_4CrGe_8, Yb_4FeGe_8 and Yb_4CoGe_8, correspondingly.

The distortion creates a wide distribution of distances between the Ge atoms within the net. Specifically, in Yb_4CrGe_8 the minimum Ge-Ge distance is 2.524(8) Å and the maximum 2.632(8) Å. By choosing the bonding threshold to be 2.7 Å, the Ge-net can be seen as a sequence of dimers, Figure 6-8. In Yb_4FeGe_8 the minimum distance is 2.585(18) Å and maximum 2.627(19) Å whereas in Yb_4CoGe_8 these values are 2.570(7) Å and 2.587(7) Å, respectively, see Figures 6-9 and 6-10.

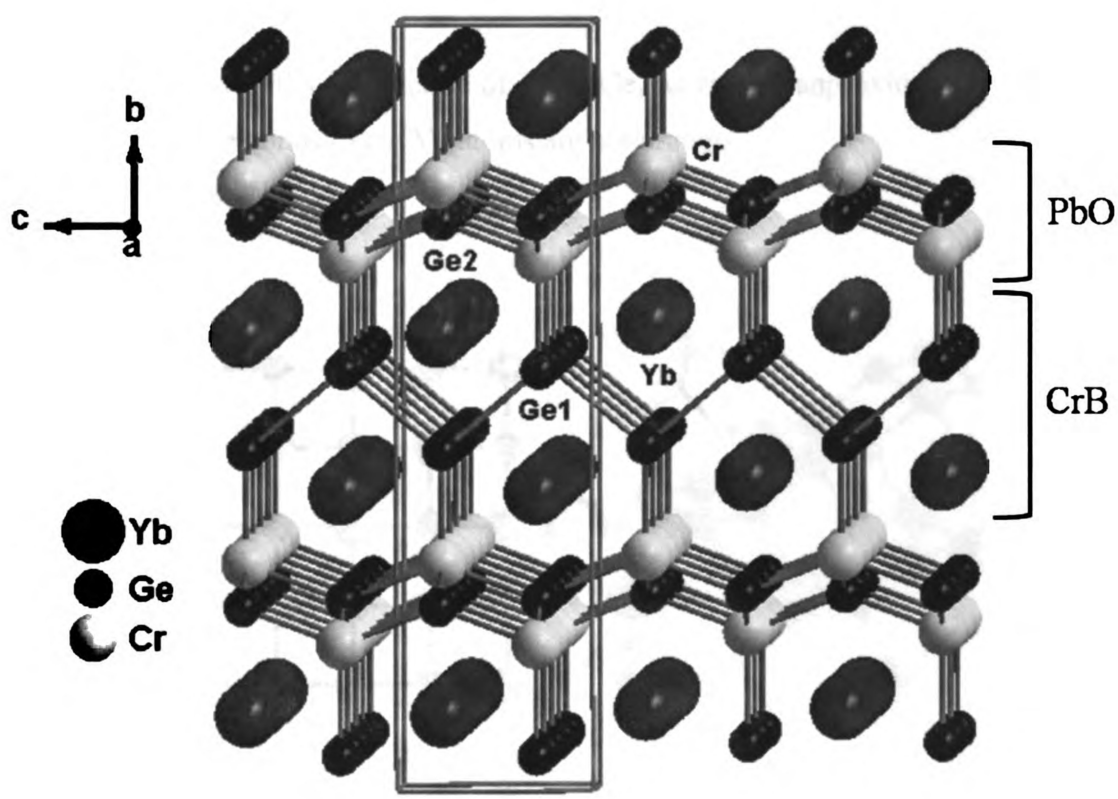

Figure 6-2. The overall sub-structure of Yb_4CrGe_8 as viewed approximately onto the *b,c*-plane. For clarity the bonds to the Yb atoms are not drawn.

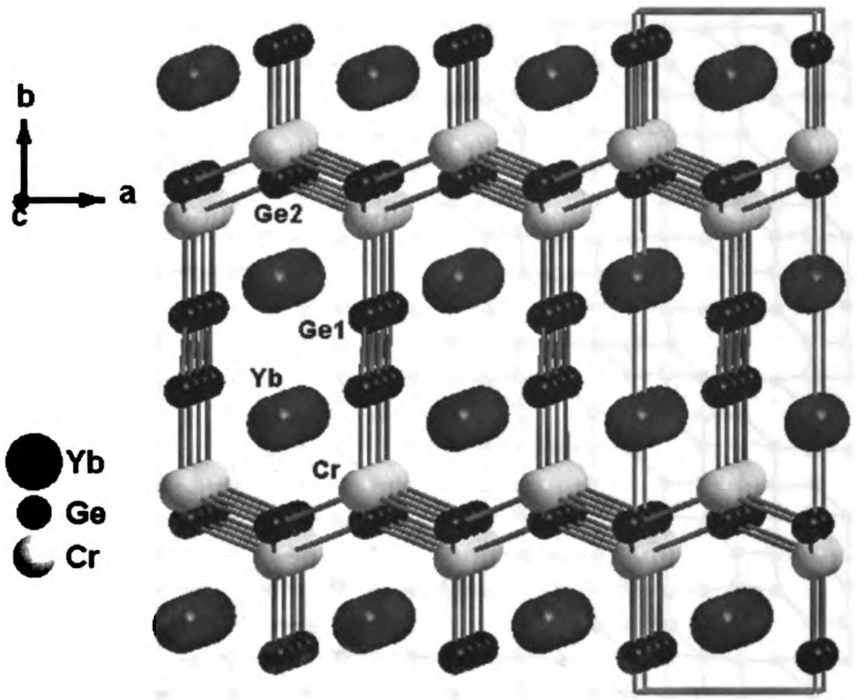

Figure 6-3. The overall sub-structure of Yb_4CrGe_8 as viewed approximately down the *c*-axis. For clarity the bonds to the Yb atoms are not drawn.

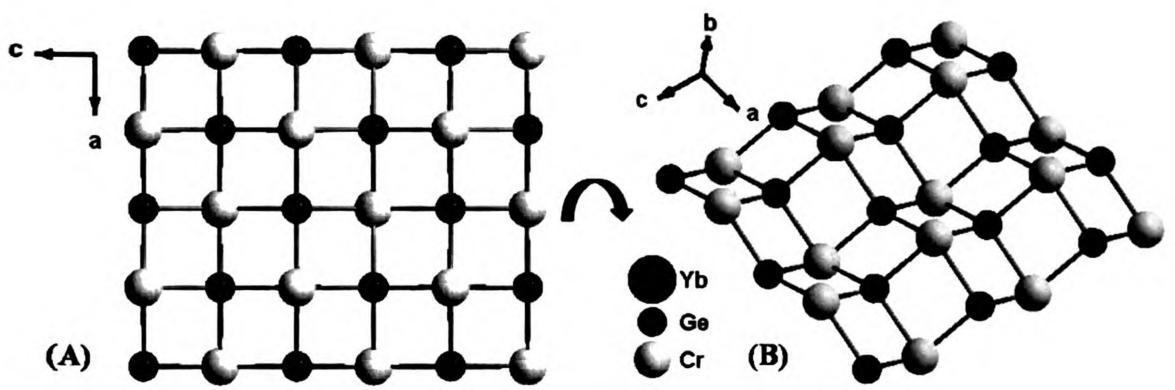

Figure 6-4. (A) Projection of a fragment of the $[Cr_{1/4}Ge(2)_2]$: PbO-type layer onto the *a*,*c*-plane (B) a rotated view of the $[Cr_{1/4}Ge(2)_2]$: slab where the puckered form of the layer is emphasized.

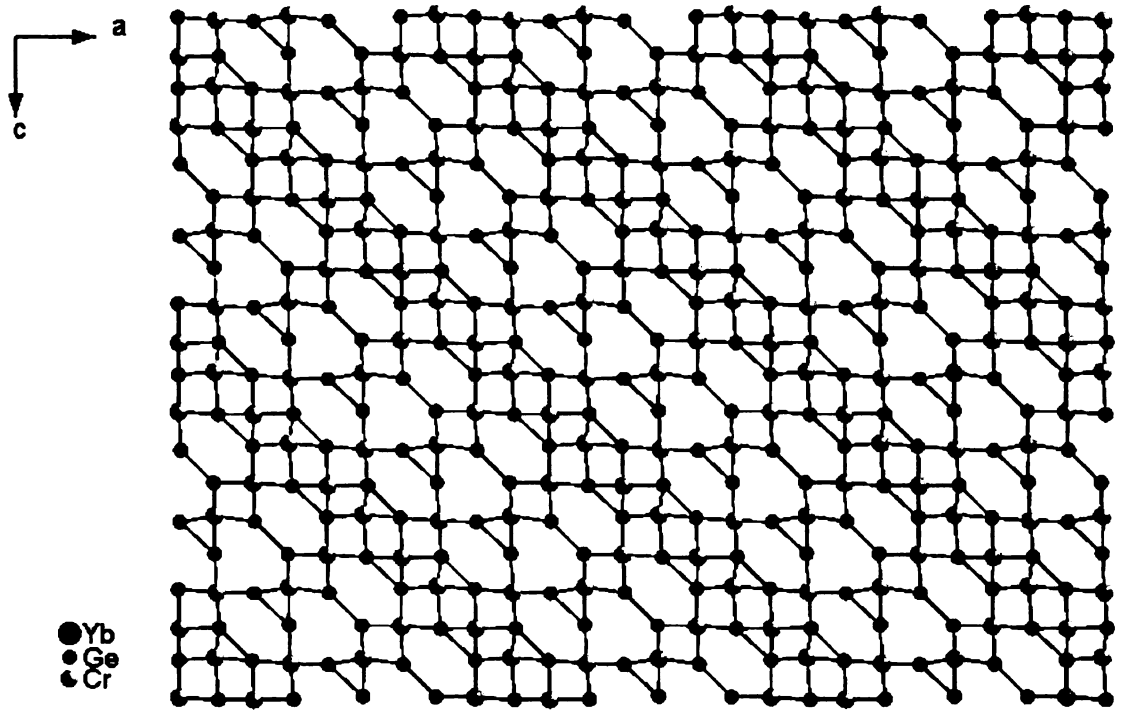

(A)

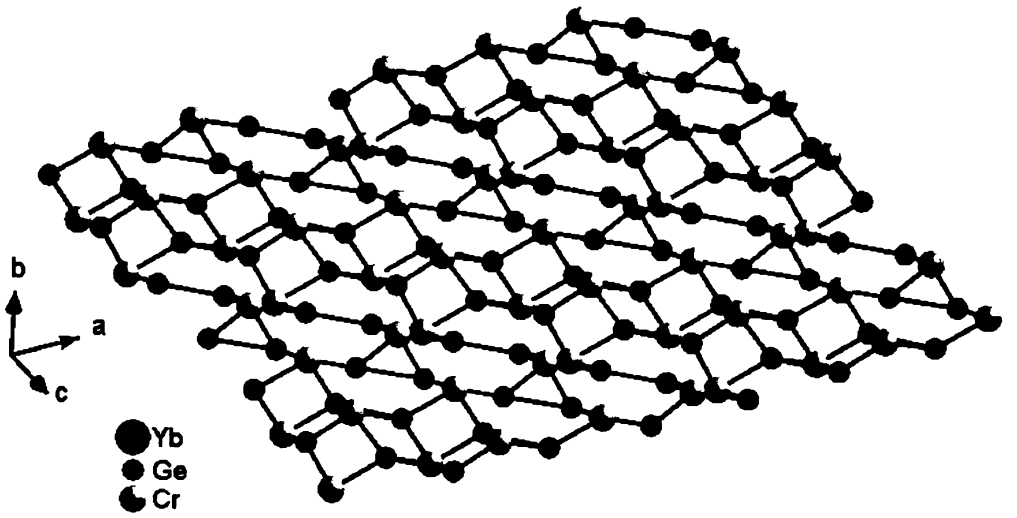

(B)

Figure 6-5. (A) Projection of a fragment of a modulated *a,c*-layer for Yb_4CrGe_8. Everything with less than 20% occupancy is plotted as a vacancy. The bond distance cutoff is 2.7 Å. (B) a rotated view of the *a,c*-plane where the puckered form of the layer is emphasized.

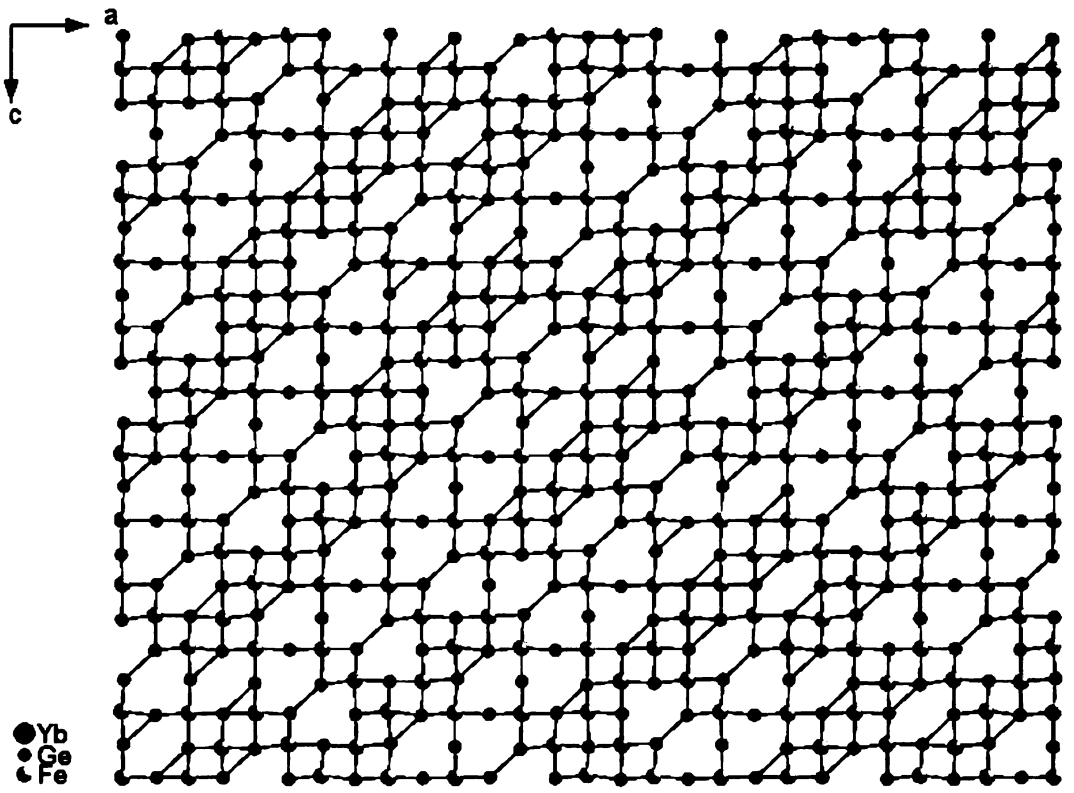

(A)

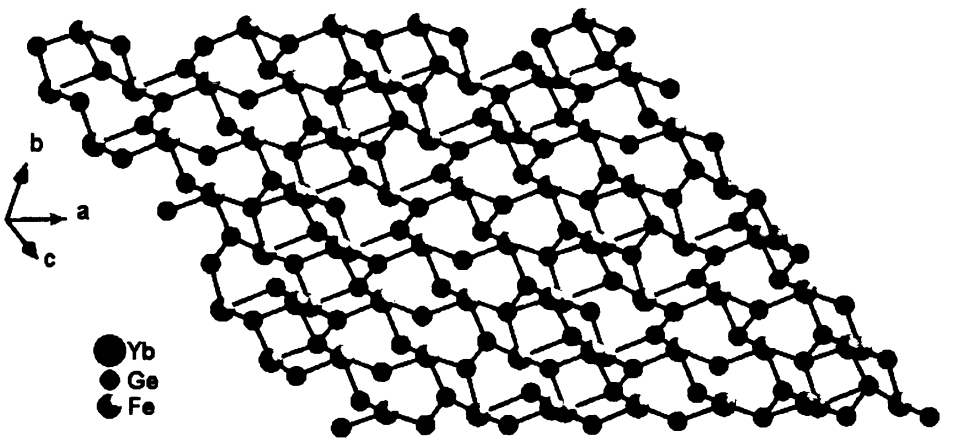

(B)

Figure 6-6. (A) Projection of a fragment of a modulated *a,c*-layer for Yb_4FeGe_8. Everything with less than 20% occupancy is plotted as a vacancy. The bond distance cutoff is 2.7 Å. (B) a rotated view of the *a,c*-plane where the puckered form of the layer is emphasized.

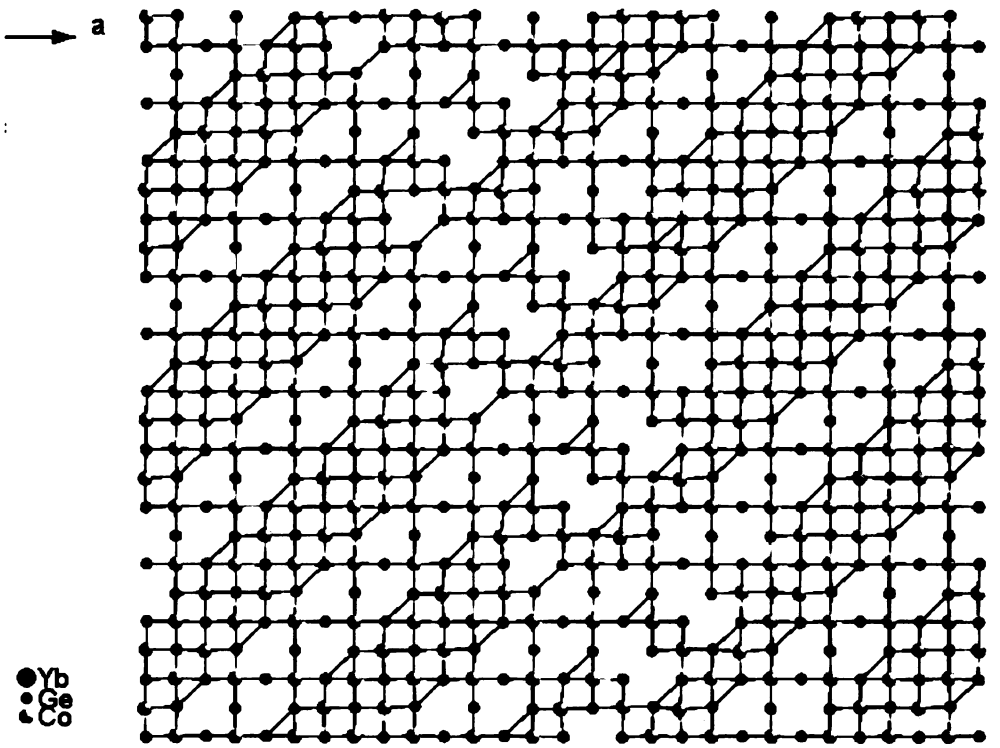

(A)

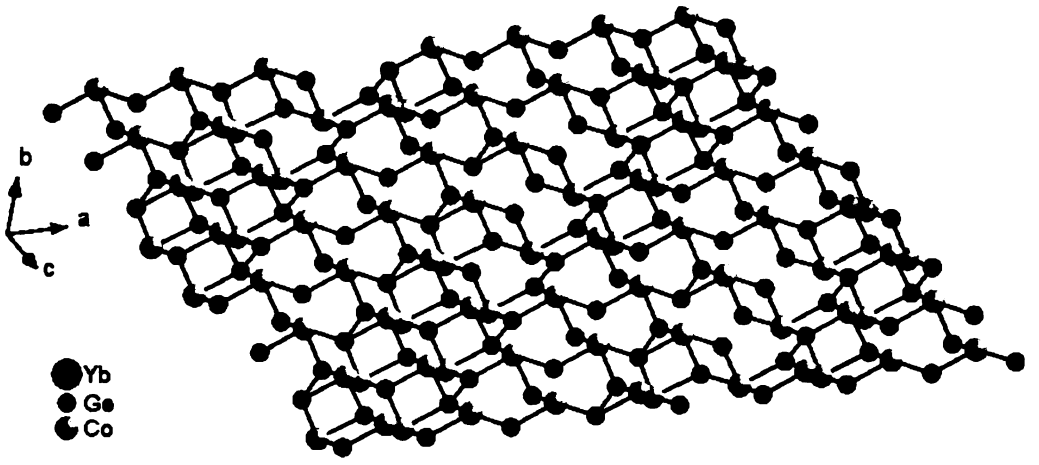

(B)

Figure 6-7. (A) Projection of a fragment of a modulated *a,c*-layer for Yb_4CoGe_8. Everything with less than 20% occupancy is plotted as a vacancy. The bond distance cutoff is 2.7 Å. (B) a rotated view of the *a,c*-plane where the puckered form of the layer is emphasized.

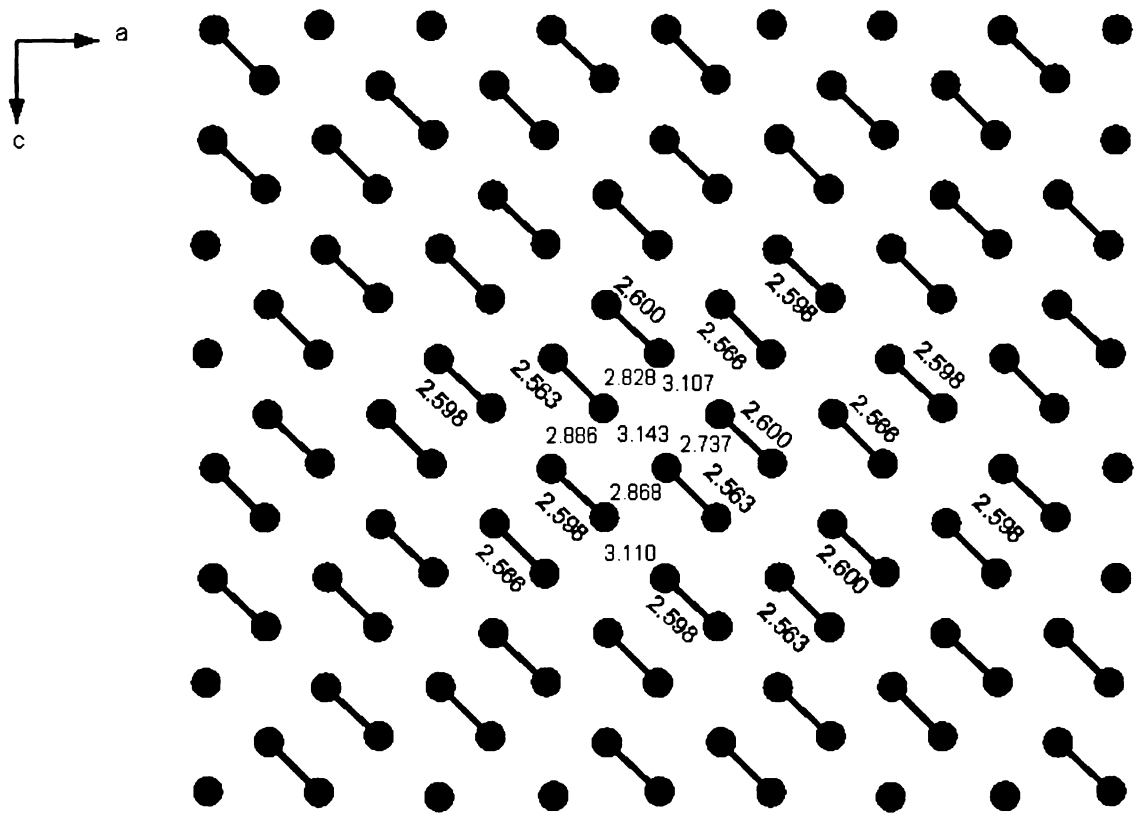

Figure 6-8. The modulated Ge square net, described with Ge-Ge dimmers in Yb_4CrGe_8. The Ge-Ge bonds were drawn within the cutoff distance of 2.7 Å. The parallel to the bonds numbers represent the Ge-Ge dimer bond lengths, whereas the horizontal numbers represent other Ge-Ge distances.

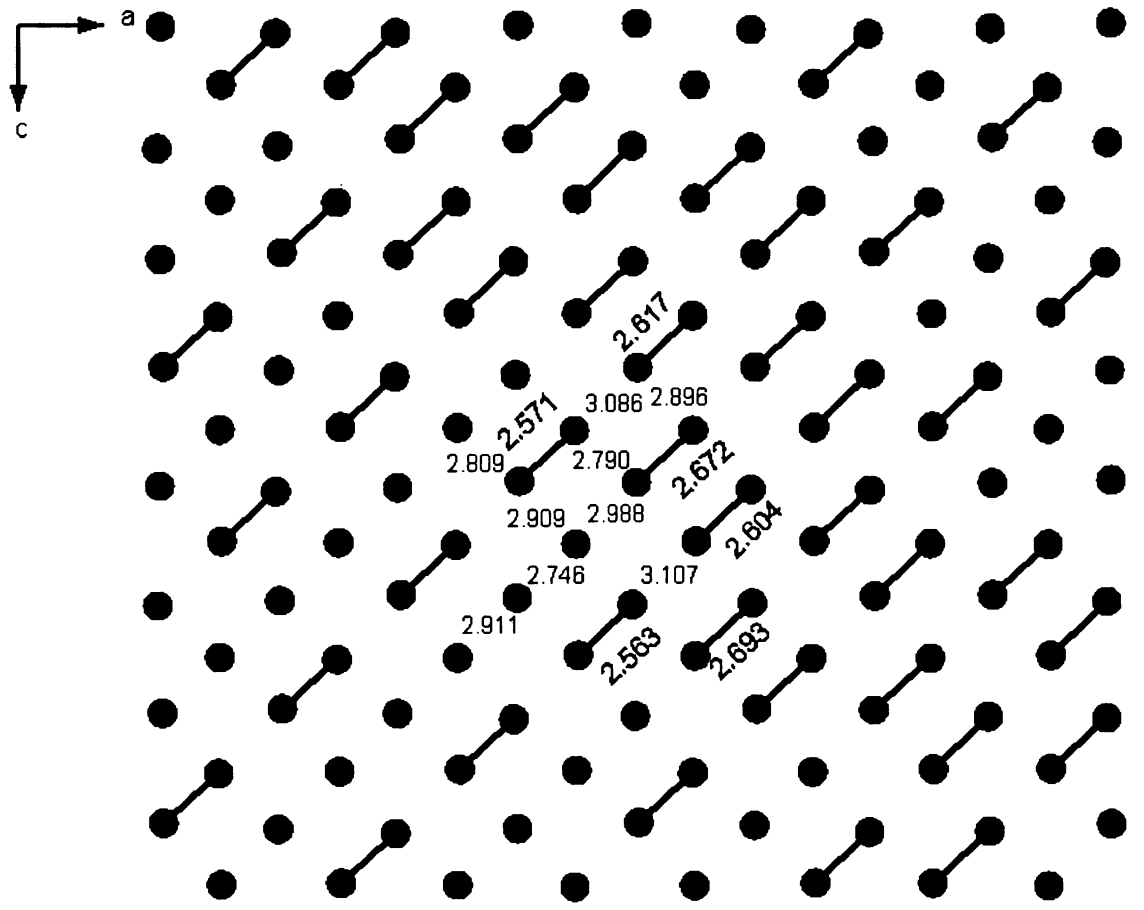

Figure 6-9. The modulated Ge square net, described with Ge-Ge dimmers in Yb_4FeGe_8. The Ge-Ge bonds were drawn within the cutoff distance of 2.7 Å. The parallel to the bonds numbers represent the Ge-Ge dimer bond lengths, whereas the horizontal numbers represent other Ge-Ge distances.

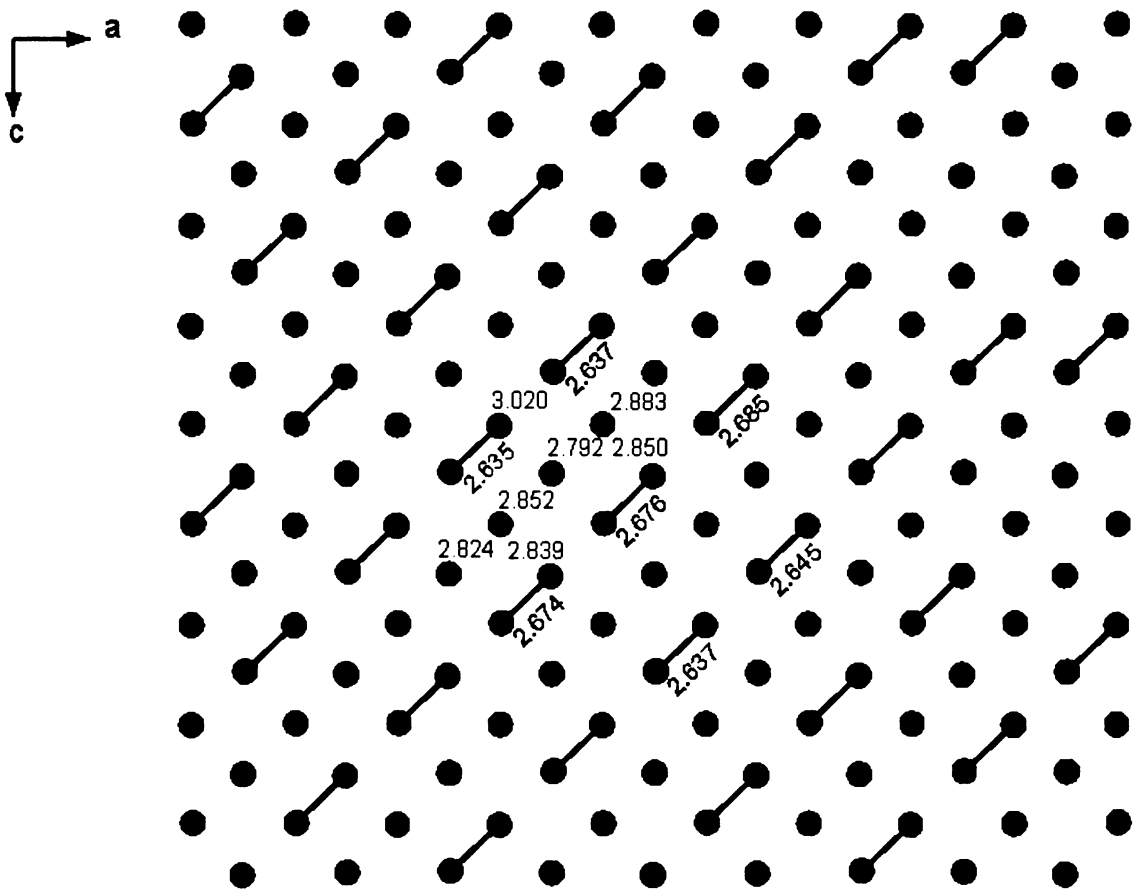

Figure 6-10. The modulated Ge square net, described with Ge-Ge dimmers in Yb_4CoGe_8. The Ge-Ge bonds were drawn within the cutoff distance of 2.7 Å. The parallel to the bonds numbers represent the Ge-Ge dimer bond lengths, whereas the horizontal numbers represent other Ge-Ge distances.

Magnetic Measurements:

Yb_4CrGe_8. Figure 6-11(A) shows the temperature dependence of the molar magnetic susceptibility $\chi_m(T)$ of an Yb_4CrGe_8 sample measured between 2 and 400 K with an applied field of 1 kG. Data were collected for both zero field cooled (ZFC, measured on warming) and field cooled (FC, measured on cooling) modes. The inset displays the inverse molar magnetic susceptibility $1/\chi_m(T)$ data versus the temperature. As it can be seen, above 100 K Yb_4CrGe_8 exhibits paramagnetic behavior and $\chi_m(T)$ nicely follows the Curie – Weiss (CW) law $\chi(T) = C/(T-\theta_p)$,[67] where $C = N_A\mu_{eff}^2/3k_B = \mu_{eff}^2/8$ is the Curie constant and θ_p is the Weiss temperature. A nonlinear least-squares fit to this equation of the data above 100 K, resulted in a Curie constant of $C = 11$, a Weiss temperature of $\theta_p \approx -122$ K suggesting antiferromagnetic interactions between the Yb atoms, and an effective moment of 4.7 μ_B / Yb atom. The estimated experimental μ_{eff} value is somewhat increased with respect to that expected for a free Yb^{3+} ion (4.54 μ_B). The increased value could be possibly due to either polarization of the conduction electrons or to the contribution of the Cr 3d electrons to the overall magnetic moment. On the other hand, below 100 K the $\chi_m(T)$ data do not obey the CW law while below ~ 20 K there is an abrupt change in the $\chi_m(T)$ curves which is indicative of ferromagnetic phase transition.

Figure 6-11(B) illustrates the field dependent magnetization data for Yb_4CrGe_8 measured at 5 K. Initially, the moments are rapidly aligned with the applied field indicating a ferromagnetic state up to ~ 10 kG; at which point the magnetization starts increasing more slowly as the material passes from the ferromagnetic into the

paramagnetic state. The magnetic response remains linear up to the highest attainable field of 60 kG, which is not enough to saturate the spins.

Yb_4FeGe_8. Figure 6-12(A) shows the temperature dependence of the molar magnetic susceptibility $\chi_m(T)$ and the inverse susceptibility $1/\chi_m(T)$ of an Yb_4FeGe_8 sample measured between 2 and 400 K with an applied field of 600 G. Data were collected for both zero field cooled (ZFC, measured on warming) and field cooled (FC, measured on cooling) modes. As it can be seen, above 100 K Yb_4FeGe_8 exhibits paramagnetic behavior and $\chi_m(T)$ follows the Curie – Weiss (CW) law $\chi(T) = C/(T-\theta_p)$,[67] where $C = N_A\mu_{eff}^2/3k_B = \mu_{eff}^2/8$ is the Curie constant and θ_p is the Weiss temperature. A nonlinear least-squares fit to this equation of the $1/\chi_m(T)$ data above 100 K, resulted in a Curie constant of C = 15 and a Weiss temperature of $\theta_p \approx$ -236 K suggesting strong antiferromagnetic interactions between the Yb atoms. Largely negative θ_p values may be also indicative of mixed-valence systems.[68,69] Additionally, the estimated experimental effective moment μ_{eff} value of 5.5 μ_B / Yb atom, is greater than the expected for a free Yb^{3+} ion (4.54 μ_B). The increased value could be possibly due to either polarization of the conduction electrons or to the contribution of the Fe 3d bands electrons to the overall magnetic moment. Perhaps, future neutron diffraction experiments could give some more insight in the nature of the increased μ_{eff} value. It should be also noted at this point that the μ_{eff} given here is only at a rough approximation above 100 K, since at it will be seen in the XANES measurements described below the Yb valence seems to be constantly changing with the temperature. Nevertheless, below 100 K the $\chi_m(T)$ data do not obey the CW law while below ~ 12 K there is an abrupt change in the $\chi_m(T)$ curves which is

indicative of ferromagnetic phase transition and a hysteresis between ZFC and FC modes occurs below ~ 4K, as it can be seen in the lower temperature $\chi_m(T)$ data, given in Figure 6-12(B). Additionally, at ~ 2.6 K there is a small peak in the ZFC curve. Figure 6-13(A) illustrates the field dependent magnetization data for Yb_4FeGe_8 measured at 2 K. The magnetization increases roughly linear up to the highest attainable field of 62 kG, which is not enough to saturate the spins.

Additional magnetic measurements for Yb_4FeGe_8 were carried out on a low field SQUID magnetometer on a sample consisting of randomly oriented crystals. Figure 6-13(B) shows the magnetic susceptibility (M/H) data for both ZFC and FC configurations for 10 G of applied field measured in a temperature range of 4.2 – 65 K. As it has been observed in the higher field measurements described above, Yb_4FeGe_8 undergoes a ferromagnetic transition at a temperature of ~ 11 -12 K. At this low field though, we see some additional features. At ~ 35 - 20 K there is a broad hump in FC curve and a hysteresis between ZFC and FC data starts to occur, which becomes significant below ~ 10 K. Furthermore, at ~ 7.5 K the ZFC data exhibit an additional peak while below 5 K both ZFC and FC curves show a sudden increase to higher moment values which could be indicative of another transition taking place at a lower temperature. Low-temperature neutron diffraction measurements could shed light on the subtleties of possible multiple magnetic transitions.

Figure

with an

Field var

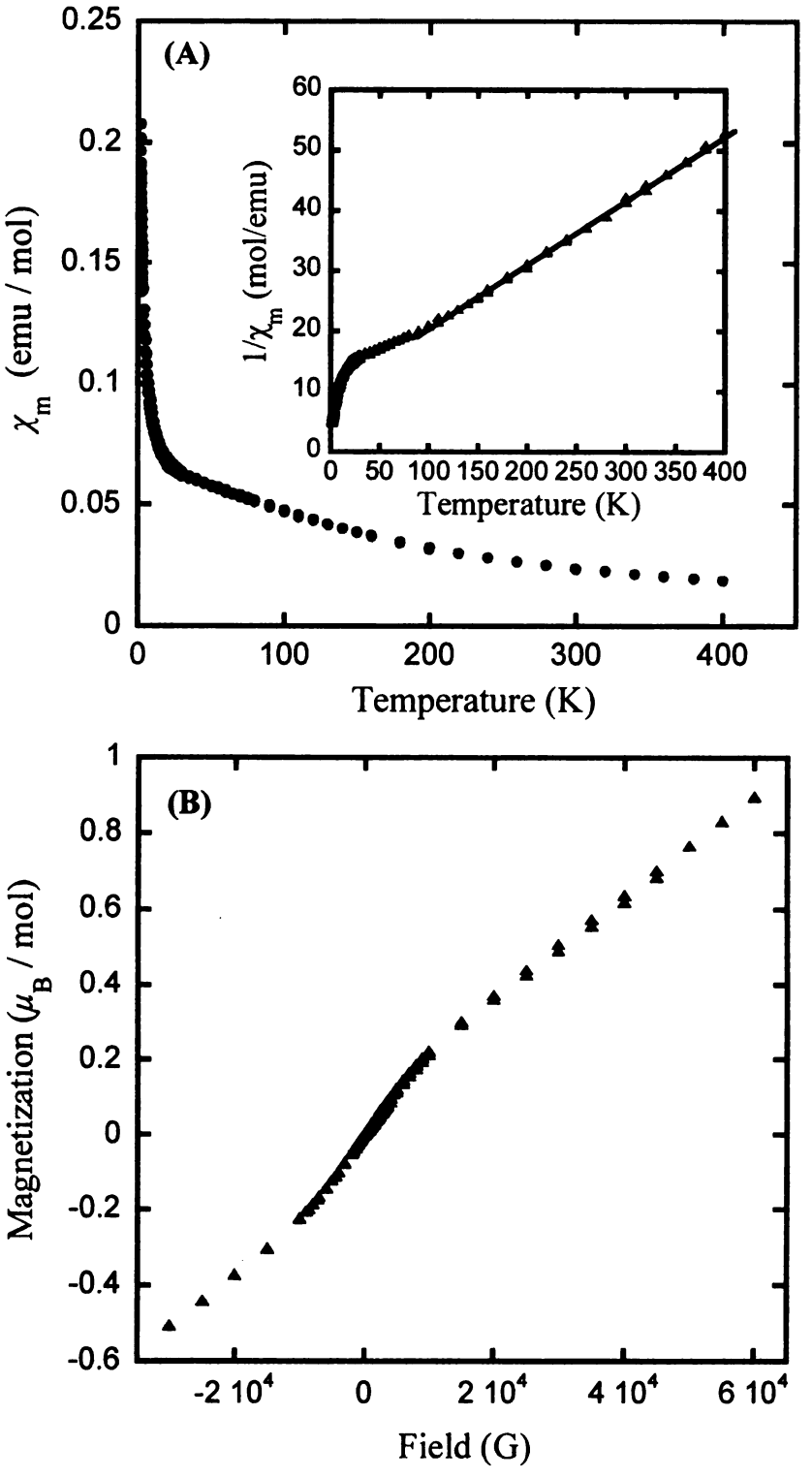

Figure 6-11. (A) Temperature dependence of the molar susceptibility $\chi_m(T)$ of Yb_4CrGe_8 with an applied field of 1 kG. Inset shows the inverse susceptibility $1/\chi_m(T)$ data. (B) Field variation of the magnetization of Yb_4CrGe_8 collected at 5 K.

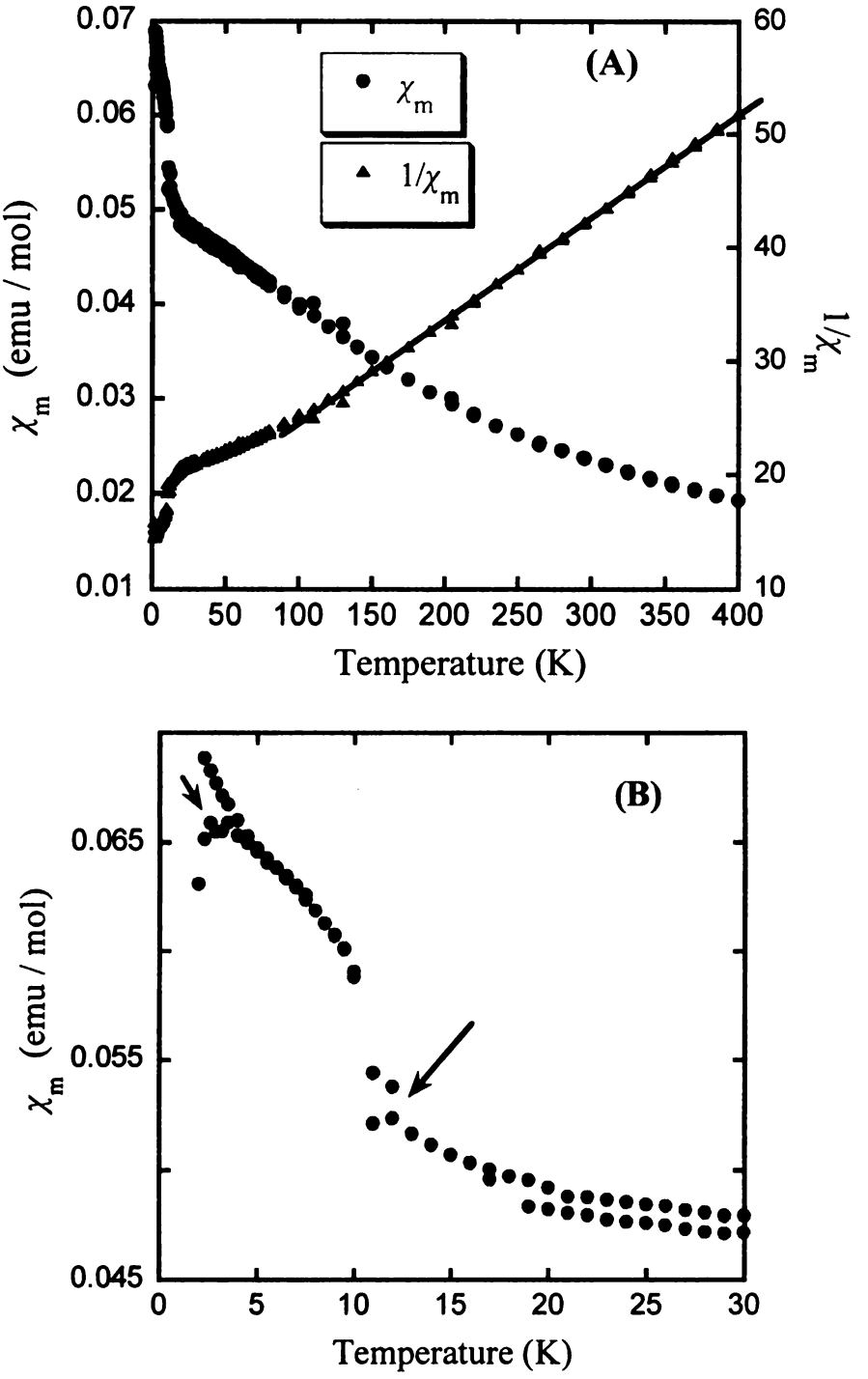

Figure 6-12. (A) Temperature dependence of the molar susceptibility $\chi_m(T)$ and inverse susceptibility $1/\chi_m(T)$ of Yb_4FeGe_8 with an applied field of 600 G. (B) Low temperature data of $\chi_m(T)$, where arrows indicate possible transitions.

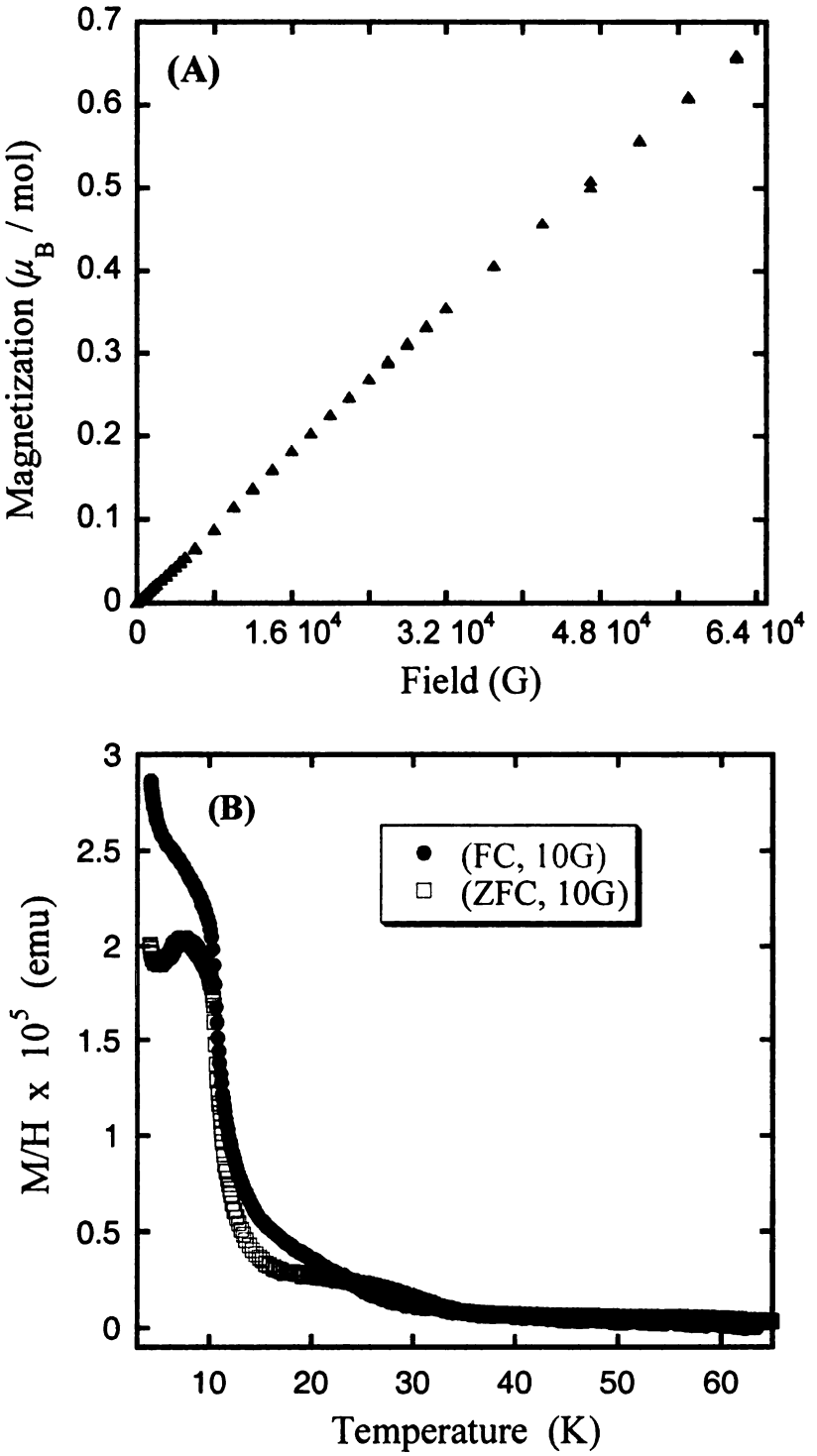

Figure 6-13. (A) Field variation of the magnetization of Yb_4FeGe_8 collected at 2 K. (B) Temperature dependence of the susceptibility M/H of Yb_4FeGe_8 measured on randomly oriented crystals with an applied of field of 10 G for ZFC mode and for FC mode.

XANES Measurements at Ambient Pressure:

To further probe the Yb valence state in the Yb_4TMGe_8 (TM = Fe, Cr and Co) compounds we performed X-ray absorption near edge spectroscopy measurements at the Yb L_{III}-edge. The near-edge spectra of Yb_4FeGe_8, Yb_4CrGe_8 and Yb_4CoGe_8 samples obtained at various temperatures within the temperature range of 15 – 300 K are given in Figures 6-14, 6-15 and 6-16, respectively. All three compounds exhibit similar absorption features. Particularly, the main absorption peak (white line) for all spectra is centered at ~ 8948 eV, which is typical of trivalent Yb in Yb-based intermetallics.[70-74] The spectra also reveal the presence of a weaker feature (shoulder) at ~ 8941-2 eV. This structure which is ~ 7 eV lower in energy relative to Yb^{3+} is attributed to divalent Yb atom.[70-74] This indicates that all three Yb materials can be classified as mixed-valence (*MV*) or intermediate-valence (*IV*) compounds.

Another interesting observation in the XANES spectra is that the relative ratio of the features at 8941-2 and 8948 eV varies with temperature. In particular, with decreasing temperature the low-energy peak originating from Yb^{2+} ion is gradually enhanced, whereas the high-energy one originating from Yb^{3+} ion is progressively depressed. This behavior, becomes even more apparent in the Figures 6-17 – 6-19, which give the difference plots generated by subtracting the data collected at 100 and 300 K from the 15 K data for the Yb_4CrGe_8 compound and by subtracting the data taken at 80, 160 and 300 K from the 30 K data for the Yb_4FeGe_8 and Yb_4CoGe_8 compounds, respectively. The amplified intensity at 8941-2 eV and concomitant decrease in intensity at 8948 eV reveals the systematic conversion of Yb^{3+} to Yb^{2+} on cooling the sample. The estimated RMS intensity error is ~ 0.003 for individual data points. This behavior establishes that in all

three title compounds the average Yb valence changes continuously with temperature, a characteristic of intermediate valence materials, and that the Yb^{2+} state is more populated at lower temperatures. Similar behavior was also observed in the quaternary $Yb_4TM_7InGe_{12}$ (TM = Co, Ni) compound presented in chapter 2, but with a smaller degree of overall valence change between the room and low temperature, as well as in other intermediate valence intermetallics such as in $YbCu_{5-x}Ga_x$ series[72] and in $YbAl_3$, $YbCu_2Si_2$ and $YbInCu_4$.[74]

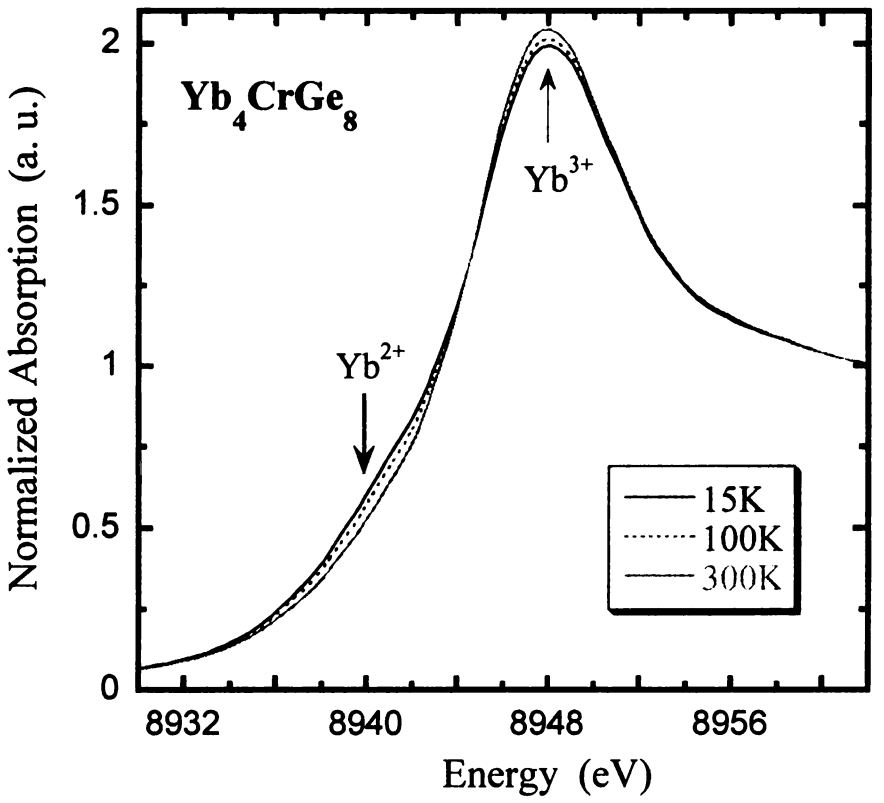

Figure 6-14. Yb L_{III}-edge absorption spectra of Yb_4CrGe_8 at 15, 100 and 300 K.

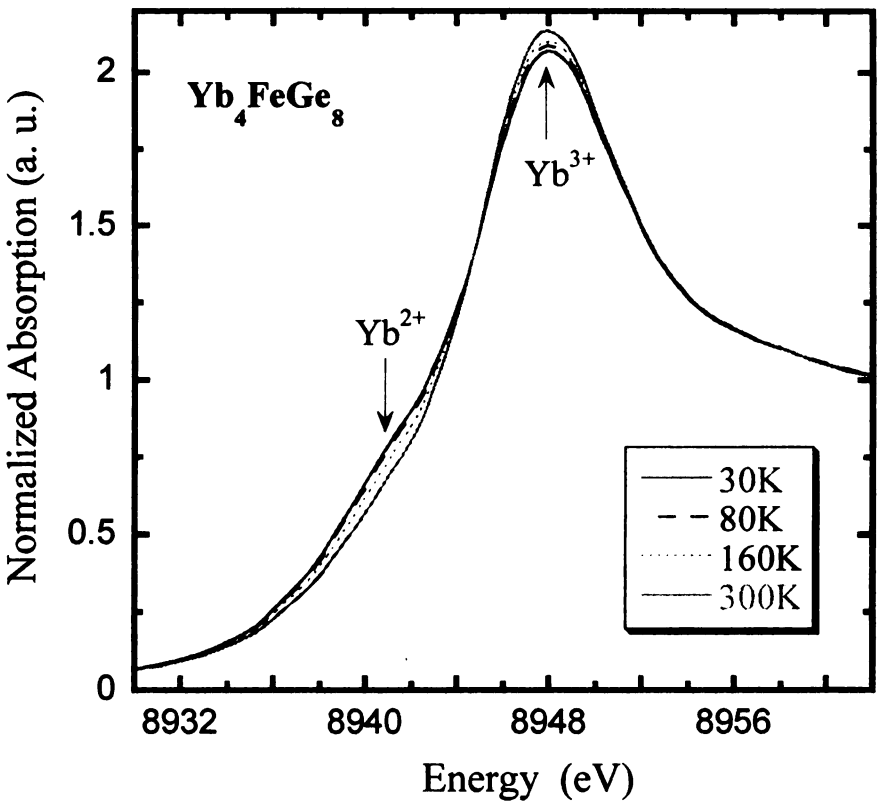

Figure 6-15. Yb L_{III}-edge absorption spectra of Yb_4FeGe_8 at 30, 80, 160 and 300 K.

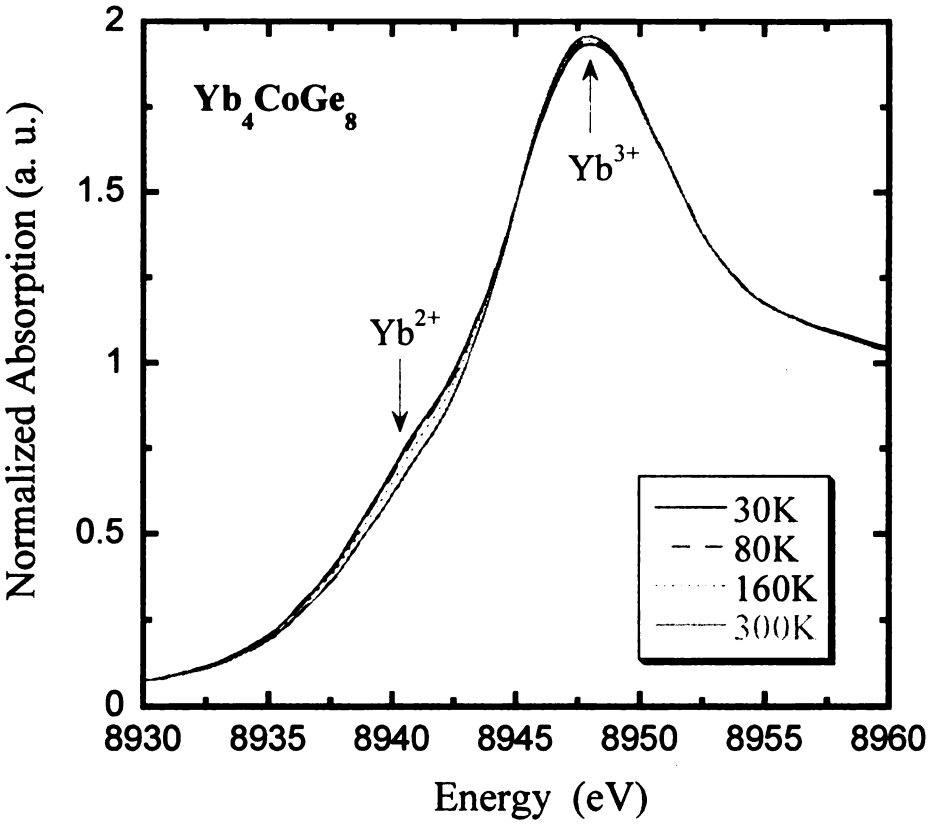

Figure 6-16. Yb L_{III}-edge absorption spectra of Yb_4CoGe_8 at 30, 80, 160 and 300 K.

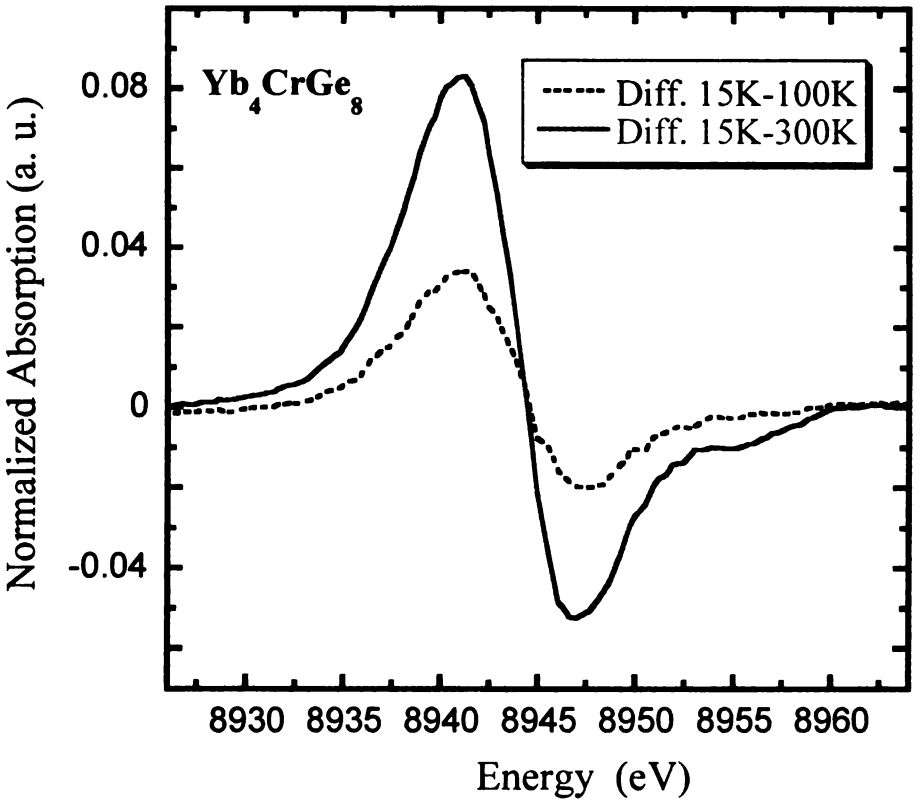

Figure 6-17. Difference plots for Yb_4CrGe_8 generated by subtracting the data taken at 100 and 300 K from the 15 K data.

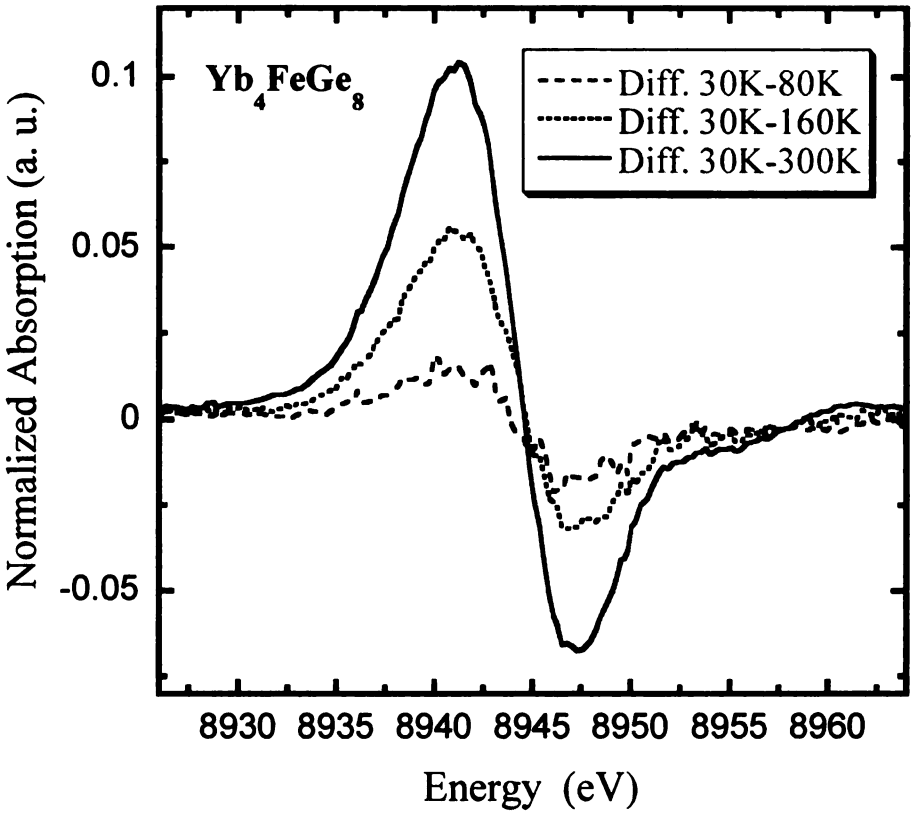

Figure 6-18. Difference plots for Yb_4FeGe_8 generated by subtracting the data taken at 80, 160 and 300 K from the 30 K data.

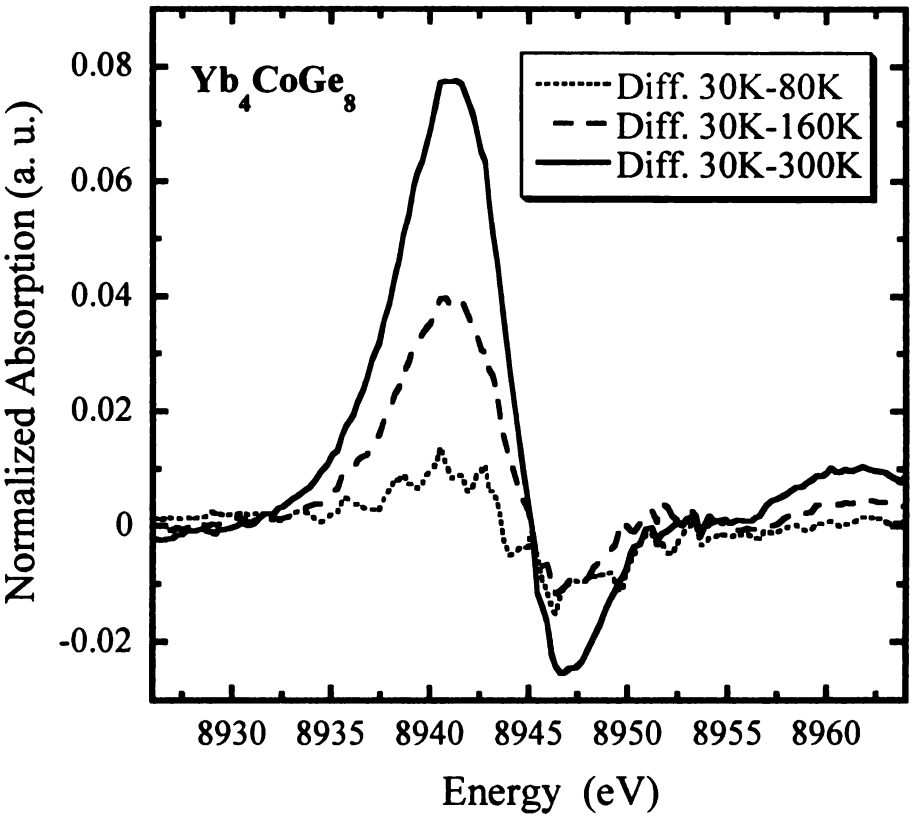

Figure 6-19. Difference plots for Yb_4CoGe_8 generated by subtracting the data taken at 80, 160 and 300 K from the 30 K data.

Temperature Dependent Single Crystal X-Ray Diffraction Measurements:

As it was observed in the temperature dependent XANES experiments for all three title compounds, there is an increase in amplitude of the feature at ~ 8941 eV, which represents absorption from the divalent component of the mixed-valence materials, indicating the lowering of the average Yb valence upon cooling. Considering the fact that Yb^{2+} has a larger ionic radius comparing to Yb^{3+} one, this could potentially counteract the normal lattice shrinkage observed on cooling a solid material and the total volume change could become zero. In order to assess this hypothesis, we performed temperature dependent single crystal X-ray diffraction experiments, where a refinement of the cell parameters was performed at various temperatures for all three Yb_4TMGe_8 (TM = Cr, Fe, Co) compounds.

Tables 6-19 to 6-22 include the temperature variation data of the cell parameters for single crystals of Yb_4CrGe_8 (for two crystals namely Yb_4CrGe_8_1 and Yb_4CrGe_8_2), Yb_4FeGe_8 and Yb_4CoGe_8 measured within the temperature range of 10 – 320 K. For Yb_4CrGe_8_1, Yb_4CrGe_8_2 and Yb_4CoGe_8 crystals the data between 10 and 90 K were collected with the diffractometer at ANL (MSD) facilities while the data between 100 and 300 K were obtained with the diffractometer at N.W. facilities. Data for Yb_4FeGe_8 were collected at N.W. for the whole temperature range. The Figures 6-20 – 6-23, show the corresponding temperature dependence of the *a,b,c* axes as well as the volumes for all four measured crystals. As it can be seen in Figures 6-20(A) and (B), the length of the *a* and *c* axes for both Yb_4CrGe_8 crystals stays almost stable through the whole temperature range. However, the *b* axis besides the small anomaly between 15 and 30 K, changes slightly up to ~ 100 K but at higher temperatures it exhibits a regular linear dependence

with temperature. The combination of the different temperature dependence between the *a,c* and *b* axes results in an almost negligible volume expansion from 15 K up to ~ 100 K, while above this temperature the volume shows normal positive thermal expansion with roughly linear response to temperature, see Figure 6-21. The temperature variation of the Yb_4FeGe_8 cell parameters suggests similar behavior, see Figures 6-22(A) and (B). The *a,c* axes remain basically temperature independent whereas the *b* axis even though it does not change significantly up to ~ 120 K beyond this point it increases linearly with temperature. This leads to a nearly zero thermal expansion for the cell volume within the range of ~ 10 – 120 K and normal positive thermal expansion at higher temperatures. Finally, similar temperature variation of the *a,c* and *b* cell axes for the Yb_4CoGe_8 results in very small changes of the volume cell until ~ 90 – 100 K, while it continuously expands at higher temperatures, see Figures 6-23(A) and (B).

Table 6-19. Temperature dependent cell parameters for Yb_4CrGe_8_2 crystal. Temperature range of 15 – 90 K was measured at ANL and 100 – 300 K at NU.

Temp. (K)	*a* (Å)	Δ*a*	*b* (Å)	Δ*b*	*c* (Å)	Δ*c*	Volume (Å^3)	ΔV
15	4.0811	0.00063	15.4605	0.00336	3.9636	0.00060	250.09	0.077
30	4.0791	0.00064	15.4762	0.00341	3.9624	0.00062	250.14	0.078
50	4.0791	0.00058	15.4750	0.00312	3.9635	0.00056	250.19	0.071
70	4.0788	0.00059	15.4716	0.00312	3.9636	0.00056	250.12	0.071
90	4.0775	0.00059	15.4749	0.00318	3.9649	0.00057	250.18	0.073
100	4.0801	0.0006	15.4778	0.0019	3.9626	0.0006	250.25	0.05
120	4.0805	0.0004	15.4814	0.0019	3.9632	0.0006	250.37	0.05
140	4.0810	0.0005	15.4863	0.0019	3.9640	0.0005	250.53	0.05
160	4.0808	0.0005	15.4895	0.0019	3.9645	0.0006	250.60	0.05
180	4.0815	0.0004	15.4928	0.0019	3.9652	0.0005	250.73	0.05
200	4.0822	0.0004	15.4977	0.0018	3.9663	0.0005	250.93	0.05
220	4.0823	0.0004	15.5026	0.0019	3.9664	0.0005	251.02	0.05
240	4.0824	0.0005	15.5045	0.0019	3.9667	0.0006	251.07	0.05
260	4.0839	0.0005	15.5104	0.0019	3.9674	0.0006	251.31	0.05
280	4.0840	0.0005	15.5150	0.0019	3.9682	0.0006	251.44	0.05
300	4.0846	0.0004	15.5183	0.0018	3.9690	0.0005	251.58	0.05

Table 6-20. Temperature dependent cell parameters for Yb_4CrGe_8_3 crystal. Temperature range of 15 – 90 K measured at ANL and 100 – 300 K at NU.

Temp. (K)	*a* (Å)	Δ*a*	*b* (Å)	Δ*b*	*c* (Å)	Δ*c*	Volume (Å^3)	ΔV
15	4.0781	0.00074	15.4633	0.00276	3.9641	0.00065	249.98	0.076
30	4.0784	0.00079	15.4751	0.00300	3.9643	0.0010	250.20	0.095
50	4.0787	0.00062	15.4692	0.00236	3.9650	0.00081	250.17	0.074
70	4.0782	0.00064	15.4718	0.00241	3.9645	0.00083	250.15	0.076
90	4.0781	0.00062	15.4721	0.00234	3.9651	0.00081	250.18	0.074
100	4.0787	0.0006	15.481	0.0026	3.9622	0.0009	250.18	0.080
120	4.0786	0.0006	15.4822	0.0025	3.9623	0.0009	250.20	0.080
140	4.0782	0.0006	15.4873	0.0026	3.9626	0.0009	250.28	0.080
160	4.0792	0.0006	15.4922	0.0026	3.9624	0.0010	250.40	0.080
180	4.0793	0.0006	15.4928	0.0026	3.9636	0.0009	250.50	0.080
200	4.0794	0.0006	15.5021	0.0027	3.9636	0.0010	250.65	0.080
220	4.080	0.0006	15.5068	0.0026	3.9650	0.0010	250.86	0.080
240	4.0803	0.0006	15.5127	0.0026	3.9649	0.0009	250.97	0.080
260	4.0812	0.0006	15.5162	0.0026	3.9672	0.0010	251.22	0.080
280	4.0821	0.0006	15.5156	0.0027	3.9671	0.0010	251.26	0.080
300	4.0825	0.0006	15.5228	0.0026	3.9689	0.0010	251.51	0.080

Table 6-21. Temperature dependent cell parameters for Yb_4FeGe_8 crystal. Whole temperature range was measured at NU.

Temp. (K)	*a* (Å)	Δ*a*	*b* (Å)	Δ*b*	*c* (Å)	Δ*c*	Volume (Å^3)	ΔV
10	4.0681	0.0008	15.4108	0.0024	3.9554	0.0006	247.97	0.07
20	4.0674	0.0008	15.4098	0.0024	3.9548	0.0006	247.88	0.07
40	4.0662	0.0008	15.4100	0.0024	3.9547	0.0006	247.8	0.07
60	4.0682	0.0008	15.4102	0.0023	3.9545	0.0006	247.92	0.07
80	4.0672	0.0008	15.4105	0.0024	3.9541	0.0006	247.84	0.07
100	4.0715	0.0008	15.4115	0.0025	3.9519	0.0006	247.97	0.07
120	4.0712	0.0008	15.4132	0.0025	3.9524	0.0006	248.01	0.07
140	4.0717	0.0008	15.4197	0.0025	3.9534	0.0006	248.21	0.07
160	4.0724	0.0008	15.4250	0.0025	3.9538	0.0006	248.37	0.07
180	4.0723	0.0008	15.4298	0.0025	3.9542	0.0006	248.46	0.07
200	4.0727	0.0008	15.4333	0.0025	3.9551	0.0006	248.60	0.07
220	4.0734	0.0008	15.4374	0.0026	3.9560	0.0006	248.76	0.08
240	4.0737	0.0008	15.4452	0.0025	3.9574	0.0006	248.99	0.07
260	4.0748	0.0008	15.4500	0.0025	3.9582	0.0006	249.19	0.07
280	4.0754	0.0009	15.4567	0.0026	3.9591	0.0006	249.39	0.08
300	4.0744	0.0010	15.4597	0.0029	3.9610	0.0007	249.50	0.09
320	4.0747	0.0008	15.4647	0.0025	3.9608	0.0006	249.59	0.07

Table 6-22. Temperature dependent cell parameters for Yb_4CoGe_8 crystal. Temperature range 15 – 90 K measured at ANL and 100 – 300 K at NU.

Temp. (K)	*a* (Å)	Δ*a*	*b* (Å)	Δ*b*	*c* (Å)	Δ*c*	Volume (Å^3)	ΔV
15	4.0523	0.0006	15.4885	0.0033	3.9395	0.0007	247.26	0.08
30	4.0514	0.0006	15.489	0.0034	3.9391	0.0007	247.19	0.08
50	4.0514	0.0005	15.4898	0.0026	3.9382	0.0005	247.14	0.06
70	4.0523	0.0006	15.4931	0.0034	3.9374	0.0007	247.23	0.08
80	4.0537	0.0006	15.4920	0.0023	3.9371	0.0006	247.25	0.07
90	4.0545	0.0006	15.4951	0.0022	3.9373	0.0006	247.36	0.06
100	4.0533	0.0006	15.4979	0.0022	3.9372	0.0006	247.32	0.06
120	4.0552	0.0006	15.5050	0.0023	3.9375	0.0006	247.57	0.06
140	4.0560	0.0006	15.5055	0.0023	3.9383	0.0006	247.68	0.06
160	4.0561	0.0006	15.5112	0.0025	3.9391	0.0007	247.83	0.07
180	4.0556	0.0006	15.5179	0.0022	3.9398	0.0006	247.95	0.06
200	4.0580	0.0006	15.5196	0.0023	3.9418	0.0006	248.25	0.06
220	4.0591	0.0006	15.5238	0.0023	3.9431	0.0006	248.47	0.06
240	4.0599	0.0006	15.5313	0.0023	3.9405	0.0006	248.47	0.06
260	4.0587	0.0006	15.5335	0.0023	3.9424	0.0006	248.55	0.06
280	4.0602	0.0006	15.5363	0.0023	3.9431	0.0006	248.73	0.06
300	4.0620	0.0006	15.5455	0.0023	3.9451	0.0006	249.12	0.06

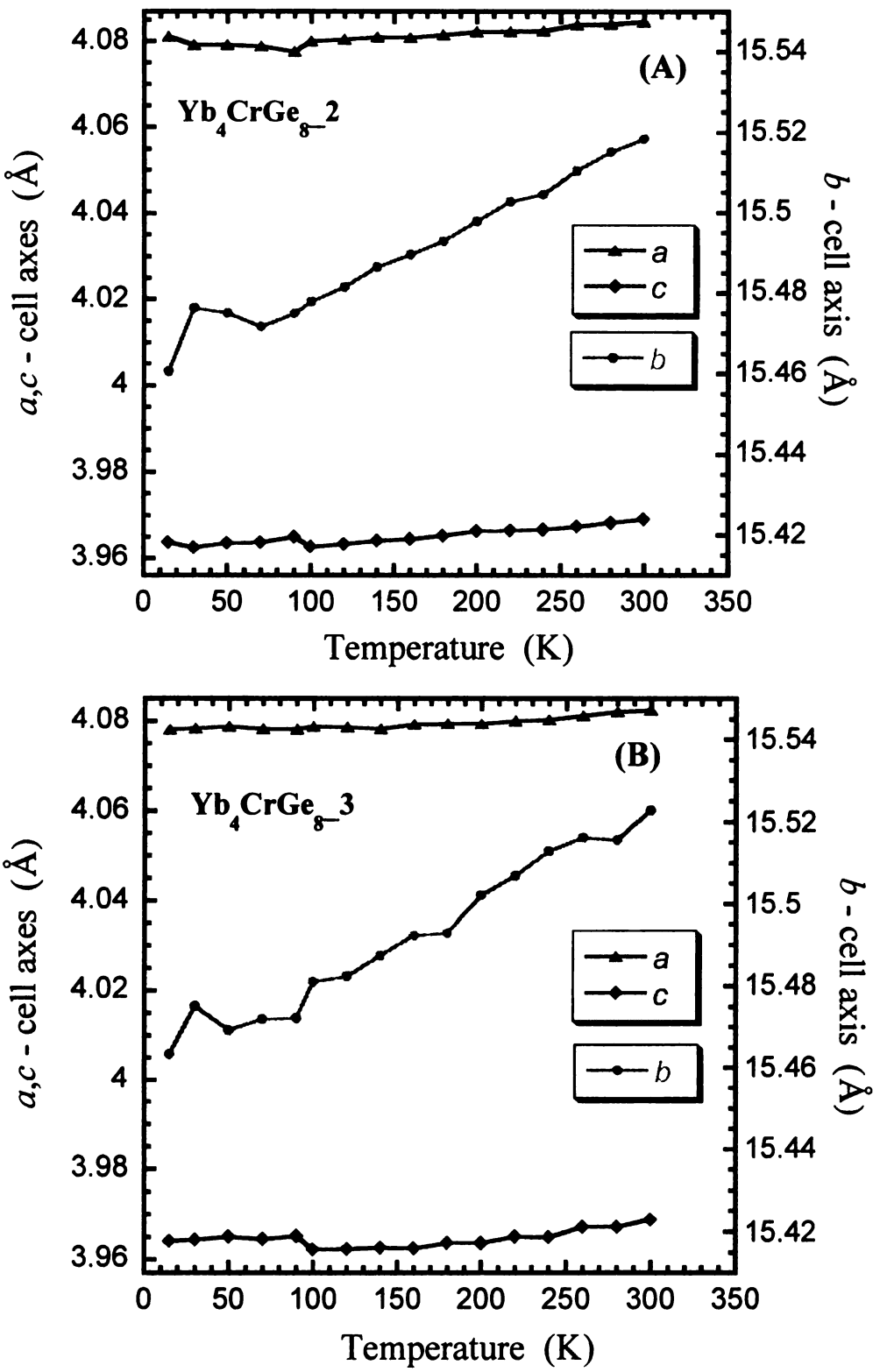

Figure 6-20. Temperature dependence of a,b,c cell axes for (A) Yb_4CrGe_8_2 and (B) Yb_4CrGe_8_3 single crystals. Temperature range 15 – 90 K measured at ANL and 100 – 300 K at NU.

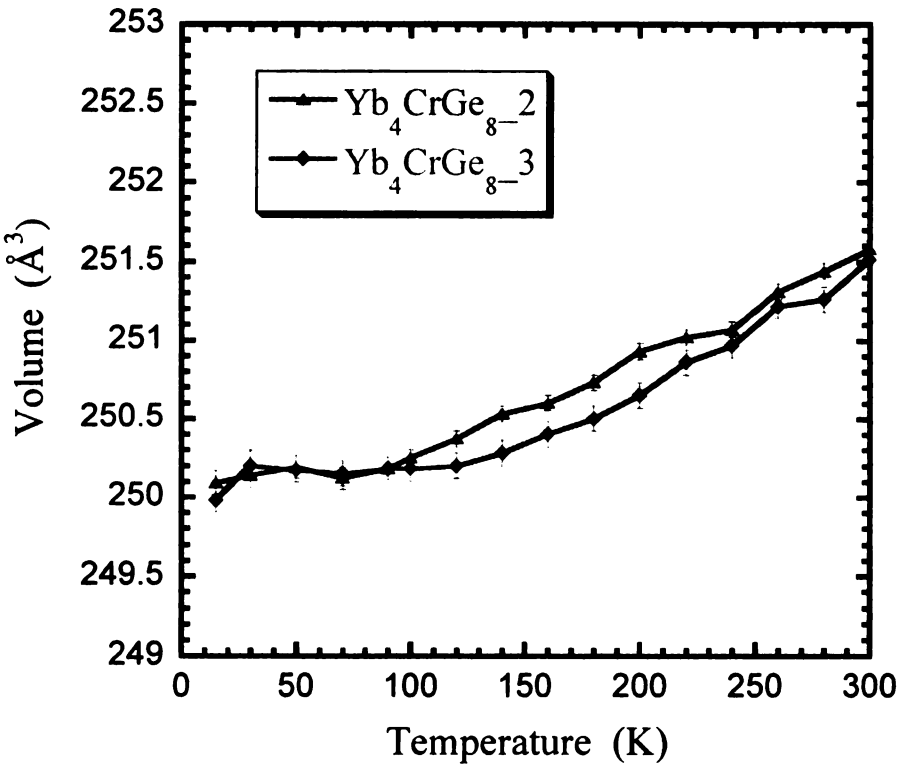

Figure 6-21. Temperature dependence of the cell volume for Yb_4CrGe_8_2 and Yb_4CrGe_8_3 crystals. Temperature range 15 – 90 K measured at ANL and 100 – 300 K at NU.

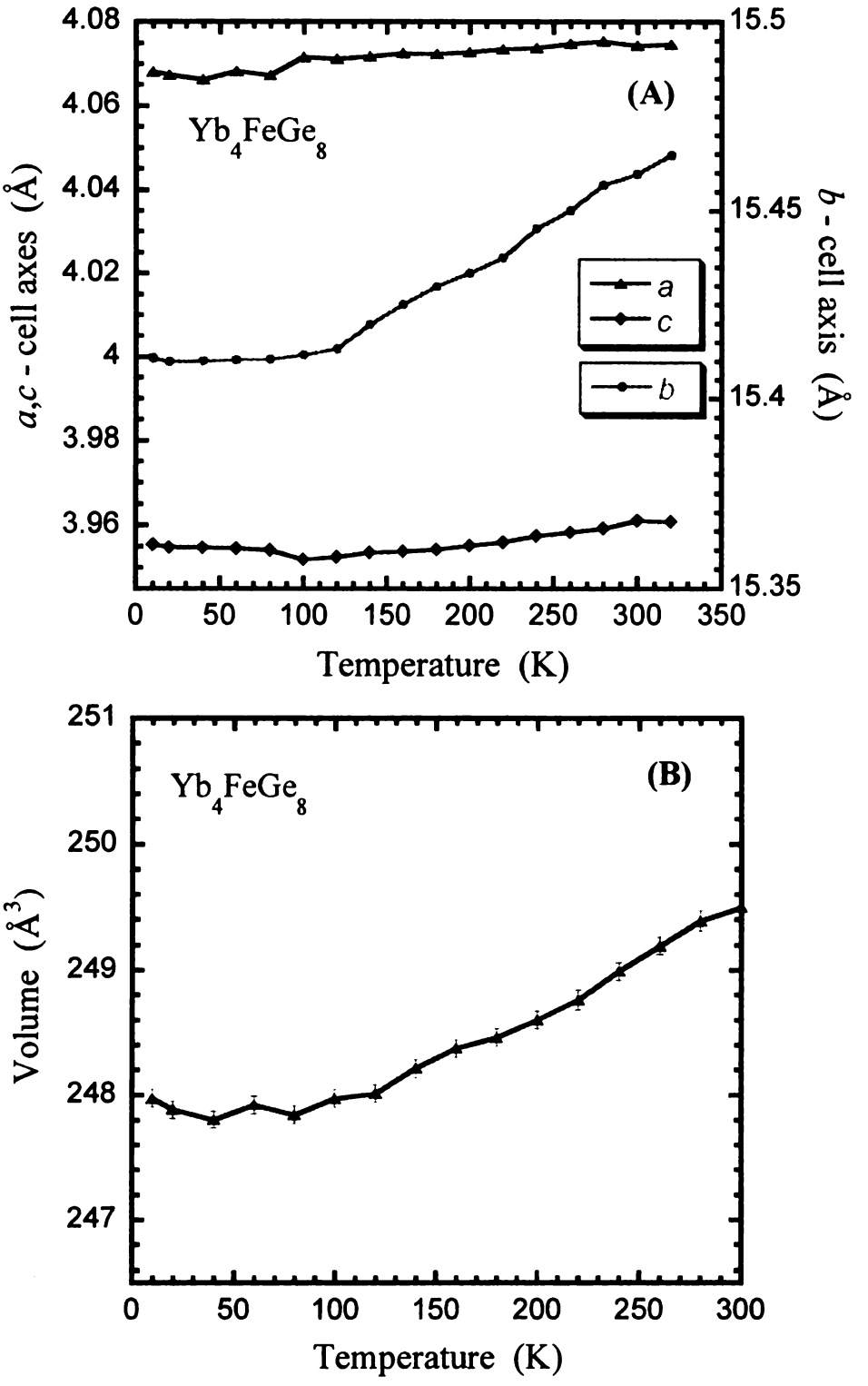

Figure 6-22. Temperature dependence (A) of *a,b* and *c* cell axes and (B) of cell volume for an Yb_4FeGe_8 single crystal. Whole temperature range 10 – 320 K measured at NU.

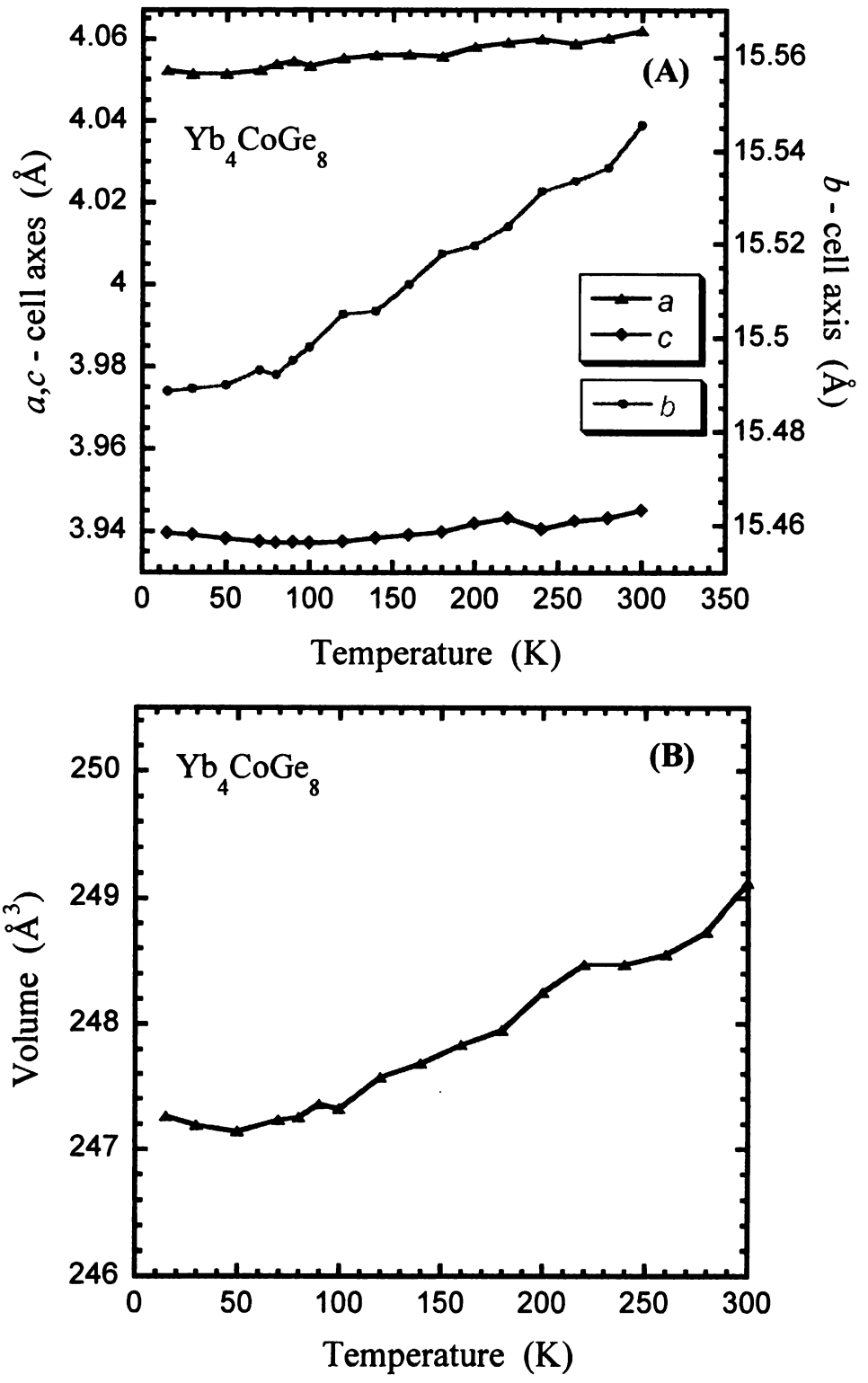

Figure 6-23. Temperature dependence of (A) cell volume and (B) *a*,*b* and *c* cell axes for an Yb_4CoGe_8 single crystal. Temperature range 15 – 90 K measured at ANL and 100 – 300 K at NU.

Heat Capacity Measurements for Yb_4CrGe_8:

The temperature dependent specific heat from 2.96 to 50.8 K for Yb_4CrGe_8 is shown in Figure 6-24. The compound seems to be a new Yb-based heavy fermion compound. For the higher temperature range of ~ 10 – 23 K the data can be fitted to the relation $C_p(T)/T = \gamma + \beta T^2$,[28] where the linear and cubic terms correspond to the electronic and lattice contributions to the specific heat, and $\beta = (1944 \times 10^3)/n\Theta_D^3$ with n = number of atoms in formula unit and Θ_D = Debye temperature. The fit resulted in an electronic specific heat coefficient $\gamma \approx 625$ mJ / mol K^2 and a $\Theta_D \approx 240$ K. On the other hand for the whole measured temperature range, the data can be described well by a Debye function (1) where the first and second term correspond to the electronic and the phonon contribution, respectively. N is the number of the atoms in the formula unit and $x = \hbar\omega/k_B T$.

$$C_p(T) = \gamma T + 9NR\left(\frac{T}{\Theta_D}\right)^3 \int_0^{\frac{\Theta_D}{T}} \frac{x^4\, dx}{(e^x - 1)^2} - KT^3 \qquad (1)$$

A fit to the experimental points resulted in a Debye temperature Θ_D of about 207 K, and an electronic specific heat coefficient $\gamma \approx 640$ mJ / mol K^2, which was determined from $\gamma\ (= C_p / T)_{T \to 0}$ at low temperatures. Both methods of estimating the values of γ and Θ_D are in a fairly good agreement and suggest that Yb_4CrGe_8 in a new Yb-based classic heavy fermion compound if one considers the arbitrary classification of these compounds into "light", "moderate" and classical heavy-fermions with γ values lying in the range of ~ 50 - 60, 100 - 400 and > 400 mJ / mol K^2 respectively. Nevertheless, this

value of electronic specific heat is one of the highest reported for Yb-based heavy fermion compounds that exhibit mixed-valence behavior as well; and compares well with the ones found for example in YbPd[75] and the family of the intermetallic compounds of $YbTM_2Zn_{20}$[76] with γ ranging at 520 – 740 mJ / mol K^2.

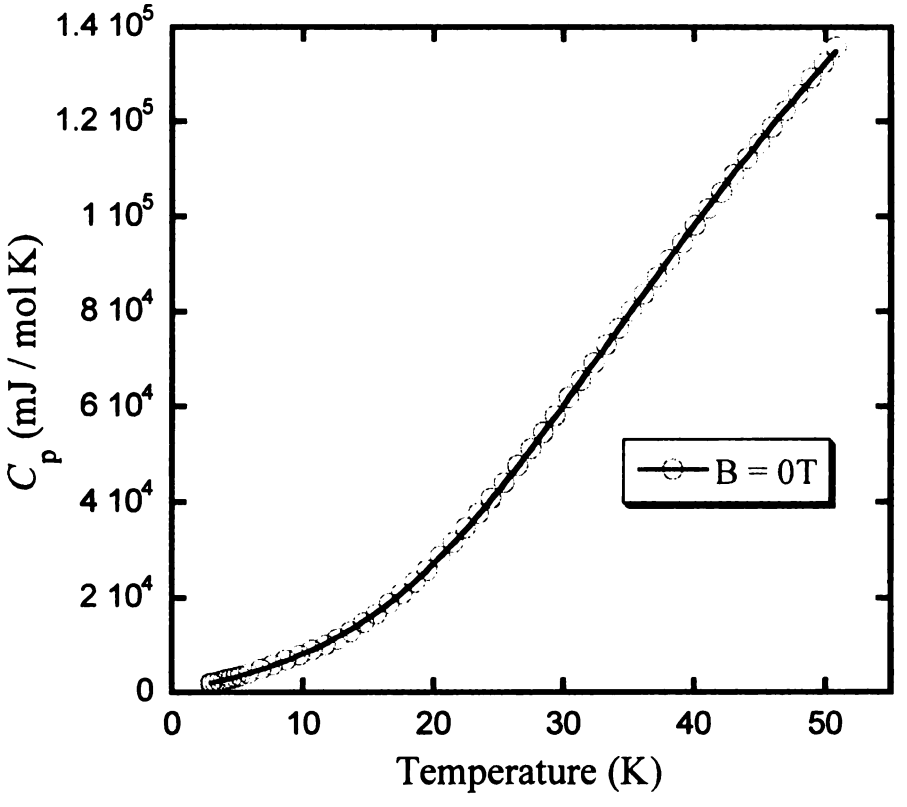

Figure 6-24. Heat capacity (C_p) for Yb_4CrGe_8 measured from 2.96 to 50.8 K. The experimental data (circles) are fitted with Debye formula (1) (solid line).

Electrical resistivity measurements for Yb_4FeGe_8:

The temperature dependence of the electrical resistivity $\rho(T)$ of Yb_4FeGe_8 measured between 2.29 and 301.7 K at zero applied field, is given in Figure 6-25. The resistivity of this material exhibits remarkable and quite unusual temperature dependence. The resistivity data above ~ 140 - 150 K are almost temperature independent, between ~ 140 – 50 K exhibit a broad curvature-like behavior while below 50 K the resistivity shows a continuous and steep drop. Similar overall behavior of $\rho(T)$ has been observed also in other mixed-valence compounds such as in $CeIr_2Si_2$,[77] $CeRhSi_2$,[22] $Ce_2Ni_3Si_5$,[78] $CePd_3$,[79] YbPdBi[80] and $YbCo_2Ge_2$.[81] In these cases, this behavior of the resistivity was suggested to be due to various processes as the onset of coherent effects or/and it could reflect the interplay of Kondo and crystal-field interactions. The room value of $\rho(300K) \approx$ 162 $\mu\Omega$ cm reveals a rather moderate metallic behavior and it is of the same order of magnitude as other known Yb-based intermediate-valence compounds.[82-84] The $d(\rho)/d(T)$ curve exhibits a sharp change in the slope below 5 K which could be associated with the sudden increase to higher magnetic susceptibility values that was observed at the same temperature in low field measurements (10 G) for Yb_4FeGe_8 described above and could suggest a transition at lower temperature.

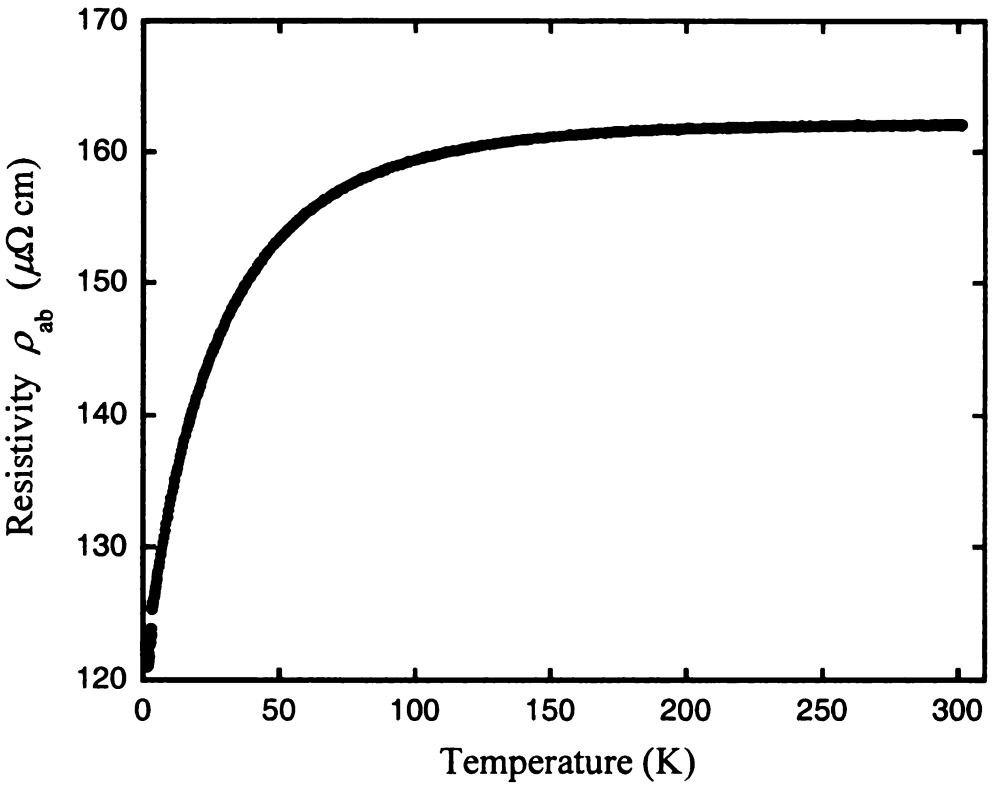

Figure 6-25. Temperature variation of the electrical resistivity $\rho(T)$ of Yb_4FeGe_8 from 2.28 to 301.75 K with at zero applied field.

6-4. Conclusions

Single crystals of the ternary intermetallic compounds Yb_4TMGe_8 (TM = Cr, Fe and Co) were obtained in reactions involving excess of liquid In metal. This an example of a non-reactive behavior of In flux in the quaternary system of Yb/TM/Ge/In. The title compounds have been found to exhibit very interesting structural features and physical properties.

We have successfully elucidated the new Yb_4TMGe_8 (TM = Cr, Fe and Co) superstructures by single crystal X-ray diffraction and (3+1) dimensional crystallography. The refinements revealed both occupational and positional modulation along the *a,c*-plane due to the modulation of the Ge atoms in the extended square net and the partial occupation of the TM sites. The structural findings for Yb_4TMGe_8 challenge the correctness of the reported $RETM_{1-x}Ge_2$ disordered compounds and reinforces the re-investigation call made in the case of Tb_4FeGe_8 which was also found to have a modulated square net of the Ge atoms.[14]

Magnetic properties measurements for Yb_4CrGe_8 and Yb_4FeGe_8 revealed ferromagnetic transitions for both compounds below 20 K. Curie-Weiss law fit to the $1/\chi_m(T)$ data above 100 K, resulted in a somewhat increased μ_{eff} value comparing to the expected theoretical value for a free Yb^{3+} ion.

Temperature dependent X-ray absorption near edge spectroscopy at the Yb L_{III}-edge revealed double peaked spectra for all Yb_4TMGe_8 compounds indicating that the title Yb materials can be classified as mixed-valence (*MV*) or intermediate-valence (*IV*) compounds. In addition, the Yb^{3+}/Yb^{2+} average ratio changes continuously with temperature and reaches smaller values when going from room temperature down to lower temperatures.

The above XANES observation inspired us to perform temperature dependent single crystal X-ray diffraction experiments in order to investigate for any possible effects of the Yb valence fluctuation on the thermal expansion of the present materials. Cell parameters refinements at a temperature range of 10 – 320 K, showed different behavior with temperature between the *a,c* and *b* axes which resulted in an anomalous

near

in th

temp

speci

measu

behav

materi

compo

examir

propert

observ

substitu

behavi

active

nearly zero thermal expansion of the cell volume up to ~ 100 – 120 K, depending the TM in the Yb_4TMGe_8 systems and a normally observed positive thermal expansion at higher temperatures.

Heat capacity measurements for Cr compound showed an enhanced electronic specific heat coefficient γ suggesting possible heavy-fermion behavior. Finally, resistivity measurements for the Fe compound exhibited an unusual temperature dependence behavior bearing similarities with the ρ(T) data reported for other mixed-valence materials.

Due to the intriguing structural and physical properties exhibited by the title compounds it will be of benefit to study more analogs of the Yb_4TMGe_8 series in order to examine the effect that the different employed transition metals could bring to the properties of these compounds. This could perhaps shed more light to the phenomena observed such as the nearly ZTE expansion behavior between 10 - 100 K, and right substitution or doping of these materials could extend the temperature range of the ZTE behavior. Discovering materials whose size does not change with temperature is a highly active field of study, both for technological applications and fundamental understanding.

References:

(1) Szytula, A.; Leciejewicz, J. *"Handbook of Crystal Structures and Magnetic Properties of Rare Earth Intermetallics"*; CRC Press: Boca Raton, Fl, 1994.

(2) Villars, P.; Calvert, L. D. *"Pearson's Handbook of Crystallographic Data for Intermetallic Phases", 2nd ed.; American Society for Metals* OH 44073, 1991.

(3) Bodak, O. I.; Gladyshevskii, E. I. *Kristallografiya* **1969**, *14*, 990.

(4) Bodak, O. P.; Gladyshe.Ei *Soviet Physics Crystallography, Ussr* **1970**, *14*, 859.

(5) Po¨ttgen, R.; Simon, A. *Z. Anorg. Allg. Chem.* **1996**, *622*, 779.

(6) Mun, E. D.; Lee, B. K.; Kwon, Y. S.; Jung, M. H. *Phys. Rev. B* **2004**, *69*, 085113.

(7) Francois, M.; Venturini, G.; Malaman, B.; Roques, B. *J. Less-Comm. Met.* **1990**, *160*, 197.

(8) M´eot-Meyer, M.; Venturini, G.; Malaman, B.; Roques, B. *Mater. Res. Bull.* **1985**, *20*, 1515.

(9) Venturini, G. ; Francois, M. ; Malaman, B.; Roques, B. *J. Less-Common Met.* **1990**, *160*, 215.

(10) Das, I.; Sampathkumaran, EV. *Solid State Commun.* **1992**, *83*, 765.

(11) Das, I.; Sampathkumaran, EV.; Hirota, K.; Ishikawa, M. *Phys. Rev. B* **1994**, *49*, 3586.

(12) Das, I.; Sampathkumaran, EV. *Physica B* **1995**, *205*, 259.

(13) Zheng, L. ; Franzen, H. *J. Alloys Compd.* **1998**, *267*, 86.

(14) Zhuravleva, M. A.; Bilc, D.; Pcionek, R. J.; Mahanti, S. D.; Kanatzidis, M. G. *Inorg. Chem.* **2005**, *44*, 2177-2188.

(15) Paccard, L. ; Paccard., D.; Allemand, J. *J. Less-Common Met.* **1990**, *161*, 295.

(16) Deitch, R. H. *Crystal Growth*; Pamplin, B. R. ed.; Pergamon Press:: Oxford and New York, 1975.

(17) Esmailzadeh, S. ; Hoffmann, R.; Po¨ttgen, R. *Z. Naturforsch.* **2004**, *59b*, 1451.

(18) Hossain, Z.; Gupta, L. C.; Geibel, C. *J. Phys.: Condens. Matter* **2002**, *14*, 9687.

(19) Gamza, M.; Slebarski, A; Rosner, H. *J. Phys.: Condens. Matter* **2008**, *20*, 025201.

(20) Jung, M. H.; N.Harrison; H.Lacerda, A.; Nakotte, H.; Pagliuso, P. G.; Sarrao, J. L.; Thompson, J. D. *Phys. Rev. B* **2002**, *66*, 054420.

(21) Pecharsky, V.K.; K.A. Gschneidner, Jr. *Phys. Rev. B* **1991**, *43*, 8238.

(22) Adroja, D.T.; Rainford, B.D. *J. Magn. Magn. Mater.* **1993**, *119*, 54.

(23) Pecharsky, V.K.; Jr., K.A. Gschneidner; Miller, L.L. *Phys. Rev. B* **1991**, *43*.

(24) Mun, E.D.; Kwon, Y.S.; Jung, M.H. *ibid* **2003**, *67*, 033103.

(25) Lee, 1W.H.; Kwan, K.S.; Klavins, P.; Shelton, R.N. *Phys. Rev. B* **1990**, *42*, 6542.

(26) Lawrence, J.; Chen, Y.-Y.; Thompson, J. *Theoretical and Experimental Aspects of Valence Fluctuations and Heavy Fermions*; Plenum: New York and London, 1987.

(27) Pikul, A. P.; Kaczorowski, D.; Bukowski, Z.; Gofryk, K.; Burkhardt, U.; Grin, Y.; Steglich, F. *Phys. Rev. B* **2006**, *73*, 092406.

(28) Stewart, G. R. *Rev. Mod. Phys.* **1984**, *56*, 755.

(29) Kowalczyk, A.; Falkowski, M.; Tolinski, T.; Chelkowska, G. *Solid State Comm.* **2006**, *139*, 5.

(30) Jaccard, D.; Wilhelm, H.; Alami-Yadri, K.; Vargoz, E.; Elsevier Science Bv: 1999, p 1-7.

(31) Alami-Yadri, K.; Wilhelm, H.; Jaccard, D. *Eur. Phys. J. B* **1998**, *6*, 5-11.

(32) Alami-Yadri, K.; Jaccard, D. *Solid State Comm.* **1996**, *100*, 385.

(33) Jaccard, D.; Link, P.; Vargoz, E.; Alami-Yadri, K. *Physica B* **1997**, *230-232*, 297.

(34) Lawrence, J. M.; Riseborough, P. S.; Parks, R. D. *Reports on Progress in Physics* **1981**, *44*, 1.

(35) Kindler, B.; Finsterbusch, D.; Graf, R.; Ritter, F.; Assmus, W.; Luthi, B. *Physical Review B* **1994**, *50*, 704.

(36) Stewart, G. R. *Rev. Mod. Phys.* **2001**, *73*, 797.

(37) Stewart, G. R. *Rev. Mod. Phys.* **2006**, *78*, 743.

(38) Kanatzidis, M. G.; Pottgen, R.; Jeitschko, W. *Angewandte Chemie-International Edition* **2005**, *44*, 6996-7023.

(39) Sieve, B.; Trikalitis, P. N.; Kanatzidis, M. G. *Z. Anorg. Allg. Chem.* **2002**, *628*, 1568-1574.

(40) Sieve, B.; Chen, X. Z.; Henning, R.; Brazis, P.; Kannewurf, C. R.; Cowen, J. A.; Schultz, A. J.; Kanatzidis, M. G. *J. Am. Chem. Soc* **2001**, *123*, 7040.

(41) Zhuravleva, M. A.; Pcionek, R. J.; Wang, X. P.; Schultz, A. J.; Kanatzidis, M. G. *Inorg. Chem.* **2003**, *42*, 6412.

(42) Zhuravleva, M. A.; Kanatzidis, M. G. *Z. Naturforch B : Sec. B* **2003**, *58*, 649.

(43) Zhuravleva, M. A.; Evain, M.; Petricek, V.; Kanatzidis, M. G. *J. Am. Chem. Soc* **2007**, *129*, 3082.

(44) Wu, X. N.; Kanatzidis, M. G. *J. Solid State Chem.* **2005**, *178*, 3233.

(45) Wu, X. U.; Latturner, S. E.; Kanatzidis, M. G. *Inorg. Chem.* **2006**, *45*, 5358.

(46) Latturner, S. E.; Bilc, D.; Mahanti, S. D.; Kanatzidis, M. G. *Inorg. Chem.* **2003**, *42*, 7959.

(47) Latturner, S. E.; Kanatzidis, M. G. *Inorg. Chem.* **2008**, *47*, 2089.

(48) Salvador, J. R.; Bilc, D.; Gour, J. R.; Mahanti, S. D.; Kanatzidis, M. G. *Inorg. Chem.* **2005**, *44*, 8670

(49) Salvador, J. R.; Gour, J. R.; Bilc, D.; Mahanti, S. D.; Kanatzidis, M. G. *Inorg. Chem.* **2004**, *43*, 1403.

(50) Salvador, J. R.; Kanatzidis, M. G. *Inorg. Chem.* **2006**, *45*, 7091-7099.

(51) Chondroudi, M.; Balasubramanian, M.; Welp, U.; Kwok, W.-K.; Kanatzidis, M. G. *Chem. Mater.* **2007**, *19*, 4769.

(52) Salvador, J. R.; Hoang, K.; Mahanti, S. D.; Kanatzidis, M. G. *Inorg. Chem.* **2007**, *46*, 6933

(53) Zaremba, V. I.; Tyvanchuk, Y. B.; Stepien-Damm, J. *Z Kristallogr New Cryst Struct* **1997**, *212*, 291.

(54) Tobash, P. H.; Lins, D.; Bobev, S.; Lima, A.; Hundley, M. F.; Thompson, J. D.; Sarrao, J. L. *Chem. Mater.* **2005**, *17*, 5567.

(55) Sheldrick, G. M.; version 4 ed.; University of Gottingen: Gottingen, Germany, 1995.

(56) Sheldrick, G. M.; version 5 ed.; Siemens Analytical X-ray Instruments Inc.: Madison, WI, 1995.

(57) Petricek, V.; Dusek, M.; Institute of Physics: Praha, Czech Republic, 2000.

(58) X-AREA, IPDS Software; STOE & Cie GmbH: Darmstadt, 2006.

(59) Kraft, S.; Stumpel, J.; Becker, P.; Kuetgens, U. *Rev. Sci. Instrum.* **1996**, *67*, 681.

(60) Ravel, B.; Newville, M. *J. Synchrotron Rad.* **2005**, *12:4*, 537.

(61) *Advanced Heat Capacity with Helium-3 Application Note. Physical Property Measurement System Brochure* **1999**.

(62) Li, Qing'An; Gray, K. E.; Mitchell, J. F. *Phys. Rev. B* **1999**, *59*, 9357 - 9361.

(63) Boher, P.; Garnier, P.; Gavarri, J.R.; Hewat, A.W. *J. Solid State Chem.* **1985**, *57*, 343.

(64) Boher, P.; Garnier, P.; Gavarri, J.R.; Hewat, A.W. *Phase Trans.* **1992**, *38*, 127.

(65) Okada, S.; Atoda, T.; Higashi, I. *Acta Chemica Scandinavica* **1949**, *3*, 595.

(66) Okada, S.; Atoda, T.; Higashi, I. *J. Solid State Chem.* **1987**, *68*, 61.

(67) Kittel, C. *Introduction to Solid State Physics* 7th ed.; John Wiley & Sons: Hoboken, NJ, 1996.

(68) Potgen, R.; Lang, A.; Hoffmann, R.-D.; Kunnen, B.; Kotzyba, G.; Mullmann, R.; Mosel, B.D.; Rosenhahn, C. *Z. Kristallogr.* **1999**, *214*, 143.

(69) Sampathkumaran, E.V.; Frank, K.H.; Kalkowski, G.; Kaindl, G.; Domke, M.; Wortmann, G. *Phys. Rev. B* **1984**, *29*, 5702.

(70) Rao, C. N. R.; Sarma, D. D.; Sarode, P. R.; Sampathkumaran, E. V.; Gupta, L. C.; Vijayaraghavan, R. *Chem. Phys. Lett.* **1980**, *76*, 413.

(71) Hatwar, T. K.; Nayak, R. M.; Padalia, B. D.; Ghatikar, M. N.; Sampathkumaran, E. V.; Gupta, L. C.; Vijayaraghavan, R. *Solid State Comm.* **1980**, *34*, 617.

(72) Bauer, E.; Tuan, L.; Hauser, R.; Gratz, E.; Holubar, T.; Hilscher, G.; Michor, H.; Perthold, W.; Godart, C.; Alleno, E.; Hiebl, K. *Phys. Rev. B* **1995**, *52*, 4327.

(73) Lawrence, J.M.; Kwei, G.H.; Canfield, P.C.; DeWitt, J.G.; Lawson, A.C. *Phys. Rev. B* **1994**, *49*, 1627.

(74) Moreschini, L.; Dallera, C.; Joyce, J. J.; Sarrao, J. L.; Bauer, E. D.; Fritsch, V.; Bobev, S.; Carpene, E.; Huotari, S.; Vanko, G.; Monaco, G.; Lacovig, P.; Panaccione, G.; Fondacaro, A.; Paolicelli, G.; Torelli, P.; Grioni, M. *Physical Review B* **2007**, *75*, 035113.

(75) Jeong, T.; Kwon, Y. *Phys. Lett. A* **2007**, *362*, 500.

(76) Torikachvili, M. S.; Jia, S.; Mun, E. D.; Hannahs, S. T.; Black, R. C.; Neils, W. K.; Martien, D.; Bud'ko, S. L.; Canfield, P. C. *Proceedings of the National Academy of Sciences of the United States of America* **2007**, *104*, 9960-9963.

(77) Buffat, B.; Chevalier, B.; Tuilier, M.H.; and, B. Lioret; Etourneau, J. *Solid State Comm.* **1986**, *59*, 17.

(78) Mazumdar, C.; Nagarajan, R.; Dhar, S. K.; Gupta, L.C.; Vijayaraghavan, R.; Padalia, B.D. *Phys. Rev. B* **1992**, *46*, 9009.

(79) Schneider, H.; Wohlleben, D. *Z. Phys. B - Condensed Matter* **1981**, *44*, 193.

(80) Kaczorowski, D.; Leithe-Jasper, A.; Rogl, P.; Flandorfer, H.; Cichorek, T.; Pietri, R.; Andraka, B. *Phys. Rev. B* **1999**, *60*, 422.

(81) Trovarelli, O.; Geibel, C.; Grosche, M.; Schleser, R.; Borth, R.; Sparn, G.; Steglich, F. *Physica B* **1999**, *259-261*, 140.

(82) Wohlleben, D.; Wittershagen, B. *Adv. Phys.* **1985**, *34*, 403.

(83) Cho, B.K.; DiSalvo, F.J.; Kim, J.S.; Stewart, G.R.; Bud'ko, S.L. *Physica B* **1998**, *253*, 40.

(84) Androja, D. T.; Malik, S. K.; Padalia, B. D.; Bhatia, S. N.; Walia, R.; Vijayaraghvan, R. *Phys. Rev. B* **1990**, *42*, 2700.

CHAPTER 7

Exploratory Studies on the Ternary Systems RE/Cu/In and Yb/Ag/In Employing In as Flux

7-1. Introduction

Among the large body of rare-earth intermetallics, the systems RE/Cu/X (X = In, Ag, Au, Pd, Si, Sn, Sb etc.) especially with Ce and Yb as the RE, have received a lot of attention, both in theory and experiment. Compounds of this type exhibit a great variety of structural and physical properties[1-3] which include anomalous negative thermal expansion in $CeCu_2In$,[4] long range magnetic order in $YbCu_4Au$ and $YbCu_4Pd$,[5-7] superconductivity and heavy fermion behavior in $CeCu_2Si_2$[8, 9] and multiple successive magnetic phase transitions in the series Ce_5CuX (X = Sn, Sb, Pb)[10-12]

An especially interesting set of compounds are the $YbCu_{4+x}In_{1-x}$. This family has shown both mixed and intermediate valency characterized by a first-order temperature-induced isostructural valence phase transition as well as crossover from valence transition to Kondo behavior [13-17] Additionally, it shows valence fluctuation induced by pressure or alloying while it belongs (along with the $YbCu_4Mg$ analog) to the class of "light" heavy-fermion systems.[18-20]

In a recent review, it has been demonstrated that molten metal fluxes are excellent alternative to the conventional synthetic methods for the exploratory synthesis of new rare earth intermetallic compounds.[21] After our own successful investigations with Al and Ga fluxes in the systems RE/TM/Al/Si or Ge and RE/TM/Ga/Si or Ge which resulted in a numerous ternary and quaternary phases,[22-30] we have recently started employing molten

In metal as a solvent in analogous systems. Within this work we have been able to isolate the germanides $RE_2Zn_3Ge_6$,[31] β-$RENiGe_2$[32] and Yb_4TMGe_8 (TM = Fe, Cr, Co, described in Chapter 6) where In acts as a non-reactive flux, as well as a number of intermetallic compounds in which In gets incorporated into the products including $RE_4Ni_2InGe_4$,[33] $RE_7Co_4InGe_{12}$,[34] $Dy_4CoInGe_4$, $Yb_3AuGe_2In_3$, CeAuGeIn, $EuAuGeIn_2$ (described in Chapters 3-5) and $REAu_2In_4$.[35]

The diversity of interesting physical phenomena in the above RE/Cu/X compounds motivated us to perform synthetic investigations in the systems RE/Cu/In and RE/Ag/In with indium flux reactions. From these explorations we were able to synthesize and characterize by single crystal X-ray diffraction as well as by high resolution powder X-ray diffraction the crystal structure of the ternary $RECu_{6+x}In_{6-x}$ (RE= Ce, Nd, Sm, Gd, Dy, Ho, Er, Yb) and $YbAg_{5.18}In_{6.83}$ compounds. They all crystallize as a ternary disordered variant of the $ThMn_{12}$ structure type (*I4/mmm*)[36] in the orthorhombic *Immm* space group. The $RECu_{5.1}In_{6.9}$ (RE = Y, Ce, Pr, Nd, Sm, Gd-Lu) compounds have been previously reported to crystallize with the tetragonal $ThMn_{12}$ type structure.[36-38] In these compounds, which were studied by X-ray powder diffraction, the 2a sites are occupied by the RE atoms, the 8*f* positions are statistically mixed occupied by Cu+In (with less In), the 8*j* positions are also mixed occupied by Cu+In (with less Cu) whereas the 8i sites are occupied only by In. A later report described the compounds $RECu_6In_6$ (RE = Y, Ce, Pr, Nd, Gd, Tb, Dy),[39] which also crystallize in the tetragonal $ThMn_{12}$ type structure.[36] In this work the materials were synthesized with arc-melting and were studied by single crystal X-ray diffraction. Based on this work a proposed tetragonal model includes a split 8*j* position of Cu/In with 50/50 occupancy. The rest 2*a*, 8*f* and 8*i* sites are occupied by RE,

Cu and In only atoms, respectively. In this present work both tetragonal and orthorhombic models were examined and we propose that a distorted orthorhombic model with two split Cu/In sites as more correct to describe the $RECu_{6+x}In_{6-x}$ and $YbAg_{5.18}In_{6.83}$ compounds. Magnetic susceptibility measurements for these compounds and X-ray absorption near edge spectroscopy for RE = Yb and Ce analogs have been performed and will be discussed.

7-2. Experimental Section

Reagents:

The following reagents were used as purchased without further purification: RE, (in the form of powder ground from metal chunks, 99.9%, Chinese Rare Earth Information center, Inner Mongolia, China), Cu (~325 mesh, 99.5% Cerac, Milwaukee, WI), Ag (pieces, 99.8% Alfa Aesar, Ward Hill, MA) and In (tear drops 99.99% Plasmaterials, Livermore, CA).

Synthesis:

The $RECu_{6+x}In_{6-x}$ (RE = Ce, Nd, Sm, Gd, Dy, Ho, Er and Yb) and $YbAg_{5.18}In_{6.83}$ compounds were obtained by combining 1 mmol of the rare earth metal, 3 mmol Cu (or Ag) and 15 mmol In in an alumina (Al_2O_3) crucible under an inert nitrogen atmosphere inside a drybox. The crucible was placed in a 13 mm fused silica tube, which was flame sealed under vacuum of 10^{-4} mbar, to prevent oxidation during heating. The reactants were then heated to 1000 °C over the course of 10 h, held at 1000 °C for 72 h, and cooled to 50 °C over 36 h. To isolate the product from the excess In a quartz frit was placed in

the open end of the Al_2O_3 crucible, and then flame sealed in a new silica tube under vacuum of 10^{-4} mbar. The tube was heated to 300 °C for 15 min, to ensure the excess In was molten, and it was centrifuged for 5 min. This process was repeated three times to remove as much excess In as possible. The remaining In was etched away by soaking in glacial acetic acid and soniqation for 24 to 48 h. The crystalline product was rinsed with acetone. Several crystals, which are usually metallic silver plates or polyhedrals (occasionally reddish color due to Cu film covering the crystal's surface) for the $RECu_{6+x}In_{6-x}$ compounds and metallic silver rods for the $YbAg_{5.18}In_{6.83}$ compound were carefully selected for elemental analysis, structure characterization, magnetic susceptibility measurements and X-ray near edge spectroscopy. Main reaction byproducts for all $RECu_{6+x}In_{6-x}$ were unreacted In metal and the binary CuIn as it was indicated by EDS analysis which due to its very different crystal morphology was easily distinguishable. The yields of the reactions were 65-85% with purity ranging from 70% to 90% depending on the RE metal.

Elemental Analysis:

Semi-quantitative analysis was performed on several crystals of the compounds using a JEOL JSM-35C scanning electron microscope (SEM) equipped with a Noran Vantage Energy Dispersive Spectroscopy (EDS) detector. Data were acquired by applying a 25 KV accelerating voltage and an acquisition time of 30 s. The EDS analysis taken on visibly clean surfaces of $HoCu_{6.11}In_{5.89}$ crystals gave the atomic composition of 7.9% Ho, 47.9% Cu and 44.2% In ($HoCu_{6.1}In_{5.6}$), which is in good agreement with the results derived from the single crystal X-ray diffraction refinement. Similar

stoichiometric ratios (small variation from 1/6/6 ratio) were determined for the other RE analogs as well as the Ag one.

Single Crystal X-ray Diffraction:

Single crystal X-ray diffraction data of $RECu_{6+x}In_{6-x}$ for RE = Nd, Sm, Gd, Dy, Ho, Er and Yb and of $YbAg_{5.18}In_{6.83}$ were collected at room temperature using a Bruker SMART Platform CCD diffractometer with graphite monochromatized Mo Ka (λ = 0.71073 Å) radiation. The SMART software was used for data acquisition and SAINT for data extraction and reduction.[40] The analytical absorption correction was applied using the program SADABS[40] and the structures were solved by direct methods and refined with the SHELXTL package.[41] A STOE IPDS 2T diffractometer with graphite-monochromatized Mo Kα (λ = 0.71073 Å) radiation was used to collect single crystal X-ray diffraction data for the $CeCu_6In_6$. The X-AREA package suite[42] was used for data reduction and analytical absorption corrections and the structure was refined using the SHELXTL package.[41] The structure of $CeCu_6In_6$ was solved first, and its atomic coordinates were used as a starting model for the rest $RECu_{6+x}In_{6-x}$ analogs as well as for $YbAg_{5.18}In_{6.83}$. Initially the structure was solved in the tetragonal space group of *I4mmm* with one, almost equally occupied Cu/In split site, see Tables 7-1 – 7-3. This refinement resulted in relatively high temperature parameters for the Cu/In site (~ 17 $Å^2$ x 10^3) which is much higher than the values of the other atoms. The structure was solved in the orthorhombic space group of *Immm* with two almost equally occupied Cu/In split sites, see Tables 7-1, 7-4 and 7-5. The disordered orthorhombic model resulted in a better fit (reduced R-value and residual peaks, from 3,15% to 2.15%) and in a better agreement

between the thermal factors (everything is close to the same average value ~ 8 $Å^2$ x 10^3). In order to verify that this is characteristic for the entire sample and not just on few selected single crystals and to eliminate the existence of twin artifacts present in the X-ray data, we performed high resolution powder X-ray diffraction (PXRD) on the $CeCu_6In_6$ compound. The PXRD data confirmed, as described in the next paragraph, the disordered orthorhombic model with two split Cu/In sites as the best solution, and is chosen to describe the structure of the present compounds. The crystal data and structure refinement details for the rest $RECu_{6+x}In_{6-x}$ analogs and for $YbAg_{5.18}In_{6.83}$ are given in Tables 7-6 – 7-25.

High Resolution Powder X-ray Diffraction:

High resolution powder X-ray diffraction data were collected at room temperature using synchrotron radiation (λ = 0.58919 Å, 11-BM beam line at the Advanced Photon Source (APS) at Argonne National Laboratory (ANL)). Fine powder of the sample was packed in a kapton capillary which was rotated during data collection to minimize preferential orientation of the grains. The Rietveld method[43] was used for the structure refinement using GSAS.[44] Cell parameters, atomic coordinates, isotropic thermal factors, and occupancies were refined. Thermal parameters of atoms occupying (close to) the same position were constrained to be the same. Furthermore, parameters for fitting the background, scaling the datasets, and profiles were used. Impurities of $CuIn_3$ and In were found and their structures were fitted against the experimental data. $Cu_{11}In_9$ was also indentified as a minor impurity. Three peaks that belonged to that phase were simply omitted from the refinement.

Several models were fitted against the experimental diffraction pattern in order to investigate the disorder on the Cu/In sites, see Figure 7-1. The agreement factors after the refinement of the different models (Table 7-26) could not suggest which model is better than the other one. Instead, the agreement of the refined occupancies against the elemental analysis results and values of the thermal factors were used for evaluating the refined models.

Initially, no disorder was assumed between the Cu and In sites (undistorted orthorhombic model). Although the stoichiometry was close to the experimental one (1:6:6) and the agreement factors acceptable, the isotropic thermal factors of Cu(1) and In(3) were 0.0060(5) $Å^2$ and 0.088(1) $Å^2$ respectively (Table 7-27). These values were far away from the average expected one (~ 0.04 $Å^2$) as observed for the other atoms in the structure. Mixing the problematic sites with Cu and In was the only chemically acceptable solution since no additional reflections were observed due to possible long range ordering. This method yielded the orthorhombic distorted model #1. In this case, the two disordered sites were assumed to be occupied by Cu and In at the same position (Table 7-28, no split site). Noticeable, the values of the thermal parameters of the distorted atoms were comparable to those of the other atoms in the model but the refined occupancies were different from the ones obtained by elemental analysis. By splitting the disordered sites, orthorhombic disordered model #2 (Table 7-29), the refined occupancies converged to those found by elemental analysis and additionally the agreement factor (R against F^2) was improved of about 1%. (see Table 7-26).

Finally, two tetragonal models were tested. The first one, reported in Table 7-30, contained one split site. Although thermal factors looked reasonable the refined

occupa

rich in

=2457

tries t

20

Intensity

10

Figure

occupancies were significantly different from the expected ones yielding a composition rich in Cu. The second tetragonal model was taken from Poettgen et al.[39] (ICSD #245709) in which each split site was occupied by both Cu and In. In this case, several tries to refine the occupancies gave unphysical negative values for them.

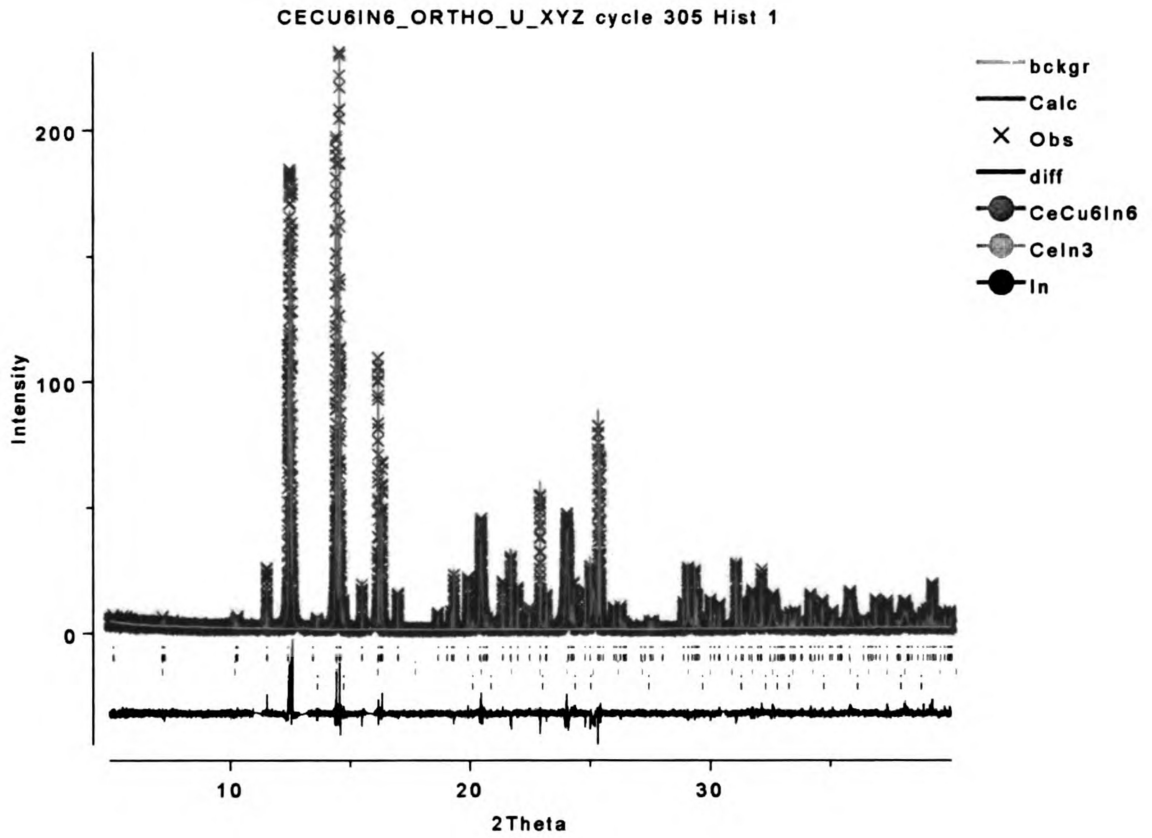

Figure 7-1. High resolution powder X-ray diffraction pattern for $CeCu_6In_6$.

Table 7-1. Crystal data and structure refinement data for $CeCu_6In_6$ in *I*4/*mmm* and *Immm* space groups.

Empirical formula	$CeCu_6In_6$	$CeCu_6In_6$
Formula weight	1210.28	1210.28
Temperature (K)	293(2)	293(2)
Wavelength (Å)	0.71073	0.71073
Crystal system	Tetragonal	Orthorhombic
Space group	*I*4/*mmm*	*Immm*
a (Å)	9.2684(13)	5.4298(10)
b (Å)	9.2684(13)	9.2636(12)
c (Å)	5.4298(10)	9.2732(13
V (Å^3) / Z	466.44(13) / 2	466.44(12) / 2
$Density_{calc}$ (Mg/m^3)	8.617	8.617
Absorption coefficient (mm^{-1}) / F(000)	32.570 / 1052	32.570 / 1052
θ range for data collection (°)	3.11 to 31.89°	3.11 to 31.89°
Index ranges	$-12 \le h \le 13$ $-12 \le k \le 13$ $-8 \le l \le 8$	$-8 \le h \le 8$ $-12 \le k \le 13$ $-13 \le l \le 12$
Reflections collected / unique / *R*(int)	2794 / 258 / 0.0535	2794 / 479 / 0.0502
Completeness to θ (%)	98.9	98.8
Data / restraints / parameters	258 / 0 / 18	479 / 0 / 37
Refinement method	Full-matrix least- squares on F^2	
Goodness-of-fit on F^2	1.258	1.226
Final R indices [$I>2\sigma(I)$] (R_1 / wR_2)[a]	0.0315 / 0.0711	0.0215 / 0.0437
R indices (all data) (R_1 / wR_2)[a]	0.0327 / 0.0718	0.0240 / 0.0445
Extinction coefficient	0.0172(4)	0.0148(5)
Largest diff. peak and hole (e. Å^{-3})	3.533 and -3.837	1.801 and -1.355

[a] $R = \Sigma||F_o|-|F_c|| / \Sigma|F_o|$, $wR = \{\Sigma[w(|F_o|^2 - |F_c|^2)^2] / \Sigma[w(|F_o|^4)]\}^{1/2}$ and calc $w = 1 / [\sigma^2(Fo^2)+(0.0219P)^2+23.6403P]$ where $P = (F_o^2+2F_c^2) / 3$

Table 7-2. Atomic coordinates ($\times 10^4$) and equivalent isotropic displacement parameters ($Å^2 \times 10^3$) for $CeCu_6In_6$ in *I*4/*mmm* space group.

Atom	Wyckoff	x	y	z	U(eq)[a]
Ce	2*a*	0	0	0	5(1)
Cu(1)	8*f*	2500	2500	2500	10(1)
In(1)	8*i*	3423(1)	0	0	11(1)
In(2)	8*j*	0	-2082(2)	5000	17(1) 52%
Cu(2)	8*j*	0	-2004(5)	5000	17(1) 48%

[a]U(eq) is defined as one third of the trace of the orthogonalized U^{ij} tensor.

Table 7-3. Anisotropic displacement parameters ($Å^2 \times 10^3$) for $CeCu_6In_6$ in *I*4/*mmm* space group. The anisotropic displacement factor exponent takes the form: $-2\pi^2[h^2a^{*2}U^{11} + ... + 2hka^*b^*U^{12}]$

Atom	U^{11}	U^{22}	U^{33}	U^{23}	U^{13}	U^{12}
Ce	4(1)	4(1)	7(1)	0	0	0
Cu(1)	10(1)	10(1)	11(1)	1(1)	2(1)	2(1)
In(1)	6(1)	8(1)	20(1)	0	0	0
In(2)	7(1)	35(1)	8(1)	0	0	0
Cu(2)	7(1)	35(1)	8(1)	0	0	0

Table 7-4. Atomic coordinates ($\times 10^4$) and equivalent isotropic displacement parameters ($Å^2 \times 10^3$) for $CeCu_6In_6$ in *I/mmm* space group.

Atom	Wyckoff	x	y	z	U(eq)[a]
Ce	2*a*	0	0	0	4(1)
In(1)	4*i*	0	0	3423(1)	10(1)
In(2)	4*g*	0	3423(1)	0	10(1)
In(a)	4*j*	-5000	0	-1959(5)	7(1) 52%
Cu(a)	4*j*	-5000	0	-2305(7)	10(1) 48%
In(b)	4*h*	-5000	-1954(5)	0	7(1) 52%
Cu(b)	4*h*	-5000	-2302(8)	0	9(1) 48%
Cu	8*k*	2500	2500	2500	9(1)

[a]U(eq) is defined as one third of the trace of the orthogonalized U^{ij} tensor.

Table 7-5. Anisotropic displacement parameters ($Å^2 \times 10^3$) for $CeCu_6In_6$ in *I/mmm* space group. The anisotropic displacement factor exponent takes the form: $-2\pi^2[h^2a^{*2}U^{11} + ... +2hka^*b^*U^{12}]$

Atom	U^{11}	U^{22}	U^{33}	U^{23}	U^{13}	U^{12}
Ce	6(1)	3(1)	3(1)	0	0	0
In(1)	19(1)	7(1)	5(1)	0	0	0
In(2)	19(1)	5(1)	8(1)	0	0	0
In(a)	6(1)	5(1)	11(1)	0	0	0
Cu(a)	10(1)	9(1)	11(2)	0	0	0
In(b)	6(1)	9(2)	6(1)	0	0	0
Cu(b)	11(1)	8(3)	8(1)	0	0	0
Cu	10(1)	9(1)	9(1)	2(1)	2(1)	1(1)

Table 7-6. Crystal data and structure refinement data for $NdCu_{6.125}In_{5.875}$ and $SmCu_6In_6$.

Empirical formula	$NdCu_{6.125}In_{5.875}$	$SmCu_6In_6$
Formula weight	1214.40	1220.51
Temperature (K)	293(2)	293(2)
Wavelength (Å)	0.71073	0.71073
Crystal system	Orthorhombic	Orthorhombic
Space group	*Immm*	*Immm*
a (Å)	5.4388(7)	5.4329(9)
b (Å)	9.2414(12)	9.2193(15)
c (Å)	9.2472(12)	9.2212(15)
V (Å^3) / Z	464.78(10) / 2	461.87(13) / 2
$Density_{calc}$ (Mg/m^3)	8.677	8.776
Absorption coefficient (mm^{-1}) / F(000)	33.375 / 1056	34.322 / 1060
θ range for data collection (°)	3.12 to 27.89	3.12 to 28.54
Index ranges	$-7 \le h \le 7$ $-12 \le k \le 11$ $-12 \le l \le 12$	$-7 \le h \le 6$ $-11 \le k \le 12$ $-12 \le l \le 12$
Reflections collected / unique / *R*(int)	2493 / 340 / 0.0460	2575 / 351 / 0.0379
Completeness to θ (%)	97.1	95.9
Data / restraints / parameters	340 / 0 / 37	351 / 0 / 37
Refinement method	Full-matrix least- squares on F^2	
Goodness-of-fit on F^2	1.257	1.271
Final R indices [$I>2\sigma(I)$] (R_1 / wR_2)[a]	0.0301 / 0.0740	0.0177 / 0.0424
R indices (all data) (R_1 / wR_2)[a]	0.0309 / 0.0745	0.0179 / 0.0425
Extinction coefficient	0.40(2)	0.0036(2)
Largest diff. peak and hole (e. Å^{-3})	2.443 and -2.797	1.390 and -1.213

$$^{a}R_1 = \Sigma\left|\,|F_o| - |F_c|\,\right| / \Sigma|F_o|;\; wR_2 = \left[\Sigma w\{|F_o| - |F_c|\}^2 / \Sigma w|F_o|^2\right]^{1/2};\; w = 1/\sigma^2\{|F_o|\}$$

Table 7-7. Atomic coordinates ($\times 10^4$) and equivalent isotropic displacement parameters ($Å^2 \times 10^3$) for $NdCu_{6.125}In_{5.875}$.

Atom	Wyckoff	x	y	z	U(eq)[a]
Nd	2*a*	0	0	0	4(1)
In(1)	4*i*	0	0	3415(1)	9(1)
In(2)	4*g*	0	3415(1)	0	10(1)
In(a)	4*j*	-5000	0	-1918(11)	6(1) 46%
Cu(a)	4*j*	-5000	0	-2270(14)	7(2) 54%
In(b)	4*h*	-5000	-1918(10)	0	5(1) 47%
Cu(b)	4*h*	-5000	-2277(13)	0	7(2) 53%
Cu	8*k*	2500	2500	2500	9(1)

[a] U(eq) is defined as one third of the trace of the orthogonalized U^{ij} tensor.

Table 7-8. Anisotropic displacement parameters ($Å^2 \times 10^3$) for $NdCu_{6.125}In_{5.875}$. The anisotropic displacement factor exponent takes the form: $-2\pi^2[h^2a^{*2}U^{11} + \ldots + 2hka^*b^*U^{12}]$

Atom	U^{11}	U^{22}	U^{33}	U^{23}	U^{13}	U^{12}
Nd	2(1)	6(1)	4(1)	0	0	0
In(1)	14(1)	9(1)	5(1)	0	0	0
In(2)	14(1)	7(1)	8(1)	0	0	0
In(a)	1(1)	8(2)	8(4)	0	0	0
Cu(a)	4(2)	5(2)	12(6)	0	0	0
In(b)	2(1)	9(3)	5(2)	0	0	0
Cu(b)	3(2)	13(6)	5(2)	0	0	0
Cu	5(1)	11(1)	9(1)	2(1)	2(1)	2(1)

Table 7-9. Atomic coordinates ($\times 10^4$) and equivalent isotropic displacement parameters ($Å^2 \times 10^3$) for $SmCu_6In_6$.

Atom	Wyckoff	x	y	z	U(eq)[a]
Sm	2*a*	0	0	0	8(1)
In(1)	4*i*	0	0	3411(1)	13(1)
In(2)	4*g*	0	3411(1)	0	13(1)
In(a)	4*j*	-5000	0	-1906(5)	9(1) 50%
Cu(a)	4*j*	-5000	0	-2310(7)	11(1) 50%
In(b)	4*h*	-5000	-1912(5)	0	10(1) 50%
Cu(b)	4*h*	-5000	-2301(8)	0	13(1) 50%
Cu	8*k*	2500	2500	2500	13(1)

[a] U(eq) is defined as one third of the trace of the orthogonalized U^{ij} tensor.

Table 7-10. Anisotropic displacement parameters ($Å^2 \times 10^3$) for $SmCu_6In_6$. The anisotropic displacement factor exponent takes the form: $-2\pi^2[h^2a^{*2}U^{11} + \ldots + 2hka^*b^*U^{12}]$

Atom	U^{11}	U^{22}	U^{33}	U^{23}	U^{13}	U^{12}
Sm	8(1)	8(1)	8(1)	0	0	0
In(1)	18(1)	11(1)	9(1)	0	0	0
In(2)	19(1)	10(1)	11(1)	0	0	0
In(a)	9(1)	8(1)	11(2)	0	0	0
Cu(a)	10(1)	12(1)	11(3)	0	0	0
In(b)	8(1)	14(2)	9(1)	0	0	0
Cu(b)	11(2)	16(3)	11(2)	0	0	0
Cu	11(1)	13(1)	13(1)	2(1)	2(1)	2(1)

Table 7-11. Crystal data and structure refinement data for $GdCu_{6.07}In_{5.93}$ and $DyCu_{6.23}In_{5.77}$.

Empirical formula	$GdCu_{6.07}In_{5.93}$	$DyCu_{6.23}In_{5.77}$
Formula weight	1227.41	1232.66
Temperature (K)	293(2)	293(2)
Wavelength (Å)	0.71073	0.71073
Crystal system	Orthorhombic	Orthorhombic
Space group	*Immm*	*Immm*
a (Å)	5.4306(8)	5.4075(12)
b (Å)	9.1954(13)	9.156(2)
c (Å)	9.2014(13)	9.160(2)
V (Å^3) / Z	459.49(11) / 2	453.47(18) / 2
$Density_{calc}$ (Mg/m^3)	8.871	9.028
Absorption coefficient (mm^{-1}) / F(000)	35.326 / 1064	36.721 / 1068
θ range for data collection (°)	3.13 to 28.02	3.15 to 28.16
Index ranges	$-6 \le h \le 7$ $-11 \le k \le 11$ $-12 \le l \le 12$	$-7 \le h \le 7$ $-11 \le k \le 12$ $-12 \le l \le 12$
Reflections collected / unique / *R*(int)	2449 / 335 / 0.0371	2462 / 337 / 0.0381
Completeness to θ (%)	96.3	97.1
Data / restraints / parameters	335 / 0 / 37	337 / 0 / 37
Refinement method	Full-matrix least- squares on F^2	
Goodness-of-fit on F^2	1.319	1.276
Final R indices [$I>2\sigma(I)$] (R_1 / wR_2)[a]	0.0188 / 0.0435	0.0268 / 0.0646
R indices (all data) (R_1 / wR_2)[a]	0.0194 / 0.0437	0.0269 / 0.0647
Extinction coefficient	0.0072(3)	0.0083(5)
Largest diff. peak and hole (e. Å^{-3})	1.093 and -1.306	2.929 and -1.521

$$^{a}R_1 = \Sigma\left||F_o|-|F_c|\right| / \Sigma|F_o|;\ wR_2 = \left[\Sigma w\{|F_o|-|F_c|\}^2 / \Sigma w|F_o|^2\right]^{1/2};\ w = 1/\sigma^2\{|F_o|\}$$

Table 7-12. Atomic coordinates (x 10^4) and equivalent isotropic displacement parameters ($Å^2$ x 10^3) for $GdCu_{6.07}In_{5.93}$.

Atom	Wyckoff	x	y	z	U(eq)[a]
Gd	2*a*	0	0	0	4(1)
In(1)	4*i*	0	0	3405(1)	15(1)
In(2)	4*g*	0	3405(1)	0	8(1)
In(a)	4*j*	-5000	0	-1892(2)	13(1) 49%
Cu(a)	4*j*	-5000	0	-2300(9)	11(1) 51%
In(b)	4*h*	-5000	-1882(6)	0	12(1) 47%
Cu(b)	4*h*	-5000	-2295(9)	0	11(1) 53%
Cu	8*k*	2500	2500	2500	10(1)

[a] U(eq) is defined as one third of the trace of the orthogonalized U^{ij} tensor.

Table 7-13. Anisotropic displacement parameters ($Å^2$ x 10^3) for $GdCu_{6.07}In_{5.93}$. The anisotropic displacement factor exponent takes the form: $-2\pi^2[h^2a^{*2}U^{11} + ... +2hka^*b^*U^{12}]$

Atom	U^{11}	U^{22}	U^{33}	U^{23}	U^{13}	U^{12}
Gd	8(1)	7(1)	8(1)	0	0	0
In(1)	18(1)	9(1)	10(1)	0	0	0
In(2)	18(1)	8(1)	11(1)	0	0	0
In(a)	8(1)	9(1)	12(2)	0	0	0
Cu(a)	12(2)	7(2)	15(4)	0	0	0
In(b)	8(1)	8(2)	9(1)	0	0	0
Cu(b)	9(2)	11(4)	10(2)	0	0	0
Cu	11(1)	12(1)	13(1)	2(1)	2(1)	2(1)

Table 7-14. Atomic coordinates (x 10^4) and equivalent isotropic displacement parameters ($Å^2$ x 10^3) for $DyCu_{6.23}In_{5.77}$.

Atom	Wyckoff	x	y	z	U(eq)[a]
Dy	2*a*	0	0	0	7(1)
In(1)	4*i*	0	0	3402(1)	11(1)
In(2)	4*g*	0	34035(1)	0	11(1)
In(a)	4*j*	-5000	0	-1889(9)	10(1) 47%
Cu(a)	4*j*	-5000	0	-2284(14)	17(3) 53%
In(b)	4*h*	-5000	-1863(9)	0	7(1) 42%
Cu(b)	4*h*	-5000	-2265(12)	0	14(2) 58%
Cu	8*k*	2500	2500	2500	11(1)

[a]U(eq) is defined as one third of the trace of the orthogonalized U^{ij} tensor.

Table 7-15. Anisotropic displacement parameters ($Å^2$ x 10^3) for $DyCu_{6.23}In_{5.77}$. The anisotropic displacement factor exponent takes the form: $-2\pi^2[h^2a^{*2}U^{11} + ... +2hka^*b^*U^{12}]$

Atom	U^{11}	U^{22}	U^{33}	U^{23}	U^{13}	U^{12}
Dy	8(1)	5(1)	8(1)	0	0	0
In(1)	16(1)	7(1)	10(1)	0	0	0
In(2)	15(1)	7(1)	11(1)	0	0	0
In(a)	7(2)	6(1)	18(3)	0	0	0
Cu(a)	12(3)	7(2)	33(7)	0	0	0
In(b)	5(2)	7(3)	8(2)	0	0	0
Cu(b)	8(2)	23(5)	10(2)	0	0	0
Cu	9(1)	10(1)	14(1)	3(1)	2(1)	2(1)

Table 7-16. Crystal data and structure refinement data for $HoCu_{6.11}In_{5.89}$ and $ErCu_{6.23}In_{5.77}$.

Empirical formula	$HoCu_{6.11}In_{5.89}$	$ErCu_{6.23}In_{5.77}$
Formula weight	1235.09	1237.42
Temperature (K)	293(2)	293(2)
Wavelength (Å)	0.71073	0.71073
Crystal system	Orthorhombic	Orthorhombic
Space group	*Immm*	*Immm*
a (Å)	5.4192(11)	5.4106(10)
b (Å)	9.1608(18)	9.1479(17)
c (Å)	9.1601(18)	9.1529(17)
V (Å^3) / Z	454.75(16) / 2	453.03(15) / 2
$Density_{calc}$ (Mg/m^3)	9.020	9.071
Absorption coefficient (mm^{-1}) / F(000)	37.102 / 1070	37.772 / 1072
θ range for data collection (°)	3.14 to 28.14	3.15 to 28.47
Index ranges	$-7 \le h \le 7$ $-12 \le k \le 11$ $-11 \le l \le 11$	$-7 \le h \le 7$ $-11 \le k \le 11$ $-11 \le l \le 11$
Reflections collected / unique / R(int)	2286 / 334 / 0.0546	2351 / 331 / 0.0492
Completeness to θ (%)	96.8	93.2
Data / restraints / parameters	334 / 0 / 37	331 / 0 / 37
Refinement method	Full-matrix least- squares on F^2	
Goodness-of-fit on F^2	1.262	1.245
Final R indices [$I>2\sigma(I)$] (R_1 / wR_2)[a]	0.0291 / 0.0709	0.0239 / 0.0612
R indices (all data) (R_1 / wR_2)[a]	0.0292 / 0.0710	0.0239 / 0.0612
Extinction coefficient	0.0105(7)	0.0071(5)
Largest diff. peak and hole (e. Å^{-3})	1.712 and -3.126	2.111 and -2.218

$$^{a}R_1 = \Sigma\left||F_o|-|F_c|\right| / \Sigma|F_o|;\ wR_2 = \left[\Sigma w\{|F_o|-|F_c|\}^2 / \Sigma w|F_o|^2\right]^{1/2};\ w = 1/\sigma^2\{|F_o|\}$$

Table 7-17. Atomic coordinates (x 10^4) and equivalent isotropic displacement parameters ($Å^2$ x 10^3) for $HoCu_{6.11}In_{5.89}$.

Atom	Wyckoff	x	y	z	U(eq)[a]
Ho	2*a*	0	0	0	9(1)
In(1)	4*i*	0	0	3398(1)	12(1)
In(2)	4*g*	0	3398(1)	0	12(1)
In(a)	4*j*	-5000	0	-1869(7)	10(1) 48%
Cu(a)	4*j*	-5000	0	-2303(10)	14(2) 52%
In(b)	4*h*	-5000	-2210(9)	0	22(2) 47%
Cu(b)	4*h*	-5000	-1815(7)	0	2(1) 53%
Cu	8*k*	2500	2500	2500	12(1)

[a] U(eq) is defined as one third of the trace of the orthogonalized U^{ij} tensor.

Table 7-18. Anisotropic displacement parameters ($Å^2$ x 10^3) for $HoCu_{6.11}In_{5.89}$. The anisotropic displacement factor exponent takes the form: $-2\pi^2[h^2a^{*2}U^{11} + ... +2hka^*b^*U^{12}]$

Atom	U^{11}	U^{22}	U^{33}	U^{23}	U^{13}	U^{12}
Ho	11(1)	9(1)	7(1)	0	0	0
In(1)	18(1)	11(1)	8(1)	0	0	0
In(2)	18(1)	11(1)	8(1)	0	0	0
In(a)	8(1)	10(1)	12(2)	0	0	0
Cu(a)	14(2)	10(2)	19(4)	0	0	0
In(b)	17(1)	38(4)	11(1)	0	0	0
Cu(b)	2(2)	1(2)	3(2)	0	0	0
Cu	12(1)	14(1)	11(1)	2(1)	2(1)	2(1)

Table 7-19. Atomic coordinates (x 10^4) and equivalent isotropic displacement parameters ($Å^2$ x 10^3) for $ErCu_{6.23}In_{5.77}$.

Atom	Wyckoff	x	y	z	U(eq)[a]
Er	2*a*	0	0	0	8(1)
In(1)	4*i*	0	0	3397(1)	11(1)
In(2)	4*g*	0	3397(1)	0	11(1)
In(a)	4*j*	-5000	0	-1853(6)	8(1) 44%
Cu(a)	4*j*	-5000	0	-2279(8)	13(1) 56%
In(b)	4*h*	-5000	-1850(5)	0	8(1) 44%
Cu(b)	4*h*	-5000	-2280(7)	0	12(1) 56%
Cu	8*k*	2500	2500	2500	11(1)

[a]U(eq) is defined as one third of the trace of the orthogonalized U^{ij} tensor.

Table 7-20. Anisotropic displacement parameters ($Å^2$ x 10^3) for $ErCu_{6.23}In_{5.77}$. The anisotropic displacement factor exponent takes the form: $-2\pi^2[h^2a^{*2}U^{11} + ... +2hka^*b^*U^{12}]$

Atom	U^{11}	U^{22}	U^{33}	U^{23}	U^{13}	U^{12}
Er	8(1)	6(1)	10(1)	0	0	0
In(1)	14(1)	8(1)	11(1)	0	0	0
In(2)	14(1)	7(1)	12(1)	0	0	0
In(a)	5(1)	5(1)	14(2)	0	0	0
Cu(a)	8(1)	7(2)	26(3)	0	0	0
In(b)	5(1)	9(2)	10(1)	0	0	0
Cu(b)	7(1)	20(3)	10(1)	0	0	0
Cu	8(1)	10(1)	15(1)	3(1)	2(1)	2(1)

Table 7-21. Crystallographic data for $YbCu_6In_6$ and $YbAg_{5.18}In_{6.83}$.

Empirical formula	$YbCu_6In_6$	$YbAg_{5.18}In_{6.83}$
Formula weight	1243.20	1514.91
Temperature (K)	293(2)	293(2)
Wavelength (Å)	0.71073	0.71073
Crystal system	Orthorhombic	Orthorhombic
Space group	*Immm*	*Immm*
a (Å)	5.4034(8)	5.7410(5)
b (Å)	9.2339(13)	9.735
c (Å)	9.2311(13)	9.7352(9)
V (Å^3) / Z	460.58(11) / 2	544.10(7) / 2
$Density_{calc}$ (Mg/m^3)	8.964	9.247
Absorption coefficient (mm^{-1}) / F(000)	38.195 / 1076	31.670 / 1295
θ range for data collection (°)	3.12 to 28.40	2.96 to 28.24
Index ranges	$-7 \le h \le 7$ $-12 \le k \le 12$ $-12 \le l \le 12$	$-7 \le h \le 7$ $-12 \le k \le 12$ $-12 \le l \le 12$
Reflections collected / unique / *R*(int)	2601 / 352 / 0.0446	2953 / 394 / 0.0397
Completeness to θ (%)	97.5	96.6
Data / restraints / parameters	352 / 0 / 37	394 / 0 / 37
Refinement method	Full-matrix least- squares on F^2	
Goodness-of-fit on F^2	1.210	1.324
Final R indices [$I>2\sigma(I)$] (R_1 / wR_2)[a]	0.0182 / 0.0380	0.0176 / 0.0414
R indices (all data) (R_1 / wR_2)[a]	0.0185 / 0.0381	0.0178 / 0.0415
Extinction coefficient	0.0098(3)	0.0070(2)
Largest diff. peak and hole (e. Å^{-3})	1.933 and -1.565	1.838 and -1.344

$$^{a}R_1 = \Sigma\left||F_o|-|F_c|\right| / \Sigma|F_o|;\ wR_2 = \left[\Sigma w\{|F_o|-|F_c|\}^2 / \Sigma w|F_o|^2\right]^{1/2};\ w = 1/\sigma^2\{|F_o|\}$$

Table 7-22. Atomic coordinates (x 10^4) and equivalent isotropic displacement parameters ($Å^2$ x 10^3) for $YbCu_6In_6$.

Atom	Wyckoff	x	y	z	U(eq)[a]
Yb	2*a*	0	0	0	8(1)
In(1)	4*i*	0	0	3399(1)	11(1)
In(2)	4*g*	0	3399(1)	0	11(1)
In(a)	4*j*	-5000	0	-1874(3)	11(1) 51%
Cu(a)	4*j*	-5000	0	-2337(6)	12(1) 49%
In(b)	4*h*	-5000	-1870(3)	0	23(1) 50%
Cu(b)	4*h*	-5000	-2332(5)	0	9(1) 50%
Cu	8*k*	2500	2500	2500	12(1)

[a]U(eq) is defined as one third of the trace of the orthogonalized U^{ij} tensor.

Table 7-23. Anisotropic displacement parameters ($Å^2$ x 10^3) for $YbCu_6In_6$. The anisotropic displacement factor exponent takes the form: $-2\pi^2[h^2a^{*2}U^{11} + ... +2hka^*b^*U^{12}]$

Atom	U^{11}	U^{22}	U^{33}	U^{23}	U^{13}	U^{12}
Yb	7(1)	9(1)	9(1)	0	0	0
In(1)	13(1)	10(1)	11(1)	0	0	0
In(2)	13(1)	10(1)	11(1)	0	0	0
In(a)	7(1)	9(1)	16(1)	0	0	0
Cu(a)	9(1)	10(1)	19(2)	0	0	0
In(b)	6(1)	13(1)	9(1)	0	0	0
Cu(b)	8(1)	17(2)	11(1)	0	0	0
Cu	9(1)	13(1)	14(1)	2(1)	2(1)	2(1)

Table 7-24. Atomic coordinates (x 10^4) and equivalent isotropic displacement parameters ($Å^2$ x 10^3) for $YbAg_{5.18}In_{6.83}$.

Atom	Wyckoff	x	y	z	U(eq)[a]
Yb	2*a*	0	0	0	13(1)
In(1)	4*i*	0	0	3460(1)	14(1)
In(2)	4*g*	0	3460(1)	0	14(1)
In(a)	4*j*	-5000	0	-1996(16)	21(1) 73%
Ag(a)	4*j*	-5000	0	-2370(20)	11(1) 27%
In(b)	4*h*	-5000	-1983(17)	0	19(1) 68%
Ag(b)	4*h*	-5000	-2350(20)	0	13(1) 32%
Ag	8*k*	2500	2500	2500	15(1)

[a]U(eq) is defined as one third of the trace of the orthogonalized U^{ij} tensor.

Table 7-25. Anisotropic displacement parameters ($Å^2$ x 10^3) for $YbAg_{5.18}In_{6.83}$. The anisotropic displacement factor exponent takes the form: $-2\pi^2[h^2a^{*2}U^{11} + ... +2hka^*b^*U^{12}]$

Atom	U^{11}	U^{22}	U^{33}	U^{23}	U^{13}	U^{12}
Yb	15(1)	12(1)	12(1)	0	0	0
In(1)	18(1)	11(1)	13(1)	0	0	0
In(2)	18(1)	13(1)	11(1)	0	0	0
In(a)	16(1)	10(1)	35(4)	0	0	0
Ag(a)	17(2)	7(2)	10(3)	0	0	0
In(b)	15(1)	33(4)	10(1)	0	0	0
Ag(b)	19(2)	14(3)	8(2)	0	0	0
Ag	12(1)	17(1)	17(1)	2(1)	4(1)	4(1)

Table 7-26. Summary of the crystallographic agreement factors and refinement statistics of the powder data for the different models.

Refined values	Orthorhombic (undistorted)	Orthorhombic #1 (distorted)	Orthorhombic #2 (distorted)	Tetragonal (distorted)
Formula	$CeCu_6In_6$	$CeCu_{6.26(2)}In_{5.74(2)}$	$CeCu_{6.05(2)}In_{5.95(2)}$	$CeCu_{6.56(2)}In_{5.44(2)}$
Rp	0.1006	0.1022	0.1018	0.1015
wRp	0.1212	0.1224	0.1215	0.1224
R (F^2)	0.1014	0.1030	0.0948	0.1030
Parameters	52	59	61	46
χ^2	1.063	1.070	1.055	1.066

Table 7-27. Atomic coordinates and equivalent isotropic displacement parameters ($Å^2$) for the orthorhombic undistorted model.

Atom	x	y	z	Occupancy	Uiso ($Å^2$)
Ce	0.0	0.0	0.0	1	0.0389(4)
In(1)	0.0	0.0	0.34039(30)	1	0.0411(7)
In(2)	0.0	0.34392(31)	0.0	1	0.0522(8)
In(3)	0.5	-0.2009(4)	0.0	1	0.088(1)
Cu(1)	0.5	0.0	-0.21156(34)	1	0.0060(5)
Cu(2)	0.25	0.25	0.25	1	0.0393(4)

Table 7-28. Atomic coordinates and equivalent isotropic displacement parameters ($Å^2$) for the orthorhombic distorted model #1.

Atom	x	y	z	Occupancy	Uiso ($Å^2$)
Ce	0.0	0.0	0.0	1.0	0.0389(4)
In(1)	0.0	0.0	0.3442(4)	1.0	0.0571(8)
In(2)	0.0	0.3409(4)	0.0	1.0	0.0360(6)
In(3)	0.5	0.0	-0.1954(4)	0.699(28)	0.051(1)
Cu(3)	0.5	0.0	-0.1954(4)	0.301(28)	0.051(1)
In(4)	0.5	-0.2186(4)	0.0	0.169(23)	0.029(1)
Cu(4)	0.5	-0.2186(4)	0.0	0.831(23)	0.029(1)
Cu(1)	0.25	0.25	0.25	1.0	0.0389(4)

Table 7-29. Atomic coordinates and equivalent isotropic displacement parameters ($Å^2$) for the orthorhombic distorted model #2.

Atom	x	y	z	Occupancy	Uiso ($Å^2$)
Ce	0.0	0.0	0.0	1.0	0.0399(4)
In(1)	0.0	0.0	0.3446(4)	1.0	0.0665(9)
In(2)	0.0	0.34183(32)	0.0	1.0	0.0301(5)
In(3)	0.5	0.0	-0.1998(5)	0.848(11)	0.050(1)
Cu(3)	0.5	0.0	-0.285(4)	0.152(11)	0.050(1)
In(4)	0.5	-0.1654(27)	0.0	0.125(10)	0.021(1)
Cu(4)	0.5	-0.2213(9)	0.0	0.875(10)	0.021(1)
Cu	0.25	0.25	0.25	1.0	0.0408(4)

Table 7-30. Atomic coordinates and equivalent isotropic displacement parameters ($Å^2$) for the tetragonal distorted model.

Atom	x	y	z	Occupancy	Uiso ($Å^2$)
Ce1	0.0	0.0	0.0	1.0	0.0374(4)
Cu1	0.25	0.25	0.25	1.0	0.0392(4)
In1	0.34272(10)	0.0	0.0	1.0	0.0463(3)
In2	0.0	-0.2230(5)	0.5	0.361(10)	0.0347(6)
Cu2	0.0	-0.1918(5)	0.5	0.639(10)	0.0347(6)

Magnetic Measurements:

Magnetic susceptibility measurements were carried out with a Quantum Design MPMS SQUID magnetometer at Michigan State University facilities as well as at Materials Science Division facilities at Argonne National Laboratory. Hand selected crystals were ground into powder, which was then sealed in Kapton tape or a gel cup and placed into the magnetometer. Temperature dependence data were collected between 2 and 400 K, with an applied field of 0.5 - 2 kG. Field dependent magnetic measurements were acquired at 2 or 3 K with field sweeping from - 55 to 55 kG.

X-ray Absorption Near Edge Spectroscopy (XANES):

X-ray absorption fine Structure (XAFS) experiments were performed in Sector 20, bending magnet beamline (PNC/XOR, 20-BM) of the Advanced Photon Source at the Argonne National Laboratory, IL, USA. Measurements at the Yb and Ce L_{III}-edges (and L_{II}-edges) for $YbTM_6In_6$ (TM = Cu, Ag) and $CeCu_6In_6$ were performed in the

transmission mode using gas ionization chambers to monitor the incident and transmitted X-ray intensities. A third ionization chamber was used in conjunction with a copper foil to provide internal calibration for the alignment of the edge positions. Monochromatic X-rays was obtained using a Si (111) double crystal monochromator. The monochromator was calibrated by defining the inflection point (first derivative maxima) of Cr foil as 5989 eV (or Zn foil as 9660.8 eV for $YbCu_6In_6$). A Rh-coated X-ray mirror was utilized to suppress higher order harmonics. Measurements were performed at a range of temperatures from 15 K to 300 K using a closed cycle refrigerator. XANES samples for the Yb compounds were prepared by mixing an appropriate amount of the finely ground Yb compound with hexagonal BN. The mixture was pressed to form a self-supporting pellet. The $CeCu_6In_6$ sample was prepared by dusting finely ground sample on Kapton tape and stacking around 4 layers together. All samples (in pellet and tape form) were mounted on the cold finger of a closed-cycle refrigerator. Sample preparation procedures were carried out inside a glove box environment. Data reduction and analysis were performed using the Athena software.[45] Care was taken to minimize thickness effects in the measurements.

7-3. Results and Discussion

Reaction Chemistry:

After the discovery of the $LaCu_7In_6$ compound[46] which crystallizes in the rhombohedral space group R-*3c*, we started employing other RE metals in the RE/Cu/In system under similar experimental conditions. The substitution of La by various RE atoms did not form $RECu_7In_6$ analogs but instead led to the formation of the $RECu_{6+x}In_{6-x}$

(RE = Ce, Nd, Sm, Gd, Dy, Ho, Er and Yb) family of compounds which crystallize as a variant of the $ThMn_{12}$ type structure in the orthorhombic space group *Immm*. Additionally, when Yb was employed as the RE atom and Cu was substituted for Ag the $YbAg_{5.18}In_{6.83}$ compound was formed which adopts the same structure type. Figure 7-2(A) - (C) shows scanning electron micrographs of typical $NdCu_{6.125}In_{5.875}$, $SmCu_6In_6$ and $YbAg_{5.18}In_{6.83}$ crystals, respectively.

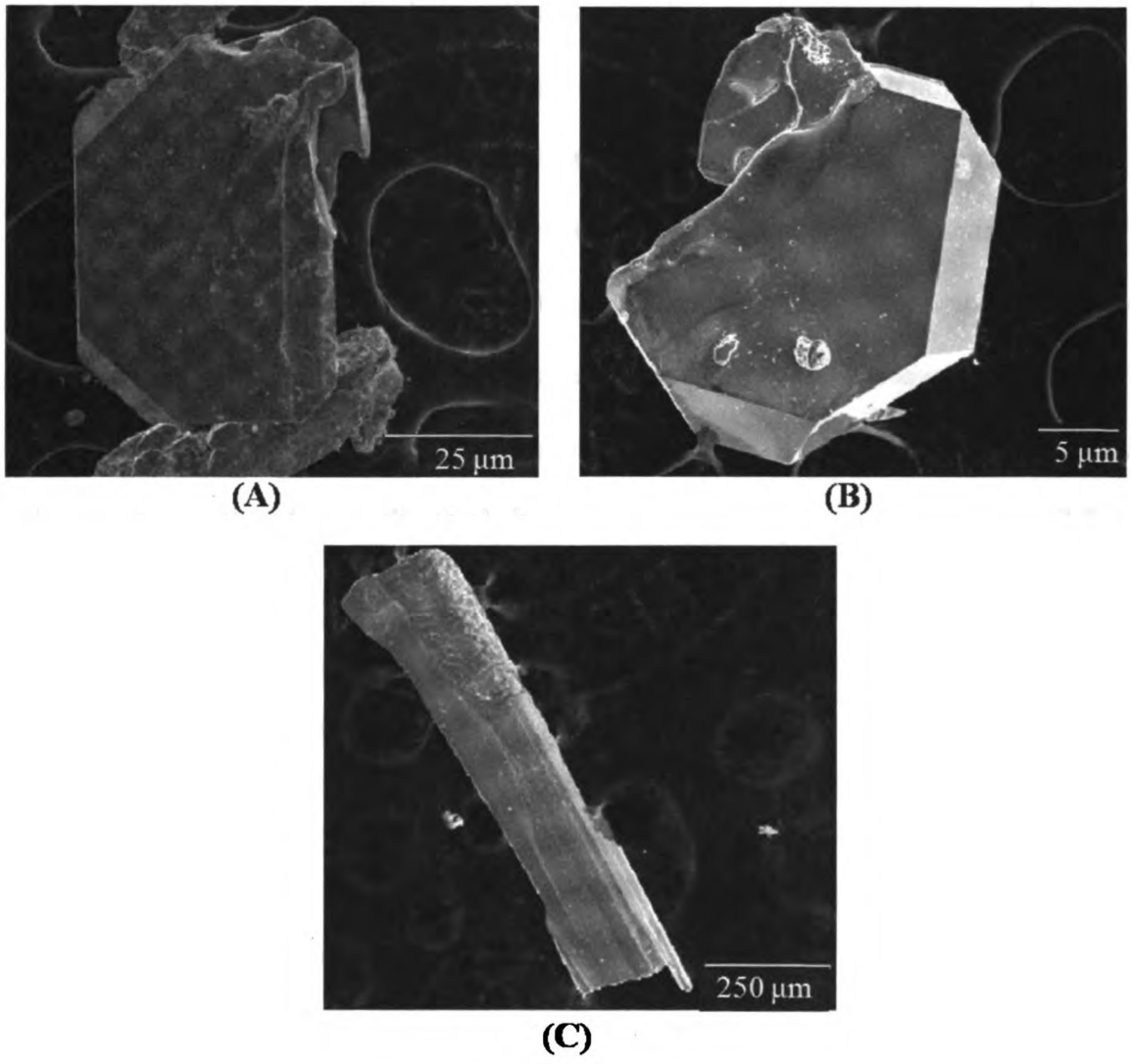

Figure 7-2. Scanning electron micrographs of some typical flux-grown crystals of (A) $NdCu_{6.125}In_{5.875}$ (B) $SmCu_6In_6$ and (C) $YbAg_{5.18}In_{6.83}$, respectively.

Structure:

The $RECu_{6+x}In_{6-x}$ (RE= Ce, Nd, Sm, Gd, Dy, Ho, Er and Yb) series and $YbAg_6In_6$ compounds crystallize as a disordered variant of the tetragonal $ThMn_{12}$ type structure[47] in the orthorhombic *Immm* space group. Because of the isostructural nature of these compounds the structure of $ErCu_{6.23}In_{5.77}$ analog will be only described. Figure 7-3, shows the overall structure of $ErCu_{6.23}In_{5.77}$ as viewed onto the *b,c*-plane. For clarity the Cu(a) and In(b) atoms occupying the two split sites In(a)-Cu(a) and In(b)-Cu(b) respectively have been omitted, as well as the bonds to the Er atoms. As it can be seen in Figure 7-3, the structure can be described as being composed of alternating Er-In (A) and Cu (B) slabs in a ABABA fashion and are stacked along the *b*-axis of the unit cell.

To describe the complexity of the atomic arrangement in this structure, it is useful to break it into the two distinct alternating slabs mentioned above. In the (B) type of layer, the Cu(b) and Cu atoms bond together to form corrugated Cu layers running along the *c*-axis, see Figure 7-4. Within adjacent layers the Cu(b) and Cu atoms are in alignment (i.e., they face each other). In the *ac*-plane of these layers, see Figure 7-5, Cu atoms form isosceles triangles, with two equal Cu(b)-Cu edges of 2.666 Å and one Cu-Cu edge of 2.705 Å. Adjacent triangles share corners forming distorted hexagonal polygons. The Cu net could also be described as corrugated Kagomé-net like structure, see Figure 7-5.

On the other hand, in the (A) type slabs, the In atoms form homoatomic cages with a hexagonal bipyramidal shape. These cages share the In(1) – In(1) edges (2.935 Å) building a chain that propagates along the *a*-axis, while neighboring chains are interconnected through elongated In(a) – In(a) bonds (3.393 Å) thus building a 2D In net,

Figure 7-6. The cages within adjacent layers are not aligned. The Er atoms are found in the void space between neighboring chains of In cages.

Another interesting feature, the coordination environment of the Er atoms is depicted in Figure 7-7. The Er atom resides at the center of a cage which is a twenty atom polyhedron with 6 tetragonal-rhombic and 24 trigonal faces. This is comprised of In atoms forming a distorted hexagonal polygon on the equatorial plane with two In(a)-In(a) bonds and four In(1)-In(a) (3.052 Å), and two additional In(2) atoms in the axial positions. Above and below the In polygon Cu atoms form puckered hexagonal polygons made of two Cu-Cu and four Cu(b)-Cu bonds. The Cu and In polygons are staggered with respect to each other. In Figure 7-8, the stacking of these polyhedral cages is highlighted. The polyhedrons around the Er atoms are sharing the Cu corners along the diagonals of the unit cell and two Cu(b)-In(a)-Cu(b)-In(a) tetragonal-rhombic faces along the *a*-axis, to build the three dimensional framework of the $ErCu_{6.23}In_{5.77}$ compound.

The variation of the unit cell volume with the rare earth is plotted in Figure 7-9. The decrease in volume as the RE radius gets smaller is regular, with the exception of Yb. This indicates that the Yb ions in $YbCu_{6.055}In_{5.945}$ may be divalent, or in a intermediate valence state which it would agree with the magnetic measurements and XANES results given in the following paragraphs.

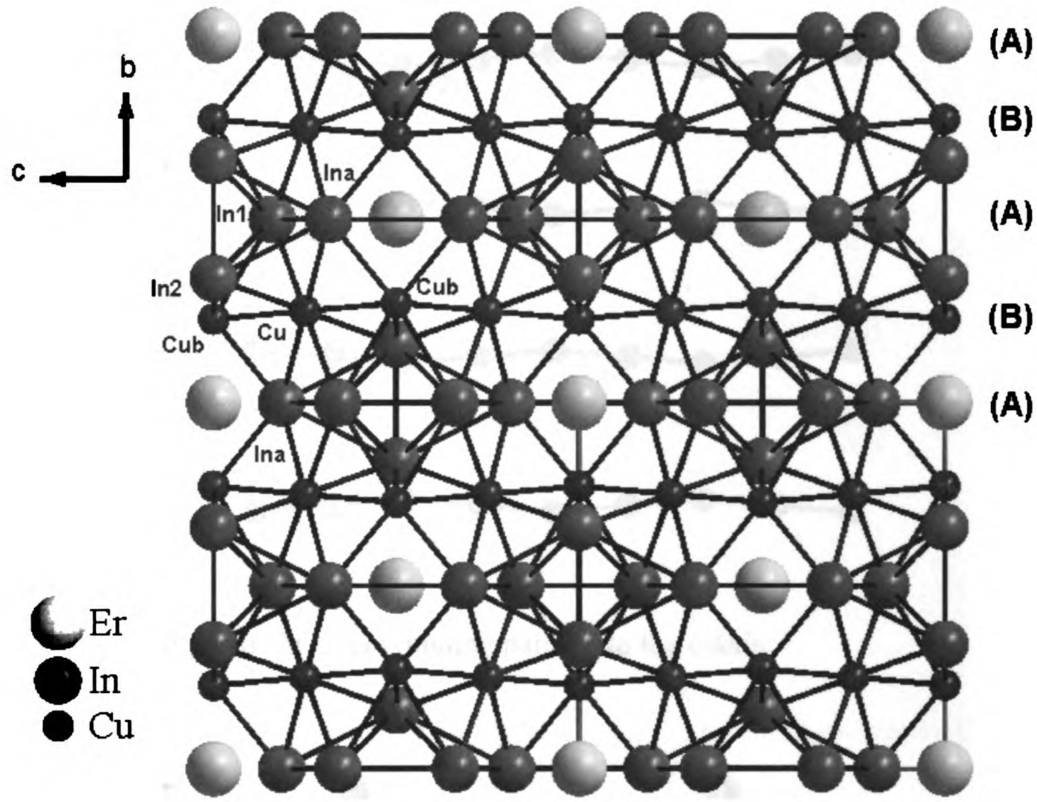

Figure 7-3. The overall structure of $ErCu_{6.23}In_{5.77}$ as viewed onto the *b,c*-plane. For clarity the bonds to the Er atoms are not drawn.

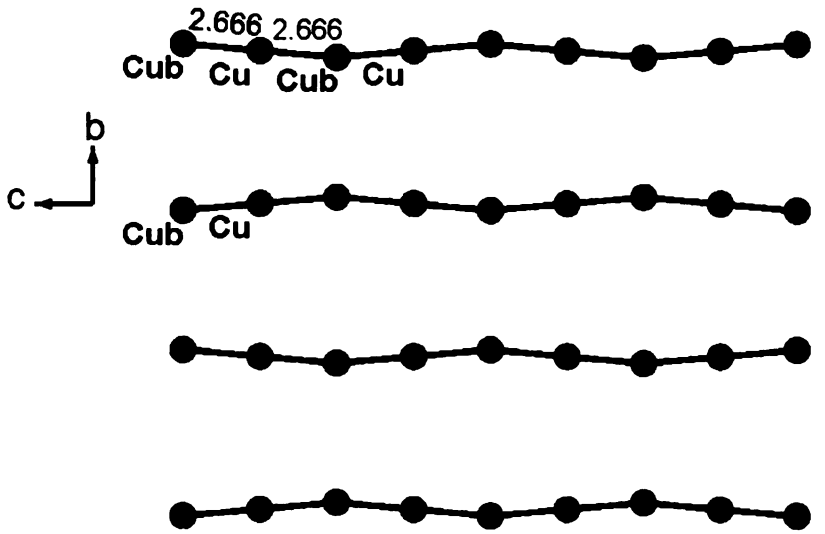

Figure 7-4. The corrugated Cu layers running parallel to the *c*-axis.

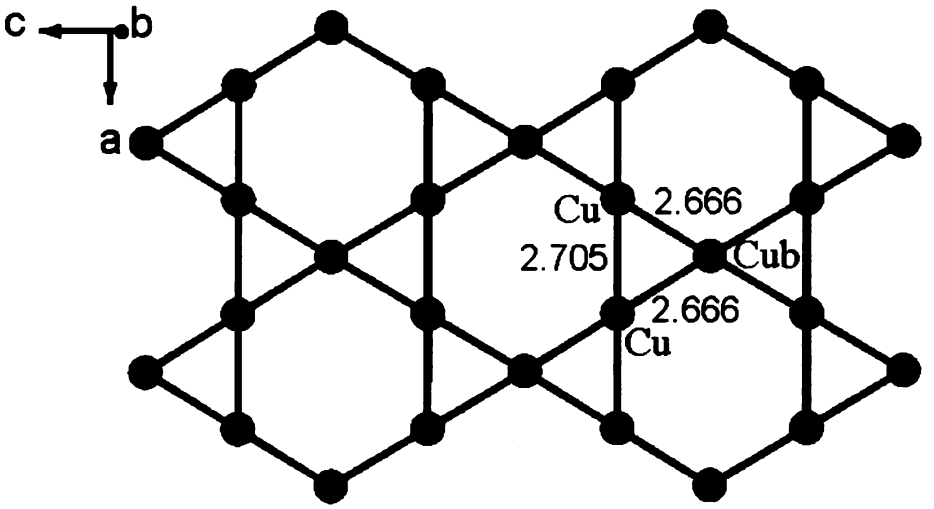

Figure 7-5. [010] projection of the Cu net along the *b*-axis.

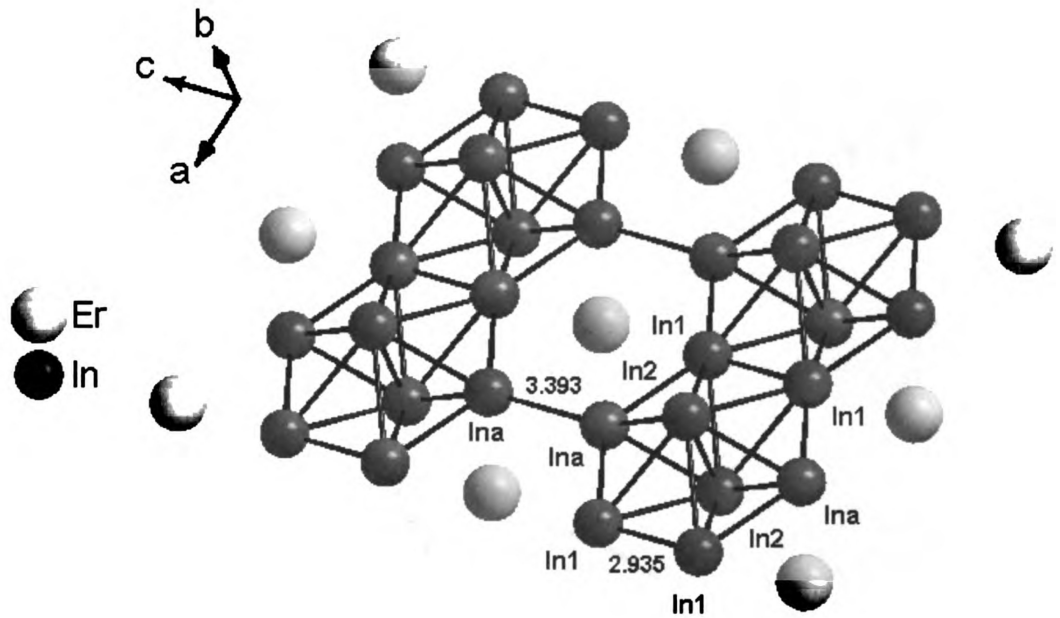

Figure 7-6. Projection of the layer of In cages and Er atoms in approximately the *a,c*-plane.

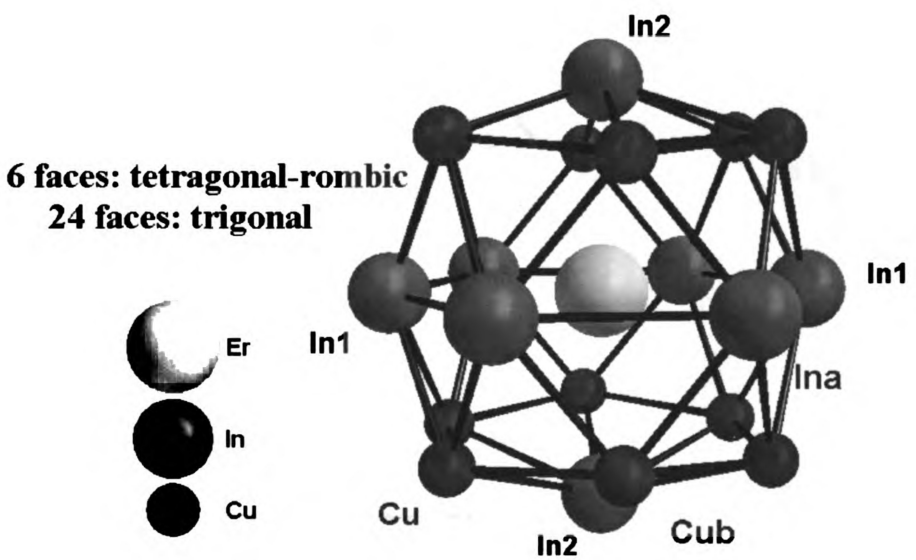

Figure 7-7. The In-Cu polyhedral cage hosting the Er atom.

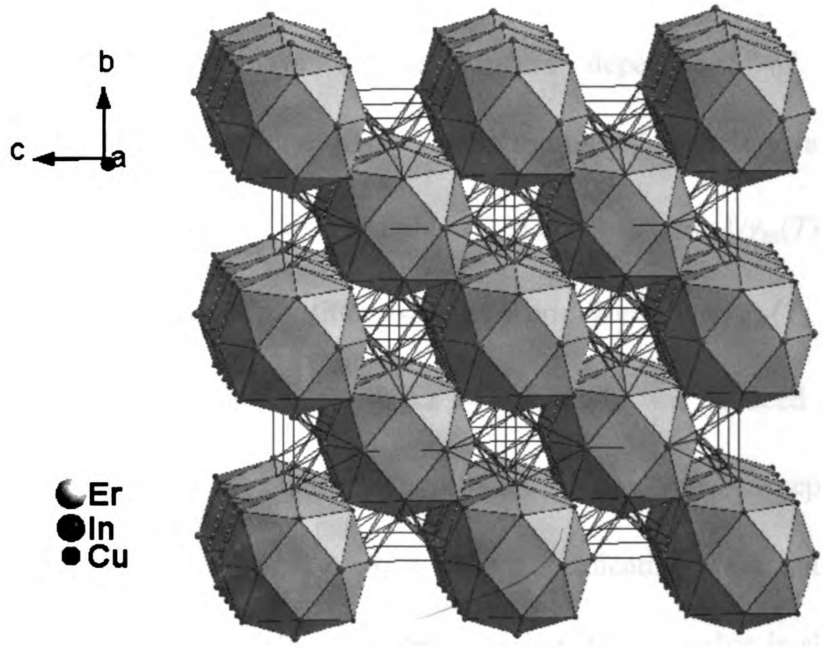

Figure 7-8. Polyhedra representation of the $ErCu_{6.23}In_{5.77}$ structure.

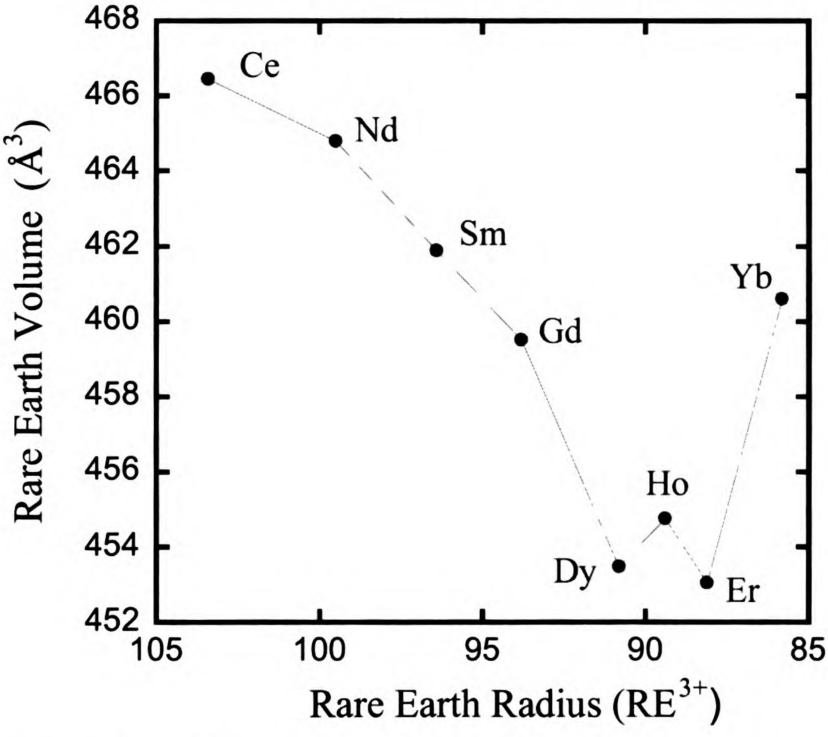

Figure 7-9. The variation of $RECu_{6+x}In_{6-x}$ unit cell volume across the rare-earth series.

Magnetic Measurements:

Figure 7-10(A) displays the temperature dependence of the magnetic susceptibility $\chi_m(T)$ and its inverse $1/\chi_m(T)$ of a sample of single crystals of $CeCu_6In_6$ between 2 K and 360 K with an applied field of 2 kG. The inverse $1/\chi_m(T)$ curve is linear to temperature and is successfully fitted with the Curie-Weiss law, $\chi_m(T) = C / (T - \theta_p)$. The effective magnetic moment of $\mu_{eff} = 2.2\ \mu_B$ / Ce atom, was deduced from the Curie constant C, ($C = \mu_{eff}^2 / 8$). The extrapolation of the linear inverse susceptibility to zero yielded a negative Weiss constant of θ_p = - 7.8 K, indicating weak antiferromagnetic interactions between the ions. The estimated experimental μ_{eff} value is slightly reduced with respect to the value expected for a free Ce^{3+} ion (2.54 μ_B) which could mean that the cerium ions in this compound may be in a mixed valence state Ce^{3+}/Ce^{4+}, or it could be due to strong crystalline field effects which tend to split the J=5/2 ground state multiplet of the Ce^{3+} ion. No magnetic ordering is observed down to 3 K. The magnetization of $CeCu_6In_6$ as function of the field is given in Figure 7-10(B). The magnetization curve responds linearly to the field up to ~ 44 kG while at higher fields the magnetization increases linearly again but with a shallower slope.

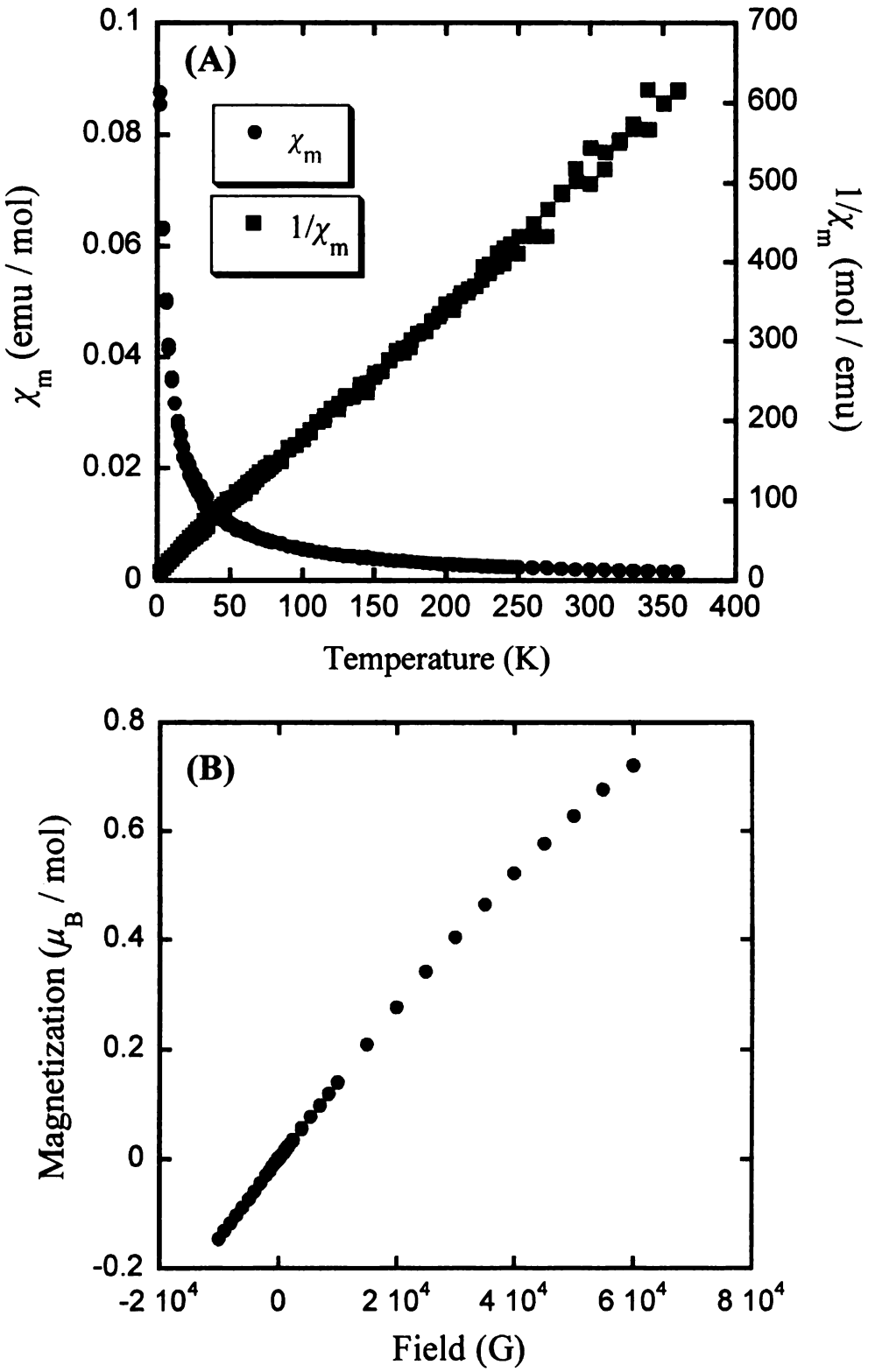

Figure 7-10. (A) Temperature dependent magnetic susceptibility $\chi_m(T)$ and its inverse $1/\chi_m(T)$ for $CeCu_6In_6$ measured with an applied field of 2 kG. (B) Field dependent magnetization measured at 3 K for $CeCu_6In_6$.

Figure 7-11(A) displays the temperature variation of the magnetic susceptibility $\chi_m(T)$ and its inverse $1/\chi_m(T)$ for $NdCu_{6.125}In_{5.875}$ between 3 K and 380 K with an applied field of 1 kG. As it can be seen, the $1/\chi_m(T)$ data do not display Curie-Weiss behavior within the measured temperature range. However, fitting of the $\chi_m(T)$ data to the modified Curie-Weiss law $\chi(T) = \chi_0 + C / (T - \theta_p)$ for the temperature range of 65 – 340 K, resulted in a temperature independent component of $\chi_0 = 7 \times 10^{-3}$ emu/mol of Nd atom, Curie - Weiss constant of $\theta_p = -31$ K suggesting antiferromagnetic interactions and an effective moment of 2.5 μ_B / Nd atom. The estimated experimental μ_{eff} value is again reduced with respect to that expected for a free Nd^{3+} ion (3.62 μ_B). Since, Nd ion is not known to exhibit mixed valence behavior the reduced μ_{eff} value could be due to strong crystalline field interactions. Additionally, Low Field magnetic measurements with a LF SQUID magnetometer (Materials Science Division at Argonne National Laboratory) at 10 G of applied field indicated an antiferromagnetic transition at ~ 6 K, (data are not provided). The field dependent magnetization curve measured at 3 K, increases in a linear fashion with the applied field up to 55 kG, Figure 7-11(B).

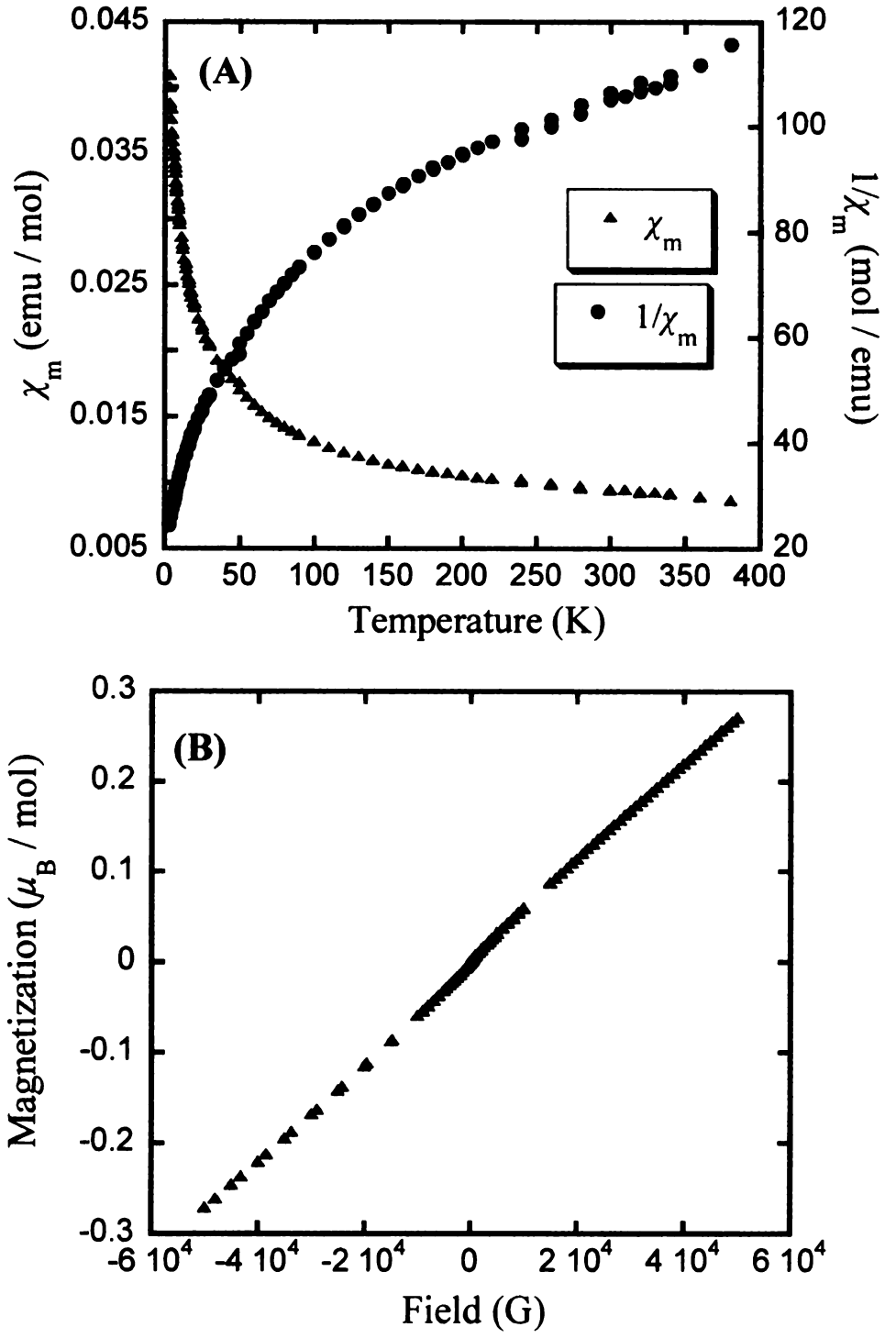

Figure 7-11. (A) Temperature dependent magnetic susceptibility $\chi_m(T)$ and inverse $1/\chi_m(T)$ data for $NdCu_{6.125}In_{5.875}$ measured with 1 kG of applied field. (B) Field dependent magnetization measured at 3 K for $NdCu_{6.125}In_{5.875}$.

The temperature variation of the magnetic susceptibility $\chi_m(T)$ for $SmCu_6In_6$ measured between 2 K and 380 K and with an applied field of 0.5 kG is given in Figure 7-12(A). The ZFC (zero field cooled) and FC (field cooled) data exhibit a significant hysteresis through the whole measured temperature range. This hysteresis suggests that there is likely a ferromagnetic component present in the $SmCu_6In_6$ compound. The inverse susceptibility data do not obey the Curie – Weiss law at any temperature range whereas at the temperatures of T_N equal to 9, 5.5 and 3 K both ZFC and FC curves exhibit antiferromagnetic like maxima. Figure 7-12(B) shows the field dependent magnetization data measured at 2 K which indicate the existence of a ferromagnetic component in $SmCu_6In_6$.The moments align rapidly with the applied field up to ~ 0.1 kG whereas at higher applied fields the magnetization continues to increase linearly but in a slower mode.

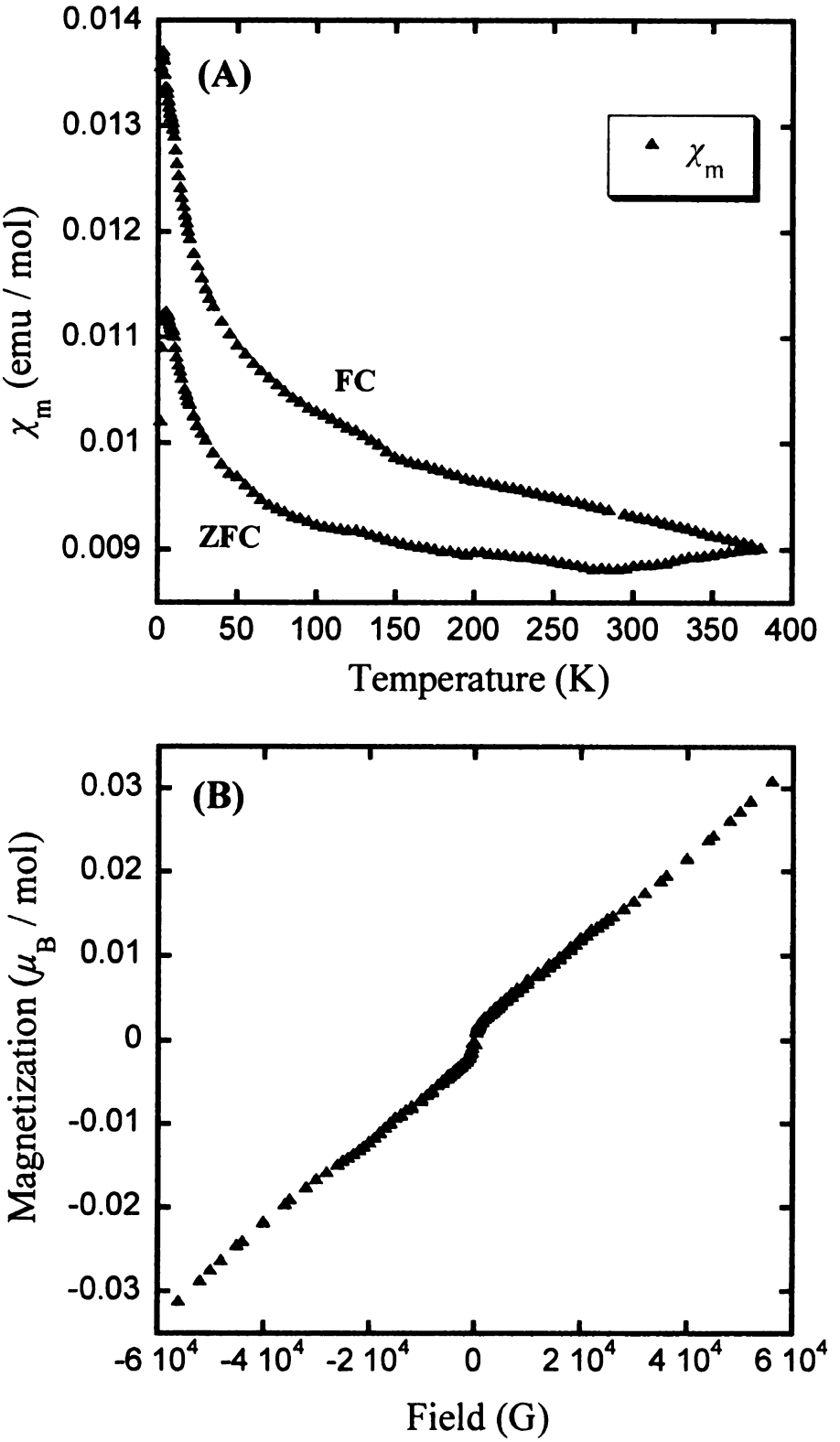

Figure 7-12. (A) Temperature dependent magnetic susceptibility $\chi_m(T)$ data for $SmCu_6In_6$ measured with an applied field of 0.5 kG. (B) Field dependent magnetization data measured at 2 K for $SmCu_6In_6$.

Temperature dependent magnetic susceptibility measurements for $GdCu_6In_6$ carried out at the temperature range of 2 – 380 K and with an applied field of 1 kG are given in Figure 7-13(A). $GdCu_6In_6$ exhibits similar behavior with $SmCu_6In_6$. The obvious hysteresis between ZFC and FC data reveal the presence of a ferromagnetic component in the compound, which remains ferromagnetic up to room temperature as it was confirmed with the attraction of the material in the vicinity of a magnet. At the temperature T_N of ~ 13 K a peak in both the ZFC and FC curves reveals an antiferromagnetic transition while below this temperature both curves rise to higher values of susceptibility, suggesting additional magnetic transitions could take place at a temperature lower than 2 K. Supplementary experimental techniques like low field, low temperature magnetic measurements or neutron diffraction experiments are required in order to further study the magnetic behavior of this compound. The inverse susceptibility data do not obey the Curie – Weiss law within the measured temperature range. The field dependent magnetization data measured at 2 and 300 K can be found in Figure 7-13(B). The magnetization curves at both temperatures exhibit strong field dependence at low fields and at ~ 0.8 kG the slope continuously changes until ~ 4 kG. At higher applied fields the magnetization increases linearly but with weaker field dependence. There is no sign of saturation up to the highest attainable field and the data at 300 K show considerably reduced moment compare to the 2 K magnetization data.

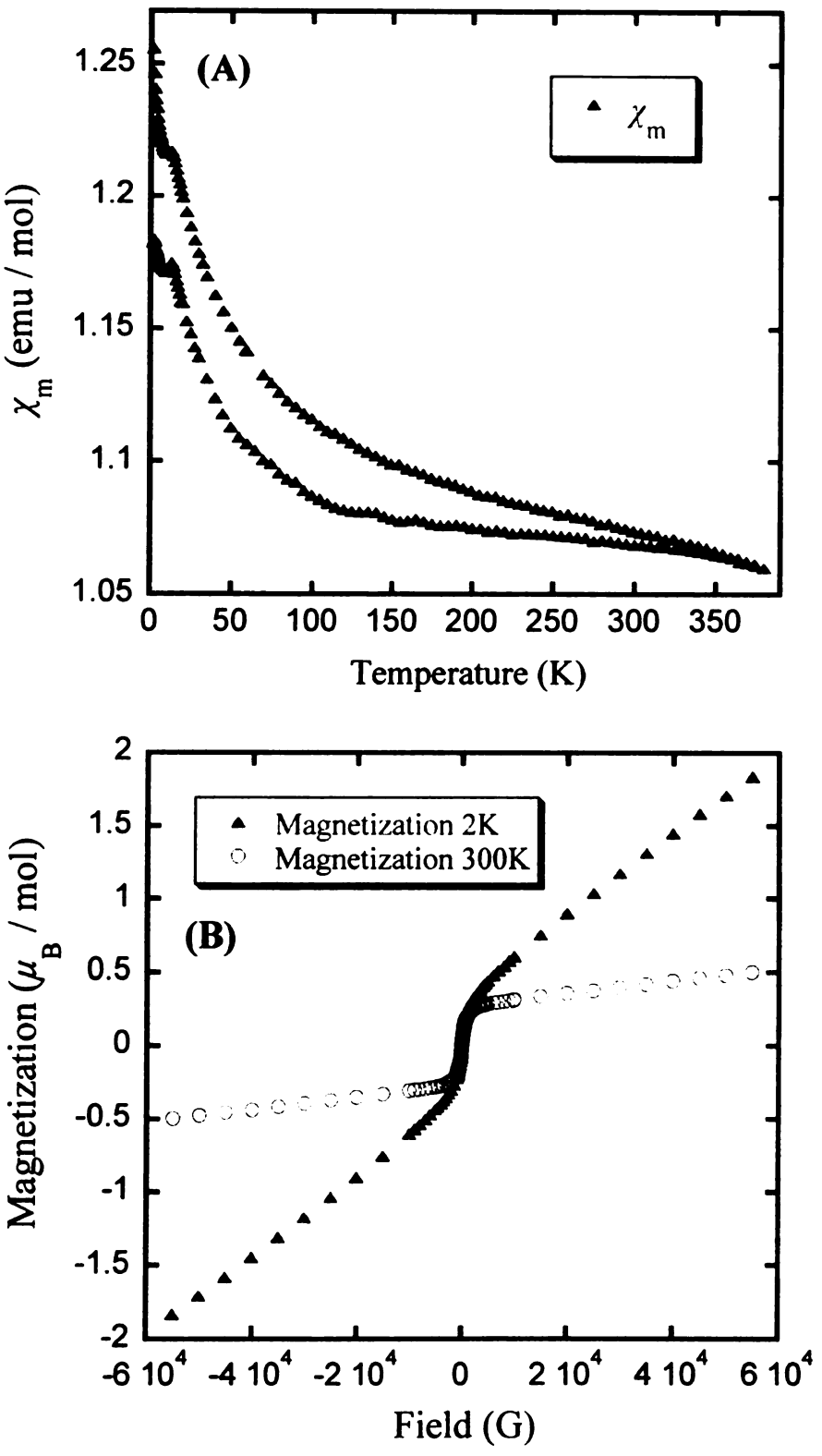

Figure 7-13. (A) Temperature dependent magnetic susceptibility $\chi_m(T)$ data for $GdCu_6In_6$ measured with an applied field of 1 kG. (B) Field dependent magnetization data measured at 2 K (solid triangles) and 300 K (open circles) for $GdCu_6In_6$.

Temperature dependent magnetic susceptibility measurements performed on $DyCu_{6.23}In_{5.77}$ are plotted in Figure 7-14(A). The maximum in the molar susceptibility $\chi_m(T)$ curve indicates antiferromagnetic ordering with a Néel temperature, T_N, of 8 K. Above 10 K, the inverse $1/\chi_m(T)$ curve is linear to temperature and is successfully fitted with the Curie-Weiss law, $\chi(T) = C / (T - \theta_p)$. The effective magnetic moment of μ_{eff} = 11.6 μ_B / Dy atom, was obtained from the Curie constant C, ($C = \mu_{eff}^2 / 8$). The observed magnetic moment is somewhat increased compared to the calculated moment for the free-ion value for Dy^{3+} (10.63 μ_B). The extrapolation of the linear inverse susceptibility to zero yielded a negative Weiss constant of θ_p = - 24.04 K, indicating antiferromagnetic interactions between the ions. Figure 7-14(B) shows the field dependence magnetization data of $DyCu_{6.23}In_{5.77}$, at 3 K. The magnetization shows a linear response to the applied field up to 12 kG, at which point there is a reorientation of the spins, as it is apparent from the kink point in the curve. Above this field the moment increases in a linear fashion again but with a stronger dependence on the applied field. This reorientation could be due to the transition from the paramagnetic into the antiferromagnetic state of the compound. The system gives no indication of saturation up to 50 kG.

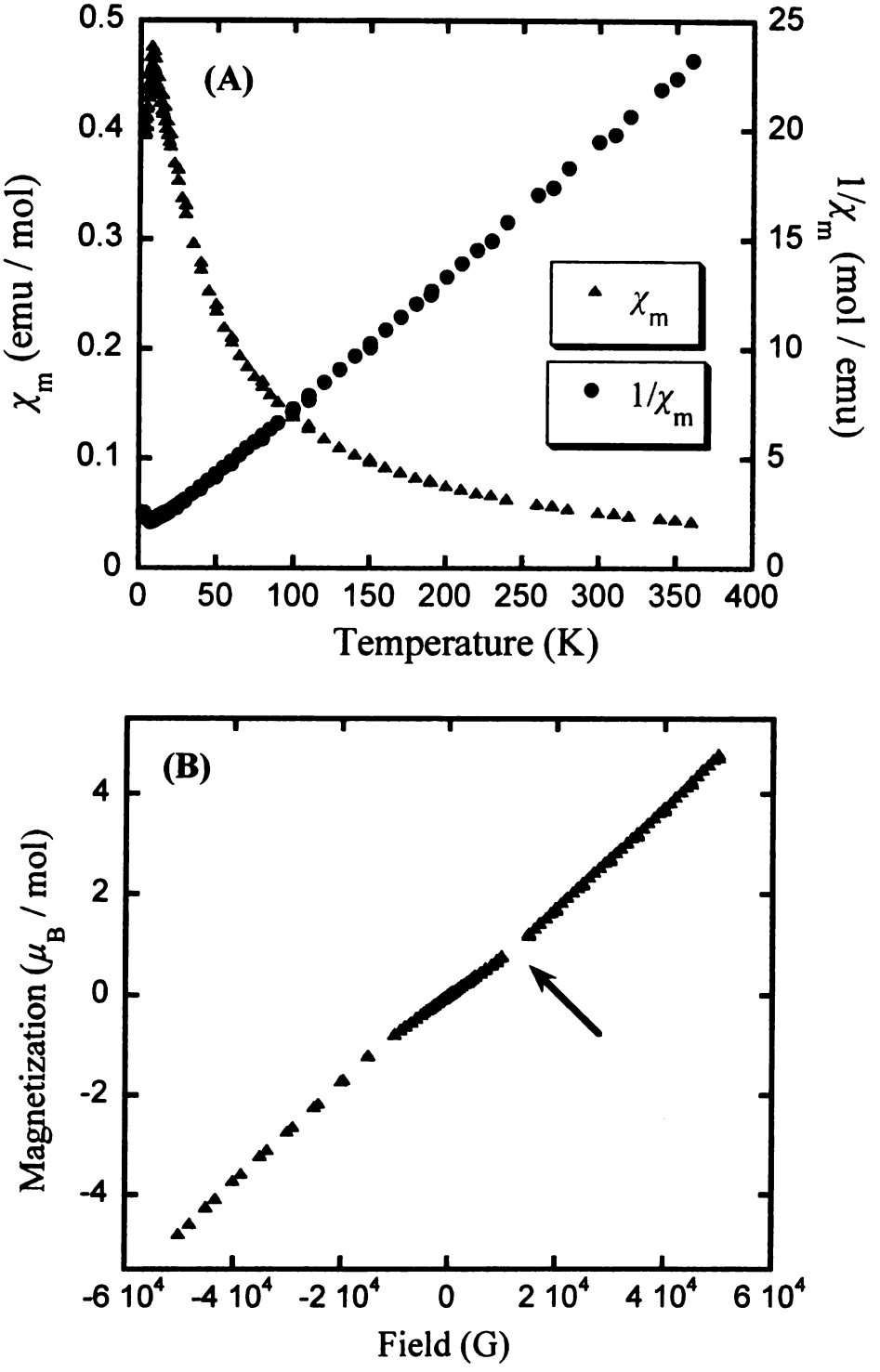

Figure 7-14. (A) Temperature dependent magnetic susceptibility $\chi_m(T)$ and its inverse $1/\chi_m(T)$ for $DyCu_{6.23}In_{5.77}$, measured at 1 kG field. (B) Field dependent magnetization at 3 K for $DyCu_{6.23}In_{5.77}$. The arrow indicates the reorientation of the spins.

The temperature variation of the magnetic susceptibility $\chi_m(T)$ and its inverse $1/\chi_m(T)$ for $HoCu_{6.11}In_{5.89}$ at the temperature range of 2 – 380 K and with an applied field of 1 kG are given in Figure 7-15(A). The $1/\chi_m(T)$ data do not display Curie-Weiss behavior within the measured temperature range whereas the small hysteresis between the ZFC and FC data suggests, as seen above for other members of the $RECu_{6+x}In_{6-x}$ family of compounds, the presence of a ferromagnetic component in the compound. Additionally, attempts to fit the $\chi_m(T)$ data with the modified Curie - Weiss law did not result in a reliable μ_{eff} value. Figure 7-15(B) shows the field dependent magnetization data at 2 and 300 K. The magnetization curve at 2 K exhibits a linear response to the field up to ~ 6 kG while at higher fields the slope continuously changes with no sign of saturation up to the highest attainable field. The data collected at 300 K reveal strong field dependence up to ~ 0.4 kG whereas at higher applied fields the magnetization increases linearly but with weaker field dependence which corroborates the existence of a small fraction of a ferromagnetic component in the compound. The moment is significantly reduced at room temperature compared to the moment observed at low temperature.

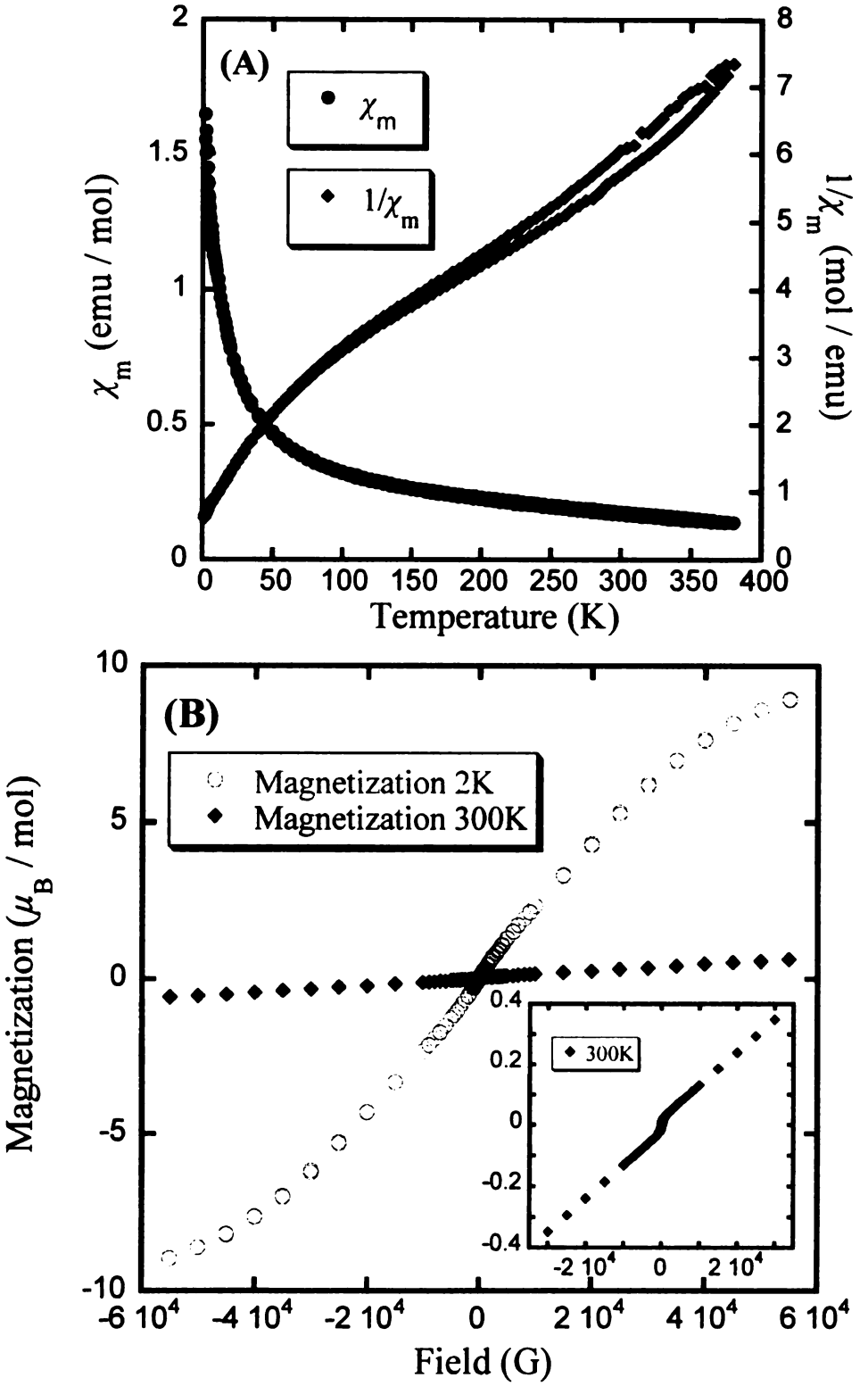

Figure 7-15. (A) Temperature dependent magnetic susceptibility $\chi_m(T)$ and inverse $1/\chi_m(T)$ data for $HoCu_{6.11}In_{5.89}$ measured with 1 kG of applied field. (B) Field dependent magnetization data measured at 2 K (open circles) and 300 K (solid rhombi) for $HoCu_{6.11}In_{5.89}$. Inset: shows data at 300 K up to 35 kG of field.

Temperature dependent magnetic susceptibility data for $ErCu_{6.23}In_{5.77}$ at 1 kG of applied field are given in Figure 7-16(A). The $\chi_m(T)$ data reveal an antiferromagnetic transition at T_N of ~ 3.5 K, as shown in the inset of Figure 7-16(A). Above this temperature the inverse molar magnetic susceptibility curve $1/\chi_m(T)$ follows the Curie-Weiss law with a calculated effective magnetic moment $\mu_{eff} = 9.51\ \mu_B$, which appears to be slightly higher than the theoretical value of 9.59 μ_B for Er^{3+}. The magnetization curves at 2 and 10 K for $ErCu_{6.23}In_{5.77}$ can be found in Figure 7-16(B). The magnetization measured at 2 K which is below the transition temperature T_N reveals a metamagnetic behavior. There is a linear response to the field up to ~ 3 kG at which point there is a reorientation of the spins and the moment increases linearly again but with stronger field dependence. At ~ 25 kG the slope changes again and the moment starts saturating. At 55 kG of applied field the magnetization reaches ~ 90 % of the expected value for a free Er^{3+} atom. In the data collected at 10 K, well above the transition temperature, the magnetization increases linearly up to an applied field of ~ 25 kG, at which point the slope continuously changes until approximately 35 kG when it becomes linear again, though with a much shallower slope, up to 55 kG.

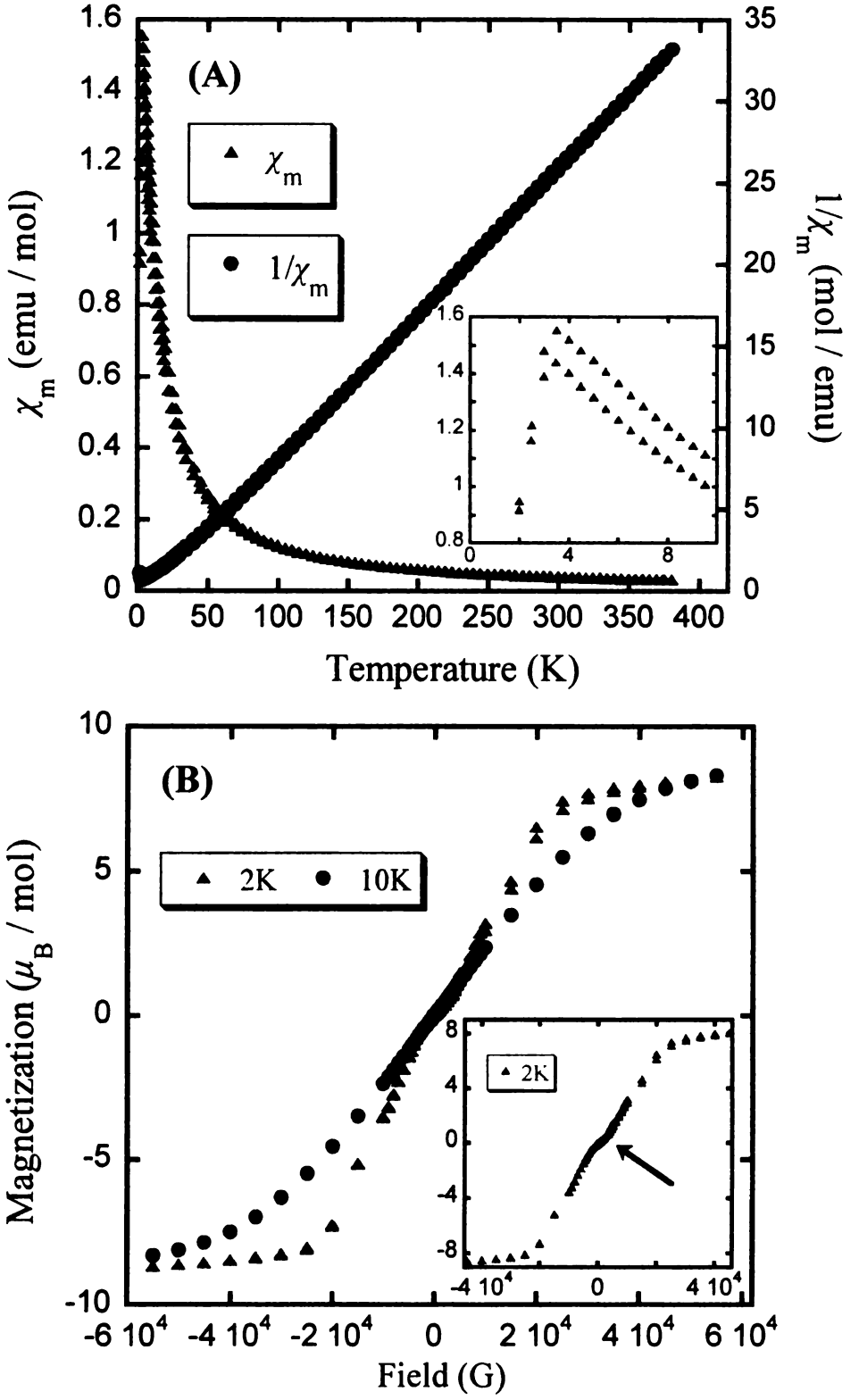

Figure 7-16. (A) Temperature dependent magnetic susceptibility $\chi_m(T)$ and its inverse $1/\chi_m(T)$ for $ErCu_{6.23}In_{5.77}$. Inset: shows the antiferromagnetic peak at 3.5 K. (B) Field dependent magnetization at 2 and 10 K for $ErCu_{6.23}In_{5.77}$.

The temperature variation of the magnetic susceptibility $\chi_m(T)$ for $YbCu_6In_6$ measured between 2 K and 380 K and with applied fields of 0.6 and 3 kG is given in Figure 7-17(A). The $\chi_m(T)$ data at 3 kG could be fitted to the modified Curie-Weiss law $\chi(T) = \chi_0 + C / (T - \theta_p)$. A nonlinear least-squares fit to this equation resulted in $\chi_0 = 8 \times 10^{-4}$ emu/mol of Yb atom, Curie - Weiss constant of θ_p = -0.9 K suggesting weak antiferromagnetic interactions and an effective moment μ_{eff} of 0.4 μ_B / Yb atom ($C = \mu_{eff}^2 / 8$). The estimated experimental μ_{eff} value is very small compared to that expected for a free Yb^{3+} ion (4.54 μ_B) suggesting that the Yb atoms in the compound are predominantly as Yb^{2+} and only a small fraction present in the trivalent state. Additionally, the hysteresis between the ZFC and FC data indicate, as seen above for other analogs, that probably there is a small ferromagnetic component in the compound. The magnetization of $YbCu_6In_6$ as function of the field at 2 K is given in Figure 7-17(B). The magnetization curve shows a strong field dependent response up to ~ 12 kG at which point the slope changes continuously until about 44 kG while at higher fields the magnetization shows the first signs of saturation. At the highest attainable field of 56 kG the magnetization reached a value of only 0.017 μ_B / Yb atom which is also suggestive of the existence of a small amount of Yb^{3+} moments in $YbCu_6In_6$.

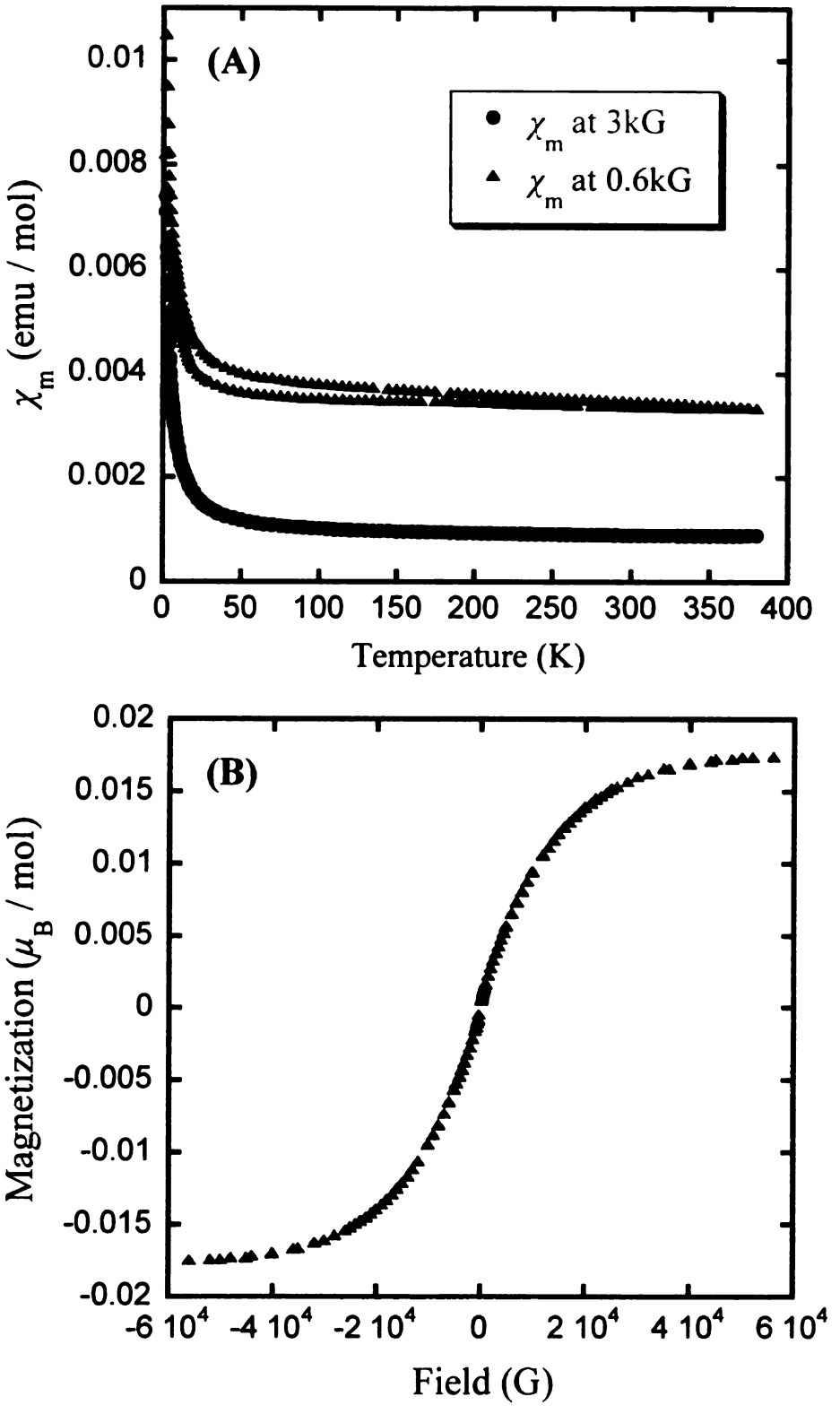

Figure 7-17. (A) Temperature dependent magnetic susceptibility $\chi_m(T)$ data for $YbCu_6In_6$ measured with applied fields of 0.6 kG (triangles) and 3 kG (circles). (B) Field dependent magnetization data measured at 2 K for $YbCu_6In_6$.

The temperature dependence of the magnetic susceptibility $\chi_m(T)$ and its inverse $1/\chi_m(T)$ for a sample of randomly oriented single crystals of $YbAg_{5.18}In_{6.83}$ measured between 2 K and 400 K and with an applied field of 2 kG is given in Figure 7-24. The $1/\chi_m(T)$ data do not obey the Curie – Weiss law. However, the $\chi_m(T)$ data could be fitted to the modified Curie-Weiss law $\chi(T) = \chi_0 + C / (T - \theta_p)$ and a nonlinear least-squares fit to this equation resulted in $\chi_0 = 16 \times 10^{-3}$ emu/mol of Yb atom, Curie - Weiss constant of $\theta_p = -3.7$ K suggesting antiferromagnetic interactions and an effective moment μ_{eff} of 1.5 μ_B / Yb atom ($C = \mu_{eff}^2 / 8$). The estimated experimental μ_{eff} value is reduced compared to that expected for a free Yb^{3+} ion (4.54 μ_B) suggesting that the Yb atoms in the compound are predominantly as Yb^{2+} and a small fraction present in the trivalent state. Additionally, the hysteresis between the ZFC and FC data indicate, as seen above for other analogs, that probably there is a small ferromagnetic component in the compound. The magnetization of $YbAg_{5.18}In_{6.83}$ as a function of the field at 2 K is given in Figure 7-25. The magnetization curve exhibits strong linear field dependence up to ~ 5 kG whereas at higher applied fields the slope continuously changes until ~ 40 kG where it becomes linear again. The field of 55 kG does not seem strong enough to saturate the spins.

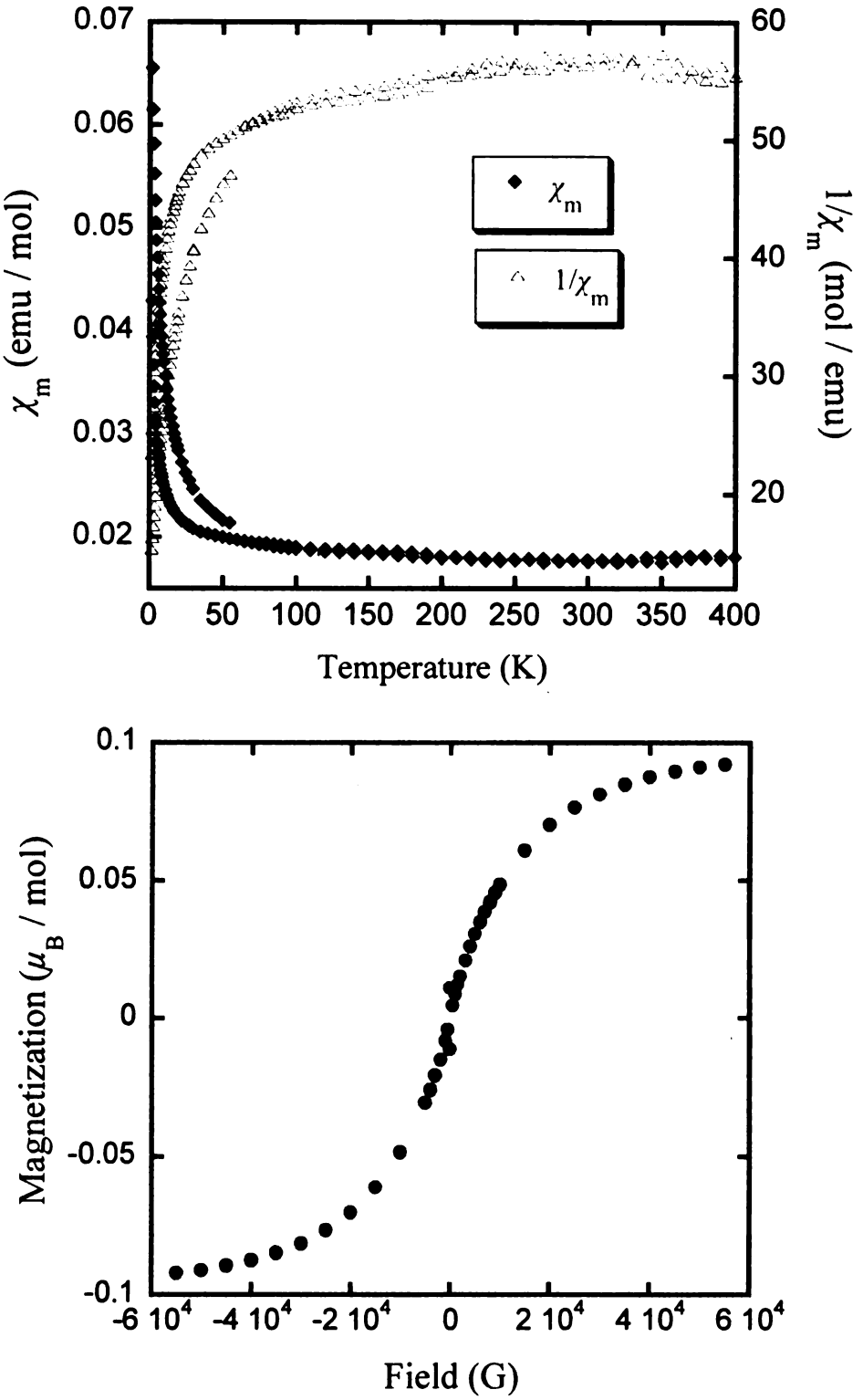

Figure 7-18. (A) Temperature dependent magnetic susceptibility $\chi_m(T)$ and inverse $1/\chi_m(T)$ data for $YbAg_{5.18}In_{6.83}$ measured with an applied field of 2 kG. (B) Field dependent magnetization data measured at 2 K for $YbAg_{5.18}In_{6.83}$.

XANES Measurements:

To further probe the Ce valence state in $CeCu_6In_6$ we performed X-ray absorption near-edge spectroscopy (XANES) measurements at the Ce L_{III}-edge. The XANES on Ce L_{III}-edge represents the excitation of an electron from the $2p_{3/2}$ core level into the conduction band so that it probes directly the electronic structure of the unoccupied valence band.[48] The energy variation of the normalized X-ray absorption at the Ce L_{III} threshold obtained at temperatures of 16 and 300 K and at ambient pressure is depicted in Figure 7-19. The spectrum of the tetravalent Ce in CeO_2 measured at 16 K is also presented for comparison. The measured near-edge spectra did not present any considerable difference between the two temperatures, suggesting that the Ce valence remained stable in the measured temperature range. Nevertheless, in the presence of both $4f^1$ and $4f^0$ final states, the L_{III}-edge is comprised by two main structures (double peak) approximately separated by 10 eV.[49, 50] As it can be seen in Figure 7-X, both spectra show a single dominant absorption peak (white line resonance), centered at ~ 5726 eV. A singly peaked edge structure in this energy region is attributed to trivalent Ce atoms,[51-54] (due to a $2p_{3/2} \rightarrow (4f^1)5d$ electron transition). On the other hand, the tetravalent Ce in CeO_2 gives a double peaked spectrum. Other intermetallic compounds where Ce (IV) is present also exhibit double peak structure.[51-54] The presence of single peaked spectrum reveals that Ce is present exclusively in the trivalent state in $CeCu_6In_6$. Thus, the XANES experiments do not provide any evidence for the existence of valence fluctuations for the Ce atoms. Examples of Ce-based intermetallic compounds exhibiting similar XANES spectra include the ternary compounds $CePt_4Ni$,[51] CePtSn,[52] $CeRu_2Si_2$,[48] CeAuIn and $CeAu_2In$[53] to name just a few.

X-ray absorption near-edge spectroscopy (XANES) measurements at the Yb L_{III}- and L_{II}-edges for the $YbCu_6In_6$ compound were carried out at 16 K and 295 K. Due to overlap of the Cu edge from the sample with the Yb L_{III}-edge only the L_{II}-edge L_{III}-edge (excitation of an electron from the $2p_{1/2}$ core level into the conduction band) spectra are shown in Figure 7-20. The resulted L_{II}-edge spectra did not present any considerable difference between the two temperatures, suggesting that the Yb valence remained stable in the measured temperature range. The main absorption peak (white line) for both spectra is centered at ~ 9676 eV, which can be assigned to divalent Yb. Relative to Yb^{2+}, trivalent Yb exhibits a white line which is ~ 8 eV higher in energy. The spectra also reveal the presence of a weaker feature (shoulder) at ~ 9684 eV, indicating that some trivalent Yb is also present. This values compare relatively well with the literature.[55]

Finally, X-ray absorption near-edge spectroscopy (XANES) measurements at the Yb L_{III}-edge were performed for the $YbAg_6In_6$ compound at 18 K and 295 K. As it can be seen in Figure 7-21, the near-edge spectra for both temperatures showed no significant difference between the two temperatures, suggesting that the Yb valence remained stable in the measured temperature range. The main absorption peak (white line resonance) of the spectra for both temperatures is centered at ~8941.5 eV, which is attributed to divalent Yb atoms while the presence of a weaker feature (shoulder) at ~8949.5 eV, indicates that some trivalent Yb is also present.[56-58]

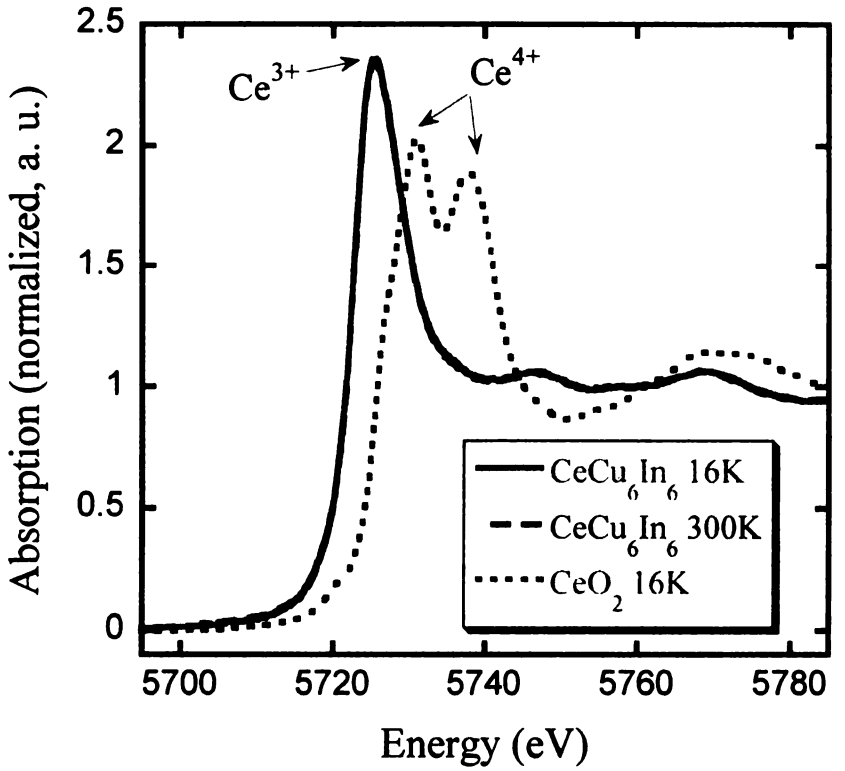

Figure 7-19. L_{III}-edge absorption spectra of Ce in $CeCu_6In_6$ at 16 K (solid line) and 300 K (dashed line). The spectrum of CeO_2 at 16 K (dotted line) is also given for comparison.

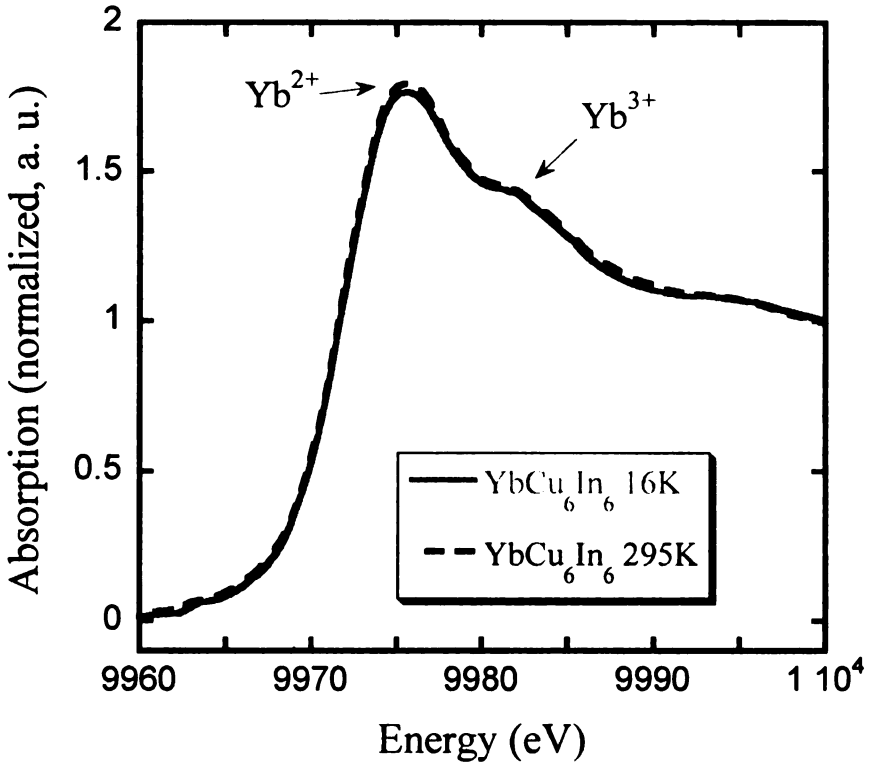

Figure 7-20. L_{II}-edge absorption spectra of Yb in $YbCu_6In_6$ at 16 K (solid line) and 295 K (dashed line). The spectrum of CeO_2 at 16 K (dotted line) is also given for comparison.

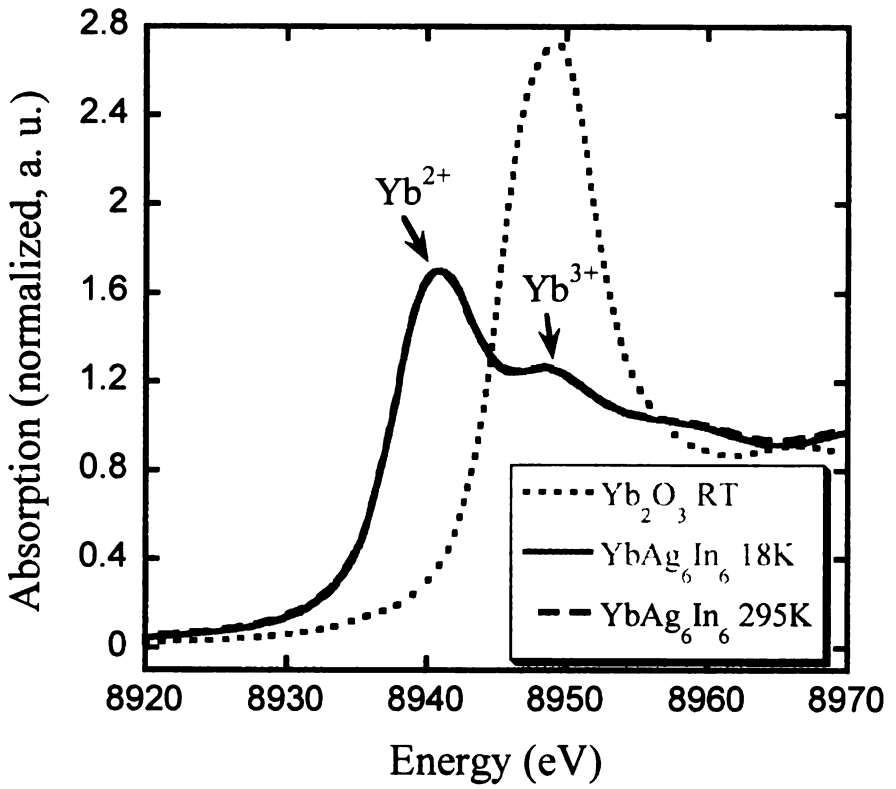

Figure 7-21. L_{III}-edge absorption spectra of Yb in $YbAg_6In_6$ at 18 K (solid line) and 295 K (dashed line).

7-4. Conclusions

Single crystals of the ternary $RECu_{6+x}In_{6-x}$ (RE= Ce, Nd, Sm, Gd, Dy, Ho, Er, Yb) and $YbAg_{5.18}In_{6.83}$ compounds were synthesized from reactions in liquid In. Similar RE/Cu/In compounds with small stoichiometric variations have been synthesized in the past by arc melting and powder X-ray and later single crystal X-ray diffraction studies proposed tetragonal (*I*4/*mmm*) structural models with two mixed occupied Cu+In sites or a split Cu/In site with 50/50 probability. Our single crystal X-ray diffraction as well as high resolution powder X-ray diffraction studies for the In flux grown single crystals of

the $RECu_{6+x}In_{6-x}$ series and $YbAg_{5.18}In_{6.83}$ indicated a distorted orthorhombic model (*Immm*) as the best one to describe the structure of these compounds. We propose an orthorhombic model with two Cu/In split sites statistically occupied.

Study of the magnetic properties of the title compounds revealed various interesting magnetic behavior for the $RECu_{6+x}In_{6-x}$ series. The Ce, Dy and Er corresponding compounds exhibited Curie-Weiss behavior above ~ 10K while the Dy and Er ones showed antiferromagnetic peaks at ~ 8 and 3.5 K, respectively. For the Sm, Gd and Ho analogs a hysteresis between the ZFC and FC magnetic susceptibility data as well as the magnetization data suggested the existence of a ferromagnetic component in the compound. The Sm compound exhibited also antiferromagnetic like maxima at 9, 5.5 and 3 K, additional experimental techniques such as neutron diffraction experiments are also needed to clarify the possible multiple magnetic phases. The Gd compound showed antiferromagnetic ordering at ~ 13 K. Finally the Nd and Yb magnetic susceptibility data could be fitted with the modified Curie-Weiss law from which for the Yb analog we found a small value of μ_{eff} suggesting that the Yb atoms exhibit mixed or intermediate valence behavior. Similar behavior was also observed for the $YbAg_{5.18}In_{6.83}$ compound.

Finally, XANES experiments for the $CeCu_6In_6$ compound revealed that the Ce atoms are in the trivalent state for both the low and high measured temperatures. The XANES studies for $YbCu_6In_6$ and $YbAg_{5.18}In_{6.83}$ confirmed the magnetic measurements in that the in these compounds the Yb atoms are in the mixed or intermediate valence state with a high Yb^{2+}/Yb^{3+} ratio that stayed stable in the measured temperature range.

References:

1. Villars, P.; Calvert, L. D., *"Pearson's Handbook of Crystallographic Data for Intermetallic Phases", 2nd ed.; American Society for Metals*. OH 44073, 1991.

2. Kalychak, Y. M., *J. Alloys Compd.* 1997, 341, 262.

3. Szytula, A.; Leciejewicz, J., *"Handbook of Crystal Structures and Magnetic Properties of Rare Earth Intermetallics"*. CRC Press: Boca Raton, Fl, 1994.

4. Visser, A. d.; Bakker, K.; Pierre, J., *Physica B* 1993, 186-188, 577.

5. Besnus, M. J.; Haen, P.; Hamdaoui, N.; Harr, A.; Meyer, A., 1990, 163, 571.

6. Bauer, E.; Hauser, R.; Gratz, E.; Payer, K.; Oomi, G.; Kagayama, T., *Phys. Rev. B* 1993, 48, 873.

7. Sarrao, J. L.; Immer, C. D.; Fisk, Z.; Booth, C. H.; Figueroa, E.; Lawrence, J. M.; Modler, R.; Cornelius, A. L.; Hundley, M. F.; Kwei, G. H.; Thompson, J. D., *Phys. Rev. B* 1999, 59, 6855.

8. Steglich, F.; Aarts, J.; Bredl, C. D.; Lieke, W.; Meschede, D.; Franz, W.; Schafer, H., *Phys. Rev. Lett.* 1972, 43, 1892.

9. Jaccard, D.; Link, P.; Vargoz, E.; Alami-Yadri, K., *Physica B* 1997, 230-232, 297.

10. Tran, V. H., *Phys. Rev. B* 2004, 70, 094424.

11. Tran, V. H.; Gamza, M.; Slebarski, A.; Miiller, W.; Jarmuska, J., *J. Alloys Comp.* 2008, 451, 457-460.

12. Tran, V. H.; Jarmulska, J.; Miiller, W., *Mater. Sci. Poland*, in press.

13. Kindler, B.; Finsterbusch, D.; Graf, R.; Ritter, F.; Assmus, W.; Lüthi, B., *Phys. Rev. B* 1994, 50, 704.

14. Felner, I.; Nowik, I., *Phys. Rev. B* 1986, 33, 617.

15. Felner, I.; Nowik, I.; Vaknin, D.; Potzel, U.; Moser, J.; Kalvius, G. M.; Wortmann, G.; Schmiester, G.; Hilscher, G.; Gratz, E.; Schmitzer, C.; Pillmayr, N.; Prasad, K. G.; Waard, H. d.; Pinto, H., *Phys. Rev. B* 1987, 35, 6956.

16. Nowik, I.; Felner, I.; Voiron, J.; Beille, J.; Najib, A.; Lachiesserie, E. d. T. d.; Gratz, E., *Phys. Rev. B* 1988, 37, 5633.

17. Sarrao, J. L., *Physica B* 1999, 259-261, 128.

18. Junhui, H. E.; Tsujii, N.; Yoshimura, K.; Kosuge, K.; Goto, T., *J. Phys. Soc. Jpn* 1997, 66, 2481.

19. Mushnikov, N. V.; Goto, T.; Rozenfeld, E. V.; Yoshimura, K.; Zhang, W.; Yamada, M.; Kageyama, H., *J. Phys.: Condens. Matter* 2003, 15, 2811.

20. Golubkov, A. V.; Parfen'eva, L. S.; Smirnov, I. A.; Misiorek, H.; Mucha, J., *Physics of the Solid State* 2007, 49, 2038-2041.

21. Kanatzidis, M. G.; Pottgen, R.; Jeitschko, W., *Angew. Chem.-Int. Edition* 2005, 44, (43), 6996-7023.

22. Sieve, B.; Chen, X. Z.; Henning, R.; Brazis, P.; Kannewurf, C. R.; Cowen, J. A.; Schultz, A. J.; Kanatzidis, M. G., *J. Am. Chem. Soc* 2001, 123, (29), 7040.

23. Sieve, B.; Trikalitis, P. N.; Kanatzidis, M. G., *Z. Anorg. Allg. Chem.* 2002, 628, 1568-1574.

24. Zhuravleva, M. A.; Kanatzidis, M. G., *Z. Naturforch B : Sec. B* 2003, 58, (7), 649.

25. Zhuravleva, M. A.; Pcionek, R. J.; Wang, X. P.; Schultz, A. J.; Kanatzidis, M. G., *Inorg. Chem.* 2003, 42, (20), 6412.

26. Zhuravleva, M. A.; Evain, M.; Petricek, V.; Kanatzidis, M. G., *J. Am. Chem. Soc* 2007, 129, (11), 3082.

27. Wu, X. N.; Kanatzidis, M. G., *J. Solid State Chem.* 2005, 178, (11), 3233.

28. Wu, X. U.; Latturner, S. E.; Kanatzidis, M. G., *Inorg. Chem.* 2006, 45, (15), 5358.

29. Latturner, S. E.; Bilc, D.; Mahanti, S. D.; Kanatzidis, M. G., *Inorg. Chem.* 2003, 42, 7959.

30. Latturner, S. E.; Kanatzidis, M. G., *Inorg. Chem.* 2008, 47, 2089.

31. Salvador, J. R.; Bilc, D.; Gour, J. R.; Mahanti, S. D.; Kanatzidis, M. G., *Inorg. Chem.* 2005, 44, (24), 8670

32. Salvador, J. R.; Gour, J. R.; Bilc, D.; Mahanti, S. D.; Kanatzidis, M. G., *Inorg. Chem.* 2004, 43, (4), 1403.

33. Salvador, J. R.; Kanatzidis, M. G., *Inorg. Chem.* 2006, 45, (18), 7091-7099.

34. Chondroudi, M.; Balasubramanian, M.; Welp, U.; Kwok, W.-K.; Kanatzidis, M. G., *Chem. Mater.* 2007, 19, 4769.

35. Salvador, J. R.; Hoang, K.; Mahanti, S. D.; Kanatzidis, M. G., *Inorg. Chem.* 2007, 46, 6933

36. Florio, J. V.; Rundle, R. E.; Snow, A. I., *Acta Crystallogr.* 1952, 5, 449.

37. Kalychak, Y. M.; Bakar, A. M., *Izv. VUZ. Tsvetn.Metall.* 1989, 6, 106.

38. Sysa, L. V.; Kalychak, Y. M.; Bakar, A. M.; Baranyak, V. M., *Krystallografiya* 1989, 34, 744.

39. Zaremba, R.; Muts, I.; Hoffmann, R.-D.; Kalychak, Y. M.; Zaremba, V. I.; Pottgen, R., *J. Solid State Chem.* 2007, 180, 2534.

40. Sheldrick, G. M. *SADABS and SAINT*, version 4; University of Gottingen: Gottingen, Germany, 1995.

41. Sheldrick, G. M. *SHELXTL, Structure Determination Program*, version 5; Siemens Analytical X-ray Instruments Inc.: Madison, WI, 1995.

42. *X-Area, IPDS Software*, STOE & Cie GmbH: D 64295 Darmstadt, Germany, 2006.

43. Rietveld, H. M., *Acta Crystallogr.* 1967, 22, 151.

44. Larson, A. C.; Dreele, V. *R. B. General structure analysis system, Report No. LAUR-86-748*, Los Alamos National Laboratory: Los Alamos, NM 87545, 2000.

45. Ravel, B.; Newville, M., *J. Synchrotron Rad.* 2005, 12:4, 537.

46. Salvador, J. R., *Unpublished results*, Michigan State University.

47. Florio, J. V.; Rundle, R. E.; Snow, A. I., *Acta Cryst.* 1952, 5, 449.

48. Materlik, G.; Muller, J. E.; Wilkins, J. W., *Phys. Rev. Lett.* 1983, 50, 267.

49. Malterre, D., *Phys. Rev. B* 1991, 43, 1391.

50. Rohler, J.; Wohlleben, D.; Kappler, J. P.; Krill, G., *Phys. Let.* 1984, 103A, 220.

51. Pikul, A. P.; Kaczorowski, D.; Bukowski, Z.; Gofryk, K.; Burkhardt, U.; Grin, Y.; Steglich, F., *Phys. Rev. B* 2006, 73, 092406.

52. Janousova, B.; Wilhelm, F.; Jaouen, N.; Rogalev, A.; Sechovsky, V. In *XANES and XMCD study of CePtSn*, 2005; Elsevier Science Bv: 2005; pp 127-129.

53. C. Giorgetti, e. a., *Phys. Rev. B* 1993, 48, 12732.

54. In Valence Fluctuations in Solids, Santa Barbara, Ca, 1981; Falikov, L. M.; Hanke, W.; Malpe, M. P., Eds. North-Holland Publishing Company, Amsterdam, New York, Oxford: Santa Barbara, Ca, 1981.

55. Okube, M.; Yoshiasa, A.; Yashima, M.; Ohuchi, K.; Ishimura, T.; Numako, C.; Koto, K., *Physica Scripta* 2005, T115, 375.

56. Rao, C. N. R.; Sarma, D. D.; Sarode, P. R.; Sampathkumaran, E. V.; Gupta, L. C.; Vijayaraghavan, R., *Chem. Phys. Let.* 1980, 76, 413.

57. Hatwar, T. K.; Nayak, R. M.; Padalia, B. D.; Ghatikar, M. N.; Sampathkumaran, E. V.; Gupta, L. C.; Vijayaraghavan, R., *Solid State Commun.* 1980, 34, 617.

58. Moreschini, L.; Dallera, C.; Joyce, J. J.; Sarrao, J. L.; Bauer, E. D.; Fritsch, V.; Bobev, S.; Carpene, E.; Huotari, S.; Vanko, G.; Monaco, G.; Lacovig, P.; Panaccione, G.; Fondacaro, A.; Paolicelli, G.; Torelli, P.; Grioni, M., *Physical Review B* 2007, 75, (3), 035113.

Chapter 8

Conclusions and Future Work

Throughout this dissertation In flux has proven to be a viable preparative tool and an excellent alternative to the conventional synthetic methods for the exploratory synthesis of new intermetallic compounds. Preliminary results from previous work in the synthetic explorations of RE/TM/In/Ge systems indicated that indium acts mainly as a non reactive flux with germanides in the same way that gallium acts as a non reactive flux with silicides in the RE/TM/Ga/Si/systems. This is in contrast with the highly reactive nature of molten Al in the systems RE/TM/Al/Si or Ge and molten Ga in the systems RE/TM/Ga/Ge where the flux was readily incorporated into the final product forming quaternary phases. However, the systematic investigations by utilizing In flux reactions in the form RE/TM/In/Ge, presented in this dissertation, led to the discovery of a number of quaternary phases that exhibit interesting structural features as well as chemical and physical properties.

Specifically, we have performed explorations of the type RE/TM/Ge/In where TM represents first raw transition metals such as Co and Ni and we have succeeded in isolating the new quaternary compounds $RE_7Co_4InGe_{12}$, $Yb_7Ni_4InGe_{12}$ and $Dy_4CoInGe_4$. Interestingly, only Dy, Ho and Yb form the $RE_7Co_4InGe_{12}$ phase and only Yb the $Yb_7Ni_4InGe_{12}$ one. Moreover, $Dy_4CoInGe_4$ was produced in the same reaction as $Dy_7Co_4InGe_{12}$ but was not observed with the rest of the RE metals. On the other hand, when the third raw transition metal of Au was employed under similar experimental conditions it led to the formation of the quaternary compounds of $Yb_3AuGe_2In_3$,

CeAuGeIn and $EuAuGeIn_2$. These results demonstrate the rich chemistry that can be explored when differing the elements involved in In flux reactions.

The formation of many of these multinary compounds is often due exclusively to the synthetic environment provided by the flux method. The overall structures of the new complex compounds vary considerably with the particular combination of constituent elements in them but similar structural features and units are often seen. These compounds exhibit many exciting physico-chemical properties which include mixed or intermediate valence behavior, multiple magnetic phase transitions or complex magnetic behavior which in case of $Yb_3AuGe_2In_3$ for example, depends strongly on the form of the measured sample and other experimental conditions and varies from being paramagnetic to exhibit ferromagnetic ordering. The intriguing magnetic properties observed for the $Yb_3AuGe_2In_3$ are not yet fully understood and future work with additional experimental techniques such as neutron diffraction experiments and detailed magnetic measurements under pressure and at various temperatures are required to further elucidate the reason behind these properties.

The ternary Yb_4TMGe_8 (TM = Cr, Fe, Co) compounds were also obtained in reactions involving excess of liquid In. This is an example of the non-reactive nature of In flux in the quaternary system of Yb/TM/Ge/In. Nevertheless, these ternary compounds do not luck in displaying structural complexity or fascinating properties. Detailed single crystal X-ray diffraction and (3+1)D crystallographic studies revealed the existence of superstructures due to both occupational and positional modulation in the extended square Ge nets and partial TM occupancies. The structural findings for Yb_4TMGe_8

challenge the correctness of the reported $RETM_{1-x}Ge_2$ disordered compounds and call for a re-investigation of their structures.

Furthermore, all three Yb_4TMGe_8 compounds exhibit Yb mixed-valence behavior with the Yb^{3+}/Yb^{2+} ratio constantly changing with the temperature and an anomalous nearly zero thermal expansion of the cell volume up to ~ 100 – 120 K, depending on the TM and a normally observed positive thermal expansion at higher temperatures. Additionally, heat capacity measurements for the Cr analog suggest possible heavy-fermion behavior whereas resistivity measurements for the Fe analog show unusual temperature dependence.

Due to the intriguing structural and physico-chemical properties exhibited by the latter compounds it will be of benefit to study more analogs of the Yb_4TMGe_8 series in order to examine the effect that the different employed transition metals could bring to the properties of these compounds. This could perhaps help to further elucidate the phenomena observed such as the nearly ZTE expansion behavior between 10 - 100 K, and right substitution or doping of these materials could extend the temperature range of the ZTE behavior. Discovering materials whose size does not change with temperature is a highly active field of study, both for technological applications and fundamental understanding.

The present work has principally concentrated in the synthetic explorations of the quaternary systems RE/TM/Ge/In by utilizing molten In as a solvent and a 1st row transition metal or the 3rd row transition metal of Au as TM. Many new and interesting compounds have been discovered however, these results represent only a small area of the overall potential of this method. This research should expand to include other

transition metals from the 2nd and 3rd row which holds promise for the discovery of potentially novel compounds or even isostructural analogs. These compounds could be interesting as simply new compounds or provide the opportunity to compare and contrast the chemistry and reactivity of the 1st row TM with that of the 2nd and 3rd row TM.

Finally, it would be of great importance for the future of this project to incorporate additional tetrelide elements in the study of the systems RE/TM/In such as Si. By studying In/Ge(Si) systems analogous to Al/Ge(Si) and Ga/Ge(Si) ones, which were investigated previously by other members of this group, could help draw parallel and trends in this chemistry which in turn could further shed light in understanding the chemical reactivity of the systems as well as the composition, structure and properties of the resulting products.